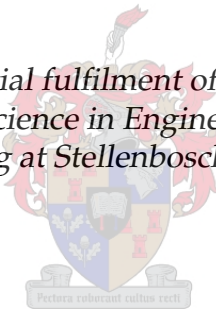# Accurate Autonomous Landing of a Fixed-Wing Unmanned Aircraft under Crosswind Conditions

by

Andrew de Bruin

Thesis presented in partial fulfilment of the requirements for the degree of Master of Science in Engineering in the Faculty of Engineering at Stellenbosch University

Department of Electrical & Electronic Engineering,
Stellenbosch University

Supervisor: Prof. T. Jones

March 2017

Declaration

By submitting this thesis electronically, I declare that the entirety of the work contained therein is my own, original work, that I am the sole author thereof (save to the extent explicitly otherwise stated), that reproduction and publication thereof by Stellenbosch University will not infringe any third party rights and that I have not previously in its entirety or in part submitted it for obtaining any qualification.

Date: March 2017

Abstract

This thesis presents the design, implementation and verification of an autopilot system with strong disturbance rejection characteristics, capable of landing a fixed-wing unmanned aircraft accurately under crosswind conditions. All aspects of the autopilot design are considered, from first principles to the final practically verified product. A mathematical aircraft model is derived, verified and analysed in detail to ensure the design of a high-fidelity, high-bandwidth flight control system. A synergistic controller architecture is proposed, where the approach is to design a structure capable of executing one of three crosswind landing techniques, or a combination thereof, by strategically sequencing controllers throughout the landing procedure. Various landing techniques, developed for manned aircraft, are investigated and emulated by the flight control system to exploit the advantages of each and to mitigate the risks associated with crosswind landings. A high-bandwidth acceleration-based control architecture was augmented with Direct Lift Control to improve gust alleviation performance in the aircraft's longitudinal axis. A state machine was used to facilitate effective controller sequencing and continuous hierarchical monitoring through strategically planned state transitions. Monte Carlo simulations were used to develop a landing accuracy prediction system that provides statistical information regarding the expected touchdown region given certain atmospheric conditions. Results from sixteen days of flight tests demonstrate the autopilot's success, and correspond exceptionally well with results obtained from high-fidelity hardware-in-the-loop simulations. Verification of the autopilot through practical flight testing and extensive simulations proved that the system is capable of performing crosswind landings accurate to within 0.5 m of the intended touchdown point.

Opsomming

Hierdie tesis stel bekend die ontwerp, implementering en verifikasie van 'n selfvliegstelsel met sterk versteuringsverwerpingseienskappe, wat 'n vastevlerk-onbemande vliegtuig in staat stel om akkuraat onder dwarswindtoestande te land. Alle aspekte van die selfvlieg-ontwerp word in ag geneem, vanaf eerste beginsels tot by die finale, prakties geverifieerde produk. 'n Wiskundig ontwikkelde vliegtuigmodel word afgelei, geverifieer en in fyn besonderhede ontleed om die ontwerp van 'n hoëtrou-, hoëbandwydte-vlugbeheerstelsel te verseker. 'n Sinergistiese beheerder-argitektuur word voorgestel, waar die benadering is om 'n struktuur te ontwerp wat in staat is tot die uitvoer van een van drie dwarswind-landingstegnieke, of 'n kombinasie daarvan, deur opeenvolgende beheerders strategies te gebruik regdeur die landingsproses. Verskeie landingstegnieke wat vir bemande vliegtuie ontwikkel is, word ondersoek en deur die vlugbeheerstelsel nagemaak om die voordele van elkeen te ontgin, en om die risiko's wat met dwarswindlandings verband hou, te verminder. 'n Hoëbandwydte-versnellingsgebaseerde beheerargitektuur is aangevul met direkte stygbeheer om die rukwind-verligtingsprestasie van die vliegtuig se longitudinale-as te verbeter. 'n Toestandsmasjien is gebruik vir effektiewe beheerder-opeenvolging en deurlopende hiërargiese monitering deur middel van strategies beplande toestandsoorgange. Monte Carlo-simulasies is gebruik om 'n akkurate landingsvoorspellingstelsel te ontwikkel, wat statistiese inligting aangaande die verwagte landingstreek onder sekere gegewe atmosferiese toestande kon bied. Die resultate van vlugtoetse wat oor 'n periode van sestien dae versamel is, bewys die sukses van die selfvliegstelsel, en stem besonder goed ooreen met die resultate verkry uit hoëtrou-hardeware-in-die-lus-simulasies. Verifikasie van die selfvliegstelsel deur dit aan praktiese vlugtoetse en uitgebreide simulasies te onderwerp, bewys dat die stelsel in staat is om onder dwarswind-toestande akkuraat tot binne 0.5 m van die beplande landingspunt te land.

Acknowledgements

I would like to thank the following people and organisations:

- Professor Thomas Jones for your support, guidance, advice and continuous motivation throughout the course of this project.

- My mother, father and brother for your continued love, support and encouragement.

- Chané Bunning for your understanding and motivation offered throughout the project. Thank you to and your family for being there to support me through the tough times.

- My flatmate Samuel Dodson for your careful and precise review of this document.

- Dr Japie Engelbrecht for your support, input and guidance offered throughout the course of this project.

- Armscor and the Electronic Systems Laboratory for funding the project.

- Christopher Fourie, Cornelus Le Roux, Gideon Hugo, Ryan Maggott and Piero Ioppo for all your assistance during the flight tests.

- Wessel Kroukamp for providing technical assistance with various aspects of the project.

- Micheal Basson for doing an excellent job as the safety pilot and for your charismatic personality that undoubtedly made flight testing more enjoyable.

- Clinton Basson for providing the necessary expertise and equipment required during the build.

- All my colleagues in the ESL for your motivation and good company.

Dedication

Aeronautics confers beauty and grandeur, combining art
and science for those who devote themselves to it...The
aeronaut, free in space, sailing in the infinite, loses
himself in the immense undulations of nature. He
climbs, he rises, he soars, he reigns, he hurtles the
proud vault of the azure sky...

Georges Besançon, founder of the first successful
aviation journal L'Aérophile, February 1902

Contents

List of Figures

List of Tables

Nomenclature

Acronyms

ADC	Analog-to-Digital Converter
AGL	Above Ground Level
ALS	Autoland System
AoA	Angle of Attack
AoSS	Angle of Sideslip
ATOL	Autonomous Take-Off and Landing
AV	Aerial Vehicle
AVL	Athena Vortex Lattice
CG	Centre of Gravity
DCM	Direction Cosine Matrix
DDC	Direct Drag Control
DGPS	Differential Global Positioning System
DLC	Direct Lift Control
ESL	Electronic Systems Laboratory
FCS	Flight Control System
FLC	Fuzzy Logic Control
GPS	Global Positioning System
HIL	Hardware-In-the-Loop
HOT	Higher-Order Terms
IAS	Indicated Airspeed
IMU	Inertial Measurement Unit
LQR	Linear Quadratic Regulator
LSA	Lateral Specific Acceleration
MAC	Mean Aerodynamic Chord
MIMO	Multi-Input, Multi-Output
MSL	Mean Sea Level
NMP	Non-Minimum Phase
NP	Neutral Point
NSA	Normal Specific Acceleration

NSADLC	Normal Specific Acceleration Direct Lift Control
OBC	On-Board Computer
PC	Personal Computer
PCB	Printed Circuit Board
PD	Proportional Derivative
PI	Proportional Integral
PIO	Pilot-Induced Oscillation
PTI	Programmed Test Input
PWM	Pulse Width Modulation
RC	Remote Control
RF	Radio Frequency
RPV	Remotely Piloted Vehicle
RTK	Real Time Kinematic
SAAF	South African Air Force
SISO	Single-Input, Single-Output
SMC	Standard Mean Chord
SU	Stellenbosch University
TAS	True Airspeed
TRA	Technology Readiness Assessment
TRL	Technology Readiness Level
TSS	Time Scale Separation
TUAV	Tactical Unmanned Aerial Vehicle
UART	Universal Asynchronous Receiver and Transmitter
UA	Unmanned Aircraft
UAS	Unmanned Aerial System
UAV	Unmanned Aerial Vehicle
UCAV	Unmanned Combat Aerial Vehicles
USB	Universal Serial Bus
VASI	Visual Approach Slope Indicator
VLOS	Visual Line Of Sight

Greek Letters

α	Angle of attack
β	Angle of sideslip
δ_a	Aileron perturbation from trim condition
δ_A	Total aileron deflection
δ_e	Elevator perturbation from trim condition
δ_E	Total elevator deflection
δ_f	Flap perturbation from trim condition
δ_F	Total flap deflection
δ_r	Rudder perturbation from trim condition
δ_R	Total rudder deflection
ΔT_c	Throttle perturbation from trim condition
ΔT	Thrust perturbation from trim condition
ϵ	Downwash angle
ϕ	Roll angle perturbation
λ	Eigenvalue
θ	Pitch angle perturbation
ρ	Air density
τ_e	Engine time constant
τ_c	Complementary filter time constant
ω_n	Natural frequency
ψ	Yaw angle perturbation
ζ	Damping ratio
Φ	Roll angle
Θ	Pitch angle
Ψ	Yaw angle
ξ	Spatial gradient

Small Letters

b	Wing span
$\bar{c}$	Standard Mean Chord
$\bar{\bar{c}}$	Mean aerodynamic chord
$\mathbf{c}$	Control Array
$\mathbf{c}_A$	Aerodynamic control array
e	Oswald efficiency factor
$\mathbf{e}$	Euler angle array
g	Gravitational acceleration
h	Altitude perturbation
l_F	Fin moment arm
l_T	Tailplane moment arm
m	Mass

p	Roll rate perturbation
q	Pitch rate perturbation
$\bar{q}$	Dynamic pressure
r	Yaw rate perturbation
s	Semi-span
u	Axial velocity perturbation
v	Lateral velocity perturbation
w	Normal velocity perturbation
y	Cross-track error
$\dot{y}$	Cross-track error rate

Capital Letters

A	Aspect ratio
C_D	Aerodynamic drag coefficient
C_L	Aerodynamic lift coefficient
C_l	Aerodynamic rolling moment coefficient
C_m	Aerodynamic pitching moment coefficient
C_n	Aerodynamic yawing moment coefficient
C_x	Aerodynamic axial force coefficient
C_y	Aerodynamic lateral force coefficient
C_z	Aerodynamic normal force coefficient
I	Moment of inertia
I_{xx}	Moment of inertia about the roll axis
I_{yy}	Moment of inertia about the pitch axis
I_{zz}	Moment of inertia about the yaw axis
I_{xy}	Roll and pitch product of inertia
I_{xz}	Roll and yaw product of inertia
I_{yz}	Pitch and yaw product of inertia
L	Rolling moment
M	Pitching moment
N	Yawing moment
P_D	Position in the down direction
P_E	Position in the east direction
P_N	Position in the north direction
P	Roll rate
Q	Pitch rate
R	Yaw rate
S	Wing area
T	Engine thrust magnitude
U	Axial velocity
V	Lateral velocity

$\bar{V}$	Velocity magnitude
W	Normal velocity
X	Axial force
Y	Lateral force
Z	Normal force

Constants

g	9.81 m/s^2
ρ	1.225 kg/m^3

Subscripts

0	Trim and zero angle of attack
ac	Aerodynamic centre
B	Body reference frame
E	Earth/Inertial reference frame
F	Fin
W	Wing
T	Tailplane

Superscripts

A	Aerodynamic
G	Gravitational
T	Thrust as well as matrix transpose

CHAPTER 1

Introduction and Overview

1.1 Background

An Unmanned Aerial Vehicle (UAV) is a class of aircraft that is either piloted by remote control or by means of an on-board computer. UAVs are used around the world for various surveillance, reconnaissance, intelligence, and strike missions for both military and commercial applications. The earliest recorded application of a UAV on the battlefield was in 1849 when the Austrians attacked the city of Venice with lighter-than-air balloons loaded with explosives [1]. The application of UAVs for a variety of missions in Operation Enduring Freedom (OEF) and Operation Iraqi Freedom (OIF) represents a culmination of over 60 years of technological development [2]. During the Vietnam war, UAVs were used for gathering signals data, electronic warfare information, and photo/video reconnaissance [2]. Recent UAV developments include the introduction of Tactical Unmanned Aerial Vehicles (TUAVs) as well as Unmanned Combat Aerial Vehicles (UCAVs), of which the General Atomics MQ-1 Predator is perhaps the best known. These aircraft are expected to display high levels of autonomy and precision flight for accurate payload delivery. In South Africa there are two large companies that develop UAVs for both the South African Air Force (SAAF) and others abroad. Denel Dynamics' Hungwe UAV is capable of both piloted and fully autonomous flight, whilst their Seeker 400 system is capable of performing Autonomous Take-Off and Landing (ATOL). Paramount Group's Vulture Unmanned Aerial System (UAS) has an operational range of up to 40 km and also features ATOL capabilities. Motivated by this rapidly developing field of autonomous aircraft, the Electronic Systems Laboratory (ESL) at Stellenbosch University started their own research group in 2001. The subject of autonomous flight has been studied in the ESL ever since Peddle [3] successfully demonstrated autonomous waypoint navigation of a Reliance 0.46 trainer aircraft, using low-cost commercial off-the-shelf components in 2005.

1.2   Project History

Autonomous navigation of a UAV is an integral part of its operation. The ability of an aircraft to essentially "fly itself" is what makes these systems an attractive alternative to conventional manned flight. As mentioned above, Peddle [3] successfully demonstrated the successful autonomous flight of a small aircraft using low-cost commercial off-the-shelf components. The resulting autopilot system was able to conduct fully autonomous waypoint navigation once the aircraft was in the air, but lacked the ability to take off and land autonomously. This meant that a safety pilot would have to manually taxi the aircraft during the take-off phase, before engaging the autopilot once the aircraft was in a straight and level flight configuration. A similar procedure was repeated for the landing phase - a safety pilot would take control during the final approach and land the aircraft manually before bringing it to a complete stop on the runway. This lack of autonomy motivated Roos [4] to further expand the project, which led to the development of a successful ATOL system. Various projects have since been undertaken at the ESL with a focus on advanced flight control, aerobatic manoeuvres, and ATOL systems. In particular, the latest work done at the ESL includes the following research:

Autonomous Flight of a Model Aircraft: I. K. Peddle 2005 [3]. The outcome of this project showed the successful autonomous navigation of a fixed-wing aircraft.

Autonomous Take-Off and Landing of a Fixed-wing UAV: J. C. Roos 2007 [4]. The controllers designed in this project followed a classical control systems approach whereby successive loop closure was the primary technique.

Precision Landing of an UAV: B. Visser 2008 [4]. The controllers designed in this project followed an Acceleration-Based Controller (ABC) architecture that was developed internally (ESL) by Peddle [1]. This UAS made use of visual guidance techniques for position and attitude determination.

Accurate Autonomous Landing of a Fixed-Wing Unmanned Aerial Vehicle: F. N. Alberts 2012 [5]. The controllers designed and developed in this project also made use of an ABC architecture, but were extended to investigate the benefits of employing Direct Lift Control (DLC) during a landing approach.

Autonomous Landing of a Fixed-Wing Unmanned Aerial Vehicle using Differential GPS: S. J. Smit 2013 [6]. Smit made use of an ABC architecture, but focused more specifically on improving landing accuracy by making use of a Differential Global Positioning System (DGPS).

Autonomous Landing of a Fixed-Wing Unmanned Aerial Vehicle on a Moving Platform Using Energy Principles: C. T. Le Roux 2016 [7]. The controllers developed in this project make use of the law of conservation of energy to design optimal controllers for landing a fixed-wing aircraft on a moving platform.

The aforementioned research highlights the recent developments of the studies undertaken at the ESL. The research presented in this thesis is an extension of this work, and was commissioned as one of the final implementations of accurate fixed-wing ATOL systems. Control system techniques that were implemented in previous projects at the ESL were not explicitly designed to land an aircraft in adverse atmospheric conditions; instead, practical landing tests were conducted during ideal or close-to-ideal wind conditions.

1.3 Problem Statement

UAVs used for military applications in particular are required to operate in "dull, dirty and dangerous conditions", where they are exposed to a host of uncertainties and inherent complications associated with the modern battlefield. They typically operate in dangerous environments and are therefore at constant risk of being destroyed by enemy fire. Furthermore, due to the long-range capabilities of modern UAVs, they are required to operate in various weather conditions, the most challenging of which can be attributed to severe crosswind scenarios during a typical autonomous landing approach. Landing any aircraft in crosswind conditions is not a trivial task, even for experienced human pilots: the unpredictability of wind gusts and turbulence complicate the final approach. Crosswind landings often result in severely degraded landing accuracy and may cause damage to the undercarriage if touchdown occurs with excessive crab angles. The following statistical data published by Airbus [8] motivates this problem statement:

- Adverse wind conditions (i.e. strong crosswinds, tailwinds and wind shear) are involved in 33% of approach and landing accidents

- Crosswind in association with runway conditions is a circumstantial factor in nearly 70% of runway excursion events

- 85% of crosswind incidents and accidents occur at landing

In order to mitigate the aforementioned risks, pilots make use of various crosswind landing techniques, each with their own advantages and disadvantages, that they will employ during the final approach. This research is focused on the development of an Autoland System (ALS) capable of landing a fixed-wing Unmanned Aircraft (UA) accurately under adverse weather conditions. The ALS consists of a synergistic, high-bandwidth controller architecture designed to emulate one of three crosswind landing techniques, or a combination thereof, by simply activating various controllers at different stages of the final approach. A state machine governs the controller activation times and monitors all system states to ensure a safe, successful, and accurate landing.

1.4 Research Objectives

Main objective: Design and develop an autoland system for a fixed-wing unmanned aircraft, capable of executing accurate crosswind landings by emulating various techniques developed for manned aircraft. The autoland system should be able to land the aircraft within a 1.5 m radius of the intended touchdown point.

Secondary objective: Minimise landing gear side-loads and the amount of lateral runway deviation experienced after touchdown. The heading angle error (crab angle) should be less than 5° at touchdown.

The following list provides a detailed description of the objectives to be achieved, which will be referred to in the concluding chapter as a method of quantifying the extent to which the project was successfully completed:

1. **Modelling**

    a) Determine the stability and control derivatives

    b) Obtain the non-linear aircraft dynamic equations

    c) Linearise the equations of motion

    d) Critically analyse the linear aircraft model

2. **Control system design**

    a) Design the longitudinal flight controllers

    b) Design the lateral flight controllers

    c) Design the runway controllers

    d) Analyse the controller interactions

3. **Navigation and landing strategies**

    a) Design and implement the navigation logic

    b) Investigate the landing constraints and limitations

    c) Develop the controller sequencer logic

    d) Design and implement the landing state machine

4. **Verification**

    a) Design and establish a high-fidelity, non-linear simulation environment

    b) Analyse the software-in-the-loop simulation results

    c) Analyse the hardware-in-the-loop simulation results

    d) Analyse and compare the practical flight test results

1.5   Thesis Layout

This thesis is partitioned into nine chapters, the structure of which is illustrated by the flow diagram depicted in Figure 1.1. It is apparent from the diagram that this thesis covers all aspects of the autopilot design, from first principles to the final, practically verified product. A literature study is conducted in Chapter 2, where both internal and external research into the field of autonomous UAVs is presented. Chapter 3 describes the definitions and dynamic equations required to accurately model the aircraft and its environment. This chapter concludes with the development

of a non-linear aircraft model required for stability analysis, control system design, and autopilot verification through non-linear simulations. The non-linear model is then linearised in Chapter 4 using small disturbance theory. Chapter 4 concludes with a critical analysis of a linearised aircraft model specific to the airframe used for practical verification. This analysis sets the scene for the controller design detailed in Chapter 5, where a synergistic architecture is developed and the design details are presented. Chapter 6 presents the final algorithms required for fully autonomous navigation, and discusses the constraints and limitations associated with crosswind landings. This chapter concludes with the development of a state machine responsible for continuous hierarchical monitoring and controller sequencing. The development of a non-linear simulation environment is detailed in Chapter 7, before system performance is evaluated through high-fidelity software-in-the-loop simulations. The avionics and ground station hardware and software design are then considered in Chapter 8, before hardware-in-the-loop simulations and flight test results are presented and analysed in detail. The concluding chapter, Chapter 9, presents a summary of the research, discusses the results obtained and details the contributions made to the existing knowledge base of the ESL research group. Recommendations for further research are also presented in the concluding chapter.
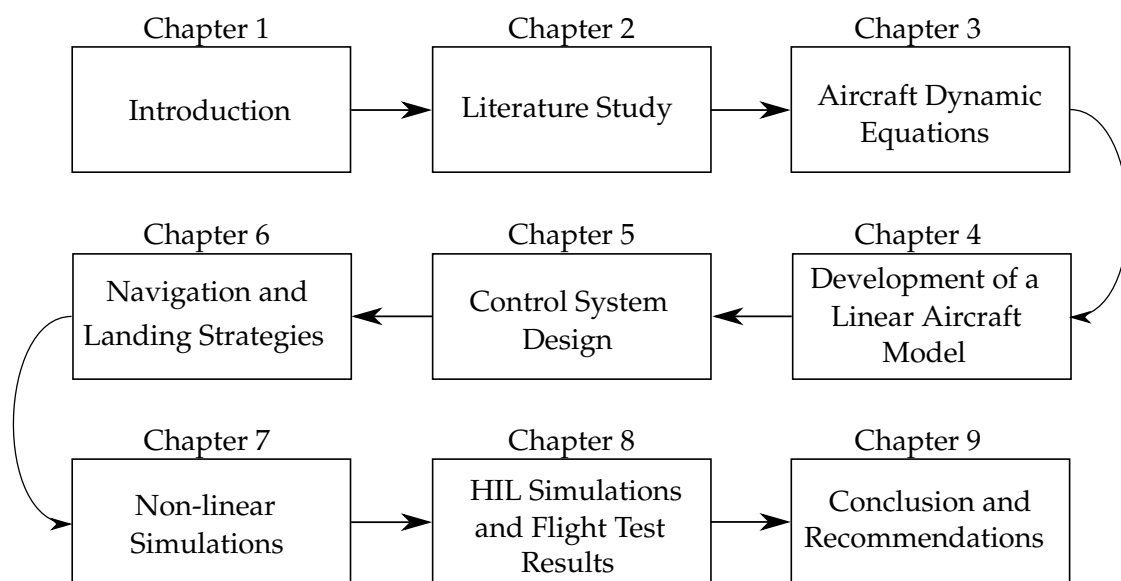
Figure 1.1: Thesis layout flow diagram

CHAPTER 2

Research and Associated Literature

The purpose of this chapter is to highlight similar work that has been conducted both internally (ESL) and externally. Relevant works help to clarify the scope of the project, as they provide some background information about the current state of the research as well as possible research gaps to be filled. The chapter starts by firstly expanding on some internal work done at the ESL before moving on to an explanation of similar external works.

2.1   Internal Projects (ESL)

In 2007 Roos [4] demonstrated the successful ATOL of a Reliance 0.46 model aircraft based on the work done by Peddle [3]. Runway controllers, designed based on the dynamics of a simplified runway model, would guide the aircraft down the runway centreline during take-off and landing. A landing state machine was also developed, which would switch between take-off, nominal flight, and finally the landing state. An altitude and guidance controller would guide the aircraft along a particular landing glideslope until the landing gear was in contact with the runway surface. Runway controllers would then take over and bring the aircraft to a complete stop on the runway. The controllers were designed based on a classical control architecture. Non-linear aircraft dynamics were investigated in great detail before root locus design techniques were employed to achieve predefined closed-loop specifications. Both software-in-the-loop (SIL) and hardware-in-the-loop (HIL) simulations were conducted at various stages of the project to evaluate system performance. Practical flight tests showed that the system was capable of ATOL; however, landing accuracy was not very high even in ideal weather conditions.

In 2008 Visser [9] investigated the possibility of designing an ATOL system using the ABC architecture developed by Peddle [1]. This architecture has superior disturbance rejection capabilities when compared to those of classical controller design techniques. This project differed somewhat from the majority of the autonomous landing projects at the ESL in the way that the outer-loop guidance controller determined the position of the aircraft. Computer vision tech-

niques were employed on the information obtained from a pin-hole camera located on the front end of the aircraft. The position of the aircraft relative to the runway was determined based on visual references as opposed to GPS references, as used by Peddle [3] and Roos [4]. The guidance controller used visual feedback techniques to guide the aircraft along the runway and glideslope. A disaster occurred during one of the practical test flights when the aircraft became unresponsive to any commands (both autopilot and manual), which resulted in the destruction of the airframe. As a result, a practical landing test was never conducted, although simulations showed that it would work in practice.

In 2012 Alberts [5] also made use of ABC techniques for accurate fixed-wing aircraft landing. This work differed from the work done by Visser in that the longitudinal controllers were augmented to include Direct Lift Control (DLC) capabilities. DLC is a method of actively using flaps to generate lift [10] and has shown to significantly improve disturbance rejection capabilities in the aircraft's longitudinal axis. Research conducted by Gerrits [10] showed that employing DLC on a full-sized Cessna Citation II aircraft improved longitudinal control characteristics, thereby increasing landing accuracy. Alberts successfully augmented the ABC longitudinal controller to use flaps as the primary DLC surface. The flaps of an aircraft have the advantage of instantaneously generating a lift force, whereas the conventional moment-based elevator control surface has a delayed response due to Non-Minimum Phase (NMP) zero characteristics. A complementary filter-type controller was designed, which would send the high-frequency commands to the flaps-based portion of the Normal Specific Acceleration (NSA) controller, and the low-frequency commands to the moment-based NSA controller. This type of complementary filtering exploited the high bandwidth effect that flaps have on generating lift, and would therefore be used primarily to negate the effects of high-frequency wind disturbances. The deflection of the flaps control surface would inherently induce either a positive or negative pitching moment (aircraft-dependent), which was minimised with the aid of what Alberts referred to as a "gearing term". This was essentially a proportional mixing parameter that uses the elevator to negate adverse pitching moments resulting from flap perturbations. The project showed promise of improved longitudinal control of an aircraft, especially during the glideslope tracking phase of the landing sequence. Non-linear guidance logic developed by Park et al. [11] was used in the lateral guidance controller to minimise cross-track errors, and proved capable of guiding the aircraft along a particular trajectory with high precision. One of the shortfalls encountered during this project was the fact that the altitude controller was a type 1 system (no free integrators) and would therefore follow a ramp input command (characteristic of a glideslope trajectory) with a steady-state error. This meant that during the final stages of a landing approach, the aircraft would be slightly above or below the intended glideslope trajectory. In an attempt to reduce the amount of overshoot/undershoot of the desired landing point and improve the overall landing accuracy, Alberts would first make the aircraft perform a fly-by to determine the amount of steady-state tracking error. He argued that simply moving the origin of the glideslope in the Z-axis, by an amount equal to the steady-state tracking error, would increase the accuracy of the landing. Practical flight tests in ideal weather conditions showed that the aircraft was able to land within 5 m of the intended landing point after the glideslope origin was adjusted by an amount proportional to the steady-state tracking error.

In 2013 Smit [6] made use of Peddle's ABC architecture, but focused on improving the landing accuracy by making use of a DGPS. Similar to the work done by Alberts [5], Smit also made

use of flaps during the landing approach, although not for the purposes of DLC. Instead, Smit used the flaps in a more passive configuration in the sense that the flaps would be deployed to a predefined deflection angle at a certain altitude during the landing approach. Deploying flaps has the advantage of simultaneously increasing the lift and drag forces on an aircraft, thereby lowering the stall speed (due to increased lift) and allowing for greater descent angles during landing. The aircraft landed within a 7.5 m radius of the intended touchdown point, with the heading aligned with the runway centreline. The longitudinal position error contributed the most to the observed landing inaccuracy, and was attributed to the combination of a shallow glideslope angle and a bias on the estimated climb rate.

In 2016 an ATOL system was developed by Le Roux [7] where the concept of Total Energy Control (TEC) was used in the design of optimal feedback controllers. The inner-loop controllers still made use of ABC techniques, whilst the outer-loop controllers used conservation of energy principles to guide the aircraft along a certain trajectory. Le Roux made use of hybrid linear guidance logic to minimise cross-track errors by commanding relevant roll angles. The goal of this project was to land a fixed-wing aircraft on a moving platform (linear translation) under ideal weather conditions.

2.2   External Projects

This section explains similar work done in the field of aeronautics outside of the ESL, and more specifically, work done on autonomous landing systems for unmanned aircraft.

2.2.1   Autonomous Navigation and Landing

Cho et al. [12] developed a UAS capable of automatic taxiing, take-off, and landing of a UAV based on a single-antenna GPS receiver. The controllers designed in the project specifically did not make use of any inertial sensors, such as gyroscopes and accelerometers, in an attempt to show the full potential of a single-antenna, GPS-receiver-based attitude determination system [12]. A DGPS is used to give high-accuracy position information necessary during take-off and landing procedures. They showed that for a fixed-wing aircraft in coordinated flight, attitude information can be estimated from measurements from a single GPS receiver. A GPS does not have the ability to determine airspeed, which is a vitally important measurement, especially during the take-off and landing phases. A pitot-static tube was thus fitted to the aircraft and used to obtain accurate airspeed measurements. Linear Quadratic Regulator (LQR) controllers were designed for take-off and landing based on linearised equations of motion. Practical flight tests proved that the UAV was able to taxi along the runway, follow a predefined waypoint path, and land fully autonomously.

A paper by Liu et al. [13] adopted a different longitudinal controller design approach to that of Alberts [5]. Instead of using a complementary filter pair and compensating for adverse pitching moments with "gearing", altitude and pitch angle were quasi-decoupled by using flaps for altitude control and elevator for pitch angle control - airspeed was thus controlled with throttle. A fuzzy logic gain scheduled controller and adaptive neural network were introduced to improve the trajectory trace performance in the presence of wind disturbances during the landing phase.

Flight tests indicated that the aircraft was able to track a specified ground track robustly and was capable of landing with high security against modelling errors and disturbances.

During a landing approach, it is essential that the controllers be robust against wind disturbances and that the altitude controller can control height accurately enough to support an autoland function. A study done by Lopez et al. [14] compared two different altitude tracking controllers: H_∞ and Quantitative Feedback Theory (QFT). The design accomplished in this study was performed using a sideslip technique (low-wing approach), where the heading of the aircraft is aligned with the runway whilst the resulting side force due to sideslip angle is countered by banking in the direction of the crosswind. It was shown that both controllers (QFT and H_∞) provide robust stability and are able to attenuate high-frequency noise. Practical flight test results showed that the QFT design gives a smoother performance and a control effort slightly less than the one obtained with the H_∞ controller. The H_∞ design showed improved trajectory tracking in comparison to the QFT controller, and proved to be less user-dependent.

A paper presented by Salfi et al. [15] proposed and implemented control laws for the autolanding phase of a UAV up until the touchdown point (no runway controllers). Non-linear guidance logic was used for lateral control, whilst glideslope control consisted of airspeed regulation and off-glideslope distance controlled in the pitch axis. A new non-linear guidance logic in the pitch axis was devised for accurate glideslope tracking, and its performance was compared with a linear PID controller. The controllers were designed for stability margins such that they showed robustness against modelling inaccuracies and external atmospheric disturbances. The guidance and control laws performed well in the complete 6DoF non-linear simulation environment, and showed robustness against wind disturbances and aircraft asymmetry. It was shown that the non-linear lateral guidance law gives nearly zero cross-track error, even in the presence of 20% crosswind. The new non-linear guidance law in the longitudinal plane helped avoid noisy pitch angle measurements and showed increased performance over the PID controller. Both controllers exhibited good robustness against wind disturbance and it was said that the guidance and control laws may be deployed in the actual autolanding of a UAV.

Singh and Padhi [16] presented a non-linear control approach using dynamic inversion for automatic landing of UAVs. This technique relies on the philosophy of feedback linearisation, where the feedback control structure cancels non-linearities in the plant, such that the closed-loop plant behaves like a linear system [16]. The purpose of this linearisation is so that linear control systems theory can be applied in the design of the feedback controllers. Some advantages of using this type of feedback linearisation include simplicity in the control structure, ease of implementation and global exponential stability of the tracking error. The underlying assumption of dynamic inversion involves accurate knowledge of the dynamic model and a true estimate of the states, both of which can be achieved by augmenting dynamic inversion with neuro-adaptive techniques and using an Extended Kalman Filter (EKF) for non-linear state estimation. The control laws were tested in a non-linear simulation environment and showed promising results; however, the non-linear simulation was not conducted in the presence of wind shear and wind gusts.

Pouya and Saghafi [17] developed a controller for autonomous lateral alignment of a fixed-wing UAV with the runway centreline during a landing approach. Fuzzy Logic Control (FLC) is used in order to allow the vehicle to mimic the decision-making procedure that a human pilot would follow in the same situation. The longitudinal controller that was used for glideslope

tracking was designed using pole-placement techniques. The controller structure presented in this paper was focused on vision-based flight control systems. A built-in vision system and associated image processing unit provided the runway relative position and orientation for the outer-loop controllers. The controller developed in this paper does not directly depend on aircraft-specific dynamics (which is not the case with classical control) and therefore has the potential of being a generic autonomous landing controller that only needs to be slightly tuned when controlling a similar airframe. Non-linear simulations proved the FLC to have satisfactory performance and robustness against modelling inaccuracies.

Hueschen [18] designed and developed an autoland system using full-state feedback modern control theory techniques. Feedback gains were determined directly in the discrete domain from linear aircraft, desired path, and wind models. Various control modes were then developed by formulating appropriate desired path commands, changing a few gains for each mode, and by augmenting the control structure (adding integrators) to achieve the desired performance characteristics. Practical flight tests demonstrated that each of the six control modes of the Digital Integrated Automatic Landing System (DIALS) successfully performed its intended function. The system showed robustness against wind disturbances when subjected to a crosswind shear of magnitude 8 knots/100 ft. Although the system performed well, it still had the disadvantage of making use of full-state feedback, which meant that a Kalman filter had to be designed to provide estimated states to the feedback law. This is not usually an issue when there are only a few states to estimate; however, in the case of DIALS this resulted in 16 longitudinal and 13 lateral states that had to be estimated at each sample period.

Rui et al. [19] adopted a mixed H_2/H_∞ robust control method in order to track a desired trajectory even when the UAV is under the influence of uncertainties and disturbances. The H_2 component of the controller was used to achieve an excellent dynamic response, whilst the H_∞ component was used to minimise the effect of disturbances. A Linear Matrix Inequality (LMI) approach was used for the derivation of the optimal feedback control gains. In another paper, Wang et al. compared the performance of the robust H_2/H_∞ to that of a classical PID controller under the same circumstances. A non-linear simulation showed that the robust H_2/H_∞ controller provides excellent dynamic response and a smaller steady-state tracking error when compared to the classical controller. The H_2/H_∞ proved more robust than the PID controller when exposed to uncertainties such as ground effect and atmospheric disturbances.

2.2.2 Crosswind Landing Techniques

A pilot landing an aircraft in ideal weather conditions (in the absence of a crosswind) typically aligns the aircraft's longitudinal axis (heading) with the runway centreline, whilst descending at a constant rate along a particular glideslope in a wings-level configuration. At larger airports, pilots make use of the Visual Approach Slope Indicator (VASI) to determine whether they are on the correct glideslope or not. These approach lights may be visible from up to 8 km during the day and up to 32 km or more at night [20]. Just before touchdown, a flare manoeuvre is executed, which effectively slows down the rate of descent and ultimately allows for a more graceful touchdown. The aircraft enters a roll-out phase once the landing gear has made contact with the runway surface, and continues to reduce its ground speed until it comes to a complete stop.

In adverse weather conditions, and more specifically in the presence of a crosswind, the landing approach needs to be altered somewhat to ensure a safe and successful landing. Due to the natural directional stability of most aircraft, aerodynamic effects produce yawing moments that force an alignment between the longitudinal body axis and the resultant velocity vector. The angle between an aircraft's longitudinal axis and its velocity vector is commonly referred to as the angle of sideslip and denoted by β. During final approach in the presence of a crosswind, an aircraft will therefore naturally transition into a zero sideslip configuration, where its nose is pointing in the direction of the oncoming airflow. However, a crosswind means that the direction of the oncoming airflow in the inertial frame, with which the aircraft has now aligned itself, is not aligned with the runway on which the aircraft needs to land. The angle between the aircraft's longitudinal axis and the runway heading is commonly referred to as the crab angle and denoted by Ψ_{crab}. Figure 2.1 shows an aircraft approaching the runway and landing in a crabbed configuration. It is intuitive that larger crab angles will result in more violent lateral deviations from the point of touchdown and cause excessive side forces on the aircraft's landing gear. Touchdown in a crab-only configuration is therefore not recommended when landing on a dry runway [14]. On wet runways, which are inherently more slippery, the drift towards the upwind side of a touchdown is significantly reduced, and is therefore used as a viable landing configuration in certain scenarios [14].
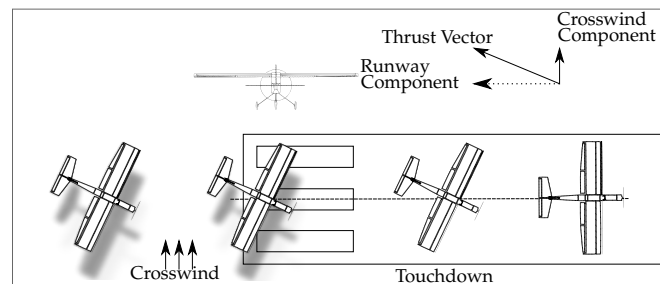
Figure 2.1: Crabbed landing technique

There are three main techniques that pilots will adopt when landing during typical crosswind conditions. One of these techniques has already been discussed (crabbed landing), and the two remaining techniques are discussed below:

De-crab:
The idea of this technique is to maintain a wings-level configuration throughout the entire landing phase [14]. The aircraft will approach the runway in a crabbed configuration, tracking the glideslope and maintaining flight path using appropriate longitudinal control. The crabbed and de-crab crosswind landing techniques are identical for most of the landing procedure; however, the difference between them is apparent during the final phase of landing. When a pilot executes a flare manoeuvre moments before touchdown, downwind rudder is applied to de-crab the aircraft and essentially minimise the angle between the aircraft's longitudinal axis and the runway centreline. In order to ensure a wings-level configuration upon touchdown, immediate opposite aileron is required to oppose the rolling moment caused by differential lift as the aircraft experiences a yaw rate perturbation. Figure 2.2a illustrates the de-crab landing technique.

(a) De-crab landing technique   (b) Low-wing landing technique
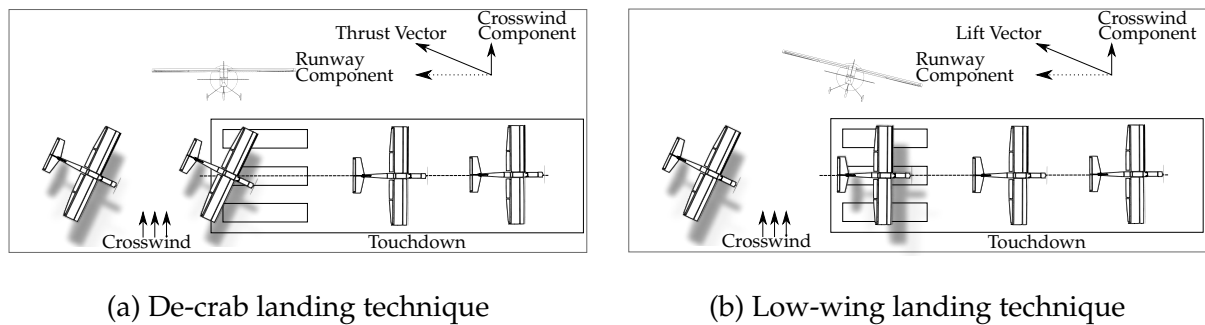
Figure 2.2: Crosswind landing techniques

Low-wing [1]**:**

The goal of this technique is to maintain the aircraft's heading aligned with the runway centreline throughout the approach and landing phase [14]. In this configuration, the aircraft's longitudinal axis is no longer aligned with the oncoming airflow, and thus there exists a non-zero sideslip angle ($\beta \neq 0$). The dihedral action of the wings has a tendency to cause the aircraft to roll, therefore sufficient rudder and aileron must be applied simultaneously to maintain the sideslip angle at a constant value [14]. In order to maintain a constant flight path by ensuring that the aircraft travels in the direction of the runway whilst flying in a sideslip configuration, it is necessary to coordinate a component of the lift vector to counter the side force by banking in the direction of the crosswind. Figure 2.2b illustrates the sideslip landing technique, and shows the aircraft approaching in a crabbed configuration before transitioning into a sideslip configuration during the final phase of landing. At the top left corner of the figure is an illustration of the residual bank angle necessary to maintain a constant flight path. Touchdown typically occurs with the upwind main wheel first, and it is therefore important to monitor the amount of bank angle so as to mitigate the risk of possible wingstrike[2].

2.2.3   Effect of Wind on Flight Characteristics

The unpredictability of wind effects often complicates the final approach and landing procedure of any aircraft. It is therefore necessary to examine the effects of non-uniform and unsteady motion of the atmosphere on the aircraft [21]. There are various forms of atmospheric effects that an aircraft will experience throughout the duration of a flight, namely wind gusts, turbulence effects, wind shear, and downbursts to name a few.

Wind gusts refer to the irregular wind velocity experienced at a single point in the atmosphere. An aircraft flying in gusty conditions will experience large variations in measured wind speed, and as a consequence, aerodynamic forces will accelerate the aircraft and vary its inertial speed. Wind gusts are usually modelled as having a build-up phase, a quasi-constant phase, and a decay phase. These encapsulate the principal effects of the gust. Turbulence refers to the random, chaotic and often violent movement of air as a result of varying wind currents. Turbulence effects are often modelled using either the von Kármán or the Dryden form of the spectra, where band-limited white noise is passed through shaping filters to generate turbulence velocities and angular

---

[1]Sometimes referred to as a sideslip landing.
[2]Collision of the upwind wing with the runway.

rates. The principal wind effects are those associated with atmospheric turbulence [21]; however, wind may have a mean structure which is not uniform in space. Etkin and Reid [21] describe this non-uniformity as spatial gradients in the time-averaged velocity, of which downbursts and the boundary layer next to the ground are of most concern. Downbursts result from vertical outflows from low-level clouds that impinge on the ground, usually in the form of a circular jet [21]. This results in strong vertical and horizontal wind gradients, which have led to many aircraft accidents.

Schänzer describes wind shear as an alteration of horizontal wind with time, height, and distance. Spatial gradients resulting from wind shear may crucially restrict flight safety during take-off and landing, and in some situations, hazards may be caused by limited flight performance [22]. It is apparent that the wind shear phenomenon is not well understood by most pilots, which often leads to incorrect decisions being made at crucial points in the flight. Wind shear is not only apparent in stormy, windy weather as one might expect. It is also related to misty summer mornings and bright sunshine in periods of fair weather [23]. According to Schänzer [22] flight safety may be reduced by wake turbulence caused by large buildings and mountains. He also states that the influence of wind shear on flight safety, during take-off and go-around, differs very much from the situation during approach and landing.

Schänzer claims that the majority of wind shear accidents, during approach and landing, can be avoided if the pilot or automatic control system reacts in the correct manner. He writes that the total energy of an uncontrolled aircraft in a wind shear situation is nearly constant - airspeed deviations are negligibly small and the aircraft will be accelerated without significant time delay with the time-varying wind [22]. This makes it difficult for the pilot or the control system to indicate a wind shear situation based on airspeed deviation, or even from criteria based on total energy deviation. A powerful wind shear indication is deviation from flight path [22]. Some control structures separate autopilot from autothrottle, and tend to avoid high-throttle activity as a response to high-frequency gusts by means of complementary filtering. The disadvantage of this is a delayed counteraction against the low-frequency wind shear disturbances, which leads to relatively great offsets in airspeed and flight path [22]. Schänzer [24] shows that the employment of a stronger cross-coupled control system, no longer separated into autopilot and autothrottle, leads to a considerable reduction in total energy expenditure.

Brockhaus and Wüst [25] show that offsets in airspeed and flight path, caused by wind shear, can be eliminated almost entirely by means of open-loop compensation. This method of compensation is based on the on-board measurement of the wind vector components, their time derivatives and a corresponding thrust command signal. This results in ideal thrust generation for given wind shear conditions, without changing the stability of the controlled aircraft [22]. In order to determine the individual wind components, this method of compensation requires that complete air data and inertial data be available. They conclude that this method cannot be successfully employed until the problem of separating the wind shear and gust signals has been solved.

A pilot should keep angle of attack, airspeed, and flight path angle constant during downdraft or downburst situations [22]. In the case of a downdraft, a pilot should pull back on the control column to increase the aircraft's pitch angle [24]. The idea of pitching nose-up in a situation where airspeed is decreasing seems counter-intuitive and goes against a pilot's training and gut feeling. In most cases, a pilot will try to keep the pitch angle constant, which will result in an undesirable glideslope deviation. Ground-based wind shear warning systems are worthwhile but

not sufficient. Some aircraft are equipped with wind shear warning display systems that inform the pilot about the current atmospheric conditions, and ultimately help to improve safety during wind shear landing situations.

One of the most important tasks that semi-automatic and automatic flight control systems should perform is damping the vibrations caused by atmospheric turbulence. Borowski and Wieslaw [26] show that atmospheric turbulence brings about substantial changes in the aircraft's angle of attack, which the control system should regulate by deflecting the elevator control surface. Most modern aircraft come equipped with anti-turbulence systems, which are designed to alleviate the effect of vibrations due to turbulent air. Birds are able to sense disturbances in airflow through their feathers, allowing them to fly gracefully through the air. Inspired by this natural phenomenon, one specific anti-turbulence system makes use of the concept of phase-advanced sensing to sense flow disturbances before they result in aircraft movement. They conclude that the correct choice of control law invalidates the need for a complex, specialised, and very expensive anti-turbulence system.

2.3   Summary

The findings documented in this chapter provide possible solutions to the host of challenges associated with landing a fixed-wing aircraft in crosswind conditions. Previous work conducted in the ESL provides a fundamental framework that can be adapted as required to maximise efficiency and system fidelity. Practical verification of non-linear simulation models by previous internal research will aid in the design of a high-performance control system capable of meeting strict specifications. It is clear from the findings presented in this chapter that there is no lack of knowledge in the field of autonomous unmanned aircraft. Particular aspects of these works will be incorporated in the design of the autopilot system presented in this thesis. Research into crosswind landing techniques for manned aircraft provides some insight as to how the control system should be structured for successful emulation of these techniques. The effect of wind on flying characteristics and handling qualities will influence various design decisions made throughout the development of a flight control system in this thesis.

CHAPTER 3

Aircraft Dynamic Equations

This chapter starts by defining the various reference systems used extensively throughout the aircraft modelling and control system design chapters. Thereafter, translational and rotational equations of motion are derived from Newton's laws and expressed in terms of forces and moments acting on the aircraft in the body axis. An attitude system is then defined, followed by a derivation of kinematic equations, which are added to the equations of motion to provide a complete set of non-linear aircraft dynamic equations. A short description of the aircraft reference geometry is provided, after which the chapter concludes with the derivation of the forces and moments responsible for driving the equations of motion.

3.1 Axis System Definition

Reference will be made to four axis systems in particular throughout this thesis. These axis systems will now be discussed in detail.

3.1.1 Inertial Axis System

Before Newton's equations of motion can be used to develop a dynamic aircraft model, an inertial axis system must be defined. The standard North-East-Down (NED) axis system, $F_E(O_E X_E Y_E Z_E)$ shown in Figure 3.1, adequately approximates an inertial axis system for localised flight [27]. The origin of the NED axis system is conveniently chosen to coincide with a point on the earth's surface, usually chosen as the starting point on the runway. The X_E-axis will then point in the north direction, the Y_E-axis will point in the east direction, and the Z_E-axis will point vertically downward perpendicular to the horizontal plane to complete the right-handed orthogonal axis system.

It is important to note that for the purposes of this thesis, the earth is considered flat and non-rotating - two essential properties of an inertial axis system [3]. These are reasonable assumptions given the short ranges of flight involved (only a few hundred metres), and the fact that the typical
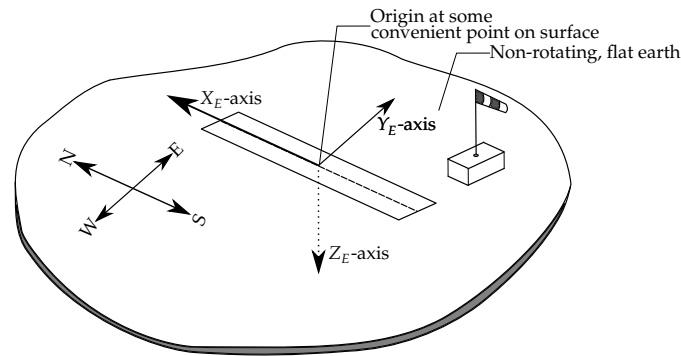
Figure 3.1: Inertial axis system

aircraft angular rates are far greater than the earth's rate of rotation. The north, east, and down position of the aircraft in inertial space is summarised in the following vector array form:

$$\boldsymbol{P}_I = \begin{bmatrix} N & E & D \end{bmatrix} \tag{3.1}$$

3.1.2 Body Axis System and Standard Aircraft Notation

The body axis system, $F_B(O_B X_B Y_B Z_B)$ shown in Figure 3.2, is fixed to the aircraft with the origin chosen to coincide with its centre of mass. The X_B-axis lies in the plane of symmetry and is conveniently chosen to point towards the nose of the aircraft. The Y_B-axis is perpendicular to the plane of symmetry and points in the direction of the starboard (right) wing. The Z_B-axis also lies in the plane of symmetry and points vertically downwards relative to the aircraft's cockpit to complete the right-handed orthogonal axis system. An aircraft is said to *pitch* about the Y_B-axis, *roll* about the X_B-axis, and *yaw* about the Z_B-axis.
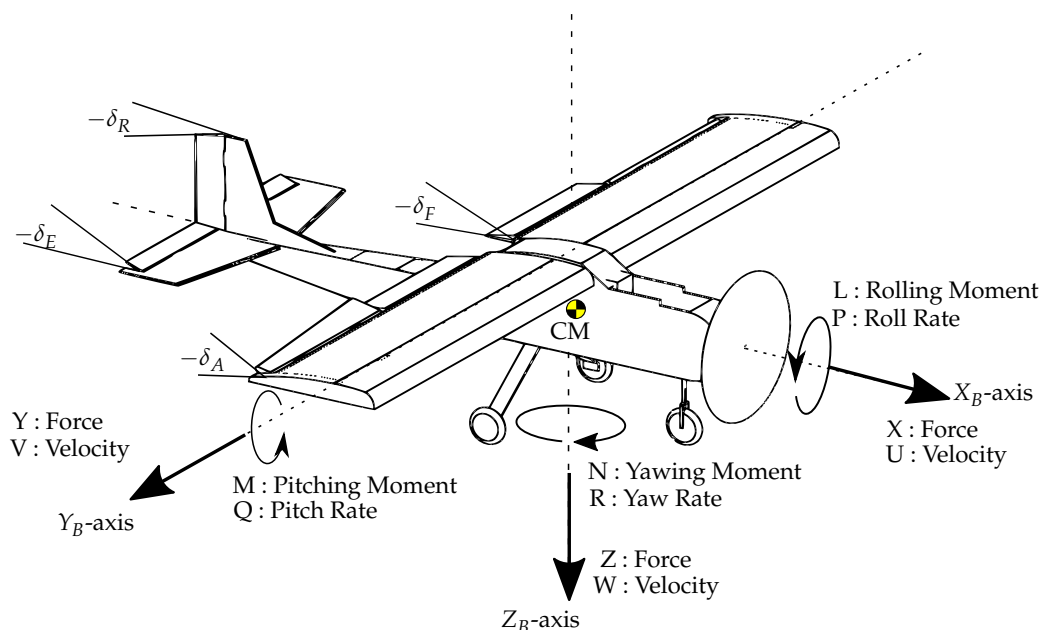
Figure 3.2: Body axis system with standard notation

Table 3.1 gives a detailed description of the symbols used in Figure 3.2.

Table 3.1: Standard aircraft notation

Symbol	Label	Description
X, Y, Z	Axial, lateral, and normal force	Coordinates of the force vector
L, M, N	Rolling, pitching, and yawing moment	Coordinates of the moment vector
U, V, W	Axial, lateral, and normal velocity	Coordinates of the linear velocity
P, Q, R	Roll, pitch, and yaw rate	Coordinates of the angular velocity
$\delta_E, \delta_F, \delta_A, \delta_R$	Elevator, flaps, aileron, and rudder deflection angles	A positive deflection is defined as one that produces a negative moment

Although not depicted in Figure 3.2, it is important to include the thrust command, denoted by T_c, which is proportional to the thrust vector magnitude. The aerodynamic control array can thus be extended to include the thrust command,

$$c = \begin{bmatrix} \delta_E & \delta_F & \delta_A & \delta_R & T_c \end{bmatrix} \tag{3.2}$$

3.1.3 Stability and Wind Axis System

It is often convenient to define a fixed aircraft axis system such that the X-axis coincides with the total velocity vector V_B. The stability axis $F_S(O_S X_S Y_S Z_S)$ is obtained by rotating the body axis through the angle of attack (α) about the centre of mass, as seen in Figure 3.3a. The origin of the stability axis system coincides with that of the body axis system, and follows a right-handed orthogonal axis convention. Aerodynamic stability and control derivatives are often specified in the stability axis, as it has the advantage of simplifying the aerodynamic model to maximise visibility of the physical phenomena involved. The wind axis $F_W(O_W X_W Y_W Z_W)$ is obtained by rotating the stability axis F_S through the sideslip angle (β), as seen in Figure 3.3b.

(a) Rotation through α

(b) Rotation through β
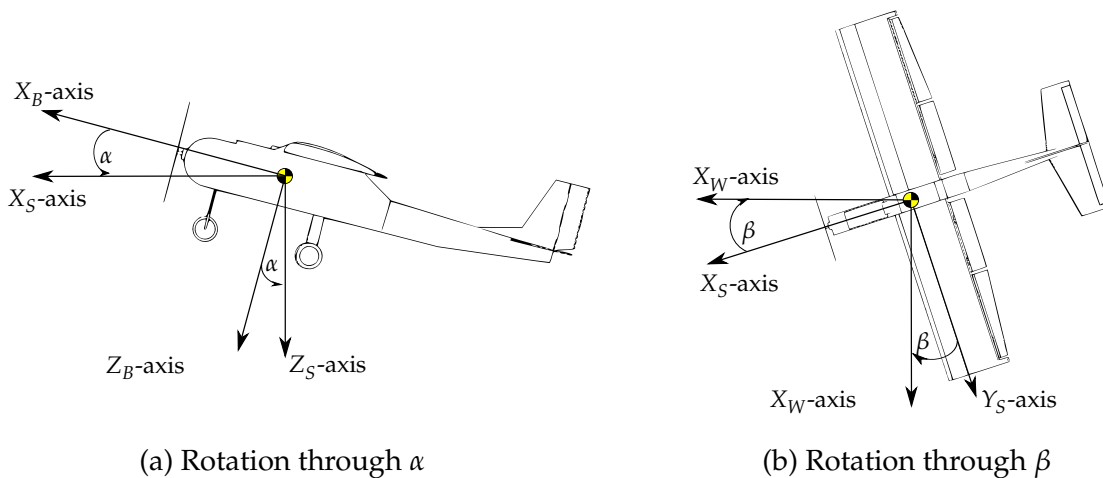
Figure 3.3: Stability and wind axis definitions

A vector V_B coordinated in the body axis can be transformed to the stability axis using the following rotation through angle of attack,

$$V_S = R_\alpha V_B \tag{3.3}$$

$$= \begin{bmatrix} \cos\alpha & 0 & \sin\alpha \\ 0 & 1 & 0 \\ -\sin\alpha & 0 & \cos\alpha \end{bmatrix} V_B \tag{3.4}$$

Furthermore, rotating the stability reference frame through the angle of sideslip, as shown in Figure 3.3b, yields the following rotation matrix,

$$V_W = R_\beta R_\alpha V_B \tag{3.5}$$

$$= \begin{bmatrix} \cos\beta & \sin\beta & 0 \\ -\sin\beta & \cos\beta & 0 \\ 0 & 0 & 1 \end{bmatrix} R_\alpha V_B \tag{3.6}$$

The aforementioned rotation matrices can then be multiplied to obtain a Direction Cosine Matrix (DCM), which relates a vector coordinated in the body axis to a vector coordinated in the wind axis,

$$R_\beta R_\alpha = \mathbf{DCM}_{B \to W} \tag{3.7}$$

$$= \begin{bmatrix} \cos\alpha\cos\beta & \sin\beta & \sin\alpha\cos\beta \\ -\cos\alpha\sin\beta & \cos\beta & -\sin\alpha\sin\beta \\ -\sin\alpha & 0 & \cos\alpha \end{bmatrix} \tag{3.8}$$

It is intuitive that the inverse of Equation (3.7) transforms a vector coordinated in the wind axis to a vector coordinated in the body axis through,

$$\mathbf{DCM}_{W \to B} = \left(\mathbf{DCM}_{B \to W} \right)^{-1} \tag{3.9}$$

Similarly, inverting the rotation matrix of Equation (3.3) relates a vector coordinated in the stability axis to a vector coordinated in the body axis. Section 3.3.1 details a more thorough investigation into the development of rotation matrices between corresponding frames of reference.

Now that the aforementioned rotation matrices have been defined, the translational and rotational velocity vectors, as well as the external forces and moments acting on the aircraft, are defined in Cartesian coordinates below,

$$V_B = i_B U + j_B V + k_B W \tag{3.10}$$

$$\omega_B = i_B P + j_B Q + k_B R \tag{3.11}$$

$$F_B = i_B X + j_B Y + k_B Z \tag{3.12}$$

$$M_B = i_B L + j_B M + k_B N \tag{3.13}$$

where $\pmb{i}_B$, $\pmb{j}_B$, and $\pmb{k}_B$ represent unit vectors in the X_B-, Y_B-, and Z_B-axis respectively. Although these vectors are measured with respect to inertial space, they are all coordinated in the body axis frame, as denoted by the subscript B. It is often convenient to express the velocity vector $\pmb{V}_B$ in terms of spherical coordinates, represented by a magnitude and two angles, as shown in Figure 3.4.
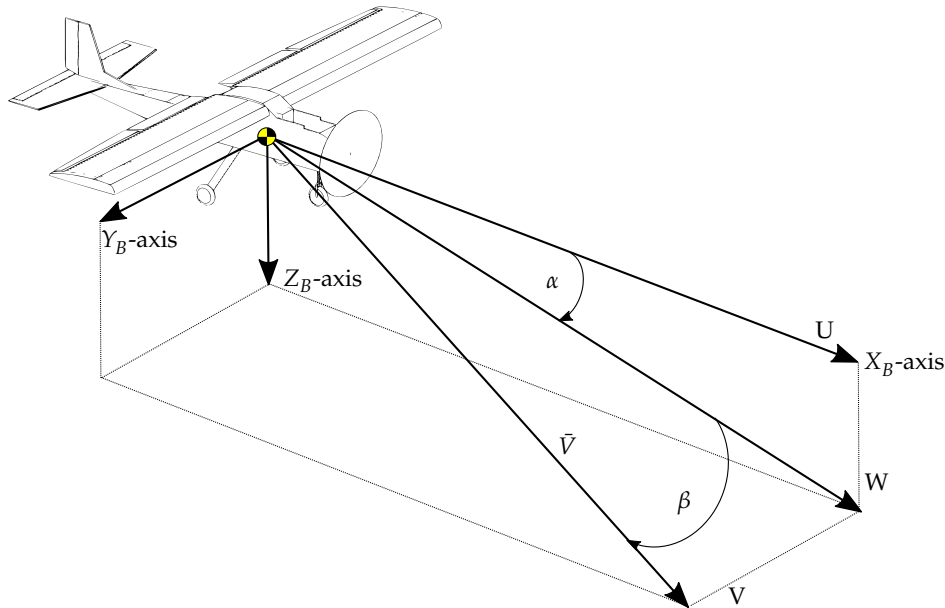
Figure 3.4: Spherical velocity coordinates

The velocity magnitude $\bar{V}$, angle of attack α, and sideslip angle β are expressed as, [1]

$$\bar{V} = \sqrt{U^2 + V^2 + W^2} \tag{3.14}$$

$$\alpha = \tan^{-1}(W/U) \tag{3.15}$$

$$\beta = \sin^{-1}(V/\bar{V}) \tag{3.16}$$

with their inverse relationships given by,

$$U = \bar{V} \cos\alpha \cos\beta \tag{3.17}$$

$$V = \bar{V} \sin\beta \tag{3.18}$$

$$W = \bar{V} \sin\alpha \cos\beta \tag{3.19}$$

3.2 Development of the Equations of Motion

The equations of motion acting on an aircraft can be derived from Newton's second law of motion. This law of motion states that the sum of all external forces acting on a body must be equal to the time rate of change of its momentum, and that the sum of all external moments acting on a

---

[1]The velocity magnitude $\bar{V}$ should not be confused with the lateral velocity component denoted by V.

body must be equal to the time rate of change of its angular momentum [28]. The time rates of change are with respect to inertial space, where it is assumed that the mass of the aircraft remains constant. Choosing the earth as an inertial reference, the time rates of change can be expressed by the following vector equations,

$$F_B = \frac{d}{dt}(mV_B)\Big|_E \tag{3.20}$$

$$M_B = \frac{d}{dt}(H_B)\Big|_E \tag{3.21}$$

where $\big|_E$ indicates the time rate of change of the vector with respect to inertial space, m represents the aircraft's mass, V_B its translational velocity, and H_B its angular momentum.

It would be convenient if the derivatives in Equations (3.20) and (3.21) were with respect to the body axis. Since the body axis system rotates with angular velocity ω_B with respect to the inertial frame, the Coriolis Equation [28] can be used to relate the inertial time derivative to the body time derivative with the following relationship,

$$\frac{d}{dt}(S)\Big|_E = \frac{d}{dt}(S)\Big|_B + \omega_B \times S \tag{3.22}$$

where S is an arbitrary vector. Applying Equation (3.22) to Equations (3.20) and (3.21) yields,

$$F_B = \frac{d}{dt}(mV_B)\Big|_B + \omega_B \times mV_B \tag{3.23}$$

$$M_B = \frac{d}{dt}(H_B)\Big|_B + \omega_B \times H_B \tag{3.24}$$

Evaluating the first term in Equation (3.23) if,

$$V_B = i_B U + j_B V + k_B W$$

then,

$$\frac{d}{dt}(mV_B)\Big|_B = m(i_B \dot{U} + j_B \dot{V} + k_B \dot{W}) \tag{3.25}$$

Now, evaluating the second term if,

$$\omega_B = i_B P + j_B Q + k_B R$$

then,

$$\omega_B \times mV_B = m \begin{vmatrix} i_B & j_B & k_B \\ P & Q & R \\ U & V & W \end{vmatrix} \tag{3.26}$$

Expanding,

$$\omega_B \times mV_B = m\left[i_B(WQ - VR) + j_B(UR - WP) + k_B(VP - UQ) \right] \tag{3.27}$$

Combining Equations (3.25) and (3.27) yields,

$$\boldsymbol{F}_B = m\left[\boldsymbol{i}_B(\dot{U} + WQ - VR) + \boldsymbol{j}_B(\dot{V} + UR - WP) + \boldsymbol{k}_B(\dot{W} + VP - UQ)\right] \tag{3.28}$$

From Equation (3.12), $\boldsymbol{F}_B$ can be written in terms of its components as follows,

$$\boldsymbol{F}_B = \boldsymbol{i}_B F_x + \boldsymbol{j}_B F_y + \boldsymbol{k}_B F_z$$

Equating the components of Equations (3.28) and (3.12), the equations of linear translational motion are obtained:

$$F_x = m(\dot{U} + WQ - VR) \tag{3.29}$$

$$F_y = m(\dot{V} + UR - WP) \tag{3.30}$$

$$F_z = m(\dot{W} + VP - UQ) \tag{3.31}$$

To obtain the equations of rotational motion, it is necessary to return to Equation (3.24), repeated below for convenience:

$$\boldsymbol{M}_B = \left.\frac{d}{dt}(\boldsymbol{H}_B)\right|_B + \boldsymbol{\omega}_B \times \boldsymbol{H}_B \tag{3.32}$$

It is necessary to obtain an expression for $\boldsymbol{H}_B$ before proceeding with the derivation. $\boldsymbol{H}$ is defined as the angular momentum, or moment of momentum, of a revolving body [28]. The momentum of the element of mass dm, shown in Figure 3.5, due to the angular velocity $\boldsymbol{\omega}$ is equal to the tangential velocity of the element of mass about the instantaneous centre of rotation, multiplied by dm. The incremental momentum resulting from the tangential velocity of the element of mass
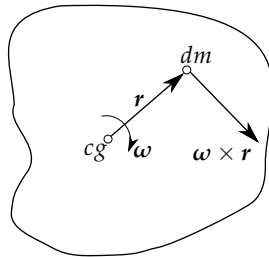
Figure 3.5: Fictitious body with an angular velocity $\boldsymbol{\omega}$ about its centre of gravity

can be expressed as,

$$d\boldsymbol{M} = (\boldsymbol{\omega} \times \boldsymbol{r})dm \tag{3.33}$$

Since the moment of momentum is the momentum multiplied by the lever arm [28], and taking the integral over the entire mass of the aircraft yields,

$$\boldsymbol{H}_B = \int \boldsymbol{r}_B \times (\boldsymbol{\omega}_B \times \boldsymbol{r}_B)dm \tag{3.34}$$

Evaluating the triple cross product using Equation (3.11) and,

$$\boldsymbol{r}_B = \boldsymbol{i}_B x + \boldsymbol{j}_B y + \boldsymbol{k}_B z \tag{3.35}$$

yields,

$$\boldsymbol{\omega}_B \times \boldsymbol{r}_B = \begin{vmatrix} \boldsymbol{i}_B & \boldsymbol{j}_B & \boldsymbol{k}_B \\ P & Q & R \\ x & y & z \end{vmatrix} \tag{3.36}$$

Expanding,

$$\boldsymbol{\omega}_B \times \boldsymbol{r}_B = \boldsymbol{i}_B(zQ - yR) + \boldsymbol{j}_B(xR - zP) + \boldsymbol{k}_B(yP - xQ) \tag{3.37}$$

Then,

$$\boldsymbol{r}_B \times (\boldsymbol{\omega}_B \times \boldsymbol{r}_B) = \begin{vmatrix} \boldsymbol{i}_B & \boldsymbol{j}_B & \boldsymbol{k}_B \\ x & y & z \\ zQ - yR & xR - zP & yP - xQ \end{vmatrix} \tag{3.38}$$

Expanding and substituting into (3.34) becomes,

$$\boldsymbol{H}_B = \int \boldsymbol{i}_B \left[(y^2 + z^2)P - xyQ - xzR \right] dm$$

$$+ \int \boldsymbol{j}_B \left[(z^2 + x^2)Q - yzR - xyP \right] dm$$

$$+ \int \boldsymbol{k}_B \left[(x^2 + y^2)R - xzP - yzQ \right] dm \tag{3.39}$$

Since $\int (y^2 + z^2)dm$ is defined as the moment of inertia I_{xx}, and $\int (xy)dm$ is defined as the cross product of inertia I_{xy}, Equation (3.39) can be rewritten in component form as,

$$H_x = PI_{xx} - QI_{xy} - RI_{xz}$$

$$H_y = QI_{yy} - RI_{yz} - PI_{xy}$$

$$H_z = RI_{zz} - PI_{xz} - QI_{yz} \tag{3.40}$$

It can be seen that $\boldsymbol{H}_B = \boldsymbol{I}_B \boldsymbol{\omega}_B$ where,

$$\boldsymbol{I}_B = \begin{bmatrix} I_{xx} & I_{xy} & I_{xz} \\ I_{xy} & I_{yy} & I_{yz} \\ I_{xz} & I_{yz} & I_{zz} \end{bmatrix} \tag{3.41}$$

Assuming that $I_{xy} = I_{yz} = 0$ for the case of a symmetric aircraft about the $X_B Z_B$-plane, Equation (3.40) reduces to,

$$H_x = PI_{xx} - RI_{xz}$$

$$H_y = QI_{yy}$$

$$H_z = RI_{zz} - PI_{xz} \tag{3.42}$$

Now that we have an expression for the moment of momentum H_B, the derivation can continue. Looking at the first term in Equation (3.32), the components of $\frac{d}{dt}(H_B)$ are,

$$\frac{dH_x}{dt} = \dot{P}I_{xx} - \dot{R}I_{xz}$$

$$\frac{dH_y}{dt} = \dot{Q}I_{yy}$$

$$\frac{dH_z}{dt} = \dot{R}I_{zz} - \dot{P}I_{xz} \tag{3.43}$$

The time rates of change of the moments and products of inertia are zero, since the aircraft is assumed to be a rigid body of constant mass. Evaluating the second term in Equation (3.32) yields,

$$\omega_B \times H_B = \begin{vmatrix} i_B & j_B & k_B \\ P & Q & R \\ H_x & H_y & H_z \end{vmatrix} \tag{3.44}$$

Expanding,

$$\omega_B \times H_B = i_B(QH_z - RH_y) + j_B(RH_x - PH_z) + k_B(PH_y - QH_x) \tag{3.45}$$

From Equation (3.13), M_B can be written in terms of its components as follows,

$$M_B = i_B L + j_B M + k_B N$$

Combing Equations (3.43) and (3.45) and equating the components of Equation (3.13) yields the following angular Equations of motion in component form,

$$L = \dot{P}I_{xx} - \dot{R}I_{xz} + QR(I_{zz} - I_{yy}) - PQI_{xz} \tag{3.46}$$

$$M = \dot{Q}I_{yy} + PR(I_{xx} - I_{zz}) + (P^2 - R^2)I_{xz} \tag{3.47}$$

$$N = \dot{R}I_{zz} - \dot{P}I_{xz} + PQ(I_{yy} - I_{xx}) + QRI_{xz} \tag{3.48}$$

3.3 Attitude Definition

The equations of motion developed in Section 3.2 describe how the forces and moments coordinated in the body axis cause rates of change in the linear and rotational velocities. It is therefore necessary to specify the orientation of the body axis with respect to the inertial frame so that the aircraft's motion in the inertial space can be described. The Euler 3-2-1 angles are one of the most widely used attitude parametrisation methods because they are simple and easy to work with.

3.3.1 Euler Angles and the Transformation Matrix

The transformation from the body axis to the inertial frame using the Euler 3-2-1 parametrisation method consists of a three-stage rotation through *yaw* (Ψ), *pitch* (Θ), and *roll* (Φ). The Euler angles
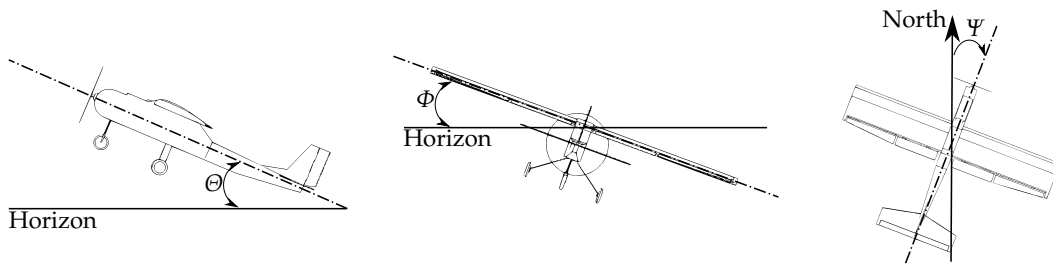
Figure 3.6: Basic illustration of attitude angles

used in the parametrisation are depicted in Figure 3.6 and summarised in the following vector array form:

$$e = \begin{bmatrix} \Phi & \Theta & \Psi \end{bmatrix} \tag{3.49}$$

Consider an axis system $F_0(O_0 X_0 Y_0 Z_0)$ that coincides with the inertial frame F_E. Now consider a vector V coordinated in F_0 such that,

$$V_0 = \begin{bmatrix} x_0 \\ y_0 \\ z_0 \end{bmatrix} \tag{3.50}$$

(a) Rotation through Ψ (b) Rotation through Θ (c) Rotation through Φ
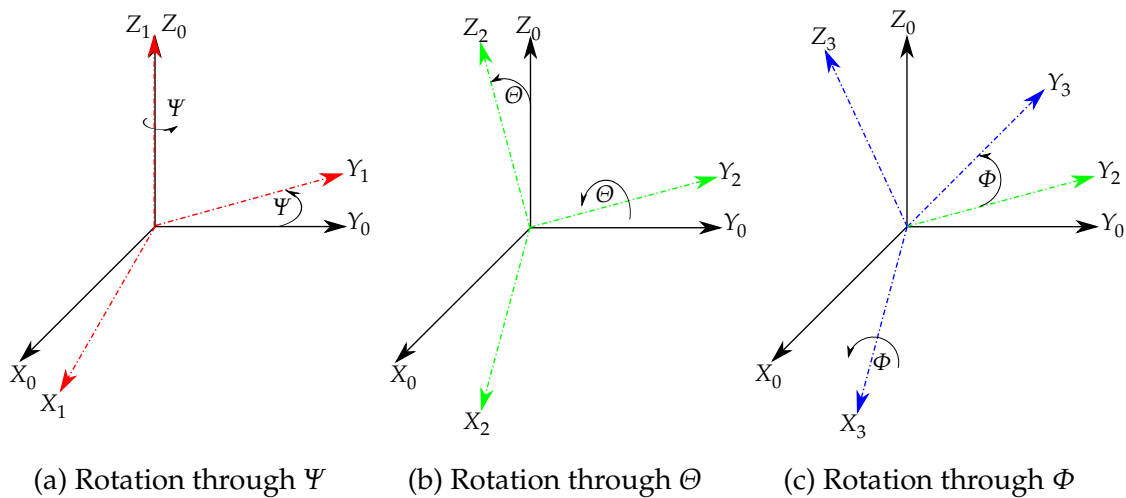
Figure 3.7: Euler 3-2-1 rotation

Rotating F_0 about the Z_0-axis through the yaw angle Ψ, as in Figure 3.7a, to create a new coordinate system $F_1(O_1 X_1 Y_1 Z_1)$ such that a vector V coordinated in F_1 becomes,

$$V_1 = R_\Psi V_0$$

$$\begin{bmatrix} x_1 \\ y_1 \\ z_1 \end{bmatrix} = \begin{bmatrix} \cos\Psi & \sin\Psi & 0 \\ -\sin\Psi & \cos\Psi & 0 \\ 0 & 0 & 1 \end{bmatrix} \begin{bmatrix} x_0 \\ y_0 \\ z_0 \end{bmatrix} \tag{3.51}$$

Rotating F_1 about the Y_1-axis through the pitch angle Θ, as in Figure 3.7b, to create a new coordinate system $F_2(O_2 X_2 Y_2 Z_2)$ such that a vector V coordinated in F_2 becomes,

$$V_2 = R_\Theta V_1$$

$$
\begin{bmatrix} x_2 \\ y_2 \\ z_2 \end{bmatrix} =
\begin{bmatrix} \cos\Theta & 0 & -\sin\Theta \\ 0 & 1 & 0 \\ \sin\Theta & 0 & \cos\Theta \end{bmatrix}
\begin{bmatrix} x_1 \\ y_1 \\ z_1 \end{bmatrix}
\tag{3.52}
$$

Finally, rotating F_2 about the X_2-axis through the roll angle Φ, as in Figure 3.7c, to create a new coordinate system $F_3(O_3 X_3 Y_3 Z_3)$ such that a vector V coordinated in F_3 becomes,

$$V_3 = R_\Phi V_2$$

$$
\begin{bmatrix} x_3 \\ y_3 \\ z_3 \end{bmatrix} =
\begin{bmatrix} 1 & 0 & 0 \\ 0 & \cos\Phi & \sin\Phi \\ 0 & -\sin\Phi & \cos\Phi \end{bmatrix}
\begin{bmatrix} x_2 \\ y_2 \\ z_2 \end{bmatrix}
\tag{3.53}
$$

The coordinate system F_3 coincides with the body axis system F_B. Equations (3.51) to (3.53) can be multiplied together to relate the coordinates of a vector V_0 coordinated in F_0 to a vector V_3 coordinated in F_3. Combining Equations (3.51), (3.52), and (3.53) yields,

$$V_3 = [R_\Phi R_\Theta R_\Psi] V_0 \tag{3.54}$$

but since V_0 coincides with a vector V_E in the inertial frame and V_3 coincides with a vector V_B in the body axis, Equation (3.54) converts inertially coordinated vectors to the body axis through the DCM shown below,

$$
\begin{bmatrix} x_B \\ y_B \\ z_B \end{bmatrix} =
\begin{bmatrix} 1 & 0 & 0 \\ 0 & \cos\Phi & \sin\Phi \\ 0 & -\sin\Phi & \cos\Phi \end{bmatrix}
\begin{bmatrix} \cos\Theta & 0 & -\sin\Theta \\ 0 & 1 & 0 \\ \sin\Theta & 0 & \cos\Theta \end{bmatrix}
\begin{bmatrix} \cos\Psi & \sin\Psi & 0 \\ -\sin\Psi & \cos\Psi & 0 \\ 0 & 0 & 1 \end{bmatrix}
\begin{bmatrix} x_E \\ y_E \\ z_E \end{bmatrix}
\tag{3.55}
$$

Expanding,

$$
\begin{bmatrix} x_B \\ y_B \\ z_B \end{bmatrix} =
\begin{bmatrix}
\cos\Psi\cos\Theta & \sin\Psi\cos\Theta & -\sin\Theta \\
\cos\Psi\sin\Theta\sin\Phi - \sin\Psi\cos\Phi & \sin\Psi\sin\Theta\sin\Phi + \cos\Psi\cos\Phi & \cos\Theta\sin\Phi \\
\cos\Psi\sin\Theta\cos\Phi + \sin\Psi\sin\Phi & \sin\Psi\sin\Theta\cos\Phi - \cos\Psi\sin\Phi & \cos\Theta\cos\Phi
\end{bmatrix}
\begin{bmatrix} x_E \\ y_E \\ z_E \end{bmatrix}
$$
$$\tag{3.56}$$

and rewriting so that,

$$V_B = (\mathbf{DCM}_{E \to B}) V_E \tag{3.57}$$

It is intuitive that the inverse transform, $[R_\Phi R_\Theta R_\Psi]^{-1}$, is required to convert vectors coordinated in the body axis to inertial space. It can be shown through simple algebraic manipulation that the transformation matrix is orthogonal, therefore its inverse exists and is merely its transpose,

$$V_E = \left[R_\Phi^T R_\Theta^T R_\Psi^T \right] V_B \tag{3.58}$$

and rewriting so that,

$$V_E = (\mathbf{DCM}_{B \to E})V_B \tag{3.59}$$

where,

$$\mathbf{DCM}_{B \to E} = (\mathbf{DCM}_{E \to B})^{-1} \tag{3.60}$$

$$= (\mathbf{DCM}_{E \to B})^T$$

3.3.2 Kinematic Equations

Kinematic equations are responsible for translating linear and angular velocities to position and attitude over time. The transformation matrix, derived in the previous section, readily transforms linear velocities coordinated in the body axis to inertial space. The inertially coordinated velocity vector can then be used to determine the aircraft's position in the inertial frame by integrating the time rate of change of position. The transformation matrix requires knowledge of the Euler angles, and it is therefore necessary to derive a set of differential equations that allow the dynamic calculation of these angles. The angular velocity of the aircraft can also be expressed as a vector sum of the Euler angular velocities [29],

$$\omega = i_\Phi \dot{\Phi} + j_\Theta \dot{\Theta} + k_\Psi \dot{\Psi} \tag{3.61}$$

where i_Φ is the unit vector along the X_2-axis, j_Θ the unit vector along the Y_1-axis and k_Ψ the unit vector along the Z_0-axis. The transformations discussed in Section 3.3.1 can be used to relate the body axis angular velocity components in Equation (3.11) to the Euler components. The unit vectors associated with the Euler components are resolved into the body axis frame F_B as follows,

$$i_{\Phi_B} = R_\Phi i_\Phi = \begin{bmatrix} 1 \\ 0 \\ 0 \end{bmatrix} \tag{3.62}$$

$$j_{\Theta_B} = R_\Phi R_\Theta j_\Theta = \begin{bmatrix} 0 \\ \cos\Phi \\ -\sin\Phi \end{bmatrix} \tag{3.63}$$

$$k_{\Psi_B} = R_\Phi R_\Theta R_\Psi k_\Psi = \begin{bmatrix} -\sin\Theta \\ \cos\Theta\sin\Phi \\ \cos\Theta\cos\Phi \end{bmatrix} \tag{3.64}$$

Equating the components of Equation (3.11) with the vector sum of Equations (3.62), (3.63) and (3.64), and scaling by their respective Euler angular rates, gives the following transformation,

$$\begin{bmatrix} P \\ Q \\ R \end{bmatrix} = \begin{bmatrix} 1 & 0 & -\sin\Theta \\ 0 & \cos\Phi & \cos\Theta\sin\Phi \\ 0 & -\sin\Phi & \cos\Theta\cos\Phi \end{bmatrix} \begin{bmatrix} \dot{\Phi} \\ \dot{\Theta} \\ \dot{\Psi} \end{bmatrix} \tag{3.65}$$

Unlike the DCM matrix, the transformation matrix given in Equation (3.65) is not orthogonal. However, its inverse does exist and is given by,

$$
\begin{bmatrix} \dot{\Phi} \\ \dot{\Theta} \\ \dot{\Psi} \end{bmatrix} = \begin{bmatrix} 1 & \sin\Phi\tan\Theta & \cos\Phi\tan\Theta \\ 0 & \cos\Phi & -\sin\Phi \\ 0 & \sin\Phi\sec\Theta & \cos\Phi\sec\Theta \end{bmatrix} \begin{bmatrix} P \\ Q \\ R \end{bmatrix}
\tag{3.66}
$$

and rewriting so that,

$$
\dot{e} = R_e \omega_B
\tag{3.67}
$$

which is subject to the constraint that $|\Theta| \neq \pi/2$, at which point there exists a mathematical singularity. Alternative parametrisation methods, such as quaternions and DCM parameters do exist, but they are less intuitive and more mathematically complex to work with. Euler angles are, however, well suited for conventional, non-aerobatic flight since $|\Theta| \ll \pi/2$, thus allowing the singularity to be ignored. It is for this particular reason that Euler angles are used throughout this thesis. Equations (3.67) and (3.68) summarise the two kinematic equations that relate angular and linear velocities to attitude and position in the inertial frame.

$$
\dot{P}_I = (\mathbf{DCM}_{B\to E})V_B
\tag{3.68}
$$

The Six Degrees of Freedom (6DoF) equations of motion are depicted graphically in Figure 3.8. The force and moment terms on the left side of the diagram act as driving inputs to the equations of motion. Kinetic equations then relate the forces and moments to linear and angular velocities respectively through Equations (3.29), (3.30), (3.31), (3.46), (3.47), and (3.48). The kinematic Equations of (3.68) and (3.67) in turn relate the linear and angular velocities to the time rates of change of position and attitude in inertial space.
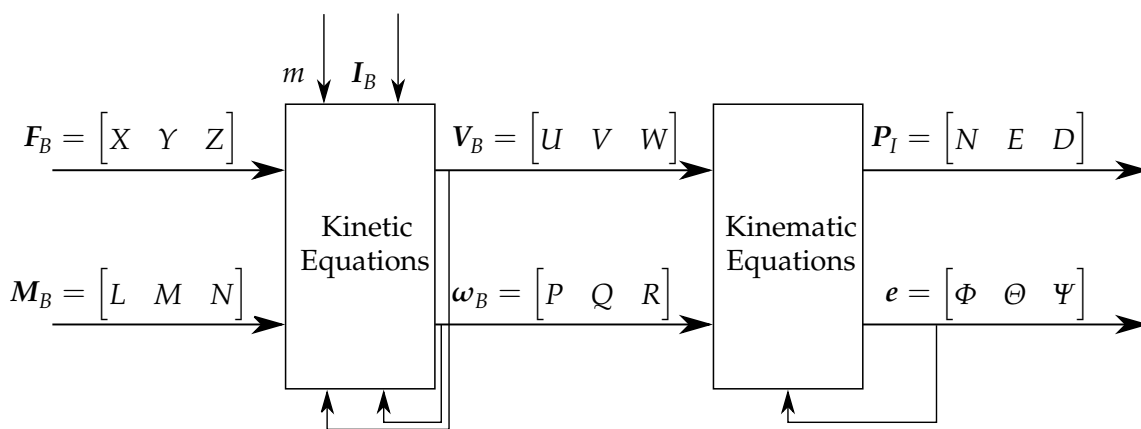
Figure 3.8: Block diagram overview of 6DoF equations of motion

3.4 Forces and Moments

This section will focus on the development of equations used to describe the various forces and moments acting on an aircraft as a function of its current state. Up until this point the dynamic

equations developed in the previous sections were applicable to any rigid body, and therefore no aircraft-specific dynamics have yet been modelled. Since this thesis is focused on the automatic control of an unmanned aircraft, application-specific forces and moments are now introduced into the model. There are three categories of forces and moments acting on most aircraft:

- Aerodynamic

- Thrust

- Gravitational

The contributions of individual forces and moments are summed together in order to determine their combined effect on the aircraft in the body axis. The individual contributions are summed according to,

$$\sum \boldsymbol{F}_B = \boldsymbol{F}^A + \boldsymbol{F}^T + \boldsymbol{F}^G \qquad \left\{ \boldsymbol{F}^i = \begin{bmatrix} X^i & Y^i & Z^i \end{bmatrix}^T \rightarrow i = A, T, G \right\} \tag{3.69}$$

$$\sum \boldsymbol{M}_B = \boldsymbol{M}^A + \boldsymbol{M}^T + \boldsymbol{M}^G \qquad \left\{ \boldsymbol{M}^i = \begin{bmatrix} L^i & M^i & N^i \end{bmatrix}^T \rightarrow i = A, T, G \right\} \tag{3.70}$$

where A, T, and G denote aerodynamic, thrust, and gravitational components respectively.

3.4.1 Aircraft Reference Geometry

It is first necessary to discuss the geometric layout of the aircraft, as this is an essential part of the mathematical modelling process. It is often convenient for the purposes of flight dynamics analysis to describe the aircraft reference geometry by a small number of dimensional reference parameters, which are defined and illustrated in Figure 3.9 [27].
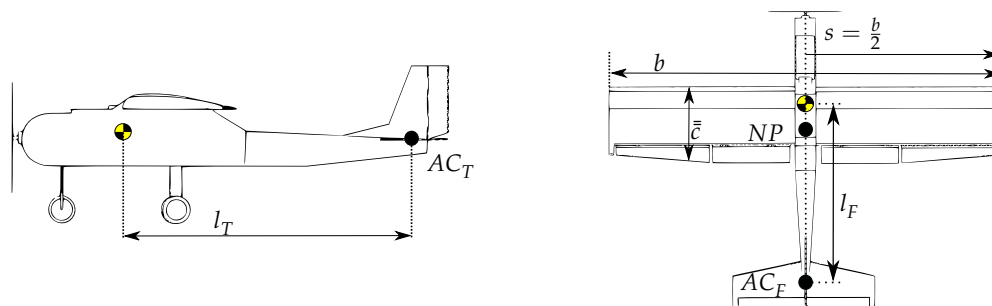
Figure 3.9: Aircraft reference geometry

The gross plan area of the wing, including the part within the fuselage, is given by, [1]

$$S = b\bar{c} \tag{3.71}$$

where b is the wing span and $\bar{c}$ is the Standard Mean Chord (SMC). The wing's SMC is given by,

$$\bar{c} = \frac{\int_{-s}^{s} c_y dy}{\int_{-s}^{s} dy} \tag{3.72}$$

---

[1]Wing area (S) should not be confused with wing semi-span (s).

for a wing of symmetric planform, where $s = b/2$ is the semi-span and c_y is the local chord at spanwise coordinate y. For a straight, tapered wing, Equation (3.72) simplifies to,

$$\bar{c} = \frac{S}{b} \tag{3.73}$$

The Mean Aerodynamic Chord (MAC) of the wing is denoted by $\bar{\bar{c}}$ and is defined as,

$$\bar{\bar{c}} = \frac{\int_{-s}^{s} c_y^2 dy}{\int_{-s}^{s} c_y dy} \tag{3.74}$$

This important parameter represents the location of the root chord of a rectangular wing, which has the same aerodynamic influence on the aircraft as the actual wing [27]. For most aircraft, the SMC and MAC are sufficiently similar in length and location that they are practically interchangeable [27]. Another important dimensional reference parameter is the aspect ratio of an aircraft's wing, defined as,

$$A = \frac{b^2}{S} \tag{3.75}$$

$$= \frac{b}{\bar{c}}$$

This parameter is a measure of spanwise slenderness and is an important indicator of the lift-induced drag created by the wing. The neutral point, denoted as NP in Figure 3.9, is the aerodynamic centre of the whole aircraft and is used to determine the static stability margin. This margin is defined as the distance between the centre of gravity (X_{cg}) and the neutral point (X_{np}) along the X_B-axis so that,

$$SM = (X_{cg} - X_{np}) \tag{3.76}$$

An aircraft is said to be longitudinally statically stable when its neutral point lies behind its centre of gravity. This ensures that any perturbation in angle of attack produces a restoring moment that brings the aircraft back to a stable flight configuration. With reference to Figure 3.9, AC_F and AC_T represent the aerodynamic centres of the horizontal and vertical stabilisers respectively, whilst l_F and l_T represent the effective lengths from the aerodynamic centres to the aircraft's centre of mass. Now that important reference geometries have been defined, the aforementioned dimensional reference parameters can be used in the development of a non-linear aircraft model in the subsections to follow.

3.4.2 Aerodynamic

The aerodynamic forces and moments acting on an aircraft are by far the most complex to model, and introduce the majority of the uncertainty into the model. Aerodynamic coefficients are usually defined in the stability axis (assuming zero sideslip angle β), and are described in terms of stability and control derivatives in the form,

$$C_{A_B} = \frac{\partial C_A}{\partial B'} \tag{3.77}$$

with,

$$B' = nB \tag{3.78}$$

where n is the appropriate normalising coefficient of B. The appropriate normalising coefficient for incidence angles and control deflection angles is unity, whilst for the pitch rate it is $\bar{c}/2\bar{V}$ and $b/2\bar{V}$ for the roll and yaw rates. These derivatives are non-dimensional and describe the forces and moments acting on the aircraft as functions of the current aircraft state and the control surface deflection angles. For instance, the non-dimensional derivative C_{L_α} describes the lift force produced by the aircraft due to angle of attack. The fact that these derivatives are non-dimensional allows for the formulation of airframe-specific parameters by simply normalising the coefficients according to particular aircraft geometric properties. Aerodynamic coefficients for a large aircraft can thus be obtained by conducting wind tunnel tests on a scale replica of the larger airframe, and then rescaling according to the geometric properties of the full-sized aircraft.

To formulate the force and moment equations acting on the aircraft, it is imperative that the derivatives and the aircraft states be coordinated in the same reference frame. This means that the angular rate vectors coordinated in the body axis should be transformed to the stability axis using Equation (3.3) as follows,

$$P_S = P_B \cos\alpha + R_B \sin\alpha \tag{3.79}$$

$$Q_S = Q_B \tag{3.80}$$

$$R_S = -P_B \sin\alpha + R_B \cos\alpha \tag{3.81}$$

The aerodynamic coefficients associated with typical subsonic, pre-stall flight coordinated in the stability axis are defined by Koen [30] as,

$$C_D = C_{D_0} + \frac{C_L^2}{\pi A e} \tag{3.82}$$

$$C_y = C_{y_\beta}\beta + C_{y_P}\left(\frac{b}{2\bar{V}}\right)P_S + C_{y_R}\left(\frac{b}{2\bar{V}}\right)R_S + C_{y_{\delta_A}}\delta_A + C_{y_{\delta_R}}\delta_R \tag{3.83}$$

$$C_L = C_{L_0} + C_{L_\alpha}\alpha + C_{L_Q}\left(\frac{\bar{\bar{c}}}{2\bar{V}}\right)Q_S + C_{L_{\delta_E}}\delta_E + C_{L_{\delta_F}}\delta_F \tag{3.84}$$

$$C_l = C_{l_\beta}\beta + C_{l_P}\left(\frac{b}{2\bar{V}}\right)P_S + C_{l_R}\left(\frac{b}{2\bar{V}}\right)R_S + C_{l_{\delta_A}}\delta_A + C_{l_{\delta_R}}\delta_R \tag{3.85}$$

$$C_m = C_{m_0} + C_{m_\alpha}\alpha + C_{m_Q}\left(\frac{\bar{\bar{c}}}{2\bar{V}}\right)Q_S + C_{m_{\delta_E}}\delta_E + C_{m_{\delta_F}}\delta_F \tag{3.86}$$

$$C_n = C_{n_\beta}\beta + C_{n_P}\left(\frac{b}{2\bar{V}}\right)P_S + C_{n_R}\left(\frac{b}{2\bar{V}}\right)R_S + C_{n_{\delta_A}}\delta_A + C_{n_{\delta_R}}\delta_R \tag{3.87}$$

where D is the drag force, y is the side force, L is the lift force, l is the rolling moment, m is the pitching moment, n is the yawing moment, C_{D_0} is the parasitic drag coefficient, C_{m_0} is the static pitching moment coefficient, and e is the Oswald efficiency factor. The Oswald efficiency factor is used most often as a parameter to account for induced drag and consists of two components:

an inviscid part which is caused by induced velocities from the wake, and a viscous part which is caused by increases in skin friction and pressure drag due to changes in angle of attack [31]. It can be shown through simple algebraic manipulation that the inverse of Equation (3.3) does exist. The result allows for aerodynamic coefficients coordinated in the stability axis to be transformed to the body axis as follows,

$$C_{x_B} = -C_D \cos\alpha + C_L \sin\alpha \tag{3.88}$$

$$C_{y_B} = C_y \tag{3.89}$$

$$C_{z_B} = -C_L \cos\alpha - C_D \sin\alpha \tag{3.90}$$

$$C_{l_B} = C_l \cos\alpha - C_n \sin\alpha \tag{3.91}$$

$$C_{m_B} = C_m \tag{3.92}$$

$$C_{n_B} = C_n \cos\alpha + C_l \sin\alpha \tag{3.93}$$

Note that the main component of drag (C_D) acts in the negative X_B-axis direction, and that the main component of lift (C_L) acts in the negative Z_B-axis direction. Shevell [32] uses Bernoulli's equation and the continuity principle for incompressible fluids to show that the forces and moments acting on an aircraft are proportional to the dynamic pressure experienced by the aircraft. Dynamic pressure is given by,

$$\bar{q} = \frac{1}{2}\rho\bar{V}^2 \tag{3.94}$$

where ρ is the air density and $\bar{V}$ is the true airspeed. For altitudes below 11 km, ρ can be calculated using [30],

$$\rho = 1.225\left(1 - 2.2558 \times 10^{-5}h\right)^{4.2559} \tag{3.95}$$

where h is the aircraft's altitude above Mean Sea Level (MSL). To this end, aerodynamic forces and moments coordinated in the body axis are calculated as follows:

$$\boldsymbol{F}^A = \begin{bmatrix} X^A & Y^A & Z^A \end{bmatrix}^T \tag{3.96}$$

$$= \begin{bmatrix} \bar{q}SC_{x_B} & \bar{q}SC_{y_B} & \bar{q}SC_{z_B} \end{bmatrix}^T$$

$$\boldsymbol{M}^A = \begin{bmatrix} L^A & M^A & N^A \end{bmatrix}^T \tag{3.97}$$

$$= \begin{bmatrix} \bar{q}SbC_{l_B} & \bar{q}S\bar{c}C_{m_B} & \bar{q}SbC_{n_B} \end{bmatrix}^T$$

It is clear from the preceding discussion that stability and control derivatives describe the aerodynamic properties of a particular airframe. In order to derive an aircraft-specific model, it is necessary to first obtain the stability and control derivatives associated with a particular airframe. There are a number of methods which can be used to obtain these non-dimensional derivatives, each with their own advantages and disadvantages. It is not uncommon for engineers to make use

of a combination of the various techniques in an attempt to obtain the most accurate results. Due to the strict time constraints associated with this project, Athena Vortex Lattice (AVL) was used to determine the necessary stability and control derivatives.[1] This technique has been shown to produce adequate results when compared to first principle methods, and has been validated extensively through work done in [5, 6, 9, 33], in which successful autopilot systems were developed.

3.4.3 Gravitational

The gravitational acceleration vector is modelled as providing a force proportional to the aircraft's mass in the down direction (in the NED axis system.). The inertially coordinated force due to gravity is expressed in the following vector array form:

$$\boldsymbol{F}_I^G = \begin{bmatrix} 0 & 0 & mg \end{bmatrix}^T \tag{3.98}$$

Transforming to the body axis using the DCM of Equation (3.56) yields,

$$\boldsymbol{F}^G = \begin{bmatrix} X^G & Y^G & Z^G \end{bmatrix}^T \tag{3.99}$$

$$= (\mathbf{DCM}_{E \to B})\boldsymbol{F}_I^G$$

$$= \begin{bmatrix} -\sin\Theta \\ \cos\Theta\sin\Phi \\ \cos\Theta\cos\Phi \end{bmatrix} mg$$

For the case of a rigid body in a uniform gravitational field, it is safe to assume that gravity only acts at the centre of mass and thus no moments (torques) exist. Thus,

$$\boldsymbol{M}^G = \begin{bmatrix} L^G & M^G & N^G \end{bmatrix}^T \tag{3.100}$$

$$= \begin{bmatrix} 0 & 0 & 0 \end{bmatrix}^T$$

3.4.4 Thrust

In order to fully describe the thrust model, it is necessary to encapsulate various complex interactions associated with the particular propulsion system. For the sake of simplicity, a first-order lag model tends to suffice for most UAV applications, as it adequately captures the significantly band-limited nature of most propulsion systems [34]. The simplified thrust model can be described by,

$$\dot{T} = -\frac{1}{\tau_e}T + \frac{1}{\tau_e}T_c \tag{3.101}$$

where T is the output thrust magnitude, T_c is the commanded thrust, and τ_e is the engine lag time constant. It is assumed that for the case of an aircraft with a tractor configuration propulsion system, the thrust line coincides with the X_B-axis and passes through the centre of mass. Ignoring

---

[1]AVL makes use of vortex lattice codes to determine stability and control derivatives.

all torques produced by aerodynamic phenomena and gyroscopic effects, the forces and moments associated with the thrust model are expressed as follows:

$$\boldsymbol{F}^T = \begin{bmatrix} X^T & Y^T & Z^T \end{bmatrix}^T \tag{3.102}$$

$$= \begin{bmatrix} T & 0 & 0 \end{bmatrix}^T$$

$$\boldsymbol{M}^T = \begin{bmatrix} L^T & M^T & N^T \end{bmatrix}^T \tag{3.103}$$

$$= \begin{bmatrix} 0 & 0 & 0 \end{bmatrix}^T$$

3.5   Summary

Reference frames and aircraft-specific notation were defined at the start of the chapter in order to establish convention early on in the thesis. Dynamic equations that govern aircraft motion were then developed from first principles in order to obtain an in-depth understanding of the mechanics involved. Various transformation matrices were created for the purpose of elegantly converting between the aforementioned reference frames. Furthermore, kinematic equations responsible for translating linear and angular velocities to position and attitude over time were developed. Finally, forces and moments acting on the aircraft were identified, modelled, and described in detail. Figure 3.10 summarises the aircraft model in block diagram form.
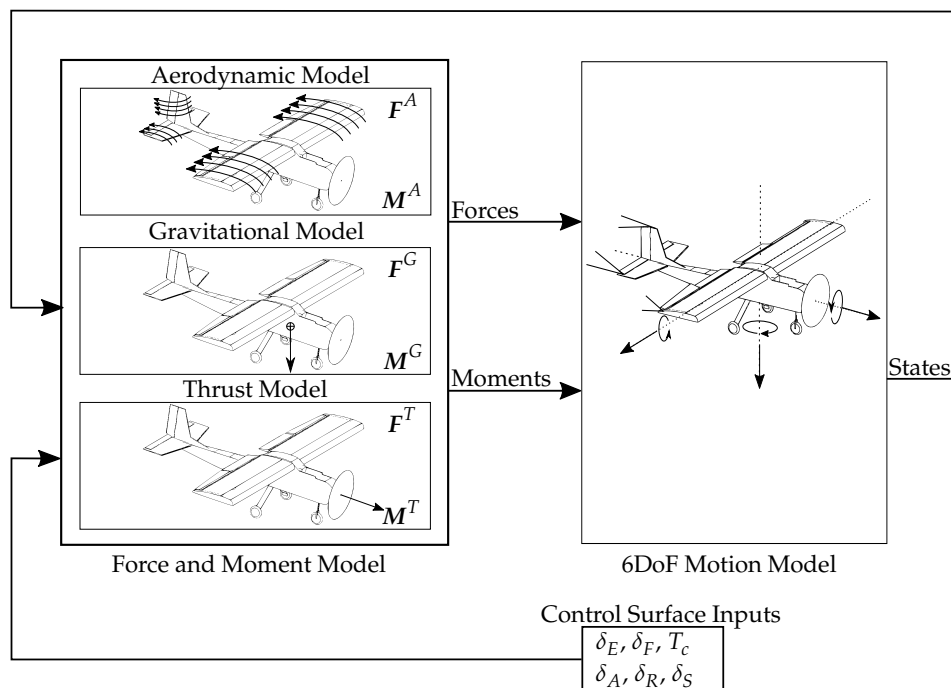
Figure 3.10: Aircraft model block diagram

The six degrees of freedom (6DoF) equations of motion developed in this chapter are responsible for modelling the dynamics of any rigid body given the forces and moments that act on it.

These equations are driven by the combined force and moment models shown on the left-hand side of Figure 3.10. Aircraft states are then fed back to the force and moment block, which in turn determines the future of the states as the system propagates forward in time. The thrust command and control surface inputs are fed into the thrust and aerodynamic force and moment models to manipulate the system as desired. Now that the core fundamentals of a non-linear aircraft model have been established, the next chapter will focus on the development of a linearised aircraft model.

CHAPTER 4

Development of a Linear Aircraft Model

In this chapter, the dynamic model discussed in Chapter 3 is linearised about a steady, level flight trim condition in order to develop a linear aircraft model for analysis and control system design purposes. Trim condition variables are first defined and then calculated using the Newton-Raphson method for non-linear simultaneous equations. The non-linear aircraft dynamic equations are then linearised about the trim condition using small disturbance theory, the details of which are discussed in Section 4.2. A linear aircraft model is required so that well-developed, linear systems analysis techniques can be used to gain insight into the aircraft's natural modes of motion, which will assist in the design of an effective flight control system.

4.1   Defining and Calculating Trim State Variables

A full-sized manned aircraft is said to be in a trimmed state when it continues to fly at a chosen flight condition after the controls have been released. It can thus be said that all the forces and moments acting on the aircraft are in a state of equilibrium. Intuitively, this force balance can be approximated as the requirement for lift to equal weight and for thrust to equal drag. The aircraft dynamics could theoretically be linearised about any equilibrium trajectory; however, the most common and useful of these is *straight and level flight* [34]. The following should hold true for a straight and level flight condition:

$$\sum F_i = F_i^A + F_i^G + F_i^T = 0 \quad \text{where } i = x, y, z \tag{4.1}$$

$$\sum M_i = M_i^A + M_i^G + M_i^T = 0 \quad \text{where } i = x, y, z \tag{4.2}$$

Substituting the individual force and moment equations of Sections 3.4.2 through 3.4.4 into Equations (4.1) and (4.2) yields six non-linear dynamic equations. Solving this set of equations will allow for the calculation of the trim state variables represented in the following vector array form:

$$\boldsymbol{R}_T = \begin{bmatrix} \alpha_T & \beta_T & \Phi_T & \delta_{E_T} & \delta_{F_T} & \delta_{A_T} & \delta_{R_T} & T_T \end{bmatrix} \tag{4.3}$$

where subscript T denotes trim. Substituting these variables back into the force and moment equations of (3.69) and (3.70) should then satisfy the equilibrium requirement,

$$\sum F_B = \sum M_B = 0 \tag{4.4}$$

It is clear from Equations (4.1) and (4.2) that there are six equations to be solved, and from Equation (4.3) that there are eight unknowns. One of the unknowns can be eliminated by trimming the aircraft for a specific flap configuration by setting the value of δ_{F_T} to the desired trim value. A second unknown can be eliminated by trimming the aircraft for a specific flight configuration; trim for zero bank angle by setting $\Phi_T = 0$ or trim for zero sideslip angle by setting $\beta_T = 0$. It makes little difference which trim configuration the designer chooses, since both Φ_T and β_T will equal zero for a symmetric aircraft. The problem now reduces to solving six non-linear equations to obtain the six unknowns contained in the trim state vector of Equation (4.3). Consider the Taylor series expansion of the function $f(x)$ about a point $x = x_0$,

$$f(x) = f(x_0) + f'(x_0)(x - x_0) + \frac{f''(x_0)}{2!}(x - x_0)^2 + ... + \frac{f^n(x_0)}{n!}(x - x_0)^n \tag{4.5}$$

A first approximation to the root of the equation,

$$f(x) = 0 \tag{4.6}$$

is obtained by only using the first two terms of the expansion,

$$f(x) = 0 \approx f(x_0) + f'(x_0)(x_1 - x_0) \tag{4.7}$$

Rewriting so that,

$$x_1 = x_0 - \frac{f(x_0)}{f'(x_0)} \tag{4.8}$$

The Newton-Raphson method obtains improved values of the approximate root through recurrent application of Equation (4.8) [35]. Generalising this iterative procedure yields,

$$x_{i+1} = x_i - \frac{f(x_i)}{f'(x_i)} \tag{4.9}$$

where i represents the iteration number. It is important to note that the convergence condition,

$$|f(x_{i+1})| < \epsilon \tag{4.10}$$

should be satisfied on each iteration of Equation (4.9). The Newton-Raphson method is able to hone in on the roots of the non-linear equations with exceptional efficiency, and allows for the calculation of the trim state variables contained in vector R_T of Equation (4.3).

4.2   Small Disturbance Theory

With the trim condition defined and the trim state vector obtainable through use of the Newton-Raphson method, the process of linearising the aircraft dynamics can begin. A linear aircraft model is required so that linear systems analysis and control design techniques can be used to

gain insight into the aircraft's flying characteristics. This will supplement the design of an effective control system, capable of landing a fixed-wing aircraft accurately under adverse weather conditions. The dynamic aircraft equations will be linearised about a straight and level flight condition using the concept of small disturbance theory. Small disturbance theory is centred around the assumption that aircraft motion consists of small deviations from a reference condition of steady flight. The success of this method can be attributed to [21]:

1. its ability to encapsulate the major aerodynamic effects which are nearly linear functions of the disturbances

2. the fact that disturbances of considerable violence can occur with relatively small values of linear and angular velocities

The following assumptions are made during the linearisation of the equations of motion [3]:

1. Products of small perturbations are insignificantly small and can be ignored

2. The sine of a small angle is merely the angle itself (in radians)

3. The cosine of a small angle is unity

4.3   Linearising the Equations of Motion

To this end, Equations (3.29) through (3.31) and (3.46) through (3.48) are rewritten so that the state derivatives $(\dot{U}, \dot{V}, \dot{W}, \dot{P}, \dot{Q}, \dot{R})$ are the subject of the formula. The roll and pitch angle dynamics of Equation (3.67) are included into the state vector so that,

$$\dot{x} = f(x, u) \tag{4.11}$$

where,

$$x = \begin{bmatrix} U & V & W & P & Q & R & \Phi & \Theta \end{bmatrix} \tag{4.12}$$

$$u = \begin{bmatrix} \delta_E & \delta_F & \delta_A & \delta_R & T \end{bmatrix} \tag{4.13}$$

and f is the vector function representing the respective dynamic equations. The dynamic states Ψ, N, E, and D are omitted from the state vector, since they do not form part of the fundamental aircraft dynamics. They are simply kinematic results of the primary aircraft dynamics [34]. Rewriting each state and control as the sum of a trim value and a perturbation about trim yields,

$$x = x_T + \Delta x \tag{4.14}$$

$$u = u_T + \Delta u \tag{4.15}$$

where,

$$\Delta x = \begin{bmatrix} u & v & w & p & q & r & \phi & \theta \end{bmatrix} \tag{4.16}$$

$$\Delta u = \begin{bmatrix} \delta_e & \delta_f & \delta_a & \delta_r & \Delta T \end{bmatrix} \tag{4.17}$$

Taking the Taylor series expansion of Equation (4.11) about the trim condition yields,

$$\dot{x} + \Delta\dot{x} = f(x_T + \Delta x, u_T + \Delta u) \tag{4.18}$$

$$= f(x_T, u_T) + \left.\frac{\partial f}{\partial x}\right|_T \Delta x + \left.\frac{\partial f}{\partial u}\right|_T \Delta u + HOT$$

The higher-order terms (HOT) can be ignored under the assumption that the deviations from trim are relatively small. The dynamics can thus be approximated by the linearised sensitivities about trim,

$$\Delta\dot{x} \approx \left.\frac{\partial f}{\partial x}\right|_T \Delta x + \left.\frac{\partial f}{\partial u}\right|_T \Delta u \tag{4.19}$$

where it has been noted that at the trim condition,

$$\dot{x} = f(x_T, u_T) \tag{4.20}$$

$$= 0$$

The linearisation problem is now reduced to determining the partial derivatives that form the state and control matrices of the coupled system. Grouping the longitudinal and lateral dynamics of Equations (4.16) and (4.17) yields,

$$\Delta x = \begin{bmatrix} u & w & q & \theta & v & p & r & \phi \end{bmatrix} \tag{4.21}$$

$$\Delta u = \begin{bmatrix} \delta_e & \delta_f & \Delta T & \delta_a & \delta_r \end{bmatrix} \tag{4.22}$$

Now evaluating Equation (4.19) and expanding yields,

$$
\begin{bmatrix} \dot{u} \\ \dot{w} \\ \dot{q} \\ \dot{\theta} \\ \dot{v} \\ \dot{p} \\ \dot{r} \\ \dot{\phi} \end{bmatrix} =
\begin{bmatrix}
\frac{\partial \dot{U}}{\partial U} & \frac{\partial \dot{U}}{\partial W} & \frac{\partial \dot{U}}{\partial Q} & \frac{\partial \dot{U}}{\partial \Theta} & \frac{\partial \dot{U}}{\partial V} & \frac{\partial \dot{U}}{\partial P} & \frac{\partial \dot{U}}{\partial R} & \frac{\partial \dot{U}}{\partial \Phi} \\
\frac{\partial \dot{W}}{\partial U} & \frac{\partial \dot{W}}{\partial W} & \frac{\partial \dot{W}}{\partial Q} & \frac{\partial \dot{W}}{\partial \Theta} & \frac{\partial \dot{W}}{\partial V} & \frac{\partial \dot{W}}{\partial P} & \frac{\partial \dot{W}}{\partial R} & \frac{\partial \dot{W}}{\partial \Phi} \\
\frac{\partial \dot{Q}}{\partial U} & \frac{\partial \dot{Q}}{\partial W} & \frac{\partial \dot{Q}}{\partial Q} & \frac{\partial \dot{Q}}{\partial \Theta} & \frac{\partial \dot{Q}}{\partial V} & \frac{\partial \dot{Q}}{\partial P} & \frac{\partial \dot{Q}}{\partial R} & \frac{\partial \dot{Q}}{\partial \Phi} \\
\frac{\partial \dot{\Theta}}{\partial U} & \frac{\partial \dot{\Theta}}{\partial W} & \frac{\partial \dot{\Theta}}{\partial Q} & \frac{\partial \dot{\Theta}}{\partial \Theta} & \frac{\partial \dot{\Theta}}{\partial V} & \frac{\partial \dot{\Theta}}{\partial P} & \frac{\partial \dot{\Theta}}{\partial R} & \frac{\partial \dot{\Theta}}{\partial \Phi} \\
\frac{\partial \dot{V}}{\partial U} & \frac{\partial \dot{V}}{\partial W} & \frac{\partial \dot{V}}{\partial Q} & \frac{\partial \dot{V}}{\partial \Theta} & \frac{\partial \dot{V}}{\partial V} & \frac{\partial \dot{V}}{\partial P} & \frac{\partial \dot{V}}{\partial R} & \frac{\partial \dot{V}}{\partial \Phi} \\
\frac{\partial \dot{P}}{\partial U} & \frac{\partial \dot{P}}{\partial W} & \frac{\partial \dot{P}}{\partial Q} & \frac{\partial \dot{P}}{\partial \Theta} & \frac{\partial \dot{P}}{\partial V} & \frac{\partial \dot{P}}{\partial P} & \frac{\partial \dot{P}}{\partial R} & \frac{\partial \dot{P}}{\partial \Phi} \\
\frac{\partial \dot{R}}{\partial U} & \frac{\partial \dot{R}}{\partial W} & \frac{\partial \dot{R}}{\partial Q} & \frac{\partial \dot{R}}{\partial \Theta} & \frac{\partial \dot{R}}{\partial V} & \frac{\partial \dot{R}}{\partial P} & \frac{\partial \dot{R}}{\partial R} & \frac{\partial \dot{R}}{\partial \Phi} \\
\frac{\partial \dot{\Phi}}{\partial U} & \frac{\partial \dot{\Phi}}{\partial W} & \frac{\partial \dot{\Phi}}{\partial Q} & \frac{\partial \dot{\Phi}}{\partial \Theta} & \frac{\partial \dot{\Phi}}{\partial V} & \frac{\partial \dot{\Phi}}{\partial P} & \frac{\partial \dot{\Phi}}{\partial R} & \frac{\partial \dot{\Phi}}{\partial \Phi}
\end{bmatrix}
\begin{bmatrix} u \\ w \\ q \\ \theta \\ v \\ p \\ r \\ \phi \end{bmatrix} +
\begin{bmatrix}
\frac{\partial \dot{U}}{\partial \delta_E} & \frac{\partial \dot{U}}{\partial \delta_F} & \frac{\partial \dot{U}}{\partial T} & \frac{\partial \dot{U}}{\partial \delta_A} & \frac{\partial \dot{U}}{\partial \delta_R} \\
\frac{\partial \dot{W}}{\partial \delta_E} & \frac{\partial \dot{W}}{\partial \delta_F} & \frac{\partial \dot{W}}{\partial T} & \frac{\partial \dot{W}}{\partial \delta_A} & \frac{\partial \dot{W}}{\partial \delta_R} \\
\frac{\partial \dot{Q}}{\partial \delta_E} & \frac{\partial \dot{Q}}{\partial \delta_F} & \frac{\partial \dot{Q}}{\partial T} & \frac{\partial \dot{Q}}{\partial \delta_A} & \frac{\partial \dot{Q}}{\partial \delta_R} \\
\frac{\partial \dot{\Theta}}{\partial \delta_E} & \frac{\partial \dot{\Theta}}{\partial \delta_F} & \frac{\partial \dot{\Theta}}{\partial T} & \frac{\partial \dot{\Theta}}{\partial \delta_A} & \frac{\partial \dot{\Theta}}{\partial \delta_R} \\
\frac{\partial \dot{V}}{\partial \delta_E} & \frac{\partial \dot{V}}{\partial \delta_F} & \frac{\partial \dot{V}}{\partial T} & \frac{\partial \dot{V}}{\partial \delta_A} & \frac{\partial \dot{V}}{\partial \delta_R} \\
\frac{\partial \dot{P}}{\partial \delta_E} & \frac{\partial \dot{P}}{\partial \delta_F} & \frac{\partial \dot{P}}{\partial T} & \frac{\partial \dot{P}}{\partial \delta_A} & \frac{\partial \dot{P}}{\partial \delta_R} \\
\frac{\partial \dot{R}}{\partial \delta_E} & \frac{\partial \dot{R}}{\partial \delta_F} & \frac{\partial \dot{R}}{\partial T} & \frac{\partial \dot{R}}{\partial \delta_A} & \frac{\partial \dot{R}}{\partial \delta_R} \\
\frac{\partial \dot{\Phi}}{\partial \delta_E} & \frac{\partial \dot{\Phi}}{\partial \delta_F} & \frac{\partial \dot{\Phi}}{\partial T} & \frac{\partial \dot{\Phi}}{\partial \delta_A} & \frac{\partial \dot{\Phi}}{\partial \delta_R}
\end{bmatrix}
\begin{bmatrix} \delta_e \\ \delta_f \\ \Delta T \\ \delta_a \\ \delta_r \end{bmatrix} \tag{4.23}
$$

which represents the full 8x8 coupled system, including lateral and longitudinal cross-coupling terms. It is more common, however, to work with velocity magnitude, angle of attack, and sideslip angle perturbations ($\bar{v}, \alpha, \beta$) in the state vector instead of axial, normal, and lateral velocity perturbations (u, v, w) as are currently used. Considering Equations (3.17) through (3.19), the following approximations can be made for a straight and level flight condition, assuming that the angle of attack and sideslip angles are small:

$$U = \bar{V}_T \cos\alpha \cos\beta \approx \bar{V}_T \tag{4.24}$$

$$V = \bar{V}_T \sin\beta \approx \bar{V}_T\beta \tag{4.25}$$

$$W = \bar{V}_T \sin\alpha \cos\beta \approx \bar{V}_T\alpha \tag{4.26}$$

where $\bar{V}_T$ represents the velocity magnitude at the trim condition. For the case of a symmetric aircraft, longitudinal and lateral dynamics are often decoupled to simplify the linear aircraft model. The coupled system in Equation (4.23) can be represented as follows:

$$
\begin{bmatrix} \Delta \dot{x}_{long} \\ \Delta \dot{x}_{lat} \end{bmatrix} = \begin{bmatrix} A_{T_{11}} & A_{T_{12}} \\ A_{T_{21}} & A_{T_{22}} \end{bmatrix} \begin{bmatrix} \Delta x_{long} \\ \Delta x_{lat} \end{bmatrix} + \begin{bmatrix} B_{T_{11}} & B_{T_{12}} \\ B_{T_{21}} & B_{T_{22}} \end{bmatrix} \begin{bmatrix} \Delta u_{long} \\ \Delta u_{lat} \end{bmatrix}
\tag{4.27}
$$

where T_{12} and T_{21} represent the longitudinal and lateral cross-coupling terms. Since the aircraft is symmetrical about the XZ-plane, $A_{T_{21}}$ and $B_{T_{21}}$ in the above dynamics will be exactly zero [34]. Furthermore, it is required by the linearisation assumption that the deviations from trim be small; then, to a good approximation, $A_{T_{12}}$ and $B_{T_{12}}$ also fall away. With this in mind, and considering the approximations given by Equations (4.24) through (4.26), the system can then be decoupled, with the longitudinal dynamics given as,

$$
\begin{bmatrix} \dot{\bar{v}} \\ \dot{\alpha} \\ \dot{q} \\ \dot{\theta} \end{bmatrix} = \begin{bmatrix} \frac{\partial \dot{U}}{\partial U} & \bar{V}_T \frac{\partial \dot{U}}{\partial W} & \frac{\partial \dot{U}}{\partial Q} & \frac{\partial \dot{U}}{\partial \Theta} \\ \frac{1}{\bar{V}_T}\frac{\partial \dot{W}}{\partial U} & \frac{\partial \dot{W}}{\partial W} & \frac{1}{\bar{V}_T}\frac{\partial \dot{W}}{\partial Q} & \frac{1}{\bar{V}_T}\frac{\partial \dot{W}}{\partial \Theta} \\ \frac{\partial \dot{Q}}{\partial U} & \bar{V}_T \frac{\partial \dot{Q}}{\partial W} & \frac{\partial \dot{Q}}{\partial Q} & \frac{\partial \dot{Q}}{\partial \Theta} \\ \frac{\partial \dot{\Theta}}{\partial U} & \bar{V}_T \frac{\partial \dot{\Theta}}{\partial W} & \frac{\partial \dot{\Theta}}{\partial Q} & \frac{\partial \dot{\Theta}}{\partial \Theta} \end{bmatrix} \begin{bmatrix} \bar{v} \\ \alpha \\ q \\ \theta \end{bmatrix} + \begin{bmatrix} \frac{\partial \dot{U}}{\partial \delta_E} & \frac{\partial \dot{U}}{\partial \delta_F} & \frac{\partial \dot{U}}{\partial T} \\ \frac{1}{\bar{V}_T}\frac{\partial \dot{W}}{\partial \delta_E} & \frac{1}{\bar{V}_T}\frac{\partial \dot{W}}{\partial \delta_F} & \frac{1}{\bar{V}_T}\frac{\partial \dot{W}}{\partial T} \\ \frac{\partial \dot{Q}}{\partial \delta_E} & \frac{\partial \dot{Q}}{\partial \delta_F} & \frac{\partial \dot{Q}}{\partial T} \\ \frac{\partial \dot{\Theta}}{\partial \delta_E} & \frac{\partial \dot{\Theta}}{\partial \delta_F} & \frac{\partial \dot{\Theta}}{\partial T} \end{bmatrix} \begin{bmatrix} \delta_e \\ \delta_f \\ \Delta T \end{bmatrix}
\tag{4.28}
$$

and the lateral dynamics given as,

$$
\begin{bmatrix} \dot{\beta} \\ \dot{p} \\ \dot{r} \\ \dot{\phi} \end{bmatrix} = \begin{bmatrix} \frac{\partial \dot{V}}{\partial V} & \frac{1}{\bar{V}_T}\frac{\partial \dot{V}}{\partial P} & \frac{1}{\bar{V}_T}\frac{\partial \dot{V}}{\partial R} & \frac{1}{\bar{V}_T}\frac{\partial \dot{V}}{\partial \Phi} \\ \bar{V}_T\frac{\partial \dot{P}}{\partial V} & \frac{\partial \dot{P}}{\partial P} & \frac{\partial \dot{P}}{\partial R} & \frac{\partial \dot{P}}{\partial \Phi} \\ \bar{V}_T\frac{\partial \dot{R}}{\partial V} & \frac{\partial \dot{R}}{\partial P} & \frac{\partial \dot{R}}{\partial R} & \frac{\partial \dot{R}}{\partial \Phi} \\ \bar{V}_T\frac{\partial \dot{\Phi}}{\partial V} & \frac{\partial \dot{\Phi}}{\partial P} & \frac{\partial \dot{\Phi}}{\partial R} & \frac{\partial \dot{\Phi}}{\partial \Phi} \end{bmatrix} \begin{bmatrix} \beta \\ p \\ r \\ \phi \end{bmatrix} + \begin{bmatrix} \frac{1}{\bar{V}_T}\frac{\partial \dot{V}}{\partial \delta_A} & \frac{1}{\bar{V}_T}\frac{\partial \dot{V}}{\partial \delta_R} \\ \frac{\partial \dot{P}}{\partial \delta_A} & \frac{\partial \dot{P}}{\partial \delta_R} \\ \frac{\partial \dot{R}}{\partial \delta_A} & \frac{\partial \dot{R}}{\partial \delta_R} \\ \frac{\partial \dot{\Phi}}{\partial \delta_A} & \frac{\partial \dot{\Phi}}{\partial \delta_R} \end{bmatrix} \begin{bmatrix} \delta_a \\ \delta_r \end{bmatrix}
\tag{4.29}
$$

Evaluating the system of partial differential equations, with respect to the force and moment models of Section 3.4, is a lengthy process that is prone to mistakes when evaluated by hand. For the sake of simplicity, accuracy, and speed, MATLAB's Symbolic Toolbox was used to solve the system of partial differentials. For the sake of completeness, the MATLAB script was designed to solve the full 8x8 system, and as expected, the cross-coupling terms in the solution were negligibly small for the symmetric aircraft approximations. The outcome of the linearisation was verified through work done by Etkin and Reid [21], which gives an approximated, decoupled linear model for symmetric aircraft. This linear model was extended to include the flaps control surface, as shown in Appendix B, so that the MATLAB linearisation script could be validated, as shown in Sections 4.5.1 and 4.5.2.

4.4 Overview of the Practical Test Vehicle

Up until this point, the axis system definitions, the development of the equations of motion, as well as the derivation of force and moment equations have not been specific to one particular airframe. The focus now shifts towards the analysis of an airframe specific to this project - the Phoenix 0.60 size trainer aircraft shown in Figure 4.1a. This particular aircraft was purpose-built from scratch, which allowed for the optimisation of sensor placement and freedom of customisation. Table C.1 in Appendix C gives an indication of the hardware on board this aircraft. Trainer

aircraft have the advantage of being more statically stable than aerobatic aircraft due to the dihedral configuration of the top wing design. They are also quite robustly built and are able to accommodate a considerable payload of sensors and avionics.

(a) Test Vehicle - ESL Vulture

(b) 3D rendered model

Figure 4.1: ESL Vulture test vehicle - realistic and 3D rendered view

4.5   Analysis of the Aircraft Model

This section focuses on the investigation of the mathematical model pertaining to the aforementioned airframe. The aerodynamic, gravitational as well as the thrust forces and moments are characteristic of a particular airframe, since they are determined by physical and measurable facets of the aircraft. A detailed discussion of how the parameters were obtained is provided in Appendix B. To this end, it is now possible to analyse a linearised model of this specific airframe so that an in-depth understanding of the flying characteristics can be used in the design of an effective Flight Control System (FCS). The following procedure was adhered to in the process of obtaining a linear aircraft model:

1. Obtain the aircraft-specific parameters

2. Determine the trim conditions

3. Calculate the trim state variables using the Newton-Raphson method

4. Linearise the dynamic equations about the trim state using small disturbance theory

The trim airspeed was chosen intuitively by investigating an upper and lower bound based on certain criteria. The lower bound was determined as the recommended landing airspeed given by most aircraft flight manuals and was calculated to be 1.3×(Stall Speed). An aircraft will stall when the critical angle of attack is surpassed, at which point flow separation starts to occur and the lift due to angle of attack decreases. The stall point is largely dependent on the airfoil section of the main lifting surface, its aspect ratio, its planform as well as several other factors which contribute to the non-linear effects of flow separation. Figure 4.2 shows the relationship between total lift and angle of attack for the Clark-Y airfoil specific to the test vehicle used in this project.
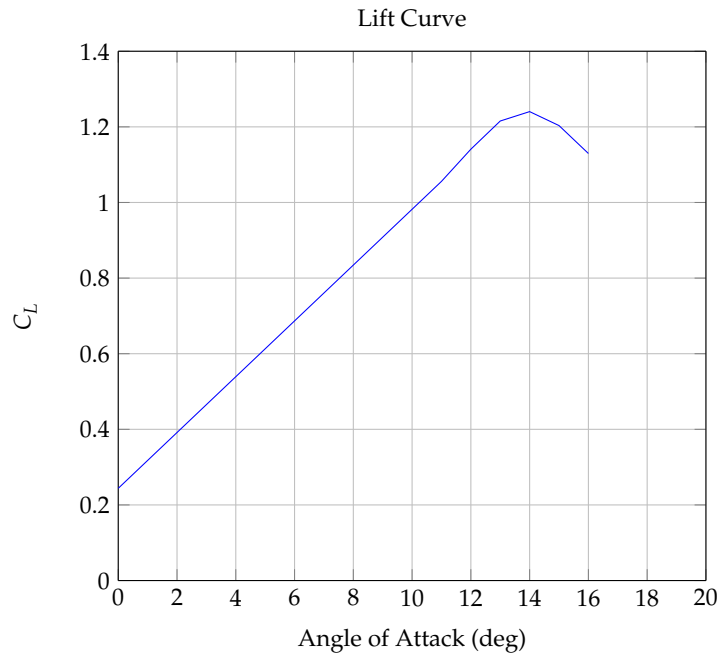
Figure 4.2: Clark-Y airfoil lift curve used to determine stall characteristics

Work done by Cavcar [36] reveals that stall speed is dependent on the following parameters: air density (ρ), wing area (S), coefficient of lift at the critical angle of attack ($C_{L_{max}}$), aircraft mass (m), and gravitational acceleration (g). Stall speed can be calculated using the following relationship:

$$V_{stall} = \sqrt{\frac{2mg}{\rho S C_{L_{max}}}} \qquad (4.30)$$

Evaluating Equation (4.30) with $C_{L_{max}} = 1.25$ from Figure 4.2 yields,

$$V_{stall} = 10.8 \text{ m/s} \qquad (4.31)$$

and therefore,

$$V_{land} = 1.3(V_{stall}) \qquad (4.32)$$

$$= 14 \text{ m/s}$$

The upper bound was determined to be the maximum attainable airspeed for straight and level flight, measured as $V_{max} = 25$ m/s following a series of practical flight tests under safety pilot control. With the upper and lower bounds defined, it was decided to trim the aircraft at a conservative airspeed of,

$$\bar{V}_T = 18 \text{ m/s} \qquad (4.33)$$

Now that the trim airspeed has been defined, it is possible to obtain the trim state variables of Equation (4.3) using the Newton-Raphson method. Table B.4 in Appendix B provides the values of the trim state variables for this particular aircraft when trimming for zero sideslip at an airspeed of 18 m/s and with $\rho = 1.225$ kg/m^3. To this end, a linear model for the longitudinal

and lateral aircraft dynamics can be obtained by evaluating Equations (4.28) and (4.29) (with a MATLAB script) using the trim state variables and other aircraft-specific parameters described in Appendix B. The result of the MATLAB linearisation script was validated via the linear aircraft model developed by Etkin and Reid [21].

4.5.1 Longitudinal Dynamics

Evaluating Equation (4.28) yields the following longitudinal aircraft model:

$$
\begin{bmatrix} \dot{\bar{v}} \\ \dot{\alpha} \\ \dot{q} \\ \dot{\theta} \end{bmatrix} = \begin{bmatrix} -0.0551 & 9.1299 & -1.0133 & -9.7948 \\ -0.0605 & -5.1734 & 0.9136 & -0.0303 \\ 0 & -76.4721 & -7.1412 & 0 \\ 0 & 0 & 1.0000 & 0 \end{bmatrix} \begin{bmatrix} \bar{v} \\ \alpha \\ q \\ \theta \end{bmatrix}
$$

$$
+ \begin{bmatrix} -0.0657 & -0.1468 & 0.1575 \\ -0.5085 & -1.1361 & 0 \\ -90.2895 & 10.9492 & 0 \\ 0 & 0 & 0 \end{bmatrix} \begin{bmatrix} \delta_e \\ \delta_f \\ \Delta T \end{bmatrix} \tag{4.34}
$$

which agrees well with Equation (B.20) in Appendix B. Figure 4.3 shows the open-loop pole locations of the linearised longitudinal aircraft model. The figure illustrates that there are two complex pole pairs that govern the longitudinal modes of motion. The high-frequency complex pole pair is known as the *short period mode* whilst the lower-frequency pair is known as the *phugoid mode*. These two modes of motion are analysed in the subsections to follow.
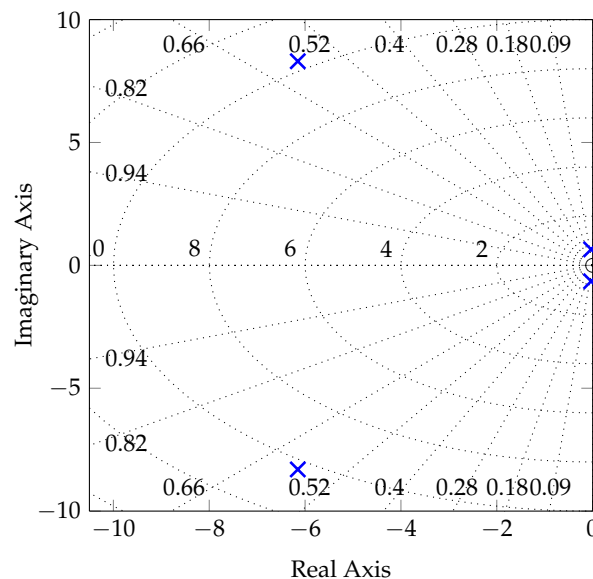
Figure 4.3: Longitudinal aircraft model pole-zero map

4.5.1.1 Phugoid Mode

The phugoid mode poles are summarised below.

$$\lambda = -0.0327 \pm 0.6494i \tag{4.35}$$

$$\zeta = 0.05 \tag{4.36}$$

$$\omega_n = 0.65 \text{ rad/s} \tag{4.37}$$

These poles form a stable, lightly damped oscillatory mode which manifests as a low-frequency oscillation in speed that couples into pitch and altitude. The period of oscillation is nearly independent of vehicle parameters and has an inverse relationship with airspeed, whilst the damping ratio of the phugoid mode is proportional to the ratio C_D/C_L, which is small for efficient airframes [37]. This dynamic mode can be described as an exchange between the kinetic and potential energy of the aircraft, damped by aerodynamic drag [3]. Consider an aircraft trimmed for straight and level flight that experiences a sudden velocity perturbation. The increased airspeed results in additional lift, which will cause the aircraft to pitch its nose up and start to climb. During the climb, the aircraft will start to lose kinetic energy in exchange for the increased potential energy, and will experience a reduction in airspeed. This, in turn, reduces the amount of lift, and the aircraft will start to pitch nose-down and lose potential energy in exchange for kinetic energy. The cycle will repeat itself, with the motion typically damped by energy removed through aerodynamic drag.

4.5.1.2 Short Period Mode

The short period mode poles are summarised below.

$$\lambda = -6.1521 \pm 8.3046i \tag{4.38}$$

$$\zeta = 0.6 \tag{4.39}$$

$$\omega_n = 10.3 \text{ rad/s} \tag{4.40}$$

These poles form a stable, well-damped, high-frequency oscillatory mode that describes the aircraft's tendency to realign itself with the incident airflow when disturbed. The period of oscillation is largely determined by the aircraft's pitch stiffness, quantified by the derivative C_{m_α}. This derivative is called the static longitudinal stability derivative and is of major importance to aircraft stability and control. Short period mode damping is determined by pitch and angle of attack damping, quantified by the derivatives C_{m_Q} and $C_{m_{\dot{\alpha}}}$ respectively [37]. This dynamic mode is best described as a torsional mass-spring-damper system, where the aircraft can be thought of as constrained to move only about its Y_B-axis, as depicted in Figure 4.4. A pitch disturbance from trim causes the spring to produce a restoring moment, quantified by C_{m_α}, which gives rise to an oscillation in pitch. Damping is induced from the pitch rate motion, quantified by C_{m_Q}, which removes energy from the system, resulting in stable oscillatory behaviour. Spring stiffness arises from the natural "weathercock" tendency of the tailplane to align itself with the incident flow, whilst the damping is due to the induced angle of incidence on the tailplane as it oscillates through the oncoming airflow [27]. The large tailplane of the test vehicle behaves like a sort of viscous paddle damper, which would explain its favourable natural damping characteristics.
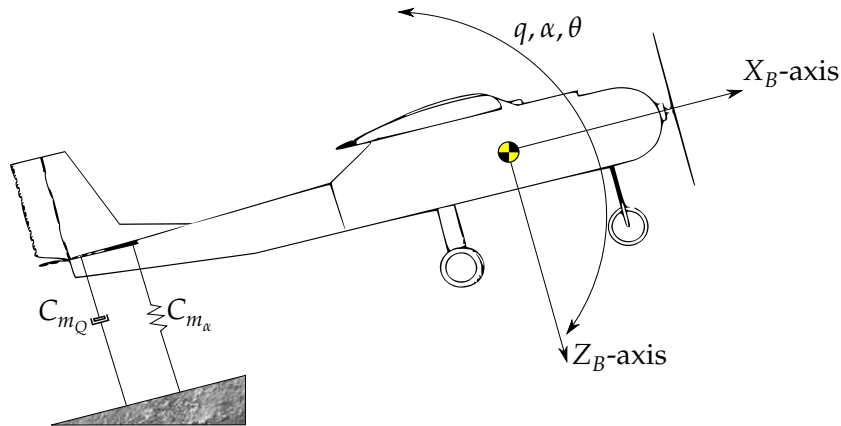
Figure 4.4: Short period mode spring damper illustration

4.5.2   Lateral Dynamics

Evaluating Equation (4.29) yields,

$$
\begin{bmatrix} \dot{\beta} \\ \dot{p} \\ \dot{r} \\ \dot{\phi} \end{bmatrix} = \begin{bmatrix} -0.2555 & 0.0621 & -0.9899 & 0.5442 \\ -21.5627 & -8.2361 & 2.1241 & 0 \\ 10.0452 & -0.7823 & -0.9740 & 0 \\ 0 & 1.0000 & 0.0557 & 0 \end{bmatrix} \begin{bmatrix} \beta \\ p \\ r \\ \phi \end{bmatrix} \tag{4.41}
$$

$$
+ \begin{bmatrix} 0.0009 & 0.1402 \\ -94.7346 & 1.3603 \\ -2.0475 & -14.3057 \\ 0 & 0 \end{bmatrix} \begin{bmatrix} \delta_a \\ \delta_r \end{bmatrix} \tag{4.42}
$$

which agrees well with Equation (B.21) in Appendix B. Figure 4.5 shows the open-loop pole locations of the linearised lateral aircraft model. The figure illustrates that there are two real poles and one complex pole pair that govern the lateral modes of motion. The set of complex poles is known as the *Dutch roll mode*, whilst the low-frequency real pole is known as the *spiral mode*, and the high-frequency real pole is commonly referred to as the *roll mode*. These three modes of motion are analysed in the subsections to follow.

4.5.2.1   Roll Mode

The roll mode pole is located at

$$
\lambda = -8.29 \tag{4.43}
$$

which corresponds to a fast, first-order exponential response with a time constant $\tau = 0.121$ s. This non-oscillatory pole manifests itself as an exponential lag characteristic in rolling motion, and is usually substantially decoupled from the spiral and Dutch roll modes [27]. With reference to Figure 4.6, consider an aircraft that is trimmed for straight and level flight, constrained to the single
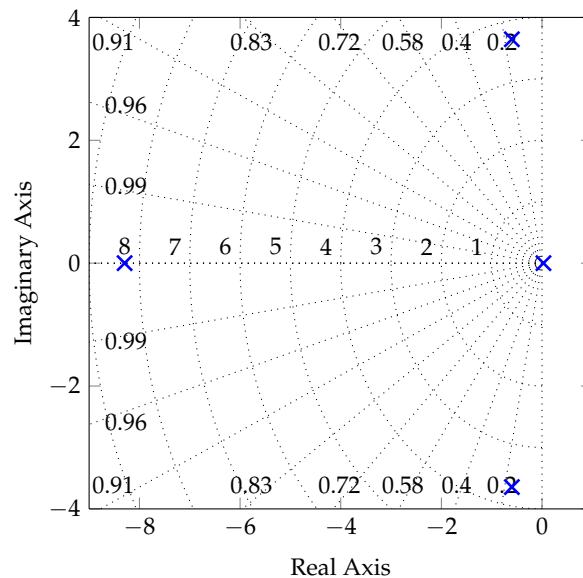
Figure 4.5: Lateral aircraft model pole-zero map

degree of freedom motion in roll about the X_B-axis. If the aircraft experiences a rolling-moment disturbance, it will begin to roll with an angular acceleration in accordance with Newton's second law of motion. This will result in an increased angle of incidence on the down-going wing, and a subsequent decrease in angle of incidence on the up-going wing. This differential lift will result in a restoring rolling moment, as indicated in Figure 4.6, which balances the disturbing moment until a steady roll rate is established. The *damping in roll* is quantified by the stability derivative C_{l_p}, as indicated in the figure.
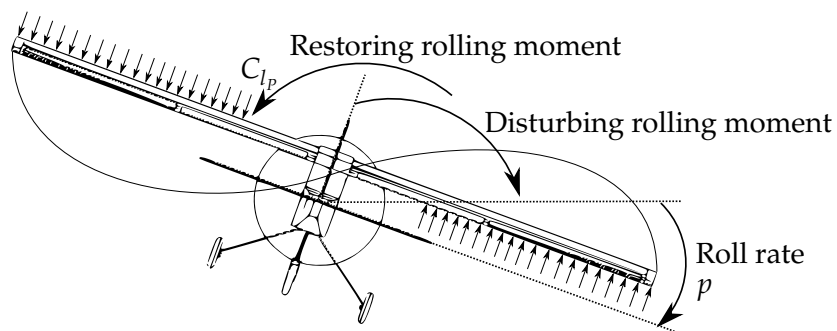
Figure 4.6: Roll mode illustration

4.5.2.2 Dutch Roll Mode

The Dutch roll mode poles are summarised below.

$$\lambda = -0.595 \pm 3.64i \tag{4.44}$$

$$\zeta = 0.16 \tag{4.45}$$

$$\omega_n = 3.69 \,\text{rad/s} \tag{4.46}$$

These poles manifest as a classical damped oscillation in yaw which couples into roll, and to a lesser extent, into sideslip. The Dutch roll mode is therefore a complex interaction between all three lateral degrees of freedom of the aircraft's motion. Fundamentally, the Dutch roll mode is considered the lateral equivalent of the short period mode, with the vertical stabiliser acting as a sort of paddle damper that produces an opposing yawing moment. Although these modes are considered fundamentally equivalent, the Dutch roll mode is typically less damped than the short period mode, since the vertical stabiliser is usually less aerodynamically efficient than the horizontal stabiliser.

With reference to Figure 4.7, consider an aircraft trimmed for straight and level flight, restrained in yaw and roll by a torsional spring damper system acting about the Z_B- and Y_B-axis. If the aircraft is disturbed in yaw, the aerodynamic damping effect of the tail fin, quantified by C_{n_R}, will produce an opposing yawing moment, which results in classical damped oscillatory motion. As the aircraft yaws, the forward-moving wing will experience more lift than the aft-moving wing, which results in differential lift. The differential lift then causes a rolling moment, which is approximately $90°$ out of phase with the yawing oscillation. The oscillations in yaw and roll cause the wingtips to have an elliptical orbit as the aircraft moves forward through the air. The perturbations in roll are further constrained by their own torsional spring damper system, as depicted in Figure 4.7.
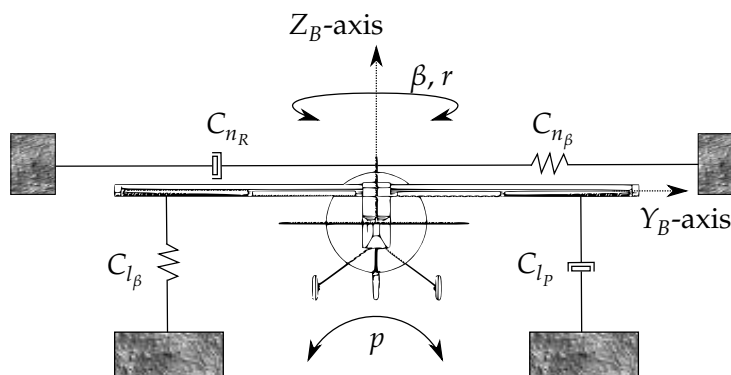
Figure 4.7: Dutch roll mode illustration

The natural "weathercock" tendency of an aircraft to re-align itself with the incident airflow is commonly referred to as natural directional stability, and is quantified by the C_{n_β} derivative. The aerodynamic stiffness and damping in yaw are largely determined by the aerodynamic properties of the vertical stabiliser - a large fin is desirable for a well-damped and stable Dutch roll mode. Unfortunately, this contradicts the requirements for a stable spiral mode, which leads to

the aerodynamic design compromise of a mildly unstable spiral mode and a poorly damped Dutch roll mode [27]. It should be noted that an aircraft's natural directional stability can be improved through additional aerodynamic design considerations, such as wing dihedral and swept-back wings [38].

4.5.2.3   Spiral Mode

The spiral mode pole is located at

$$\lambda = 0.028 \tag{4.47}$$

which corresponds to a very slow, unstable real pole. The spiral mode describes the aircraft's ability to return to wings-level flight after a disturbance in sideslip, which typically follows a perturbation in roll. With reference to Figure 4.8, consider an aircraft trimmed for straight and level flight that experiences a disturbance in sideslip. The sideslip creates an angle of incidence β, which produces a positive yawing moment, quantified by C_{n_β}, which will turn the aircraft into the direction of the sideslip. The yawing motion produces differential lift, which induces a positive rolling moment, quantified by C_{l_R}, which further exacerbates the situation, as it causes the starboard wing to drop even more. This effect is divergent and therefore unstable if the restoring moment, largely dependent on wing dihedral and quantified by C_{l_β}, is not sufficient to return the aircraft to wings-level flight. When the dihedral effect is greater, the spiral mode is stable, and when the fin effect is greater, the spiral mode is unstable [27]. The following relationship describes the requirement for a stable spiral mode:

$$C_{l_\beta} C_{n_R} > C_{n_\beta} C_{l_R} \tag{4.48}$$
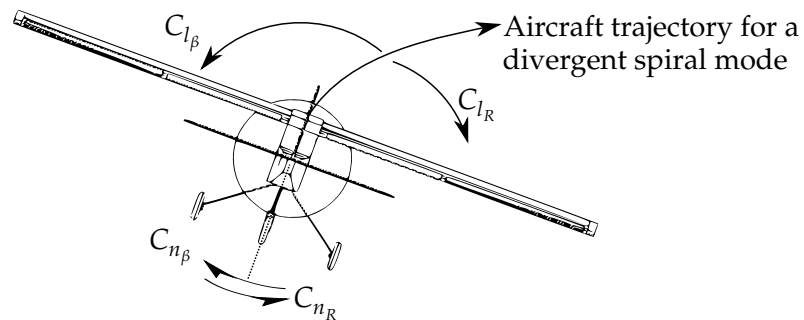
Figure 4.8: Spiral mode illustration

The pole-zero locations pertaining to the aforementioned state-space representation of the aircraft dynamics provide some insight regarding particular flight characteristics. A general description of the modes of motion for small to medium-sized UAVs by Peddle [1] and Cook [27] validates the pole locations discussed in the preceding sections. This specific aircraft model is further validated through work done in [3, 5, 6, 9], in which successful autopilot systems for fixed-wing unmanned aircraft were developed.

4.5.3 Effect of AoA and AoSS on Stability

In the preceding section, special mention was made of some important stability derivatives that characterise natural aircraft stability, and contribute to the various dynamic modes of motion which govern particular flying qualities. Figures 4.9 and 4.10 show how some of these derivatives change as a function of Angle of Attack (AoA) α and Angle of Sideslip (AoSS) β. It is important to note that the derivatives have been scaled according to their corresponding geometric contributions and maximum expected values in order to obtain results that are more easily comparable. The scaled derivatives are denoted as $\acute{C}_{A_B}$.

Figure 4.9a shows how some of the steady-state coefficients change as a function of AoA when $\beta = 0$. It is apparent that the longitudinal static stability derivative $\acute{C}_{m_\alpha}$ remains negative throughout the AoA range, which ensures that the aircraft always experiences a restoring moment for angle of attack perturbations. This derivative is proportional to the distance between the aerodynamic centre (neutral point) of the aircraft and its CG. The dihedral effect, quantified by $\acute{C}_{l_\beta}$, is seen to become more negative over the range of positive α, thereby increasing spiral mode stability in accordance with Equation (4.48). It does, however, cross the zero line and become a positive value around $\alpha = -3^\circ$, which results in spiral mode instability as the dihedral effect no longer produces a restoring rolling moment for sideslip perturbations. The directional static derivative, quantified by $\acute{C}_{n_\beta}$, is seen to become increasingly positive over the range of α, which simultaneously improves weathercock stability whilst decreasing spiral mode stability in accordance with Equation (4.48). At high angles of attack, C_{n_β} will be affected significantly as the fin becomes submerged in the wing-body wake [39].

(a) Steady-state coefficients

(b) Perturbed-state coefficients
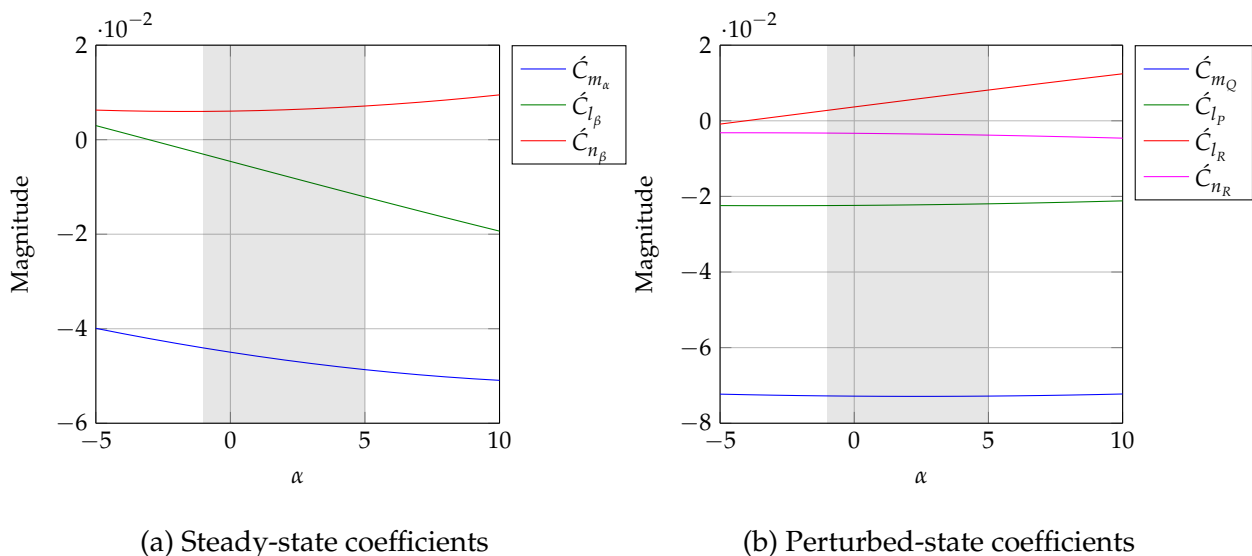
Figure 4.9: Coefficients for changing AoA scaled according to their individual geometric contributions and maximum expected values. Shaded area represents typical AoA range for conventional flight. Note $\beta = 0$ in each case.

Figure 4.9b shows how some of the perturbed-state coefficients change as a function of AoA when $\beta = 0$. The pitch-damping derivative, quantified by $\acute{C}_{m_Q}$, is seen to become slightly less

negative throughout the range of α. Usually more negative values of C_{m_Q} signify increased damping; however, the sign is generally negative for both stable and unstable configurations [39]. On observation of Figure 4.9b, there is a clear reduction in the damping-in-roll derivative, quantified by $\acute{C}_{l_P}$, for increased angles of attack, which is consistent with work done by Raol et al. [39]. This derivative does, however, remain negative throughout the range of α, which means that the aircraft will still experience a restoring moment for roll rate perturbations, even for negative angles of attack. The perturbed-state derivative $\acute{C}_{l_R}$ quantifies the rolling moment produced through yaw rate perturbations and is seen to increase with AoA, resulting in decreased spiral mode stability in accordance with Equation (4.48). Furthermore, it can be seen that this derivative crosses the zero line and becomes a negative value for $\alpha < -4°$. The damping-in-yaw derivative $\acute{C}_{n_R}$ quantifies the yawing moment produced by the aircraft due to yaw rate perturbations, and is seen to become slightly more negative with increasing angles of attack. Larger negative values of C_{n_R} signify increased yaw rate damping and improved spiral mode stability in accordance with Equation (4.48).

Figures 4.10a and 4.10b show how some of the steady-state and perturbed-state coefficients change as a function of AoSS when $\alpha = 3.5°$. It is clear to see that the coefficients remain fairly constant for varying AoSS and that each remains within their stable region as $\beta \to 15°$. It is also clear that the aforementioned stability analysis resulted in the finding of two potential regions of concern, where stability coefficients crossed the zero line and changed their sign for certain angles of attack. Yet these findings should not result in any unexpected behaviour, since the typical range of AoA for this particular aircraft lies between $-1° < \alpha < 5°$, depicted as the shaded area in Figures 4.9a and 4.9b. In conclusion, it can be said that the aforementioned stability derivatives vary more with increased AoA than with AoSS, although in both cases they remain within their stable region, and there seem to be no obvious anomalies that may cause unexpected instabilities for the AoA range specified above.

(a) Steady-state coefficients

(b) Perturbed-state coefficients
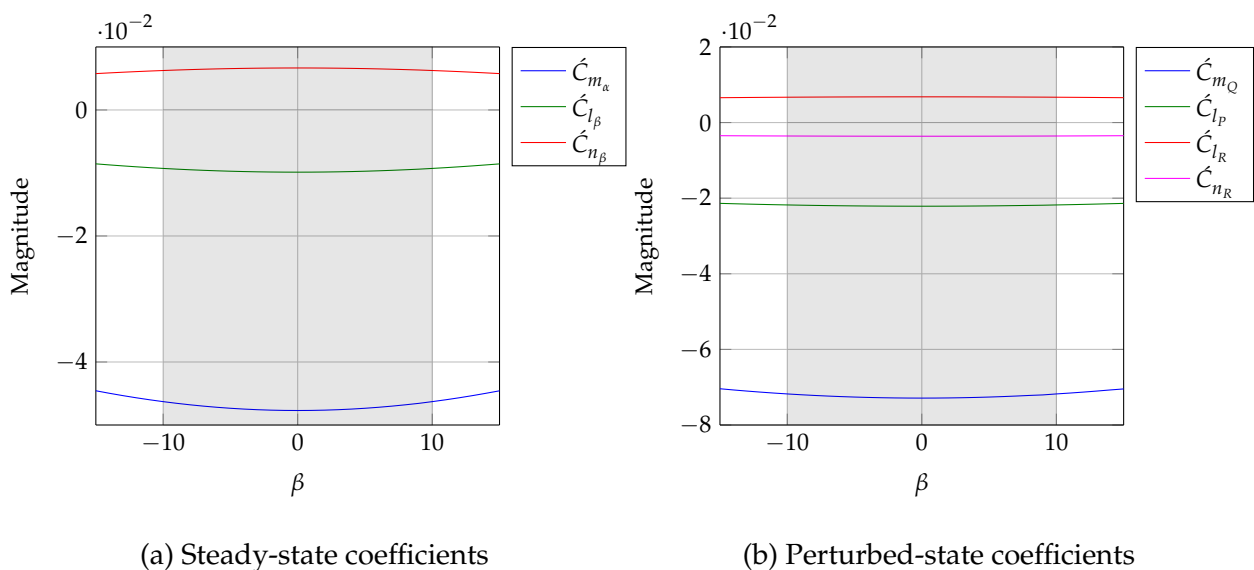
Figure 4.10: Coefficients for changing AoSS scaled according to their individual geometric contributions and maximum expected values. Shaded area represents typical AoSS range for conventional flight. Note $\alpha = 3.5°$ in each case.

4.5.4   Effect of Wind on Stability

In the preceding analysis of the longitudinal modes of motion, the atmosphere has been assumed to be at rest, with a uniform velocity and constant in time. Since this thesis is focused on landing an unmanned aircraft under adverse weather conditions, it is necessary to examine the effects of non-uniform and unsteady motion of the atmosphere on flight characteristics. Random gusts and atmospheric turbulence effects are important to consider for structural analysis and passenger comfort; however, it was found that wind shear was the primary cause of touchdown inaccuracies and large variations in sink rate during automatic landings [40]. In order to introduce wind into the model, additions to the non-linear force and moment equations are required. A model would have to be introduced which describes the aerodynamic forces and moments for a whole range of speeds and attitudes experienced by an aircraft throughout the transient during take-off and landing. Such an analysis is considered outside of the scope of this thesis. Etkin and Reid [21] discuss a relevant steady-state condition which can be investigated with the linear model developed in the preceding sections. Horizontal flight in the boundary layer (wind shear) is one flight condition that is readily introduced into the linearised dynamics and can be used to analyse the effects on stability in the aircraft's longitudinal axis. The vertical extent of the boundary layer is largely determined by the roughness of the underlying terrain, but is usually apparent for hundreds of feet above the surface [21]. Etkin and Reid [21] provide a graph of the power-law profiles associated with different terrain roughnesses in the form of a generic exponential function,

$$W = kh^n \tag{4.49}$$

so that the vertical gradient is then given by,

$$\frac{dW}{dh} = nkh^{n-1} \tag{4.50}$$

where h is height above the ground, k is the appropriate function gain parameter, and n is the terrain roughness characterisation factor. For example, for a smooth terrain (n = 0.16) and for a wind of 15 m/s at the reference altitude of 15 m,

$$15 = k(15)^{0.16} \rightarrow k = 9.7256 \tag{4.51}$$

Now evaluating Equation (4.50) yields,

$$\frac{dW}{dh} = 0.16 \tag{4.52}$$

so that every metre of altitude gained would result in a 0.16 m/s increase in wind speed. The effect of wind shear will be introduced into the following simplified longitudinal aircraft model, linearised for small perturbations around a reference state of horizontal flight at speed u_0 and

pitch angle $\theta_0 = 0$ [21],

$$\Delta X = m(\dot{u}^E + g\theta) \tag{4.53}$$

$$\Delta Z = m(\dot{w}^E - u_0^E q) \tag{4.54}$$

$$\Delta M = I_{yy}\dot{q} \tag{4.55}$$

$$\dot{\theta} = q \tag{4.56}$$

$$\dot{z}_E = -u_0^E \theta + w^E \tag{4.57}$$

with,

$$\boldsymbol{V}^E = \boldsymbol{V} + \boldsymbol{W} \tag{4.58}$$

where ΔX and ΔZ denote force perturbations in the X_B- and Z_B-axis respectively, ΔM denotes pitching moment perturbations about the Y_B-axis, $\dot{\theta}$ denotes pitch rate, and $\dot{z}_E$ represents the aircraft's velocity coordinated in the inertial frame. Equation 4.58 describes True Airspeed (TAS) as a function of the inertially coordinated wind velocity vector ($\boldsymbol{W}$) and the aircraft's CG relative to the air ($\boldsymbol{V}$). Wind speed is specified parallel to the XZ-plane and to vary linearly with altitude and with spatial gradient,

$$\xi = \frac{dW}{dz_E} \tag{4.59}$$

where,

$$dz_E = -dh \tag{4.60}$$

The wind vector is prescribed in the inertial frame $F_E(O_E X_E Y_E Z_E)$ as,

$$\boldsymbol{W}_E = \begin{bmatrix} 1 \\ 0 \\ 0 \end{bmatrix} (W_0 + \xi z_E) \tag{4.61}$$

where W_0 represents a tailwind at the reference altitude z_E. The wind vector coordinated in the inertial frame is transformed to the body axis frame using the DCM of Equation (3.56) with $\phi = \psi = 0$. Using small-angle approximations, the wind vector coordinated in the body axis is given by,

$$\boldsymbol{W}_B = \begin{bmatrix} W_0 + \xi z_E \\ 0 \\ (W_0 + \xi z_E)\theta \end{bmatrix} \approx \begin{bmatrix} W_0 + \xi z_E \\ 0 \\ W_0\theta \end{bmatrix} \tag{4.62}$$

where the second-order product $z_E\theta$ is assumed to be negligibly small and has therefore been eliminated from the vector. The wind vector, now coordinated in the body axis, is introduced into

the system of equations using Equation (4.62) together with (4.58) to eliminate u^E and w^E from Equations (4.53), (4.54), and (4.57) which yields,

$$\Delta X = m(\dot{u} + \xi \dot{z}_E + g\theta) \tag{4.63}$$

$$\Delta Z = m(\dot{w} + W_0\dot{\theta} - u_0^E q) \tag{4.64}$$

$$\dot{z}_E = -u_0^E \theta + w + W_0\theta \tag{4.65}$$

Noting once again that $u_0^E = u_0 + W_0$ and eliminating $\dot{\theta}$ and $\dot{z}_E$ by substituting Equations (4.56) and (4.65) into (4.63) and (4.64) yields,

$$\Delta X = m(\dot{u} + \xi[-u_0\theta + w] + g\theta) \tag{4.66}$$

$$\Delta Z = m(\dot{w} - u_0 q) \tag{4.67}$$

$$\dot{z}_E = -u_0\theta + w \tag{4.68}$$

It is apparent that the only explicit effect of wind on the system of equations is the term containing ξ in Equation (4.66). Since a uniform wind with spatial gradient $\xi = 0$ should not influence the aircraft dynamics, the system should then also be independent of the term W_0, which is indeed the case. Rewriting Equation (4.66) so that $\dot{u}$ is the subject of the formula,

$$\dot{u} = \frac{\Delta X}{m} - \xi w - (g + \xi u_0)\theta \tag{4.69}$$

and noting that $\Delta X = \Delta X_u u + \Delta X_w w + \Delta X_c c$ yields,

$$\dot{u} = \frac{\Delta X_u}{m}u + \left(\frac{\Delta X_w}{m} - \xi\right)w - (g + \xi u_0)\theta + \frac{\Delta X_c}{m}c \tag{4.70}$$

where c is the control input vector. It is apparent that Equation (4.70) is of the same form as the linearised aircraft model given in (4.23). The terms containing ξ can therefore be introduced into the longitudinal model as follows:

$$A = \begin{bmatrix} \frac{X_u}{m} & \left(\frac{X_w}{m} - \xi\right) & 0 & (-g + \xi u_0) \\ & & A' & \end{bmatrix} \tag{4.71}$$

where A' is a 3x4 matrix consisting of the last three rows of Equation (4.28). Figure 4.11 shows the effect of the wind shear gradient on the longitudinal aircraft modes of motion for ξ ranging from -0.36 (the headwind case) to +0.36 (the tailwind case).

It is apparent that the wind shear gradient has negligible effects on the short period mode, whilst the frequency and damping ratio of the phugoid motion vary considerably. This finding corresponds well with work published by NASA's Langley Research Centre [40], where it was found that in the situation of an increasing headwind or decreasing tailwind with altitude, the phugoid mode became unstable for sufficiently large spatial gradients. On observation of Figure 4.11 it can be seen that for the particular airframe modelled in this thesis, the phugoid mode moves from a set of complex poles to a set of stable real poles when $\xi = 0.24 \, \text{s}^{-1}$. One of the real poles is seen to become unstable at the unlikely value of $\xi = 0.3 \, \text{s}^{-1}$ at an airspeed of 40 m/s, indicating diverging, aperiodic motion.

(a) Phugoid mode

(b) Short period mode - note figure scale
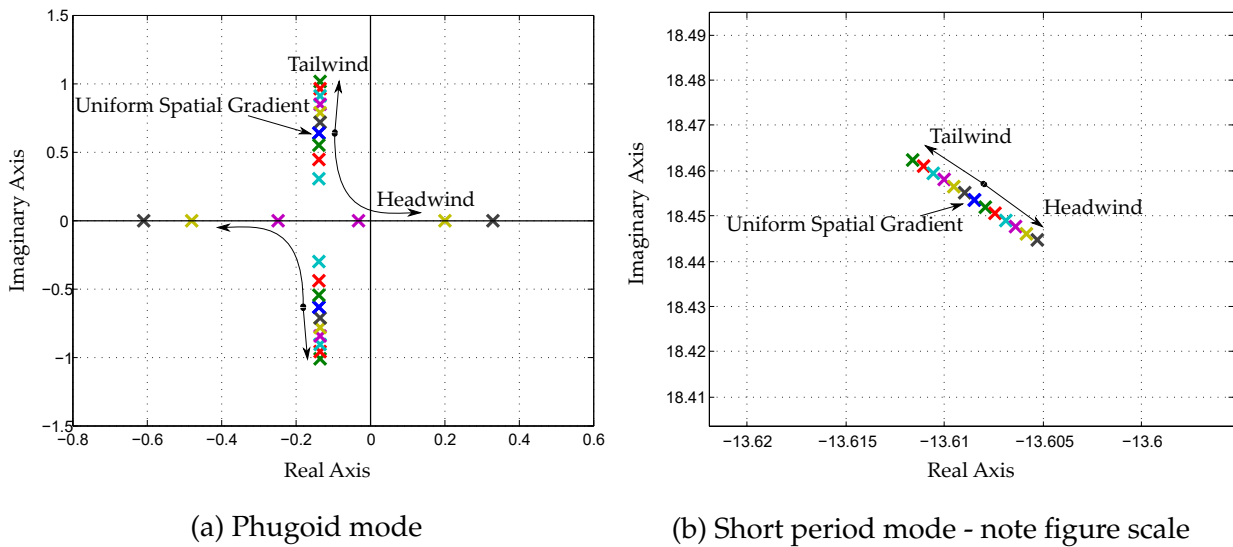
Figure 4.11: The effect of wind shear on the longitudinal modes of motion with spatial gradient ranging from -0.36 (the headwind case) to +0.36 (the tailwind case)

The root locus of the phugoid mode poles is best described in terms of the distorting effect that the wind spatial gradient has on the kinetic and potential energy exchange. For the case of an increasing headwind with altitude, it is intuitive that an aircraft will climb higher in comparison to flight in still air at the same airspeed, angle of attack, and throttle setting. This additional climb rate manifests as an additional amount of potential energy added to the system as the aircraft attains a higher altitude. The additional energy added to the system ultimately decreases the frequency of the phugoid motion and reduces the damping ratio considerably. The time required for the phugoid to damp to half of its original amplitude increases in a climb and decreases in a dive as expected [40]. It can be seen that this effect is amplified for the case of an increasing headwind, even to the extent of instability in extreme cases. For the case of a decreasing headwind with altitude, the phugoid motion is seen to have an increase in frequency and a simultaneous decrease in damping ratio. An aircraft will experience a higher sink rate in comparison to flight in still air, which manifests as an additional amount of kinetic energy, thereby increasing the natural frequency of the oscillatory poles.

In addition to the effects seen in Equation (4.70), there exist some implicit effects of the wind gradient on the aerodynamic derivatives. It is intuitive that the pressure distribution over the aerodynamic surfaces of the aircraft are not the same at each point, and hence the basic aerodynamic derivatives will be different when the incident flow has a gradient ζ in comparison to flight in spatially uniform atmospheric conditions. Consider an aircraft flying straight and level in a nonuniform atmosphere with gradient ζ. If the aircraft experiences a perturbation in angle of attack (α), the tail moves downward into a region of lower air velocity, which results in a reduction of pitch stiffness as C_{m_α} will be smaller than normal - this reduction in restoring moment could lead to further instabilities. Now consider a similar scenario with an aircraft that experiences a perturbation in roll angle (Φ). The down-going wingtip enters a region of low air velocity whilst the up-going wingtip experiences a region of high air velocity. The differential air velocity across the span generates derivatives of C_{l_Φ} and C_{n_Φ} (where none existed before), resulting in unstable roll stiffness for upwind flight and further exacerbating the adverse yaw experienced by the aircraft.

4.6 Summary

In this chapter, the concept of small disturbance theory was used to linearise the dynamic equations developed in the preceding chapter. This led to the development of a linearised aircraft model that can be applied to any conventional fixed-wing airframe. The aerodynamic and geometric properties of the airframe specific to this project were then incorporated into the model so that a detailed analysis could be conducted. The analysis involved a thorough investigation of the longitudinal and lateral modes of motion, as well as the effects of AoA, AoSS, and wind on static and dynamic aircraft stability. It is imperative that the autopilot system designed in the next chapter encapsulate these model uncertainties and ensure that the aircraft remains stable throughout the entire flight envelope. Now that a linearised aircraft model has been developed and evaluated, the next chapter will focus on the design and implementation of a synergistic flight control system.

CHAPTER 5

Control System Design

Now that a mathematical model of the test vehicle has been derived and its flight characteristics analysed in detail, it is possible to proceed with a detailed design of the autopilot system. This chapter presents the design and development of a synergistic controller architecture with strong disturbance rejection characteristics, capable of landing a fixed-wing UAV accurately under crosswind conditions. An overview of the controller architecture is first discussed in Section 5.1, where details of the controller interactions are provided so as to create an understanding of the flight control system. Section 5.2 deals with the design of longitudinal flight controllers that are responsible for regulating airspeed and altitude, whilst Section 5.3 deals with the lateral flight controller design, responsible for waypoint navigation and heading alignment. The runway controllers, responsible for guiding the aircraft after touchdown, are not the primary focus of this thesis and thus a detailed design thereof is provided in Appendix D for further perusal.

5.1   Controller Architecture

Figure 5.1 shows a detailed layout of the controller architecture. It is apparent that the structure features a three-tiered approach that includes a series of inner-loop and outer-loop controllers driven by navigation algorithms and state machine logic. The inner-loop controllers drive the aircraft's control inputs and are primarily responsible for stability augmentation. A successive loop closure technique or cascade control structure is then employed, with each loop abstracting further from the inner loop. This type of control strategy tends to work well in practice and often yields simple, easy-to-tune controllers, with each outer layer inheriting the stability of the corresponding inner-loop controller [34]. The outer-loop controllers are responsible for regulating the aircraft's attitude and position in three-dimensional space.

Due to the inherently high-bandwidth requirements associated with the objectives stated in this thesis, an Acceleration-Based Controller (ABC) architecture is adopted for the design of the inner-loop controllers. Acceleration controllers are commonly used in missile applications; how-

ever, Peddle [1] extended the attitude independence of this type of controller and its application to aircraft manoeuvre flight control. The following list describes the advantages associated with ABC that contributed to the decision of using acceleration control in this thesis:

- Attitude-independent

- Can be used throughout the entire 3D flight envelope

- Model uncertainties remain encapsulated behind the typically high-bandwidth acceleration controllers

- Ability to reject disturbances at the acceleration level before they manifest as deviations in position, velocity, and attitude

- Practical feasibility and computational efficiency

With reference to Figure 5.1, it is apparent that the longitudinal flight control structure is comprised of an airspeed, altitude, climb rate, and Normal Specific Acceleration Direct Lift Controller (NSADLC). The airspeed controller regulates Indicated Airspeed (IAS) by commanding thrust generated by an electric motor. The NSADLC controller forms part of the longitudinal inner-loop controllers and regulates normal specific acceleration by commanding both the elevator and flap aerodynamic control surfaces. Following a successive loop closure design technique, the climb rate controller generates a normal specific acceleration command that the inner-loop NSADLC controller should regulate. Closing the loop once more allowed for the design of an altitude controller which receives reference information from the state machine before generating a climb rate command that the climb rate controller should regulate via the NSADLC controller. It is important to note that the normal specific acceleration command is initially parsed through a conversion block to compensate for the lift deficiency as the aircraft banks to turn. Additional normal specific acceleration is introduced by transforming C_n to C_w though the measured roll angle Φ, as shown in Figure 5.1. This conversion essentially aids the altitude controller in maintaining a constant altitude as the aircraft manoeuvres between various waypoints throughout the mission.

The lateral flight control structure is comprised of a guidance, roll angle, roll rate, heading, and Lateral Specific Acceleration (LSA) controller. The roll rate controller forms part of the lateral inner-loop controllers and is designed to regulate roll rate by deflecting the ailerons. Employing a successive loop closure technique, the roll angle controller is designed to command a roll rate which the inner-loop roll rate controller should regulate. Closing the loop once more allowed for the design of a guidance controller which generates a commanded roll angle according to the measured cross-track error between the current aircraft position and the waypoint track. The algorithm used to determine the cross-track and in-track distances forms part of the navigator and is further discussed in Chapter 6.

The LSA controller is responsible for controlling the aircraft's directional dynamics and works in tandem with the heading controller when executing either a de-crab or low-wing manoeuvre. The heading controller generates a lateral specific acceleration command, which the inner-loop LSA controller should regulate using the rudder. The proposed heading/LSA combination is not one typically used when controlling aircraft heading; however, the inclusion of the LSA controller proved invaluable as this allowed for a seamless integration of the acceleration-based LSA,
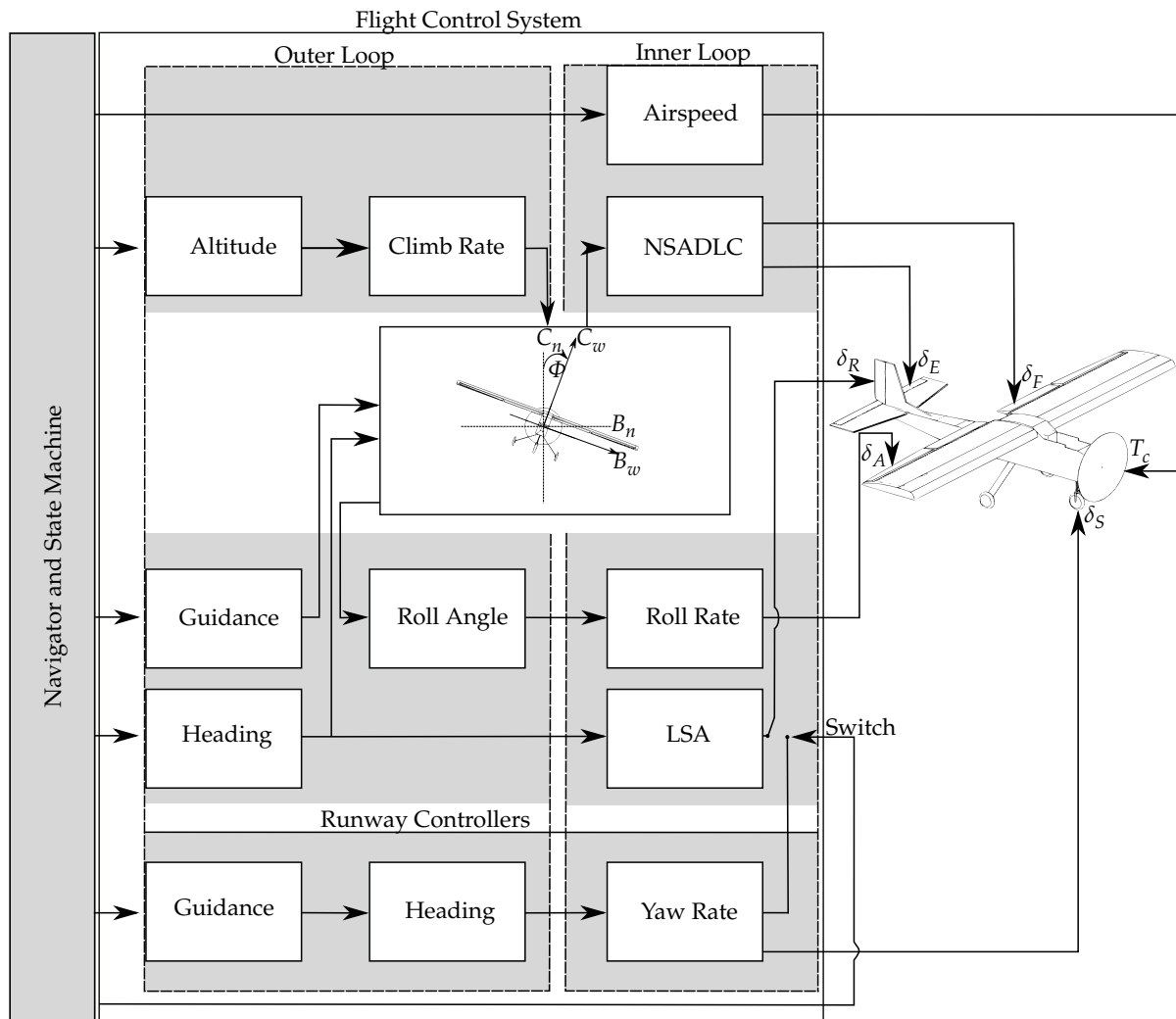
Figure 5.1: Control system architecture

NSADLC, and roll rate controllers. Furthermore, the inclusion of a controller designed to regulate lateral specific acceleration introduced additional functionality by enabling the Flight Control System (FCS) to conduct coordinated turns.

Due to the natural weathercock tendency of the aircraft to align itself with the incident airflow, it is necessary to introduce a conversion block that generates an additional bank angle command relative to the commanded heading angle to aid the guidance controller in maintaining a constant flight path. Consider an aircraft flying straight and level in still air (no wind) between two corresponding waypoints with its longitudinal axis aligned with the destination waypoint, as in Figure 5.2a. If a heading command is given that results in a misalignment between the aircraft's body axis and its velocity vector, the new alignment of the thrust vector will eventually cause the aircraft to change its direction of travel and deviate from the original flight path - this is known as skid-to-turn. In order to maintain a constant flight path during heading perturbations, the FCS should make use of cross-control between the ailerons and rudder to maintain the sideslip angle by banking in the opposite direction to the heading perturbation, as seen in Figure 5.2b.

The conversion block is essentially a feed-forward term from the heading controller to the roll angle controller, which aids the guidance controller in regulating a constant flight path by

making use of aileron/rudder cross-control. Cross-control of the lateral-directional actuators is an essential part of any crosswind landing, and it is therefore important to include in FCS design considerations. Controlling cross-track error with the ailerons and heading with the rudder allows the FCS to autonomously fly an aircraft in a straight line even if there is a misalignment between the body axis and the velocity vector. This is typical of a low-wing landing approach and will be discussed further in Chapter 6.

(a) Heading aligned with flight path   (b) Heading and flight path not aligned
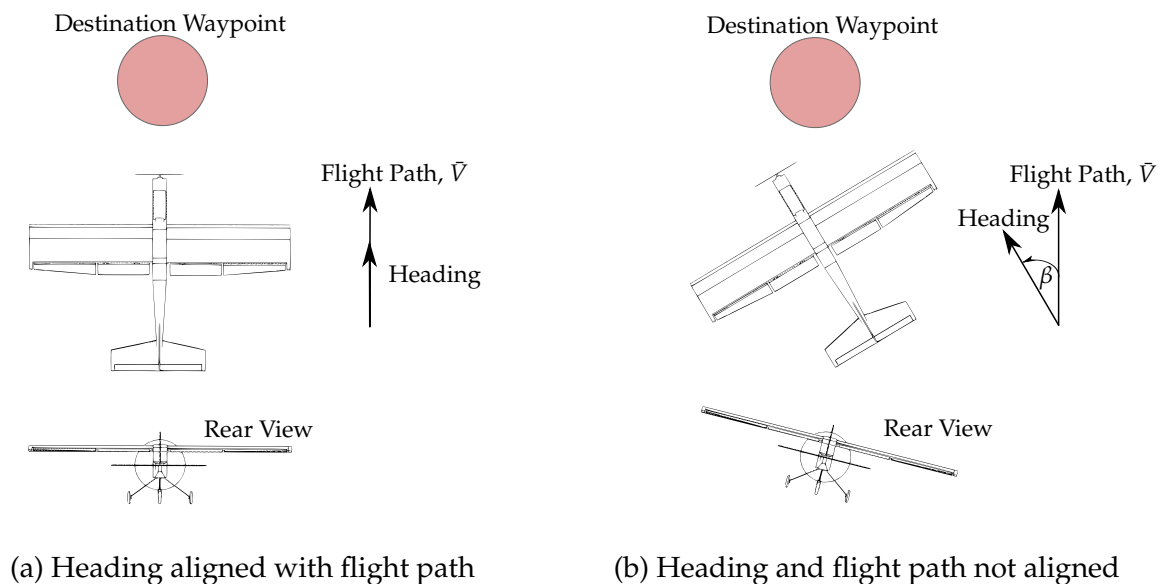
Figure 5.2: Adding roll compensation to maintain flight path

The design strategy for the FCS is to ensure high-bandwidth inner-loop controllers capable of rejecting disturbances at the acceleration level. Controllers are therefore designed according to an optimal balance between disturbance rejection capabilities and robustness to ensure optimal performance whilst operating under various model uncertainties.

All of the above-mentioned controllers play a crucial role in controlling the aircraft under adverse weather conditions. However, two of these are worth special mention, as they have been designed specifically to mitigate risks associated with crosswind landings. The NSADLC controller is responsible for the high-bandwidth disturbance rejection characteristics required to track the glideslope accurately during turbulent and gusty wind conditions. The heading controller is responsible for aligning the aircraft's longitudinal axis with the runway during final approach, and is therefore primarily used when executing a de-crab or low-wing manoeuvre.

The aforementioned controllers are all responsible for controlling the aircraft during conventional flight and will therefore be referred to as the flight controllers. Another set of controllers, which is responsible for controlling the aircraft after touchdown, will be referred to as runway controllers. It is apparent from Figure 5.1 that the runway controller structure is comprised of a guidance, heading, and yaw rate controller. The yaw rate controller directly commands both the rudder and nose wheel in a 2:1 ratio, as recommended by Roos [4]. Cascading the controllers once again allows for the design of both the heading and guidance controllers responsible for guiding the aircraft down the runway centreline after touchdown. A state machine is responsible for ac-

tivating the switch, seen in Figure 5.1, which alters the source of the rudder command from the LSA flight controller to the runway yaw rate controller. This transition occurs when an observed acceleration spike exceeds a predetermined threshold at the point of touchdown.

Once the aircraft has landed, it may be referred to as a ground craft, although it is important to note that the laws of aerodynamics still apply. For this particular reason, it is necessary to ensure that the roll angle controller remains active until the aircraft comes to a complete stop on the runway. Runway controllers are not the primary focus of this thesis and thus a detailed design thereof is provided in Appendix D for further perusal.

The detailed controller designs that follow are based on the linear, decoupled rigid body rotational dynamics models derived and analysed in the preceding chapter. Pole placement is used in the design of the inner-loop controllers to ensure stability, performance and an invariant dynamic response of the closed-loop system, in accordance with work done by Peddle [1]. Guidelines for pole placement, formulated by Peddle, are investigated and followed closely when selecting closed-loop pole locations. It is possible to use Time Scale Separation (TSS) in the design of the outer-loop controllers by approximating inner-loop dynamics as simple first-order time delays. Albeit simple, this method of successive loop closure fails to encapsulate the full dynamics of the plant, and usually results in the design of inherently slower controllers, which might not exhibit adequate disturbance rejection characteristics. It was thus decided that each control law would be augmented to the full aircraft model in order to improve controller design fidelity and maximise disturbance rejection capabilities. Now that an overview of the controller architecture has been provided, it is possible to continue with a detailed design and verification of the individual controllers that constitute this synergistic FCS architecture.

5.2 Longitudinal Controllers

The design and verification of the aircraft's longitudinal controllers are discussed in this section. Each subsection begins with a discussion of the design approach before the details of the controller are considered and the results verified by linear simulation. The cascaded design approach starts with the augmentation of an airspeed controller by closing the first control loop around the decoupled longitudinal aircraft dynamics of Equation (4.28). This is then followed by the design and verification of an inner-loop NSADLC controller, a middle-loop climb rate controller, and finally the implementation of an outer-loop altitude controller. It is important to note that active anti-windup protection was added to all of the integrators.

5.2.1 Airspeed Controller

This section presents the design and verification of an airspeed controller that regulates IAS by means of the commanded thrust. With reference to Figure 5.1, it is apparent that the airspeed reference input comes directly from the FCS state machine as the aircraft navigates a particular set of waypoints. The IAS reading on the practical test vehicle comes from a pitot-static tube mounted on the left wingtip to avoid prop-wash disturbances contaminating the airspeed reading. It should be noted that the airspeed controller is designed independently of the climb rate dynamics, despite the obvious coupling that exists. These coupling effects are typically addressed by designing a Multi-Input, Multi-Output (MIMO) controller that regulates airspeed and climb rate

simultaneously in an optimal way, using a combination of the elevator and thrust command. To illustrate this optimal control method, consider a negative airspeed step; the thrust command will decrease and allow drag to slow the aircraft down, whilst the elevator simultaneously generates a positive climb rate to allow gravitational forces to further reduce airspeed. Albeit optimal, this type of control strategy could result in oscillatory behaviour when the aircraft transitions from a straight and level flight trajectory to a glideslope reference during final approach. In light of the previous argument, if a negative step is commanded to bring the airspeed down from nominal to a reasonable approach airspeed, an optimal controller would reduce thrust and command a positive climb rate. This is the exact opposite of what is required when tracking the glideslope. The initial conflict between climb rate and airspeed could result in longitudinal oscillations, which pilots often refer to as *porpoising on final approach*. Furthermore, MIMO controllers are inherently more complex and therefore more difficult to implement and fine-tune for practical applications. To this end, it was decided that the airspeed and climb rate controllers would be designed independently under the assumption that airspeed is sufficiently maintained.

5.2.1.1 Design

Equation (3.101) describes the relationship between commanded and observed thrust as a function of the engine lag dynamics and is restated below for convenience.

$$\dot{T} = \left[-\frac{1}{\tau_e} \right] T + \left[-\frac{1}{\tau_e} \right] T_c \tag{5.1}$$

Following a simplification by Peddle [1], the wind axis system axial acceleration can be written as follows:

$$A_w = \left[\frac{1}{m} \right] T + \left[-\frac{qSC_D}{m} \right] \tag{5.2}$$

Noting that $A_w = \dot{V}$ for flight in a spatially uniform and still atmosphere, a linearised model of the simplified velocity dynamics can be written as,

$$\begin{bmatrix} \Delta\dot{T} \\ \dot{\bar{v}} \end{bmatrix} = \begin{bmatrix} -\frac{1}{\tau_e} & 0 \\ \frac{1}{m} & 0 \end{bmatrix} \begin{bmatrix} \Delta T \\ \bar{v} \end{bmatrix} + \begin{bmatrix} \frac{1}{\tau_e} \\ 0 \end{bmatrix} \Delta T_c \tag{5.3}$$

where the states are represented as perturbations from trim. The aerodynamic drag term above is treated as an unmodelled disturbance, and is therefore mitigated by augmenting an integrator to the system. This integrator is essential for robustness towards uncertain steady-state drag and thrust actuator offsets [1]. A diagram of the airspeed controller structure is shown in Figure 5.3. With reference to this figure, a PI control law is defined as,

$$\Delta T_c = -K_p \dot{e}_a - K_i e_a \tag{5.4}$$

with,

$$\dot{e}_a = \bar{v} - \bar{v}_{ref} \tag{5.5}$$
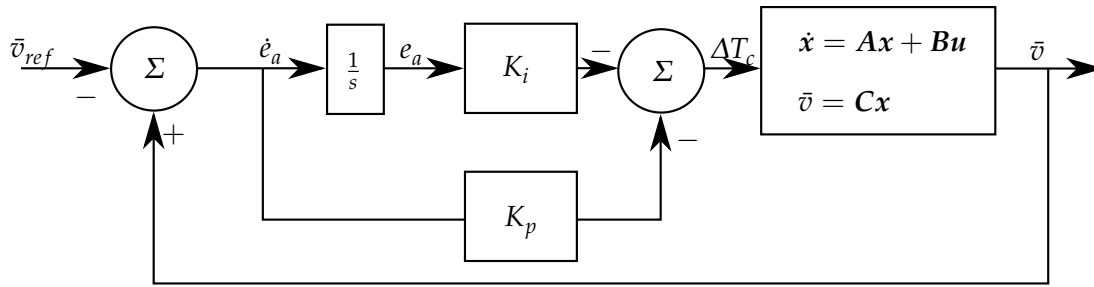
Figure 5.3: Airspeed controller block diagram

where $\bar{v}$ denotes airspeed and $\bar{v}_{ref}$ denotes the corresponding reference command. Augmenting the integrator state to the dynamics of Equation (5.3) yields,

$$
\begin{bmatrix} \Delta\dot{T} \\ \dot{\bar{v}} \\ \dot{e}_a \end{bmatrix} = \begin{bmatrix} -\frac{1}{\tau_e} & 0 & 0 \\ \frac{1}{m} & 0 & 0 \\ 0 & 1 & 0 \end{bmatrix} \begin{bmatrix} \Delta T \\ \bar{v} \\ e_a \end{bmatrix} + \begin{bmatrix} \frac{1}{\tau_e} \\ 0 \\ 0 \end{bmatrix} \Delta T_c + \begin{bmatrix} 0 \\ 0 \\ -1 \end{bmatrix} \bar{v}_{ref} \tag{5.6}
$$

Substituting the control law of Equation (5.4) yields,

$$
\begin{bmatrix} \Delta\dot{T} \\ \dot{\bar{v}} \\ \dot{e}_a \end{bmatrix} = \begin{bmatrix} -\frac{1}{\tau_e} & -\frac{K_p}{\tau_e} & -\frac{K_i}{\tau_e} \\ \frac{1}{m} & 0 & 0 \\ 0 & 1 & 0 \end{bmatrix} \begin{bmatrix} \Delta T \\ \bar{v} \\ e_a \end{bmatrix} + \begin{bmatrix} \frac{K_p}{\tau_e} \\ 0 \\ -1 \end{bmatrix} \bar{v}_{ref} \tag{5.7}
$$

Calculating the closed-loop characteristic equation gives,

$$
p(s) = s^3 + \frac{1}{\tau_e}s^2 + \frac{K_p}{m\tau_e}s + \frac{K_i}{m\tau_e} \tag{5.8}
$$

The following characteristic equation is defined to place the desired closed-loop poles:

$$
\alpha_c(s) = (s^2 + 2\zeta\omega_n s + \omega_n^2)(s + a) \tag{5.9}
$$

The closed-form solution feedback gains can then be calculated by matching the coefficients of Equations (5.8) and (5.9) to yield,

$$
K_p = m\tau_e(2\zeta\omega_n a + \omega_n^2) \tag{5.10}
$$

$$
K_i = m\tau_e\omega_n^2 a \tag{5.11}
$$

and the resulting natural frequency,

$$
\omega_n = \frac{\frac{1}{\tau_e} - a}{2\zeta} \tag{5.12}
$$

It was found that the commanded thrust is prone to integral windup especially in the event of steep climbs and descents. Active integral anti-windup was thus implemented to stop the integrator from building up whenever the controller commands a thrust that is outside the physical range of the electric motor. It should also be noted that several assumptions were made regarding motor thrust on the test vehicle. Firstly, it was assumed that the motor's thrust is commanded

directly, when in reality it is voltage from the Electronic Speed Controller (ESC) that commands motor thrust. The FCS sends a Pulse-Width-Modulated (PWM) signal to the ESC as a function of the maximum available thrust - this was measured during a static thrust test, where the motor and prop combination was mounted to a load cell. This means that there will be a discrepancy between the commanded and true thrust produced by the motor, although the integrator should be able to compensate for the error. Secondly, it was assumed that the maximum available thrust remains constant, when in reality it decreases as the Li-Po battery is depleted. Lastly, it was also assumed that the amount of thrust generated does not vary with airspeed. As airspeed increases, the angle of attack on a fixed-pitch propeller blade starts to decrease, which limits its efficiency. Again, the integrator should be able to compensate for any discrepancies.

5.2.1.2 Closed-loop System

The design conducted in the preceding section was based on simplified axial dynamics and therefore does not encapsulate the full longitudinal aircraft dynamics. To improve the design fidelity of the remaining longitudinal controllers, the dynamics of Equation (4.28) are augmented with the airspeed control law of Equation (5.4). Before augmenting the airspeed controller, it is first necessary to augment an additional state to the open-loop longitudinal aircraft model of Equation (4.28) to incorporate engine lag dynamics in the production of axial thrust. The open-loop model is augmented as follows:

$$
\begin{bmatrix} \dot{\bar{v}} \\ \dot{\alpha} \\ \dot{q} \\ \dot{\theta} \\ \Delta\dot{T} \end{bmatrix} = \begin{bmatrix} \frac{\partial \dot{U}}{\partial U} & \bar{V}_T\frac{\partial \dot{U}}{\partial W} & \frac{\partial \dot{U}}{\partial Q} & \frac{\partial \dot{U}}{\partial \Theta} & \frac{\partial \dot{U}}{\partial T} \\ \frac{1}{\bar{V}_T}\frac{\partial \dot{W}}{\partial U} & \frac{\partial \dot{W}}{\partial W} & \frac{1}{\bar{V}_T}\frac{\partial \dot{W}}{\partial Q} & \frac{1}{\bar{V}_T}\frac{\partial \dot{W}}{\partial \Theta} & \frac{1}{\bar{V}_T}\frac{\partial \dot{W}}{\partial T} \\ \frac{\partial \dot{Q}}{\partial U} & \bar{V}_T\frac{\partial \dot{Q}}{\partial W} & \frac{\partial \dot{Q}}{\partial Q} & \frac{\partial \dot{Q}}{\partial \Theta} & \frac{\partial \dot{Q}}{\partial T} \\ \frac{\partial \dot{\Theta}}{\partial U} & \bar{V}_T\frac{\partial \dot{\Theta}}{\partial W} & \frac{\partial \dot{\Theta}}{\partial Q} & \frac{\partial \dot{\Theta}}{\partial \Theta} & \frac{\partial \dot{\Theta}}{\partial T} \\ 0 & 0 & 0 & 0 & -\frac{1}{\tau_e} \end{bmatrix} \begin{bmatrix} \bar{v} \\ \alpha \\ q \\ \theta \\ \Delta T \end{bmatrix} + \begin{bmatrix} \frac{\partial \dot{U}}{\partial \delta_E} & \frac{\partial \dot{U}}{\partial \delta_F} & 0 \\ \frac{1}{\bar{V}_T}\frac{\partial \dot{W}}{\partial \delta_E} & \frac{1}{\bar{V}_T}\frac{\partial \dot{W}}{\partial \delta_F} & 0 \\ \frac{\partial \dot{Q}}{\partial \delta_E} & \frac{\partial \dot{Q}}{\partial \delta_F} & 0 \\ \frac{\partial \dot{\Theta}}{\partial \delta_E} & \frac{\partial \dot{\Theta}}{\partial \delta_F} & 0 \\ 0 & 0 & \frac{1}{\tau_e} \end{bmatrix} \begin{bmatrix} \delta_e \\ \delta_f \\ \Delta T_c \end{bmatrix} \quad (5.13)
$$

It is convenient to write Equation (5.13) in a more compact form as,

$$
\dot{x}_{long} = A_{long}x_{long} + B_{long}u_{long} \quad (5.14)
$$

where A_{long} is the longitudinal system matrix, and B_{long} is the longitudinal input matrix. Augmenting the integrator state of Equation (5.5) yields,

$$
\begin{bmatrix} \dot{x}_{long} \\ \dot{e}_a \end{bmatrix} = \begin{bmatrix} A_{long} & 0_{5\times1} \\ 1 & 0_{1\times5} \end{bmatrix} \begin{bmatrix} x_{long} \\ e_a \end{bmatrix} + \begin{bmatrix} B_{long} \\ 0_{1\times3} \end{bmatrix} u_{long} + \begin{bmatrix} 0_{5\times1} \\ -1 \end{bmatrix} \bar{v}_{ref} \quad (5.15)
$$

Writing the augmented A matrix above in a more compact form as $A_{\dot{e}_a}$ and substituting the airspeed control law of Equation (5.4) yields,

$$
\begin{bmatrix} \dot{x}_{long} \\ \dot{e}_a \end{bmatrix} = \begin{bmatrix} A_{\dot{e}_a} + \begin{bmatrix} B_{\Delta T_c} \\ 0 \end{bmatrix} \begin{bmatrix} -K_p & 0_{1\times4} & -K_i \end{bmatrix} \end{bmatrix} \begin{bmatrix} x_{long} \\ e_a \end{bmatrix} + \begin{bmatrix} B_{\delta_e} & B_{\delta_f} & K_p B_{\Delta T_c} \\ 0 & 0 & -1 \end{bmatrix} \begin{bmatrix} \delta_e \\ \delta_f \\ \bar{v}_{ref} \end{bmatrix} \quad (5.16)
$$

where,

$$
B_{\delta_e} = B_{long}\begin{bmatrix} 1 & 0 & 0 \end{bmatrix}^T ; \ B_{\delta_f} = B_{long}\begin{bmatrix} 0 & 1 & 0 \end{bmatrix}^T ; \ B_{\Delta T_c} = B_{long}\begin{bmatrix} 0 & 0 & 1 \end{bmatrix}^T \quad (5.17)
$$

The closed-loop model of Equation (5.16) will be augmented further as more control laws are added to the system. It is therefore convenient to write it in a more compact form as,

$$\dot{x}_{as} = A_{as}x_{as} + B_{as}u_{as} \tag{5.18}$$

with,

$$\bar{v} = C_{as}x_{as} \tag{5.19}$$

so that the closed-loop transfer function from airspeed reference to true airspeed is given by,

$$G_{\bar{v}_{cl}}(s) = \frac{\bar{v}(s)}{\bar{v}_{ref}(s)} \tag{5.20}$$

$$= C_{as}(sI - A_{as})^{-1}B_{\bar{v}_{ref}}$$

where,

$$C_{as} = \begin{bmatrix} 1 & 0 & 0 & 0 & 0 & 0 \end{bmatrix}; \quad B_{\bar{v}_{ref}} = B_{as}\begin{bmatrix} 0 & 0 & 1 \end{bmatrix}^T \tag{5.21}$$

5.2.1.3 Placing the Closed-loop Poles

Placement of the closed-loop poles involves selecting the damping ratio (ζ) and the location of the closed-loop integrator pole (a). The proportional and integral feedback gains (K_p and K_i) can then be calculated from Equations (5.10) and (5.11) respectively. The specific pole locations shown below are for the aircraft parameters and standard flight conditions outlined in Appendix B. It is apparent from Figure 5.4a that the PI control law introduces a zero near the dominant closed-loop pole. This results in unexpected overshoot from a design perspective, and it was thus necessary to vary the damping ratio and closed-loop integrator pole location until an adequate response was observed. Figures 5.4a and 5.4b depict the pole-zero map and step response of the airspeed controller when,

$$\zeta_{cl} = 0.9 \tag{5.22}$$

$$a = 0.5 \text{ rad/}s \tag{5.23}$$

which yields the following closed-form solution feedback gains:

$$K_p = 8.7803 \tag{5.24}$$

$$K_i = 3.0011 \tag{5.25}$$

It is apparent that the closed-loop pole locations agree with the design specifications and that the airspeed step exhibits more overshoot than expected. The step response is seen to have approximately 20% overshoot and a 2% settling time of 7 s, which is considered acceptable for this application.

(a) Pole-zero map
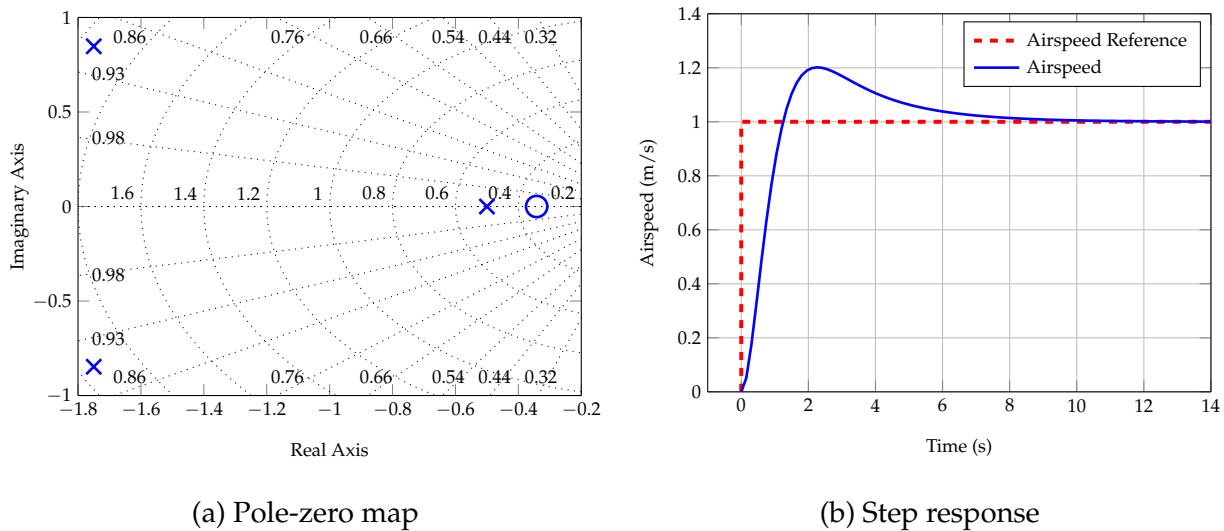
(b) Step response

Figure 5.4: Pole-zero map and step response of the airspeed controller on simplified velocity dynamics

5.2.2   Normal Specific Acceleration Direct Lift Controller

This section presents the design and verification of an augmented normal specific acceleration controller that exploits the high-bandwidth characteristics of Direct Lift Control (DLC). A three-axis accelerometer included in the avionics stack on board the practical test vehicle provided acceleration measurements for the purpose of feedback control. Conventional aircraft control systems that use the elevator to generate a pitching moment, the ailerons to generate a rolling moment, and the rudder to generate a yawing moment, are considered *Moment Control Techniques* (MCT) [10]. These techniques indirectly produce forces for controlling the motion of the aircraft via a change in the moment equilibrium. The pitching moment produced by an elevator deflection changes the angle of attack on the main lifting surface, and consequently results in a variation of the lift force experienced by the aircraft. It can therefore be said that conventional elevator-based longitudinal control is accomplished by α-generated lift produced by the wing of the aircraft. This type of lift generation will be referred to as *pitch-moment-based* longitudinal control throughout the remainder of this thesis. The DLC technique provides a direct means of producing forces with little influence on the moment equilibrium. According to Gerrits [10], such a capability removes the limitations caused by the coupling of attitude and flight path control, and offers novel and unique modes of aircraft motion. Conventional flight path control with the elevator results in two potentially adverse effects. Firstly, an elevator deflection produces some change in lift from the tailplane, quantified by $C_{L_{\delta_E}}$. While this lift force is relatively small, it is in the opposite direction to what is ultimately intended. Consequently, the aircraft initially moves in the wrong direction. Secondly, there is a delay between the initiation of the control action and the flight path response. As mentioned above, this is because a change in moment equilibrium is necessary for producing a force when using MCT to control aircraft motion. Furthermore, rotational pitch dynamics cause a delay in the change of lift, which in turn results in a delay in altitude change [10].

DLC provides the capability of producing lift instantaneously for vertical flight path control. This cannot be achieved by conventional elevator control, due to the NMP nature of the associ-

ated dynamics and the inherent delay between control action and flight path response. A previous investigation by Gerrits [10] concluded that the NMP response of the elevator is less appropriate for gust alleviation, and that a solution would be to use the principles of DLC to directly control normal acceleration. Gerrits showed that using DLC surfaces on a Cessna Citation (II) aircraft separated pitch/altitude control, which led to further improvements in gust alleviation characteristics in the aircraft's longitudinal axis.

Atmospheric gusts are inherently unpredictable and can therefore only be rejected by the FCS after their effects have been sensed. It is therefore imperative that the controllers be able to reject disturbances fast enough to ensure that the landing accuracy requirements stated in Section 1.4 are met. Pinsker [41] describes a tailgust as the most damaging gust disturbance for an aircraft in final flare before touchdown. Consider an aircraft trimmed for straight and level flight at an airspeed $\bar{V}_T$. A tailgust with velocity u_{gust} results in a simultaneous reduction in lift or an equivalent reduction in normal acceleration Δn according to [41],

$$\Delta n = 2 \left(\frac{u_{gust}}{\bar{V}_T} \right) \tag{5.26}$$

A vertical wind gust will change the direction of incident flow, and its effects are soon removed by the aircraft weathercocking into the new flow direction in accordance with the short period mode of motion. A tailgust, however, does not change the incidence angle and its effect can only be equalised after it has increased airspeed to compensate for the deficiency. This process is governed by the phugoid mode and is often too slow to restore the deficiency and minimise the resulting altitude deviations before touchdown. Pinsker [41] describes the possibility of obtaining an adequate representation of the initial response to a fore and aft gust by integrating Equation (5.26),

$$\Delta \dot{H} = \int ng \ dt \tag{5.27}$$

$$= 2gt \left(\frac{u_{gust}}{\bar{V}_T} \right)$$

and integrating Equation (5.27) to yield,

$$\Delta H = \int \dot{H} \ dt \tag{5.28}$$

$$= gt^2 \left(\frac{u_{gust}}{\bar{V}_T} \right)$$

where these increments represent deviations from the glideslope trajectory the aircraft would have followed in the absence of a gust disturbance. A tailgust equivalent of 5% of the aircraft's approach speed generates 0.1 g downwards acceleration and will therefore increase vertical velocity by 0.981 m every second. With reference to Equation (5.28), it is apparent that a delay of just 2 s would result in an altitude deviation of almost 2 m, which could be catastrophic if the incident occurred in the final flare phase. In light of this, it can be concluded that an FCS equipped with high-bandwidth DLC would be able to instantaneously compensate for the sudden lift deficiency and regulate altitude more precisely during final approach. The following properties are recommended by Gerrits [10] for DLC control surfaces:

1. Changes in lift (and drag) in positive and negative direction

2. Quick operation for high-frequency control

3. Only small adverse pitching moments

The flaps are an example of an actuator with inherent direct-lift generation properties. Deploying the flaps causes an increase in wing camber, which increases the maximum lift coefficient and results in an instantaneous change in lift produced by the wing. Since the flaps are located on the trailing edge of the main wing, the moment arm to the CG location is relatively short and results in small pitching moments due to flap perturbations, quantified by $C_{m_{\delta_F}}$. Although small, these adverse pitching moments can be mitigated through effective elevator mixing for an optimal response. The prospect of controlling the aircraft's altitude independent of its pitch attitude holds great promise for improvements in landing accuracy under adverse weather conditions. It should be noted that the DLC technique is not specific to the use of flaps as the direct-lift actuator. In general, any actuator or combination of actuators that satisfies the aforementioned requirements can be used. Flaperons are a type of hybrid actuator that combines aspects of both flaps and ailerons. In addition to generating a rolling moment when deployed differentially, flaperons can be deployed in tandem to function as a dedicated set of flaps.

In light of the preceding discussion, the focus now shifts towards implementing the proposed hybrid NSADLC controller. Several approaches to direct lift control implementation are discussed by Pinsker [41], the most promising of which involves a DLC system with relatively restricted authority. This method involves combining the pitch-moment-based control method with the direct-lift-based method to form a hybrid system that makes use of both the elevator and flaps for longitudinal aircraft control. In this hybrid configuration, the direct-lift portion is limited in controller authority whilst the pitch-moment portion can respond to commands beyond the point where the direct lift control authority is exhausted [5]. Pinsker suggests that the most efficient use of the limited direct-lift authority would be to superimpose it in transientised form upon conventional pitch-moment-based control. This essentially involves filtering the normal specific acceleration error signal so that the direct-lift portion only responds to higher-frequency disturbances, whilst the pitch-moment-based portion responds to lower-frequency signals simultaneously. This approach ensures that the long-term response characteristics of the aircraft remain entirely conventional, and the addition of DLC does not materially interfere with the usable C_L regime [41]. The DLC component should only affect the initial transient response, which allows it to be optimised solely for bandwidth improvement. A diagram of the filter structure implemented in the NSADLC controller architecture is illustrated in Figure 5.5.

An additional strategy proposed by Pinsker [41] for a DLC system with relatively restricted authority is to make use of the pitch-moment-based control actuator (elevator) to mitigate any adverse pitching moments produced by the DLC actuator (flaps) - this allows the flaps to be approximated as a pure direct-lift actuator [5]. The gain K_m in Figure 5.5 represents the *mixing* required for the elevator to cancel adverse pitching moments produced by flap perturbations. It should be noted that making use of two different control actuators to regulate the same state variable often leads to issues regarding proper control allocation. This is overcome through successful frequency separation of the two control strategies by means of the complementary filter depicted in Figure 5.5. The filter centre frequency ω_c can be thought of as being constrained to an upper and lower bound. The lower bound is the point at which the DLC controller starts to saturate
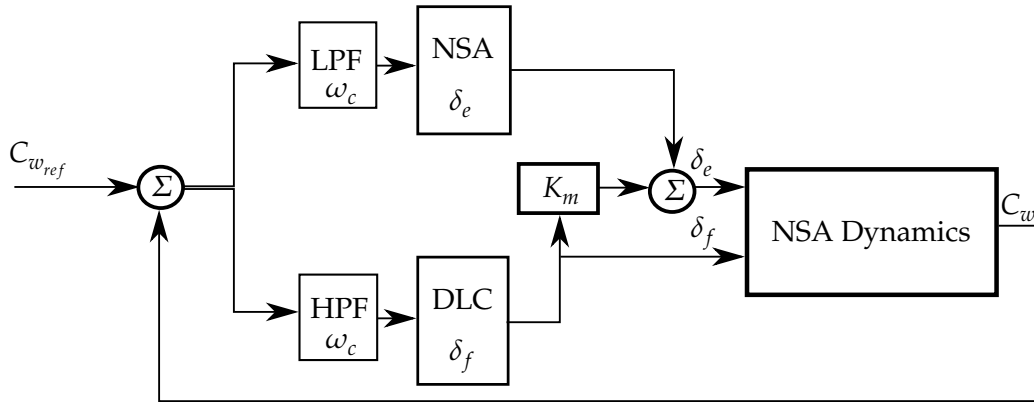
Figure 5.5: Hybrid NSADLC architecture

prematurely (due to its relatively restricted authority), whilst the upper bound is governed by the closed-loop bandwidth of the NSA controller. Since the primary objective of the DLC augmentation is to improve controller bandwidth, choosing ω_c at the upper bound yields the following:

1. maximum bandwidth improvement

2. invalidates the LPF portion of the complementary filter, which dramatically simplifies controller design

3. effectively separates the controllers in frequency, which allows for independent design and better control allocation

The focus now shifts towards the independent design of a direct lift controller, followed by the design of a pitch-moment-based NSA controller, and concluding with the augmentation of a high-performance hybrid controller.

5.2.2.1 Designing the direct-lift portion

This section presents the design of a direct-lift-based controller which makes use of the flaps as a DLC surface. Based on the work of Peddle [1], Alberts [5] describes the following unsimplified normal dynamics for a flaps input:

$$\begin{bmatrix} \dot{\alpha} \\ \dot{q} \end{bmatrix} = \begin{bmatrix} -\frac{L_\alpha}{mV_T} & 1 - \frac{L_Q}{mV_T} \\ \frac{M_\alpha}{I_{yy}} & \frac{M_Q}{I_{yy}} \end{bmatrix} \begin{bmatrix} \alpha \\ q \end{bmatrix} + \begin{bmatrix} -\frac{L_{\delta_F}}{mV_T} \\ \frac{M_{\delta_F}}{I_{yy}} \end{bmatrix} \delta_f \tag{5.29}$$

$$C_w^{df} = \begin{bmatrix} -\frac{L_\alpha}{m} & -\frac{L_Q}{m} \end{bmatrix} \begin{bmatrix} \alpha \\ q \end{bmatrix} + \begin{bmatrix} -\frac{L_{\delta_F}}{m} \end{bmatrix} \delta_f \tag{5.30}$$

where C_w^{df} represents the resultant normal specific acceleration generated by the direct-lift portion coordinated in the wind axis. Assuming that the moment produced by a flap deflection is

cancelled out perfectly by the elevator, the design of a practically feasible direct lift controller can proceed based on the following reduced normal dynamics:

$$
\begin{bmatrix} \dot{\alpha} \\ \dot{q} \end{bmatrix} = \begin{bmatrix} -\frac{L_\alpha}{m\bar{V}_T} & 1 \\ \frac{M_\alpha}{I_{yy}} & \frac{M_Q}{I_{yy}} \end{bmatrix} \begin{bmatrix} \alpha \\ q \end{bmatrix} + \begin{bmatrix} -\frac{L_{\delta_F}}{m\bar{V}_T} \\ 0 \end{bmatrix} \delta_f
\tag{5.31}
$$

$$
C_w^{df} = \begin{bmatrix} -\frac{L_\alpha}{m} & 0 \end{bmatrix} \begin{bmatrix} \alpha \\ q \end{bmatrix} + \begin{bmatrix} -\frac{L_{\delta_F}}{m} \end{bmatrix} \delta_f
\tag{5.32}
$$

where it has also been assumed that,

$$
\frac{L_Q}{m\bar{V}_T} \ll 1
\tag{5.33}
$$

which is valid for almost all aircraft and is an assumption that is commonly made in analysing aircraft dynamics [21]. The dimensional stability and control derivative notion is standard, as defined below,

$$
A_B = \bar{q}Sl \left(\frac{\partial C_A}{\partial B'} \right) n
\tag{5.34}
$$

where the length term l is unity for the force derivatives, $\bar{c}$ for the pitch moment derivatives and b for the roll and yaw derivatives. The non-dimensionalising coefficient n is taken from Equation (3.78). A proportional control law defined by Alberts [5] was found to perform quite poorly when exposed to high-frequency turbulence and accelerometer noise. The proportional controller simply passed high-frequency error signals directly to the flaps, which caused them to flutter and exacerbate the very disturbances the controller was designed to reject. Following an investigation into the matter, it was observed that an integral control law significantly improved the transient response characteristics and disturbance rejection capabilities of the hybrid controller without excessive actuator flutter. A diagram of the DLC controller structure is shown in Figure 5.6. With reference to this figure, an integral control law is defined as,

$$
\delta_f = -K_{i_f} e_f
\tag{5.35}
$$

with,

$$
\dot{e}_f = \frac{\tau_c s}{\tau_c s + 1} e_w
\tag{5.36}
$$

and,

$$
e_w = C_w^{df} - C_{w_{ref}}^{df}
\tag{5.37}
$$

where τ_c is the complementary filter time constant and $C_{w_{ref}}^{df}$ is the normal specific acceleration reference to the direct-lift portion of the hybrid controller. With reference to Figure 5.6, it is apparent that the high-pass filter and integrator dynamics can be combined as follows:

$$
\frac{e_f(s)}{e_w(s)} = \frac{\tau_c s}{\tau_c s + 1} \times \frac{1}{s}
\tag{5.38}
$$
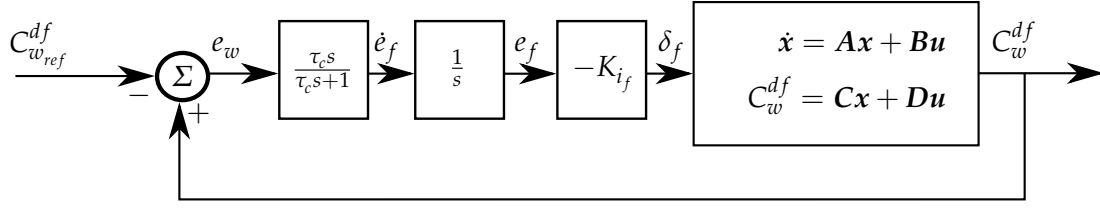
Figure 5.6: Direct lift controller block diagram

Taking the inverse Laplace transform yields the following differential equation that encapsulates both the filter and integrator dynamics associated with the DLC feedback loop:

$$\dot{e}_f = e_w - \frac{1}{\tau_c}e_f \tag{5.39}$$

Augmenting the NSA dynamics of Equation (5.31) with the control law and e_f state allows for the calculation of the closed-loop feedback gain K_i. Given the desired closed-loop characteristic equation for the normal dynamics,

$$\alpha_c(s) = (s^2 + 2\zeta\omega_n s + \omega_n^2)(s+a) \tag{5.40}$$

the closed-form solution feedback gain can be calculated by matching the characteristic equation coefficients to yield,

$$K_{i_f} = -\frac{m}{L_{\delta_F}}\left(2\zeta\omega_n + a - \frac{L_\alpha}{\bar{V}_T m} + \frac{M_Q}{I_{yy}} - \frac{1}{\tau_c}\right) \tag{5.41}$$

As mentioned in the preceding section, the mixing gain K_m depicted in Figure 5.5 is introduced to effectively minimise potentially adverse pitching moments caused by flap perturbations using the elevator. The ratio between the pitching moment produced by flap perturbations and that produced by elevator perturbations can be used to determine the mixing gain required for total pitch moment cancellation as follows:

$$K_m = -\frac{C_{m_{\delta_F}}}{C_{m_{\delta_E}}} \tag{5.42}$$

5.2.2.2 Designing the pitch-moment-based portion

This section presents the design of the pitch-moment-based portion of the hybrid NSADLC controller. This controller makes use of the elevator to generate a normal specific acceleration through the principles of MCT, as outlined in the opening discussion. The unsimplified normal dynamics for an elevator input is given by Peddle [1] as,

$$\begin{bmatrix} \dot{\alpha} \\ \dot{q} \end{bmatrix} = \begin{bmatrix} -\frac{L_\alpha}{m\bar{V}_T} & 1 - \frac{L_Q}{m\bar{V}_T} \\ \frac{M_\alpha}{I_{yy}} & \frac{M_Q}{I_{yy}} \end{bmatrix} \begin{bmatrix} \alpha \\ q \end{bmatrix} + \begin{bmatrix} -\frac{L_{\delta_E}}{m\bar{V}_T} \\ \frac{M_{\delta_E}}{I_{yy}} \end{bmatrix} \delta_e \tag{5.43}$$

$$C_w^{de} = \begin{bmatrix} -\frac{L_\alpha}{m} & -\frac{L_Q}{m} \end{bmatrix} \begin{bmatrix} \alpha \\ q \end{bmatrix} + \begin{bmatrix} -\frac{L_{\delta_E}}{m} \end{bmatrix} \delta_e \tag{5.44}$$

Peddle shows that the NMP zero associated with the pitch-moment-based controller places severe restrictions on the practically attainable upper bandwidth of the closed-loop normal specific acceleration dynamics. Following a detailed investigation into the matter, a simple frequency bound is defined that allows the NMP nature of the system to be ignored and ensures a practically feasible dynamic inversion of the flight path angle coupling. The upper frequency bound is calculated as,

$$\omega_n < \frac{1}{3} \left| \sqrt{\frac{L_\alpha}{I_{yy}} (l_T - l_N)} \right| \tag{5.45}$$

where l_T and l_N represent the effective lengths from the CG location to the tailplane and neutral point respectively. These lengths are defined as,

$$l_T \equiv -\frac{M_{\delta_E}}{L_{\delta_E}} \tag{5.46}$$

$$l_N \equiv -\frac{M_\alpha}{L_\alpha} \tag{5.47}$$

The lower-frequency bound is governed by a requirement for the normal dynamics to be time scale separated from the velocity magnitude and air density dynamics. The former typically has the higher bandwidth and is thus considered to be the limiting factor. Following a commonly used design rule for Time Scale Separation (TSS), the normal dynamics should be at least five times faster than the desired velocity magnitude bandwidth. With the TSS lower bound and the NMP upper bound as described above, Peddle concludes that the natural frequency of the normal specific acceleration controller is constrained to lying within a circular band in the s-plane, as shown in Figure 5.7.
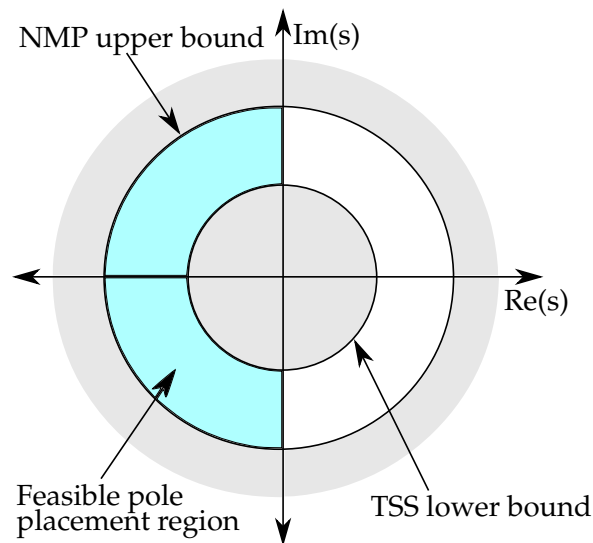
Figure 5.7: Feasible pole placement region constrained by NMP upper bound and TSS lower bound

Assuming that the aforementioned frequency bounds are met and that Equation (5.33) is satisfied, the design of a practically feasible NSA controller can proceed based on the following re-

duced normal dynamics:

$$
\begin{bmatrix} \dot{\alpha} \\ \dot{q} \end{bmatrix} = \begin{bmatrix} -\frac{L_\alpha}{mV_T} & 1 \\ \frac{M_\alpha}{I_{yy}} & \frac{M_Q}{I_{yy}} \end{bmatrix} \begin{bmatrix} \alpha \\ q \end{bmatrix} + \begin{bmatrix} 0 \\ \frac{M_{\delta_E}}{I_{yy}} \end{bmatrix} \delta_e \tag{5.48}
$$

$$
C_w^{de} = \begin{bmatrix} -\frac{L_\alpha}{m} & 0 \end{bmatrix} \begin{bmatrix} \alpha \\ q \end{bmatrix} + \begin{bmatrix} 0 \end{bmatrix} \delta_e \tag{5.49}
$$

where C_w^{de} represents the resultant normal specific acceleration generated by the pitch-moment-based portion coordinated in the wind axis. With reference to Figure 5.8, Peddle defines the following PI control law with enough degrees of freedom to place the closed-loop poles arbitrarily:

$$
\delta_e = -K_q q - K_c C_w^{de} - K_{i_e} e_c + N_c C_{w_{ref}}^{de} \tag{5.50}
$$

with,

$$
\dot{e}_c = C_w^{de} - C_{w_{ref}}^{de} \tag{5.51}
$$

where $C_{w_{ref}}^{de}$ is the normal specific acceleration reference to the pitch-moment-based portion of the hybrid controller. In order to maintain design independence, the aforementioned flap-to-elevator mixing is treated as a disturbance to the pitch-moment-based system and therefore does not appear in the control law of Equation 5.50.
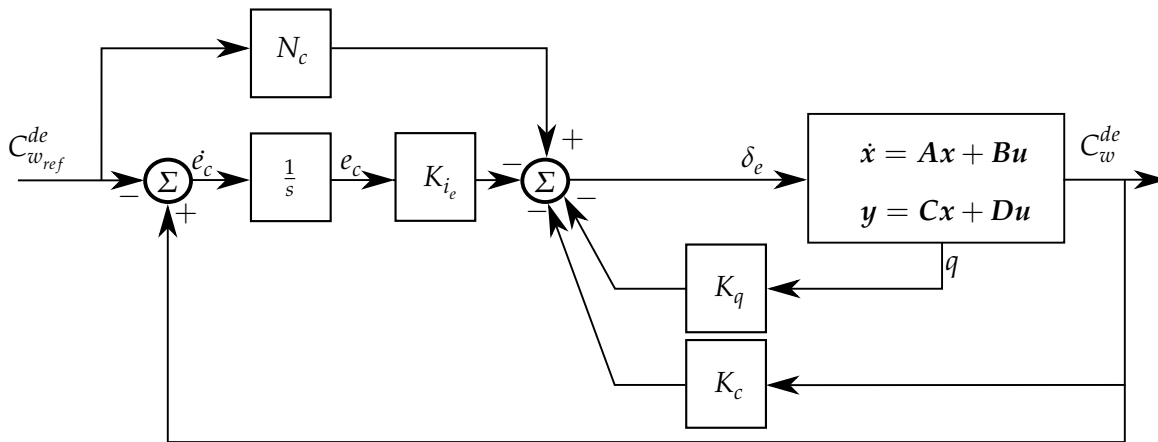
Figure 5.8: Pitch-moment-based NSA controller block diagram

A feed-forward term N_c has been incorporated into the control law to allow for slower integrator dynamics by introducing a zero at,

$$
s = -\frac{K_{i_e}}{N_c} \tag{5.52}
$$

which can be placed near the closed-loop integrator pole to minimise its transient effects. Augmenting the NSA dynamics of Equation (5.48) with the control law and integrator state allows for the calculation of the closed-loop feedback gains. Given the desired closed-loop characteristic equation for the normal dynamics,

$$
\alpha_c(s) = (s^2 + 2\zeta\omega_n s + \omega_n^2)(s + a) \tag{5.53}
$$

the closed-form solution feedback gains can be calculated by matching the characteristic equation coefficients to yield,

$$K_q = \frac{I_{yy}}{M_{\delta_E}} \left(2\zeta\omega_n + a + \frac{M_Q}{I_{yy}} - \frac{L_\alpha}{m\bar{V}_T} \right) \tag{5.54}$$

$$K_c = -\frac{mI_{yy}}{L_\alpha M_{\delta_E}} \left(2\zeta\omega_n a + \omega_n^2 + \frac{M_\alpha}{I_{yy}} - \frac{L_\alpha}{m\bar{V}_T} \left(2\zeta\omega_n + a - \frac{L_\alpha}{m\bar{V}_T} \right) \right) \tag{5.55}$$

$$K_{i_e} = -\frac{mI_{yy}}{L_\alpha M_{\delta_E}} \left(\omega_n^2 a \right) \tag{5.56}$$

where the design freedom is left to selecting the closed-loop integrator pole location (a), as well as the damping ratio (ζ) and natural frequency (ω_n) of the short period mode poles.

5.2.2.3   Closed-loop System

Up until this point, the direct-lift- and pitch-moment-based portions of the hybrid controller have been designed independently of one another. This assumption is valid, given that the complementary filter centre frequency is chosen near the upper bound so that the controllers are sufficiently separated in time scale. Following a similar approach to the airspeed controller augmentation, the hybrid controller is now augmented to the full longitudinal aircraft model of Equation (5.18) so as to maintain a high-fidelity model for a successive loop closure approach. The dynamics of Equation (5.18) are restated below for convenience.

$$\dot{x}_{as} = A_{as}x_{as} + B_{as}u_{as} \tag{5.57}$$

Using the unsimplified output C_w^{df} of Equation (5.30) and augmenting the integrator state of Equation (5.39) yields,

$$\begin{bmatrix} \dot{x}_{as} \\ \dot{e}_f \end{bmatrix} = \begin{bmatrix} A_{as} & \mathbf{0}_{6\times 1} \\ 0 \quad -\frac{L_\alpha}{m} \quad -\frac{L_Q}{m} \quad \mathbf{0}_{1\times 3} \quad -\frac{1}{\tau_c} \end{bmatrix} \begin{bmatrix} x_{as} \\ e_f \end{bmatrix} + \begin{bmatrix} B_{as} \\ 0 \quad -\frac{L_{\delta_F}}{m} \quad 0 \end{bmatrix} u_{as} + \begin{bmatrix} \mathbf{0}_{6\times 1} \\ -1 \end{bmatrix} C_{w_{ref}}^{df} \tag{5.58}$$

Writing the augmented A matrix above in a more compact form as $A_{\dot{e}_f}$ and substituting the control law of Equation (5.35) yields,

$$\begin{bmatrix} \dot{x}_{as} \\ \dot{e}_f \end{bmatrix} = \begin{bmatrix} A_{\dot{e}_f} + \begin{bmatrix} B_{\delta_f} \\ -\frac{L_{\delta_F}}{m} \end{bmatrix} \begin{bmatrix} \mathbf{0}_{1\times 6} & -K_{i_f} \end{bmatrix} \end{bmatrix} \begin{bmatrix} x_{as} \\ e_f \end{bmatrix} + \begin{bmatrix} B_{\delta_e} & \mathbf{0}_{6\times 1} & B_{\bar{v}_{ref}} \\ 0 & -1 & 0 \end{bmatrix} \begin{bmatrix} \delta_e \\ C_{w_{ref}}^{df} \\ \bar{v}_{ref} \end{bmatrix} \tag{5.59}$$

where,

$$B_{\delta_e} = B_{as} \begin{bmatrix} 1 & 0 & 0 \end{bmatrix}^T ; \quad B_{\delta_f} = B_{as} \begin{bmatrix} 0 & 1 & 0 \end{bmatrix}^T ; \quad B_{\bar{v}_{ref}} = B_{as} \begin{bmatrix} 0 & 0 & 1 \end{bmatrix}^T \tag{5.60}$$

The closed-loop model of Equation (5.59) will be augmented further as additional controllers are added to the system. It is therefore convenient to write it in a more compact form as,

$$\dot{x}_{dlc} = A_{dlc}x_{dlc} + B_{dlc}u_{dlc} \tag{5.61}$$

with,

$$C_w^{df} = C_{dlc} x_{dlc} \tag{5.62}$$

so that the closed-loop transfer function for the direct-lift portion from NSA reference to measured NSA is given by,

$$G_{C_w}^{df}(s) = \frac{C_w^{df}(s)}{C_{w_{ref}}^{df}(s)} \tag{5.63}$$

$$= C_{dlc}(sI - A_{dlc})^{-1} B_{C_{w_{ref}}}^{df}$$

where,

$$C_{dlc} = \begin{bmatrix} 0 & -\frac{L_\alpha}{m} & -\frac{L_Q}{m} & 0 & 0 & 0 & \frac{K_{i_f} L_{\delta_F}}{m} \end{bmatrix}; \quad B_{C_{w_{ref}}}^{df} = B_{dlc} \begin{bmatrix} 0 & 1 & 0 \end{bmatrix}^T \tag{5.64}$$

Now that the direct-lift portion has been augmented to the full longitudinal aircraft dynamics, it is necessary to augment the pitch-moment-based portion so that their individual contributions to lift generation can be combined to form the hybrid model. The unsimplified output C_w^{de} of Equation (5.44) with the augmented C_{dlc} matrix, which includes the NSA generated by the direct-lift portion, is given as,

$$C_w^{de} = C_{dlc} x_{dlc} - \left(\frac{L_{\delta_E}}{m} \right) \delta_e \tag{5.65}$$

With C_w^{de} as above, augmenting the integrator state of Equation (5.51) to the dynamics of Equation (5.61) yields,

$$\begin{bmatrix} \dot{x}_{dlc} \\ \dot{e}_c \end{bmatrix} = \begin{bmatrix} A_{dlc} & & & & & 0_{7\times1} \\ 0 & -\frac{L_\alpha}{m} & -\frac{L_Q}{m} & 0_{1\times3} & \frac{K_{i_f} L_{\delta_F}}{m} & 0 \end{bmatrix} \begin{bmatrix} x_{dlc} \\ e_c \end{bmatrix} \tag{5.66}$$

$$+ \begin{bmatrix} & B_{dlc} & \\ -\frac{L_{\delta_E}}{m} & 0 & 0 \end{bmatrix} u_{dlc} + \begin{bmatrix} 0_{7\times1} \\ -1 \end{bmatrix} C_{w_{ref}}^{de}$$

Writing the augmented A matrix above in a more compact form as $A_{\dot{e}_c}$ and substituting the control law of Equation (5.50) yields,

$$\begin{bmatrix} \dot{x}_{dlc} \\ \dot{e}_c \end{bmatrix} = \begin{bmatrix} A_{\dot{e}_c} + \begin{bmatrix} B_{\delta_e} \\ -\frac{L_{\delta_E}}{m} \end{bmatrix} \begin{bmatrix} 0 & \frac{K_c L_\alpha}{m - K_c L_{\delta_E}} & \frac{K_c L_Q - m K_q}{m - K_c L_{\delta_E}} & 0_{1\times3} & -\frac{K_c K_{i_f} L_{\delta_F}}{m - K_c L_{\delta_E}} & -\frac{m K_{i_e}}{m - K_c L_{\delta_E}} \end{bmatrix} \end{bmatrix} \begin{bmatrix} x_{dlc} \\ e_c \end{bmatrix} \tag{5.67}$$

$$+ \begin{bmatrix} \frac{m N_c}{m - K_c L_{\delta_E}} B_{\delta_e} & B_{C_{w_{ref}}}^{df} & B_{\bar{v}_{ref}} \\ -\left(1 + \frac{N_c L_{\delta_E}}{m - K_c L_{\delta_E}} \right) & 0 & 0 \end{bmatrix} \begin{bmatrix} C_{w_{ref}}^{de} \\ C_{w_{ref}}^{df} \\ \bar{v}_{ref} \end{bmatrix}$$

where,

$$B_{\delta_e} = B_{dlc} \begin{bmatrix} 1 & 0 & 0 \end{bmatrix}^T; \quad B_{C_{w_{ref}}}^{df} = B_{dlc} \begin{bmatrix} 0 & 1 & 0 \end{bmatrix}^T; \quad B_{\bar{v}_{ref}} = B_{dlc} \begin{bmatrix} 0 & 0 & 1 \end{bmatrix}^T \tag{5.68}$$

It is clear from Figure 5.5 that the NSA references to both the direct-lift portion and the pitch-moment-based portion of the hybrid controller are identical,

$$C_{w_{ref}} = C_{w_{ref}}^{de} = C_{wref}^{df} \tag{5.69}$$

which allows the input vectors of the individual contributions to be combined as follows,

$$
\begin{bmatrix} \dot{x}_{dlc} \\ \dot{e}_c \end{bmatrix} = \left[A_{\dot{e}_c} + \begin{bmatrix} B_{\delta_e} \\ \frac{L_{\delta_E}}{m} \end{bmatrix} \begin{bmatrix} 0 & \frac{K_c L_\alpha}{m - K_c L_{\delta_E}} & \frac{K_c L_Q - m K_q}{m - K_c L_{\delta_E}} & 0_{1 \times 3} & -\frac{K_c K_{i_f} L_{\delta_F}}{m - K_c L_{\delta_E}} & -\frac{m K_{i_e}}{m - K_c L_{\delta_E}} \end{bmatrix} \right] \begin{bmatrix} x_{dlc} \\ e_c \end{bmatrix} \tag{5.70}
$$

$$
+ \begin{bmatrix} \left(\frac{m N_c}{m - K_c L_{\delta_E}} B_{\delta_e} + B_{C_{w_{ref}}}^{df} \right) & B_{\bar{v}_{ref}} \\ - \left(1 + \frac{N_c L_{\delta_E}}{m - K_c L_{\delta_E}} \right) & 0 \end{bmatrix} \begin{bmatrix} C_{w_{ref}} \\ \bar{v}_{ref} \end{bmatrix}
$$

The closed-loop model of Equation (5.70) will be augmented further as additional controllers are added to the system. It is therefore convenient to write it in a more compact form as,

$$\dot{x}_{hyb} = A_{hyb} x_{hyb} + B_{hyb} u_{hyb} \tag{5.71}$$

with,

$$C_w = C_{hyb} x_{hyb} + D_{hyb} u_{hyb} \tag{5.72}$$

so that the closed-loop transfer function for the hybrid controller from NSA reference to measured NSA is given by,

$$G_{cw_{cl}}(s) = \frac{C_w(s)}{C_{w_{ref}}(s)} \tag{5.73}$$

$$= C_{hyb}(sI - A_{hyb})^{-1} B_{C_{w_{ref}}} + D_{hyb}$$

where,

$$C_{hyb} = \begin{bmatrix} C_{dlc} & 0 \end{bmatrix} - \frac{L_{\delta_E}}{m} \begin{bmatrix} 0 & \frac{K_c L_\alpha}{m - K_c L_{\delta_E}} & \frac{K_c L_Q - m K_q}{m - K_c L_{\delta_E}} & 0_{1 \times 3} & -\frac{K_c K_{i_f} L_{\delta_F}}{m - K_c L_{\delta_E}} & -\frac{m K_{i_e}}{m - K_c L_{\delta_E}} \end{bmatrix} \tag{5.74}$$

$$B_{C_{w_{ref}}} = B_{hyb} \begin{bmatrix} 1 & 0 \end{bmatrix}^T; \quad D_{hyb} = \begin{bmatrix} -\frac{N_c L_{\delta_E}}{m - K_c L_{\delta_E}} & 0 \end{bmatrix} \tag{5.75}$$

5.2.2.4 Placing the Closed-loop Poles

This section will discuss the selection of the closed-loop pole locations for both the direct-lift portion and the pitch-moment-based portion. Thereafter the pole locations and associated step response of the combined hybrid controller on the full longitudinal aircraft model will be analysed and compared with a pure pitch-moment-based NSA controller to verify the expected performance increase. The practical test vehicle easily satisfies the standard aerodynamic assumption of Equation (5.33) with,

$$\left| \frac{L_Q}{m \bar{V}_T} \right| = 0.0862 \ll 1 \tag{5.76}$$

which means that the simplifications made in the preceding sections are expected to yield good results. Equation (5.45) is then used to determine the NMP upper frequency bound constrained to,

$$\omega_{n_{max}} < 9.6451 \text{ rad/s} \tag{5.77}$$

which will allow the NMP nature of the plant to be ignored and ensure a practically feasible dynamic inversion of the flight path angle coupling. In light of this, the closed-loop natural frequency of the pitch-moment-based controller is chosen as,

$$\omega_{n_{pmb}} = 9.5 \text{ rad/s} \tag{5.78}$$

to obtain maximum performance in terms of bandwidth.

Direct lift controller pole placement: Placement of the closed-loop poles involves selecting the damping ratio (ζ), the natural frequency (ω_n), the complementary filter time constant (τ_c), and the location of the closed-loop integrator pole (a) so that the integral feedback gain K_{i_f} can be calculated from Equation (5.41). The design approach was to choose a fast integrator pole for maximum bandwidth improvement, and to leave the short period mode poles near their open-loop locations to be placed appropriately by the pitch-moment-based controller during the hybrid augmentation. The complementary filter centre frequency was chosen as the closed-loop bandwidth of the pitch-moment-based controller (as per the opening discussion) and calculated as,

$$\omega_c = \omega_{n_{pmb}} \tag{5.79}$$

$$= 9.5 \text{ rad/s}$$

so that the filter time constant is given by,

$$\tau_c = \frac{1}{\omega_c} \tag{5.80}$$

Figures 5.9a and 5.9b illustrate the pole-zero map and step response of the direct lift controller when,

$$\zeta_{cl} = \zeta_{sp} \tag{5.81}$$

$$= 0.59$$

$$\omega_{n_{cl}} = \omega_{n_{sp}} \tag{5.82}$$

$$= 10.30 \text{ rad/s}$$

$$a = 2\zeta_{cl}\omega_{n_{cl}} \tag{5.83}$$

$$= 12.15 \text{ rad/s}$$

which yields the following closed-form solution feedback gain:

$$K_{i_f} = -0.1238 \tag{5.84}$$

The location of the closed-loop integrator pole was chosen to be double the real component of the short period mode poles ($2\sigma_{sp}$) to maximise performance whilst avoiding excessive flap deflections. It is apparent from Figure 5.9 that the short period mode poles remain near their open-loop locations and that a fast integrator pole has been placed around 12 rad/s. It is also apparent that the step response has a large steady-state offset which can be attributed to the fact that there is no free integrator in the system after being cancelled by the high-pass filter dynamics. Moreover, it is clear that the transient response of the direct-lift portion is exceptionally fast and settles within 0.5 s without any noticeable overshoot. The considerable steady-state error is not of concern, since the pitch-moment-based portion will dominate the low-frequency characteristics of the hybrid controller using the elevator - the direct-lift portion is designed primarily to improve the speed of the initial transient response.

(a) Pole-zero map
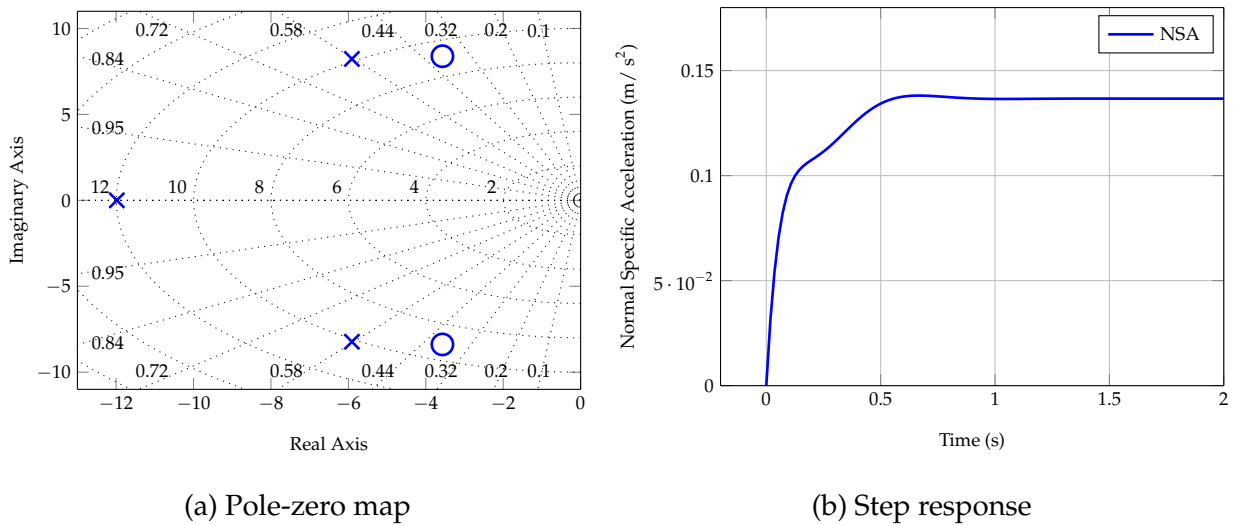
(b) Step response

Figure 5.9: Pole-zero map and step response of the direct lift controller on reduced normal dynamics

Pitch-moment-based controller pole placement: Placement of the closed-loop poles involves selecting the closed-loop integrator pole location (a), and the location of the feed-forward zero (z_f) as well as the damping ratio (ζ) and natural frequency (ω_n) of the short period mode poles. Figures 5.10a and 5.10b illustrate the pole-zero map and step response of the pitch-moment-based controller when,

$$\zeta_{cl} = 0.707 \tag{5.85}$$

$$\omega_{n_{cl}} = 9.5 \text{ rad/s} \tag{5.86}$$

$$a = \zeta_{cl}\omega_{n_{cl}} \tag{5.87}$$

$$= 6.72 \text{ rad/s}$$

$$z_f = a \tag{5.88}$$

$$= 6.72 \text{ rad/s}$$

which yields the following closed-form solution feedback gains,

$$K_q = -0.0872 \tag{5.89}$$

$$K_c = 0.0032 \tag{5.90}$$

$$K_{i_e} = 0.0726 \tag{5.91}$$

$$N_c = 0.0108 \tag{5.92}$$

The short period mode poles were chosen to be optimally damped and placed with a frequency near the upper bound for maximum performance. The integrator pole was chosen to coincide with the real component of the complex pole pair so as not to limit controller bandwidth by placing a slower integrator pole. The zero was placed on top of the integrator pole to minimise its adverse transient effects. It is apparent that the response is exceptionally fast and exhibits optimal damping characteristics as required.

(a) Pole-zero map
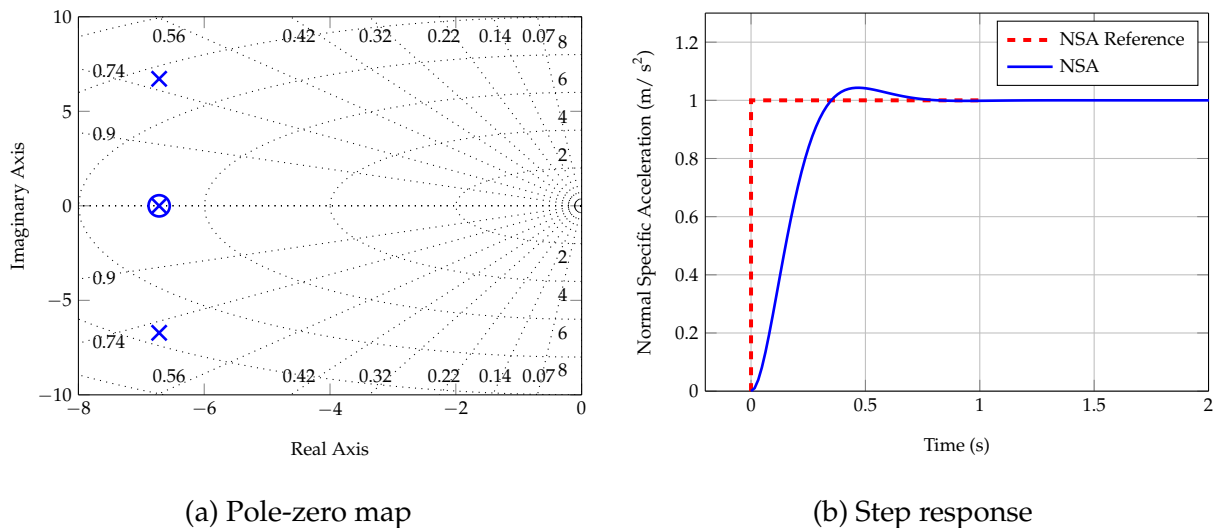
(b) Step response

Figure 5.10: Pole-zero map and step response of the pitch-moment-based controller on reduced normal dynamics

Analysis of the augmented hybrid controller: Figure 5.11 shows a comparison between the pitch-moment-based controller and the hybrid NSA controller step response on the reduced normal dynamics when,

$$K_m = 0.1213 \tag{5.93}$$

where K_m is the mixing gain calculated using Equation (5.42). It can be seen from the step response that there is a clear decrease in rise time, settling time, and maximum overshoot when the direct-lift portion is augmented to form the hybrid controller. The pole plots and step responses illustrated in the preceding discussions were based on reduced-order longitudinal aircraft dynamics following simplifications made by Peddle [1]. It is important to analyse the effect of the hybrid augmentation on the unsimplified, non-reduced aircraft dynamics for the sake of a more concrete
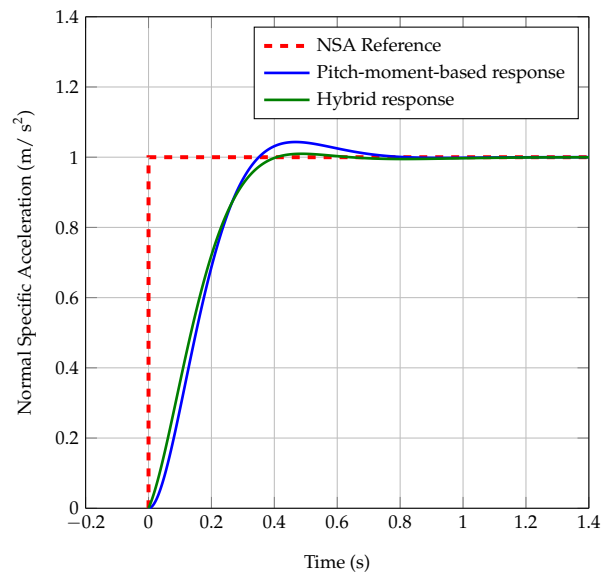
Figure 5.11: Hybrid controller step response on reduced normal dynamics

comparison between the conventional pitch-moment-based controller and the hybrid NSA controller. It should be noted that actuator dynamics were included in subsequent linear simulations to improve model fidelity. Figure 5.12 depicts a comparative pole-zero map and step response of the hybrid controller for an increasing integral gain K_{i_f} that ranges from zero to the designed value.
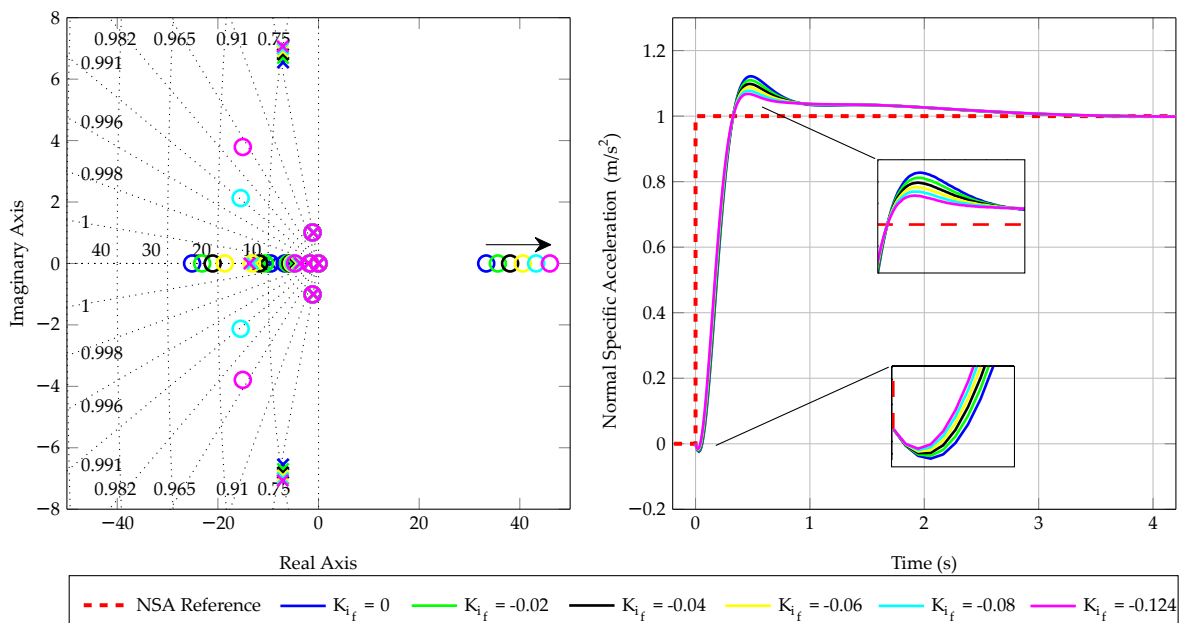
Figure 5.12: Hybrid controller pole-zero map and step response on full longitudinal dynamics

It is apparent that the NMP zero moves further to the right for an increasing gain, resulting in decreased NMP transient behaviour, as illustrated by the step response on the right-hand side of the figure. Moving the NMP zero further to the right effectively minimises its transient effects, and

results in a decreased rise time that contributes to an overall improvement in controller responsiveness. It is apparent from the step response that the amount of overshoot is effectively halved when the hybrid controller gain is increased from zero (no DLC) to the designed value. Furthermore, it is apparent that the short period mode poles hardly vary as a function of the direct-lift gain, since they are mostly dominated by the pitch-moment-based controller dynamics. To this end, it can be concluded that the augmentation of the direct-lift portion results in a hybrid NSA controller with superior transient response characteristics, which should contribute to improved gust alleviation performance. This will be further investigated in Chapter 7.

5.2.3 Climb Rate Controller

This section presents the design and verification of a high-performance climb rate controller. This controller regulates climb rate by generating a normal specific acceleration command that the aforementioned hybrid NSADLC controller will try to maintain using a combination of the flaps and elevator. It is important to note that climb rate is controlled with respect to the inertial reference frame, where a positive climb rate is defined as $-\dot{D}$. As mentioned before, the airspeed and climb rate controllers are designed independently of one another despite the inherent coupling that exists; the assumption is that airspeed is maintained sufficiently by the airspeed controller. Climb rate is measured using a differential GPS mounted on board the practical test vehicle, and propagated through an Extended Kalman Filter (EKF) to mitigate the adverse effects of GPS delay. It can be seen from Figure 5.1 that the input to the climb rate controller stems from the outer-loop altitude controller. A conversion block has been added to the output of the climb rate controller to improve altitude regulation during a turn manoeuvre by commanding additional normal specific acceleration according to the current bank angle measurement as follows:

$$C_{w_{ref}} = \frac{C_{n_{ref}}}{\cos \Phi} \tag{5.94}$$

where $C_{n_{ref}}$ denotes the inertially coordinated NSA reference generated by the climb rate controller, and Φ denotes the current bank angle measurement which is subject to the constraint that $|\Phi| \neq \pi/2$, at which point there exists a mathematical singularity. Since the climb rate controller will be designed about the trim equilibrium state with $\Phi = 0$, it is apparent from Equation (5.94) that,

$$C_{w_{ref}} = C_{n_{ref}} \tag{5.95}$$

where $C_{w_{ref}}$ has already been defined in the preceding section.

5.2.3.1 Design

Two approaches for designing outer-loop controllers based on inner-loop dynamics were investigated. The first is by means of time scale separation, which involves treating the inner-loop dynamics as a simple first-order time delay. Albeit simple to design, this approach often yields slow outer-loop controllers, as the designer is forced to accept closed-loop specifications that adhere to the constraints of time scale separation. Furthermore, this approach completely ignores the dynamics of the inner-loop controllers and neglects the intricate coupling associated with flight dynamics. In light of this, it would seem sensible to design the outer-loop controllers based on

a model that encapsulates the augmented inner-loop controllers and aircraft dynamics. This approach should yield high-bandwidth, high-fidelity controllers capable of executing accurate crosswind landings. With reference to Figure 5.13, a PI control law is defined as,

$$C_{w_{ref}} = -K_p \dot{e}_r - K_i e_r \tag{5.96}$$

with,

$$\dot{e}_r = \dot{h} - \dot{h}_{ref} \tag{5.97}$$

where $\dot{h}$ and $\dot{h}_{ref}$ denote the climb rate measurement and corresponding reference command respectively. The integrator should compensate for any acceleration measurement biases and consequently improve glideslope tracking accuracy during the final approach.
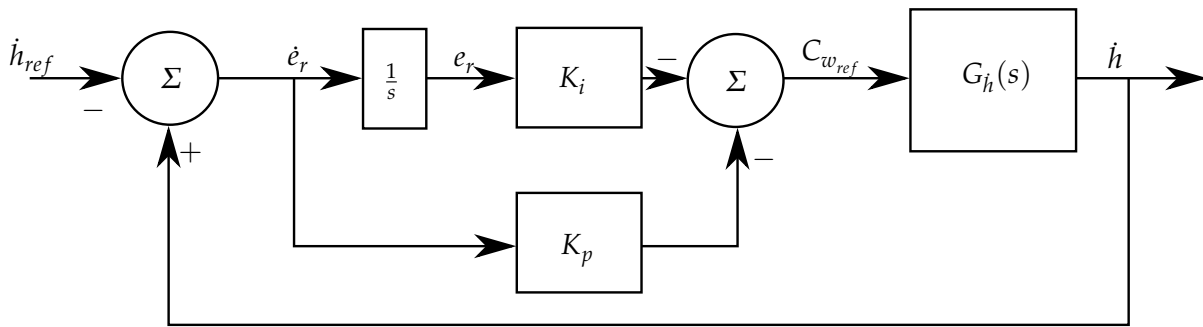
Figure 5.13: Climb rate controller block diagram

Now that the inner-loop controllers (NSADLC and airspeed) have been designed and augmented to the full longitudinal aircraft model in Equation (5.71), it is possible to design the climb rate controller using root locus techniques to place the closed-loop poles appropriately. However, it is first necessary to develop an equation that extracts climb rate from the state vector x_{hyb} so that a closed-loop transfer function from normal specific acceleration reference to climb rate can be obtained. The inertially coordinated climb rate can be obtained from the body axis velocities through the inverse DCM shown in Equation (3.56) as follows:

$$\dot{D} = -U \sin \Theta + V \cos \Theta \sin \Phi + W \cos \Theta \cos \Phi \tag{5.98}$$

Using small angle approximations and assuming that the bank angle Φ is zero, climb rate can be written as,

$$\dot{h} = -\dot{D} \tag{5.99}$$

$$= U\Theta - W$$

Rewriting under the assumption that $U \approx \bar{V}_T$ and $W \approx \bar{V}_T \alpha$ for straight and level flight yields,

$$\dot{h} = \bar{V}_T \gamma \tag{5.100}$$

with,

$$\gamma = (\Theta - \alpha) \tag{5.101}$$

where γ is the flight path angle, i.e. the pitch angle of the aircraft's velocity vector. Equation (5.100) relates climb rate to airspeed and flight path angle under the assumption that $\Phi = 0$. To this end, the transfer function from normal specific acceleration reference to climb rate can be obtained from the state space model of Equation (5.71) through,

$$G_{\dot{h}}(s) = \frac{\dot{h}(s)}{C_{w_{ref}}(s)} \tag{5.102}$$

$$= C_{\dot{h}}(s\boldsymbol{I} - \boldsymbol{A}_{hyb})^{-1}\boldsymbol{B}_{C_{w_{ref}}}$$

where,

$$C_{\dot{h}} = \begin{bmatrix} 0 & -\bar{V}_T & 0 & \bar{V}_T & \boldsymbol{0}_{1\times 4} \end{bmatrix} \tag{5.103}$$

is used to extract climb rate indirectly from the state vector $\boldsymbol{x}_{hyb}$ through Equation (5.100). Figure 5.14a shows the root locus of the climb rate controller with respect to the PI feedback gains K_p and K_i.

(a) Root locus (zoomed in)   (b) Step response
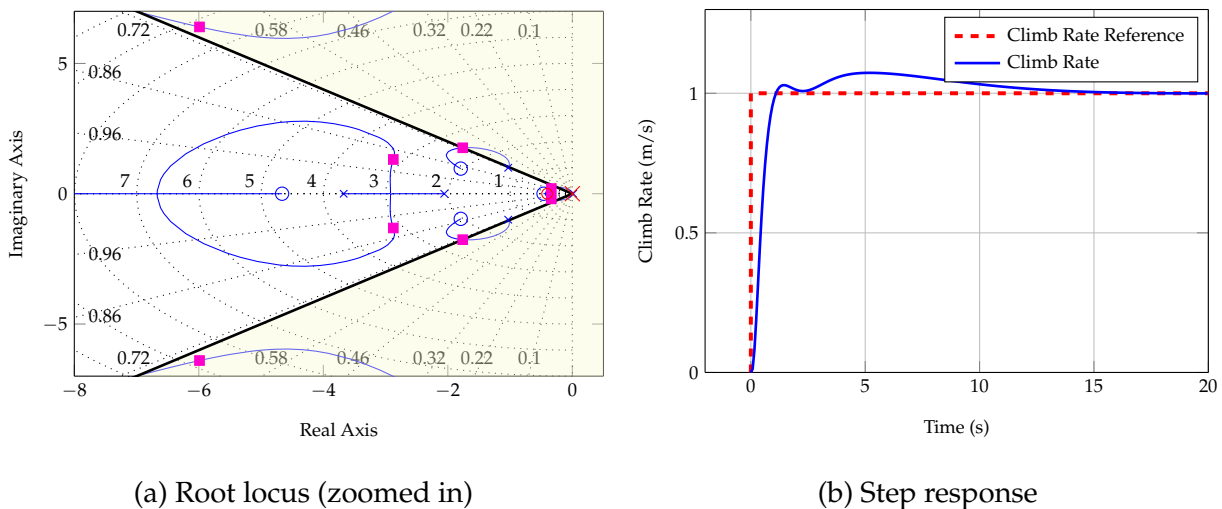
Figure 5.14: Climb rate controller root locus and step response

The location of the climb rate controller zero was adjusted until the dominant branches of the root locus passed through closed-loop pole locations with optimal damping. Figure 5.14b illustrates the climb rate controller step response when,

$$K_p = 2.496 \tag{5.104}$$

$$K_i = 1.013 \tag{5.105}$$

The additional transient behaviour that manifests as a second peak can be attributed to the residue of the slower complex pole pair that resides near the closed-loop zeros, seen in Figure 5.14a. The faster, optimally damped pole pair seems to dominate the initial transient response and contribute to the fast rise time and 5% overshoot associated with the initial peak. Placing the closed-loop poles essentially involves a trade-off between minimal overshoot, adequate rise time, and mitigation of the slower transient dynamics that manifests as a secondary peak.

5.2.3.2 Closed-loop System

In order to further maintain design fidelity, it is necessary to augment the dynamics of Equation (5.71) with the climb rate control law. Augmenting the integrator state of Equation (5.97) yields,

$$
\begin{bmatrix} \dot{x}_{hyb} \\ \dot{e}_r \end{bmatrix} = \begin{bmatrix} A_{hyb} & \mathbf{0}_{8\times1} \\ 0 & -V_T \ \ 0 \ \ V_T \ \ \mathbf{0}_{1\times5} \end{bmatrix} \begin{bmatrix} x_{hyb} \\ e_r \end{bmatrix} + \begin{bmatrix} B_{hyb} \\ \mathbf{0}_{1\times2} \end{bmatrix} u_{hyb} + \begin{bmatrix} \mathbf{0}_{8\times1} \\ -1 \end{bmatrix} \dot{h}_{ref}
\tag{5.106}
$$

Writing the augmented A matrix above in a more compact form as $A_{\dot{e}_r}$ and substituting the climb rate control law of Equation (5.96) yields,

$$
\begin{bmatrix} \dot{x}_{hyb} \\ \dot{e}_r \end{bmatrix} = \begin{bmatrix} A_{\dot{e}_r} + \begin{bmatrix} B_{C_{w_{ref}}} \\ 0 \end{bmatrix} \begin{bmatrix} 0 & K_p V_T & 0 & -K_p V_T & \mathbf{0}_{1\times4} & -K_i \end{bmatrix} \end{bmatrix} \begin{bmatrix} x_{hyb} \\ e_r \end{bmatrix}
\tag{5.107}
$$

$$
+ \begin{bmatrix} K_p B_{C_{w_{ref}}} & B_{\bar{v}_{ref}} \\ -1 & 0 \end{bmatrix} \begin{bmatrix} \dot{h}_{ref} \\ \bar{v}_{ref} \end{bmatrix}
$$

where,

$$
B_{C_{w_{ref}}} = B_{hyb} \begin{bmatrix} 1 & 0 \end{bmatrix}^T ; \ \ B_{\bar{v}_{ref}} = B_{hyb} \begin{bmatrix} 0 & 1 \end{bmatrix}^T
\tag{5.108}
$$

The closed-loop model of Equation (5.107) will be augmented further as more control laws are added to the system. It is therefore convenient to write it in a more compact form as,

$$
\dot{x}_h = A_h x_h + B_h u_h
\tag{5.109}
$$

with,

$$
\dot{h} = C_h x_h
\tag{5.110}
$$

so that the closed-loop transfer function from climb rate reference to measured climb rate is given by,

$$
G_{\dot{h}_{cl}}(s) = \frac{\dot{h}(s)}{\dot{h}_{ref}(s)}
\tag{5.111}
$$

$$
= C_h (sI - A_h)^{-1} B_{\dot{h}_{ref}}
$$

where,

$$
C_h = \begin{bmatrix} 0 & -V_T & 0 & V_T & \mathbf{0}_{1\times5} \end{bmatrix} ; \ \ B_{\dot{h}_{ref}} = B_h \begin{bmatrix} 1 & 0 \end{bmatrix}^T
\tag{5.112}
$$

5.2.4 Altitude Controller

This section presents the design and verification of an altitude controller. This controller regulates altitude by generating a climb rate command that the climb rate controller will try to regulate through the inner-loop NSADLC controller. Altitude is controlled with respect to the inertial reference frame, where it is assumed that the climb rate vector is always normal to the inertial frame,

and that the flight path angle remains small. Altitude is measured by means of a differential GPS mounted on board the practical test vehicle and propagated through an EKF to mitigate the adverse effects of GPS delay. It is clear from Figure 5.1 that the input to the altitude controller stems from the state machine, discussed in Section 6.3, whilst the output drives the climb rate controller discussed in the preceding section. Accurate glideslope tracking is essential for down-range landing accuracy, since small deviations from the reference altitude result in large longitudinal landing position offsets due to the inherently shallow glideslope angle. For conceptual purposes, consider the following open-loop altitude controller dynamics:

$$G_h(s) = \frac{1}{s} \tag{5.113}$$

which is characteristic of a pure integrator from climb rate ($\dot{h}$) to altitude (h). It is apparent that this is a type 1 system, and is therefore incapable of following a ramp trajectory with zero error in the steady state if a simple proportional control law is defined. To further motivate this argument, consider the following proportional controller:

$$D_h(s) = K_p \tag{5.114}$$

The steady-state error is then given by,

$$ess = \frac{1}{K_v} \tag{5.115}$$

where,

$$K_v = \lim_{s \to 0} sG_h(s)D_h(s) \tag{5.116}$$

so that,

$$ess = \frac{1}{K_p} \tag{5.117}$$

from which it can be concluded that the steady-state error is inversely proportional to the feedback gain K_p. A common solution to this problem is to introduce an integrator to the control law; however, integrators usually slow down the transient response and have an adverse effect on closed-loop stability. Since a ramp trajectory is usually only commanded during the landing phase of a particular mission, it does not make sense to sacrifice speed of response and loop stability during other flight modes by introducing an integrator to mitigate the steady-state error. A more sensible solution, and one that is commonly used in autoland systems, is to feed-forward the expected sink rate during the glideslope tracking phase. It is apparent from the altitude controller block diagram, depicted in Figure 5.15, that an external climb reference $\dot{h}_{ref}$ is fed-forward and added to the climb rate reference $\dot{h}_{ref}$ generated by the proportional controller. This feed-forward strategy essentially speeds up the transient response of the altitude controller whilst tracking a ramp trajectory, and can be thought of as a predictive component that aids the proportional controller by pre-injecting the expected sink rate. Without this feed-forward term, the proportional controller would have to wait for the error signal to deviate before commanding an equivalent sink rate. Pre-injecting the expected sink rate improves transient response characteristics, mitigates the steady-state error, and allows the proportional feedback component to work around a new set point with the purpose of rejecting external disturbances that result in altitude deviations.

5.2.4.1 Design

Following the principles of superposition, the feedback component will be designed under the assumption that $\dot{\bar{h}}_{ref} = 0$, with the effect of the feed-forward term further investigated in Chapter 7. To maintain design fidelity in accordance with the preceding discussion on outer-loop controller design, the altitude controller will be designed based on the full longitudinal model that encapsulates all corresponding inner-loop controller dynamics (NSADLC, airspeed, and climb rate) and inherent aircraft coupling effects. With reference to Figure 5.15, a proportional control law is defined as,

$$\dot{h}_{ref} = -K_p e_h \tag{5.118}$$

with,

$$e_h = h - h_{ref} \tag{5.119}$$

where h and h_{ref} denote the altitude measurement and corresponding reference command respectively.
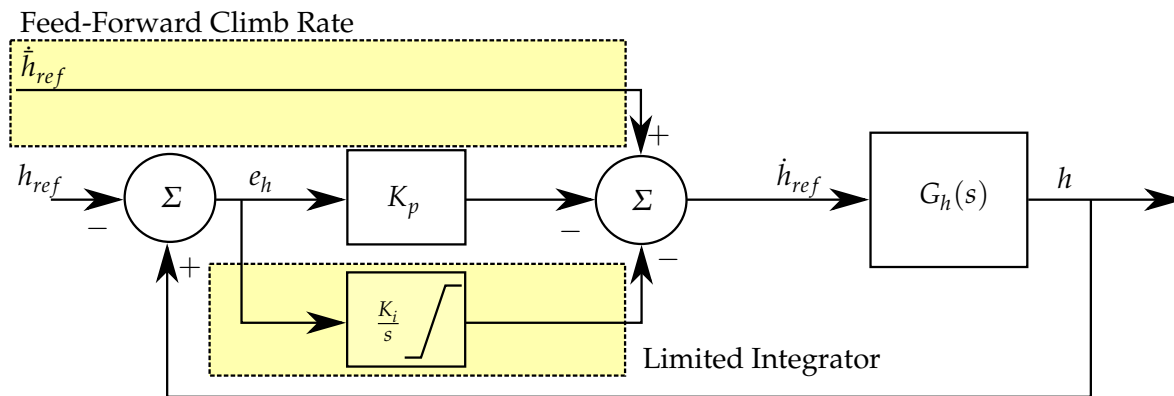
Figure 5.15: Altitude controller block diagram

The transfer function from climb rate reference to altitude is obtained from the state space model of Equation (5.109) through,

$$G_h(s) = \frac{h(s)}{\dot{h}_{ref}(s)} \tag{5.120}$$

$$= \frac{1}{s} C_{\dot{h}} (s\boldsymbol{I} - \boldsymbol{A}_{\dot{h}})^{-1} \boldsymbol{B}_{\dot{h}_{ref}}$$

The root locus of the altitude controller with respect to the proportional gain K_p is shown in Figure 5.16a. It is imperative that the altitude controller be fast enough to minimise any errors during the final approach before touchdown occurs. Consider a glideslope length of,

$$L_{gs} = 250 \text{ m} \tag{5.121}$$

An aircraft approaching the runway with a nominal ground speed of,

$$V_{ground} = 16 \text{ m/s} \tag{5.122}$$

(a) Root locus (zoomed in) (b) Step response
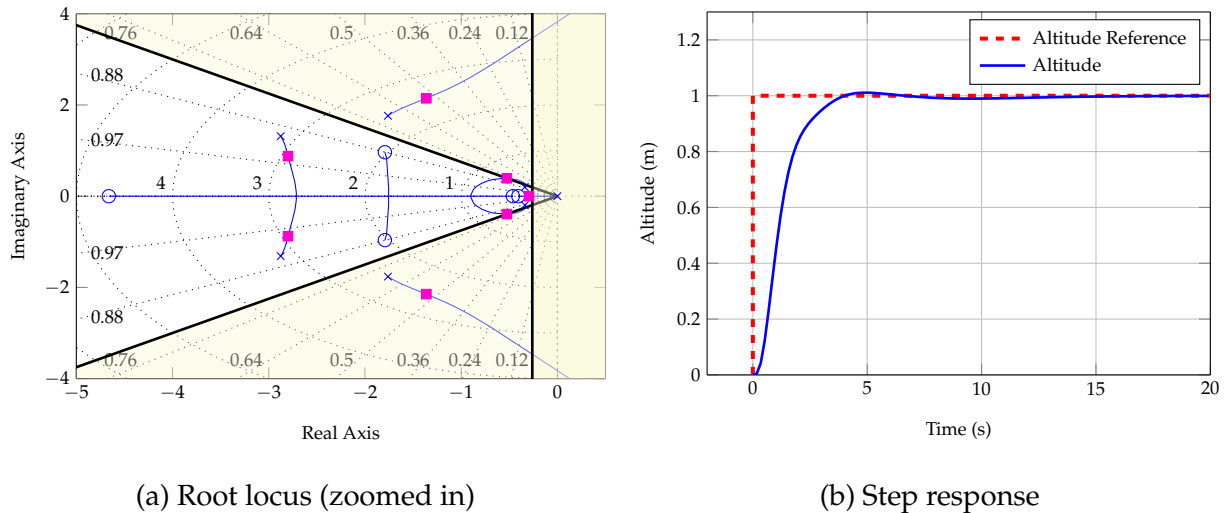
Figure 5.16: Altitude controller root locus and step response

will remain on the glideslope for,

$$t_{gs} = \frac{L_{gs}}{V_{ground}} \tag{5.123}$$

$$= 15.625 \text{ s}$$

It is obvious that increasing the approach distance would improve landing accuracy, since the controllers would have more time to settle before touchdown occurs. However, the specific glideslope length of 250 m was chosen based on certain practical limitations discussed in Chapter 6. In light of this, the K_p feedback gain value was adjusted until the dominant closed-loop poles satisfied the following settling time requirement:

$$t_s < 15 \text{ s} \tag{5.124}$$

to maximise landing accuracy by ensuring that altitude errors are adequately minimised before touchdown. It is also apparent that the damping ratio of the complex pole pair that resides near the dominant real pole is given by,

$$\zeta_{cl} = 0.8 \tag{5.125}$$

which ensures minimal overshoot from its contribution to the transient response. Figure 5.16b illustrates the altitude controller step response when,

$$K_p = 0.75 \tag{5.126}$$

A few minor adjustments were made to the altitude controller to improve performance and reliability. Firstly, a limited integrator was added to the system to compensate for climb rate biases that would otherwise result in glideslope tracking errors. By limiting the integrator to an estimated value of the climb rate bias, the system was able to benefit from the steady-state advantages of integral control without the associated adverse transient effects. Initially, a standard PI control law was suggested; however, upon further investigation it was found that the integrator reduced the

phase margin to the point of instability. Secondly, an investigation into the expected sink rate was conducted to determine the best method of calculating $\dot{\bar{h}}_{ref}$. Perhaps the simplest method would be to keep the value of $\dot{\bar{h}}_{ref}$ fixed to a nominal sink rate associated with the particular glideslope,

$$\dot{\bar{h}}_{ref} = \bar{V}_{app} \tan \gamma_g \tag{5.127}$$

where $\bar{V}_{app}$ is the predetermined approach airspeed and γ_g is the glideslope angle. This method would work well in ideal situations, where ground speed and airspeed are equal (no wind). But since climb rate is an inertially coordinated parameter, it is intuitive that this method would perform quite poorly in the presence of a strong headwind (or tailwind), as the sink rate would need to be adjusted accordingly. A possible solution to this would be to explicitly differentiate the altitude reference, which is calculated based on the inertial distance from the touchdown point. However, explicit differentiation is not recommended for practical scenarios, especially for noisy signals, as this could lead to unexpected oscillatory behaviour. A more sensible solution would be to use the current ground speed measurement (from the DGPS) to calculate the required sink rate for a specific glideslope angle γ_g,

$$\dot{\bar{h}}_{ref} = \bar{V}_{ground} \tan \gamma_g \tag{5.128}$$

where $\bar{V}_{ground}$ denotes the current ground speed measurement.

5.2.4.2 Closed-loop System

It is first necessary to augment an altitude state to the x_h state vector before the altitude control law can be augmented to the full longitudinal dynamics. Augmenting the altitude state yields,

$$\begin{bmatrix} \dot{x}_h \\ \dot{h} \end{bmatrix} = \begin{bmatrix} A_h & \mathbf{0}_{9 \times 1} \\ 0 \quad -V_T \quad 0 \quad V_T \quad \mathbf{0}_{1 \times 6} \end{bmatrix} \begin{bmatrix} x_h \\ h \end{bmatrix} + \begin{bmatrix} B_h \\ \mathbf{0}_{1 \times 2} \end{bmatrix} u_h \tag{5.129}$$

where Equation (5.100) has been used to indirectly extract climb rate ($\dot{h}$) from the x_h state vector. Writing the augmented A matrix above in a more compact form as A_h, and substituting the altitude control law of Equation (5.118) yields,

$$\begin{bmatrix} \dot{x}_h \\ \dot{h} \end{bmatrix} = \begin{bmatrix} A_h + \begin{bmatrix} B_{h_{ref}} \\ 0 \end{bmatrix} \begin{bmatrix} \mathbf{0}_{9 \times 1} & -K_p \end{bmatrix} \end{bmatrix} \begin{bmatrix} x_h \\ h \end{bmatrix} + \begin{bmatrix} K_p B_{h_{ref}} & B_{\bar{v}_{ref}} \\ 0 & 0 \end{bmatrix} \begin{bmatrix} h_{ref} \\ \bar{v}_{ref} \end{bmatrix} \tag{5.130}$$

where,

$$B_{h_{ref}} = B_h \begin{bmatrix} 1 & 0 \end{bmatrix}^T ; \quad B_{\bar{v}_{ref}} = B_h \begin{bmatrix} 0 & 1 \end{bmatrix}^T \tag{5.131}$$

It is convenient to write the dynamics of Equation (5.130) in a more compact form as,

$$\dot{x}_h = A_h x_h + B_h u_h \tag{5.132}$$

with,

$$h = C_h x_h \tag{5.133}$$

so that the closed-loop transfer function from altitude reference to measured altitude is given by,

$$G_{h_{cl}}(s) = \frac{h(s)}{h_{ref}(s)} \tag{5.134}$$

$$= C_h(sI - A_h)^{-1} B_{h_{ref}}$$

where,

$$C_h = \begin{bmatrix} 0_{1 \times 9} & 1 \end{bmatrix}; \; B_{h_{ref}} = B_h \begin{bmatrix} 1 & 0 \end{bmatrix}^T \tag{5.135}$$

5.3   Lateral Controllers

The design and verification of the aircraft's lateral controllers are discussed in this section. Each subsection begins with a discussion of the design approach, before the details of the controller are considered and the results verified by linear simulation. The cascaded design approach starts with the augmentation of a lateral specific acceleration controller by closing the first control loop around the decoupled lateral aircraft dynamics of Equation (4.29). This is then followed by the design and verification of an inner-loop roll rate controller, a middle-loop roll angle controller and finally the outer-loop guidance and heading controllers. It is important to note that active anti-windup protection was added to all of the integrators.

5.3.1   Lateral Specific Acceleration Controller

This section presents the design and verification of a Lateral Specific Acceleration (LSA) controller based on the work of Peddle [1]. To a good approximation, the lateral-directional dynamics of the aircraft can be considered as the standard roll/Dutch roll dynamics [1]. Peddle shows that under certain conditions, typically met by most conventional aircraft, it is possible to decouple the lateral and directional dynamics respectively. This allows for the independent design of two inner-loop controllers based on their individual decoupled dynamics. The first controller is designed to regulate lateral specific acceleration and is the focus of this section. The second controller is responsible for regulating the aircraft's roll rate and will be discussed in the section to follow. The LSA controller essentially governs the Dutch roll mode poles, whilst the roll rate controller governs the roll mode pole.

A number of conditions and constraints should hold for the lateral-directional dynamics to be successfully decoupled. Firstly, side forces due to the aircraft's roll rate and aileron deflections should be negligibly small,

$$Y_P = 0.7986 \approx 0 \tag{5.136}$$

$$Y_{\delta_A} = 0.1080 \approx 0 \tag{5.137}$$

Furthermore, yawing moments due to roll rate and aileron deflections should be significantly smaller than the yawing moments due to yaw rate, sideslip, and rudder deflections. Analogous to the previous statement, rolling moments due to yaw rate and rudder deflections should be significantly smaller than rolling moments due to roll rate, sideslip, and aileron deflections. Hence,

lateral dynamics should have little effect on directional dynamics and vice versa. These constraints are given mathematically by Peddle [1], and have been included in Appendix B for further perusal. Assuming that the aforementioned conditions and constraints are met, the lateral-directional dynamics can be decoupled into lateral and directional dynamics, for the purpose of simplifying the controller design. However, it is important to note that even if these are easily met by a particular airframe, the lateral-directional dynamics are not fully decoupled, since aileron deflections will still excite directional dynamics in the same way that rudder deflections will excite lateral dynamics [1]. This is commonly referred to as adverse yaw and rudder-induced roll respectively, and are usually considered to be disturbances to the individual decoupled systems. Now that the lateral-directional decoupling has been addressed, it is possible to proceed with the design and verification of an independent LSA controller based on decoupled directional dynamics. It can be seen from Figure 5.1 that this inner-loop LSA controller commands the rudder actuator to regulate lateral specific acceleration. A three-axis accelerometer included in the avionics stack on board the practical test vehicle provided lateral acceleration measurements for the purpose of feedback control. The LSA reference command is typically set to zero during conventional flight to enforce coordinated turns by minimising the sideslip angle during a turn manoeuvre. When the outer-loop heading controller is activated (typically during landing), the reference command is no longer zero, but rather the lateral acceleration required to regulate a particular heading indirectly through the sideslip angle (β) - this is further discussed in Section 5.3.5. A two-stage design strategy is followed: Firstly, the decoupled directional dynamics are used to design a controller that allows the Dutch roll mode poles to be moved arbitrarily. The sole purpose of this controller is stability augmentation and it is therefore not intended to regulate lateral specific acceleration in any way. A second, outer layer controller is then designed in stage two with the purpose of regulating lateral specific acceleration. During the design, it is assumed that the stability augmentation controller places the natural directional dynamics poles such that the principles of TSS can be used to design the regulation component. This significantly reduces design complexity, as this assumption allows the full dynamic model from rudder to lateral specific acceleration to be approximated by a steady-state gain. The regulation component of the LSA controller needs to ensure that the closed-loop bandwidth does not exceed the frequency bounds prescribed by Peddle [1].

5.3.1.1 Directional Stability Augmentation

Assuming that the aforementioned conditions and constraints are met, the design can proceed based on the following reduced-order directional dynamics:

$$\begin{bmatrix} \dot{\beta} \\ \dot{r} \end{bmatrix} = \begin{bmatrix} -\frac{Y_\beta}{m\bar{V}_T} & -1 \\ \frac{N_\beta}{I_{zz}} & \frac{N_R}{I_{zz}} \end{bmatrix} \begin{bmatrix} \beta \\ r \end{bmatrix} + \begin{bmatrix} \frac{Y_{\delta_R}}{m\bar{V}_T} \\ \frac{N_{\delta_R}}{I_{zz}} \end{bmatrix} \delta_r \tag{5.138}$$

$$B_w = \begin{bmatrix} \frac{Y_\beta}{m} & \frac{Y_R}{m} \end{bmatrix} \begin{bmatrix} \beta \\ r \end{bmatrix} + \begin{bmatrix} \frac{Y_{\delta_R}}{m} \end{bmatrix} \delta_r \tag{5.139}$$

where B_w denotes lateral specific acceleration coordinated in the wind axis, with the dimensional stability and control derivative notation as defined in Equation (5.34). With reference to Fig-

ure 5.17, the stability augmentation control law is defined as,

$$\delta_r = -K_r r - K_B B_w + \delta_{r_r} \tag{5.140}$$

where δ_{r_r} will be used as an input for the regulation control law.
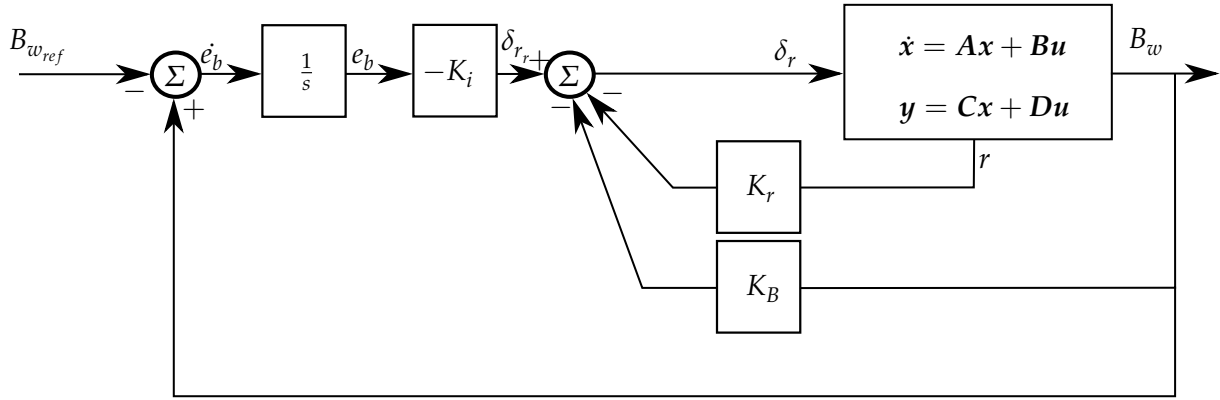
Figure 5.17: LSA controller block diagram

Substituting the control law into the directional dynamics of Equation (5.138) yields,

$$\begin{bmatrix} \dot{\beta} \\ \dot{r} \end{bmatrix} = \begin{bmatrix} -\frac{Y_\beta}{m\bar{V}_T} - K_B \frac{Y_\beta Y_{\delta_R} X}{m^2 \bar{V}_T} & -1 - K_r' \frac{Y_{\delta_R} X}{m\bar{V}_T} \\ \frac{N_\beta}{I_{zz}} - K_B \frac{Y_\beta N_{\delta_R} X}{m I_{zz}} & \frac{N_R}{I_{zz}} - K_r' \frac{N_{\delta_R} X}{I_{zz}} \end{bmatrix} \begin{bmatrix} \beta \\ r \end{bmatrix} + \begin{bmatrix} \frac{Y_{\delta_R} X}{m\bar{V}_T} \\ \frac{N_{\delta_R} X}{I_{zz}} \end{bmatrix} \delta_r \tag{5.141}$$

$$\tag{5.142}$$

where,

$$X = \left(1 + K_B \frac{Y_{\delta_R}}{m} \right)^{-1} \tag{5.143}$$

$$K_r' = K_r + K_B \frac{Y_{\delta_R}}{m} \tag{5.144}$$

Peddle [1] shows that the closed-loop poles are well approximated by the roots of the following characteristic equation:

$$p(s) = s^2 - \left(\frac{Y_\beta}{m\bar{V}_T} + \frac{N_R}{I_{zz}} - \frac{N_{\delta_R}}{I_{zz}} K_r \right) X s + \left[\frac{Y_\beta N_R}{m\bar{V}_T I_{zz}} + \frac{N_\beta}{I_{zz}} + \frac{Y_{\delta_R} Y_\beta}{m I_{zz}} \left(\frac{N_\beta}{Y_\beta} - \frac{N_{\delta_R}}{Y_{\delta_R}} \right) K_B \right] X \tag{5.145}$$

given that the following constraints hold:

$$\left| \frac{K_B}{K_r} \right| \ll \left| \frac{m l_F}{Y_R (l_D - l_F)} \right| \tag{5.146}$$

$$|K_r| \ll \left| \frac{m \bar{V}_T l_W}{Y_{\delta_R} (l_W - l_F)} \right| \tag{5.147}$$

with,

$$l_W = -\frac{N_\beta}{Y_\beta} \tag{5.148}$$

$$l_D = -\frac{N_R}{Y_R} \tag{5.149}$$

$$l_F = -\frac{N_{\delta_R}}{Y_{\delta_R}} \tag{5.150}$$

where l_W is the weathercock arm length, l_D is the damping arm length, and l_F is the effective length to the fin - all lengths are relative to the centre of mass. Given that the aforementioned constraints are met, the closed-form solution feedback gains can be calculated by matching the coefficients of the characteristic equation,

$$\alpha_c(s) = (s^2 + 2\zeta\omega_n s + \omega_n^2) \tag{5.151}$$

to yield,

$$K_r = \frac{I_{zz}}{N_{\delta_R}} \left[\frac{Y_\beta}{m\bar{V}_T} + \frac{N_R}{I_{zz}} + 2\zeta\omega_n \left(1 + K_B \frac{Y_{\delta_R}}{m} \right) \right] \tag{5.152}$$

$$K_B = \frac{\frac{Y_\beta N_R}{m\bar{V}_T I_{zz}} + \frac{N_\beta}{I_{zz}} - \omega_n^2}{\frac{Y_{\delta_R}}{m} \left[\omega_n^2 - \frac{Y_\beta}{I_{zz}} \left(\frac{N_\beta}{Y_\beta} - \frac{N_{\delta_R}}{Y_{\delta_R}} \right) \right]} \tag{5.153}$$

where the design freedom is left to selecting the damping ratio (ζ) and natural frequency (ω_n) of the Dutch roll mode poles.

5.3.1.2 Lateral specific acceleration regulation

With the aforementioned stability augmentation controller in place, the focus now shifts towards the design of the regulation component. Under the assumption that the closed-loop directional dynamics poles operate on a much faster time scale than those associated with the regulator, the transfer function from rudder to lateral specific acceleration can be approximated as follows:

$$B_w \approx K_{ss}\delta_{r_r} \tag{5.154}$$

where K_{ss} is the steady-state gain of the transfer function and is defined by Peddle [1] as,

$$K_{ss} = \frac{Y_{\delta_R}Y_\beta}{mI_{zz}\omega_n^2} \left(\frac{N_\beta}{Y_\beta} - \frac{N_{\delta_R}}{Y_{\delta_R}} \right) \left(1 + K_B \frac{Y_{\delta_R}}{m} \right)^{-1} \tag{5.155}$$

given that the constraint of Equation (5.146) holds. With reference to Figure 5.17, the regulation control law is defined as,

$$\delta_{r_r} = -K_i e_b \tag{5.156}$$

with,

$$\dot{e}_b = B_w - B_{w_{ref}} \tag{5.157}$$

where $B_{w_{ref}}$ is the lateral specific acceleration reference command. Integral control will reduce closed-loop sensitivity to parameter uncertainty, which will inevitably corrupt the steady-state gain of Equation (5.155). It is important to note that the frequency of the closed-loop integrator pole is limited by the bound of the following equation,

$$\omega_n < \frac{1}{3} \left| \sqrt{\frac{-Y_\beta (l_F - l_W)}{I_{zz}}} \right| \tag{5.158}$$

and will therefore dominate the LSA response to ensure that a practically feasible controller is designed [1]. In light of this, the stability augmentation controller discussed in the preceding section will provide fast disturbance rejection capabilities, with the gross lateral specific acceleration response being dominated by the regulation component. Substituting Equation (5.154) into (5.157) yields,

$$\dot{e}_b = [-K_{ss}K_i]e_b + [-1]B_{w_{ref}} \tag{5.159}$$

with the closed-loop characteristic equation given by,

$$s + K_{ss}K_i = 0 \tag{5.160}$$

Given the desired pole location,

$$\alpha_c(s) = s + a \tag{5.161}$$

the closed-form solution integrator feedback gain can be calculated as follows:

$$K_i = \frac{a}{K_{ss}} \tag{5.162}$$

where the design freedom is left to choosing an integrator pole location that adheres to the frequency constraint of Equation (5.158).

5.3.1.3 Closed-loop System

The design conducted in the preceding section was based on simplified directional dynamics and therefore fails to encapsulate the coupling effects associated with the full lateral aircraft dynamics. To improve the design fidelity of the remaining lateral controllers, the dynamics of Equation (4.29) are augmented with the LSA stability augmentation and regulation control laws. It is convenient to write Equation (4.29) in a more compact form as,

$$\dot{x}_{lat} = A_{lat}x_{lat} + B_{lat}u_{lat} \tag{5.163}$$

where A_{lat} is the lateral system matrix, and B_{lat} is the lateral input matrix. Substituting the stability augmentation control law of Equation (5.140) yields,

$$\left[\dot{x}_{lat}\right] = \left[A_{lat} + B_{\delta_r}M_1\right]\left[x_{lat}\right] + \left[B_{\delta_a} - \left(\frac{K_B Y_{\delta_A}}{m + K_B Y_{\delta_R}}\right)B_{\delta_r} \quad \left(\frac{m}{m + K_B Y_{\delta_R}}\right)B_{\delta_r}\right]\begin{bmatrix}\delta_a \\ \delta_{r_r}\end{bmatrix} \tag{5.164}$$

where,

$$M_1 = \left[\frac{-K_B Y_\beta}{m + K_B Y_{\delta_R}} \quad \frac{-K_B Y_P}{m + K_B Y_{\delta_R}} \quad -\left(\frac{mK_r}{m + K_B Y_{\delta_R}} + \frac{K_B Y_R}{m + K_B Y_{\delta_R}}\right) \quad 0\right] \tag{5.165}$$

and,

$$B_{\delta_a} = B_{lat} \begin{bmatrix} 1 & 0 \end{bmatrix}^T ; \quad B_{\delta_r} = B_{lat} \begin{bmatrix} 0 & 1 \end{bmatrix}^T \tag{5.166}$$

It is important to note that the full-order lateral acceleration dynamics given by,

$$B_w \begin{bmatrix} \frac{Y_\beta}{m} & \frac{Y_P}{m} & \frac{Y_R}{m} \end{bmatrix} \begin{bmatrix} \beta \\ p \\ r \end{bmatrix} + \begin{bmatrix} \frac{Y_{\delta_A}}{m} & \frac{Y_{\delta_R}}{m} \end{bmatrix} \begin{bmatrix} \delta_a \\ \delta_r \end{bmatrix} \tag{5.167}$$

was used in the above augmentation as opposed to the reduced-order model given by Equation (5.139). It is convenient to write the augmented dynamics of Equation (5.164) in a more compact form as,

$$\dot{x}_s = A_s x_s + B_s u_s \tag{5.168}$$

so that augmenting the integrator state of Equation (5.157) yields,

$$\begin{bmatrix} \dot{x}_s \\ \dot{e}_b \end{bmatrix} = \begin{bmatrix} A_s & \mathbf{0}_{4\times1} \\ M_2 & 0 \end{bmatrix} \begin{bmatrix} x_s \\ e_b \end{bmatrix} + \begin{bmatrix} B_{\delta_a} & B_{\delta_{r_r}} \\ \left(\frac{Y_{\delta_A}}{m} - \frac{Y_{\delta_R} K_B Y_{\delta_A}}{m\left(m+K_B Y_{\delta_R}\right)} \right) & \frac{Y_{\delta_R}}{m+K_B Y_{\delta_R}} \end{bmatrix} \begin{bmatrix} \delta_a \\ \delta_{r_r} \end{bmatrix} + \begin{bmatrix} \mathbf{0}_{4\times1} \\ -1 \end{bmatrix} B_{w_{ref}} \tag{5.169}$$

where,

$$M_2 = \left[\left(\frac{Y_\beta}{m} - \frac{Y_{\delta_R} K_B Y_\beta}{m\left(m + K_B Y_{\delta_R}\right)} \right) \quad \left(\frac{Y_P}{m} - \frac{Y_{\delta_R} K_B Y_P}{m\left(m + K_B Y_{\delta_R}\right)} \right) \ldots \right. \tag{5.170}$$

$$\left. \ldots \left(\frac{Y_R}{m} - \frac{Y_{\delta_R} K_r}{\left(m + K_B Y_{\delta_R}\right)} - \frac{Y_{\delta_R} K_B Y_R}{m\left(m + K_B Y_{\delta_R}\right)} \right) \quad 0 \right]$$

Writing the augmented A matrix above in a more compact form as $A_{\dot{e}_b}$, and substituting the regulation control law of Equation (5.156) yields,

$$\begin{bmatrix} \dot{x}_s \\ \dot{e}_b \end{bmatrix} = \begin{bmatrix} A_{\dot{e}_b} + \begin{bmatrix} B_{\delta_{r_r}} \\ \frac{Y_{\delta_R}}{m+K_B Y_{\delta_R}} \end{bmatrix} \begin{bmatrix} \mathbf{0}_{1\times4} & -K_i \end{bmatrix} \end{bmatrix} \begin{bmatrix} x_s \\ e_b \end{bmatrix} + \begin{bmatrix} B_{\delta_a} & \mathbf{0}_{4\times1} \\ \left(\frac{Y_{\delta_A}}{m} - \frac{Y_{\delta_R} K_B Y_{\delta_A}}{m\left(m+K_B Y_{\delta_R}\right)} \right) & -1 \end{bmatrix} \begin{bmatrix} \delta_a \\ B_{w_{ref}} \end{bmatrix} \tag{5.171}$$

where,

$$B_{\delta_a} = B_s \begin{bmatrix} 1 & 0 \end{bmatrix}^T ; \quad B_{\delta_{r_r}} = B_s \begin{bmatrix} 0 & 1 \end{bmatrix}^T \tag{5.172}$$

The closed-loop model of Equation (5.171) will be augmented further as more control laws are added to the system. It is therefore convenient to write it in a more compact form as,

$$\dot{x}_{bw} = A_{bw} x_{bw} + B_{bw} u_{bw} \tag{5.173}$$

with,

$$B_w = C_{bw} x_{bw} \tag{5.174}$$

so that the closed-loop transfer function from LSA reference to measured LSA is given by,

$$G_{bw_{cl}}(s) = \frac{B_w(s)}{B_{w_{ref}}(s)} \tag{5.175}$$

$$= C_{bw}(sI - A_{bw})^{-1} B_{B_{w_{ref}}}$$

where,

$$C_{bw} = \left[\left(\frac{Y_\beta}{m} - \frac{K_B Y_\beta Y_{\delta_R}}{m(m + K_B Y_{\delta_R})} \right) \quad \left(\frac{Y_P}{m} - \frac{K_B Y_P Y_{\delta_R}}{m(m + K_B Y_{\delta_R})} \right) ... \right. \tag{5.176}$$

$$\left. ... \quad \left(\frac{Y_R}{m} - \frac{Y_{\delta_R} K_r}{(m + K_B Y_{\delta_R})} - \frac{Y_{\delta_R} K_B Y_R}{m(m + K_B Y_{\delta_R})} \right) \quad 0 \quad \left(-\frac{K_i Y_{\delta_R}}{(m + K_B Y_{\delta_R})} \right) \right]$$

and,

$$B_{B_{w_{ref}}} = B_{bw} \begin{bmatrix} 0 & 1 \end{bmatrix}^T \tag{5.177}$$

5.3.1.4   Placing the Closed-loop Poles

This section discusses the selection of the closed-loop pole locations for both the stability augment-ation and the regulation component of the lateral specific acceleration controller. It is shown in Appendix B that the aforementioned constraints and conditions, necessary for successful lateral-directional decoupling, are easily satisfied by the practical test vehicle. To this end, it can be concluded that the decoupled, independent controller designs of Sections 5.3.1 and 5.3.2 are valid.

Placement of the closed-loop poles for stability augmentation involves selecting the damping ratio (ζ) and the natural frequency (ω_n) of the Dutch roll mode poles. A prudent closed-loop damping ratio of 0.85 was selected, since the outer regulation loop fails to encapsulate the full directional dynamics, and will consequently result in a loss of overall directional damping when implemented. The natural frequency was selected as 1.2 times the open-loop Dutch roll damping frequency to improve disturbance rejection characteristics. Given the following design require-ments,

$$\zeta_{cl} = 0.85 \tag{5.178}$$

$$\omega_{n_{cl}} = 1.2\omega_{n_{ol}} \tag{5.179}$$

$$= 4 \text{ rad/s}$$

the closed-form solution feedback gains can be calculated from Equations (5.152) and (5.153) to yield,

$$K_r = -0.3114 \tag{5.180}$$

$$K_B = -0.0608 \tag{5.181}$$

For the stability augmentation control law to be implemented, the constraints of Equations (5.146) and (5.147) must be satisfied. Investigating these gain constraints yields the following results:

$$\left| \frac{K_B}{K_r} \right| = 0.1953 \ll 124.9422 = \left| \frac{ml_F}{Y_R(l_D - l_F)} \right| \tag{5.182}$$

$$|K_r| = 0.3114 \ll 5.1546 = \left| \frac{m\bar{V}_T l_W}{Y_{\delta_R}(l_W - l_F)} \right| \tag{5.183}$$

and thus it is expected that the desired and actual closed-loop poles will be very similar. As mentioned in the preceding section, the upper frequency constraint of Equation (5.158) should be satisfied for the design of the outer regulation control law. Evaluating this frequency constraint yields,

$$\omega_n < 1.2983 \tag{5.184}$$

The desired closed-loop regulation pole is set to,

$$a = -0.7412 \text{ rad/s} \tag{5.185}$$

which is well within the frequency bound stated above. The closed-form solution integral feedback gain can then be calculated from Equation (5.162) as,

$$K_i = -0.2625 \tag{5.186}$$

It is also important to note that the Dutch roll mode poles that were placed during the stability augmentation are adequately (by a factor of 5) time scale separated from the dominant integrator pole associated with the regulation component of the LSA controller. Figures 5.18a and 5.18b illustrate the pole-zero map and step response of the LSA controller following the design conducted above.

(a) Pole-zero map
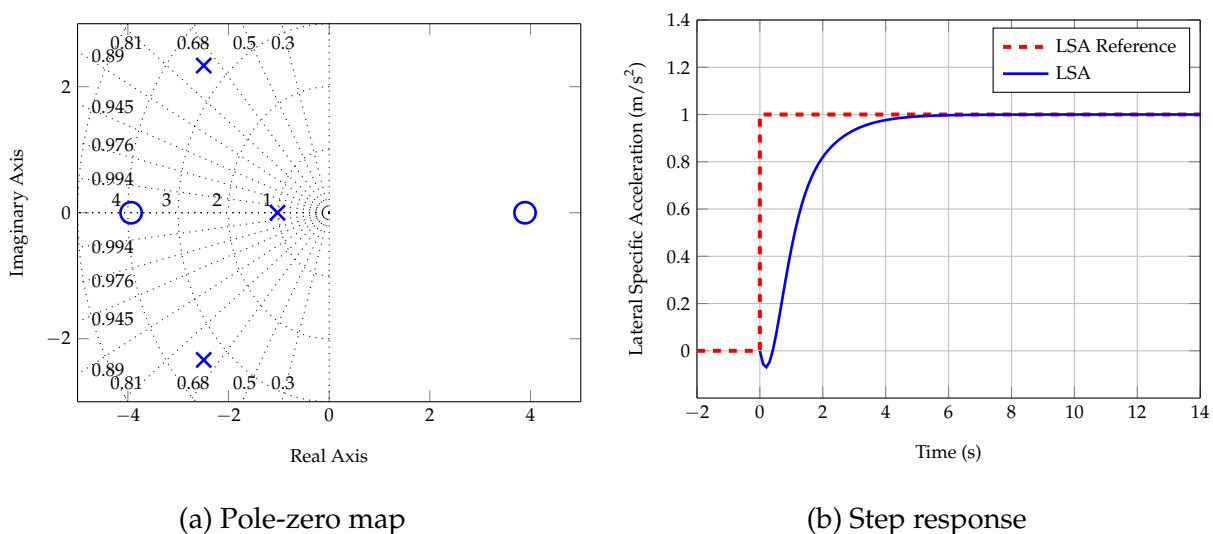
(b) Step response

Figure 5.18: Pole-zero map and step response of the LSA controller on reduced lateral dynamics

It is clear from Figure 5.18a that approximating the stability augmented directional dynamics by

its steady-state gain causes an error in the regulation pole placement algorithm. According to Peddle [1], this problem can be solved by deriving a far more mathematically complex control law that involves designing the stability augmentation and regulation control laws simultaneously. However, the current control law provides a simple decoupled design solution that can be fine-tuned to yield the desired results. To this end, the resulting closed-loop poles shown above are deemed acceptable, with a natural frequency of 3.42 rad/s and a damping ratio of 0.73, whilst the integrator pole remains within the frequency bound of Equation (5.158).

5.3.2 Roll Rate Controller

This section presents the design and verification of an inner-loop roll rate controller. With the requirements for successful lateral-directional decoupling already discussed in the preceding section, the design can proceed based on simplified, decoupled lateral dynamics. This high-bandwidth inner-loop controller makes use of the ailerons to regulate the aircraft's roll rate. A three-axis gyroscope included in the avionics stack on board the practical test vehicle provided roll rate measurements for the purpose of feedback control. It is apparent from Figure 5.1 that the input to the roll rate controller stems from the middle-loop roll angle controller designed in Section 5.3.3.

5.3.2.1 Design

A block diagram of the roll rate controller is shown in Figure 5.19.
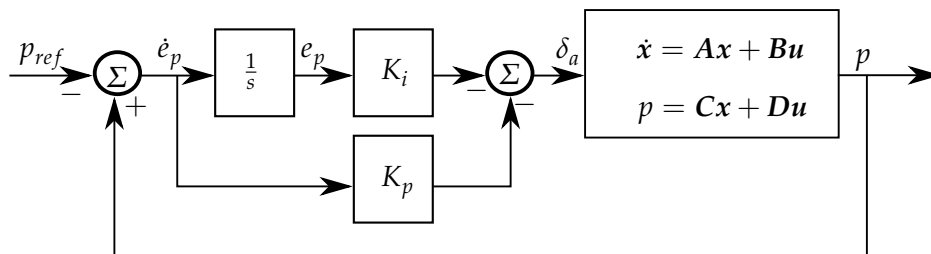
Figure 5.19: Roll rate controller block diagram

Assuming that the necessary conditions and constraints are met, the independent roll rate controller design can proceed based on the following reduced-order lateral dynamics:

$$\dot{p} = \left[\frac{L_P}{I_{xx}}\right] p + \left[\frac{L_{\delta_A}}{I_{xx}}\right] \delta_a \tag{5.187}$$

With reference to Figure 5.19, a PI control law is defined as,

$$\delta_a = -K_p \dot{e}_p - K_i e_p \tag{5.188}$$

with,

$$\dot{e}_p = p - p_{ref} \tag{5.189}$$

where p denotes roll rate and p_{ref} denotes the corresponding reference command. The integrator will reduce closed-loop sensitivity to parameter uncertainty and should mitigate steady-state errors resulting from unmodelled coupling effects. Augmenting the integrator state and substituting the roll rate control law yields,

$$
\begin{bmatrix} \dot{p} \\ \dot{e}_p \end{bmatrix} = \begin{bmatrix} \left(\frac{L_P}{I_{xx}} - \frac{K_p L_{\delta_A}}{I_{xx}} \right) & -\frac{K_i L_{\delta_A}}{I_{xx}} \\ 1 & 0 \end{bmatrix} \begin{bmatrix} p \\ e_p \end{bmatrix} + \begin{bmatrix} \frac{K_p L_{\delta_A}}{I_{xx}} \\ -1 \end{bmatrix} p_{ref}
\tag{5.190}
$$

Calculating the closed-loop characteristic equation gives,

$$
p(s) = s^2 + \left(\frac{K_p L_{\delta_A}}{I_{xx}} - \frac{L_P}{I_{xx}} \right) s + \frac{K_i L_{\delta_A}}{I_{xx}}
\tag{5.191}
$$

The following characteristic equation is defined to place the desired closed-loop poles:

$$
\alpha_c(s) = s^2 + \alpha_1 s + \alpha_0
\tag{5.192}
$$

The closed-form solution feedback gains can then be calculated by matching the coefficients of Equations (5.191) and (5.192) to yield,

$$
K_p = \frac{\alpha_1 I_{xx} + L_P}{L_{\delta_A}}
\tag{5.193}
$$

$$
K_i = \frac{\alpha_0 I_{xx}}{L_{\delta_A}}
\tag{5.194}
$$

where the design freedom is left to selecting the location of the closed-loop integrator pole and the roll mode pole.

5.3.2.2 Closed-loop System

The design conducted in the preceding section was based on simplified lateral dynamics and therefore fails to encapsulate the coupling effects associated with the full lateral aircraft dynamics. To improve the design fidelity of the remaining lateral controllers, the dynamics of Equation (5.171) are augmented with the roll rate control law defined above. Augmenting the integrator state of Equation (5.189) yields,

$$
\begin{bmatrix} \dot{x}_{bw} \\ \dot{e}_p \end{bmatrix} = \begin{bmatrix} A_{bw} & \mathbf{0}_{5 \times 1} \\ 0 \quad 1 \quad \mathbf{0}_{1 \times 4} \end{bmatrix} \begin{bmatrix} x_{bw} \\ e_p \end{bmatrix} + \begin{bmatrix} B_{bw} \\ \mathbf{0}_{1 \times 2} \end{bmatrix} u_{bw} + \begin{bmatrix} \mathbf{0}_{5 \times 1} \\ -1 \end{bmatrix} p_{ref}
\tag{5.195}
$$

Writing the augmented A matrix above in a more compact form as $A_{\dot{e}_p}$ and substituting the roll rate control law of Equation (5.188) yields,

$$
\begin{bmatrix} \dot{x}_{bw} \\ \dot{e}_p \end{bmatrix} = \begin{bmatrix} A_{\dot{e}_p} + \begin{bmatrix} B_{\delta_a} \\ 0 \end{bmatrix} \begin{bmatrix} 0 & -K_p & \mathbf{0}_{1 \times 3} & -K_i \end{bmatrix} \end{bmatrix} \begin{bmatrix} x_{bw} \\ e_p \end{bmatrix} + \begin{bmatrix} K_p B_{\delta_a} & B_{B_{w_{ref}}} \\ -1 & 0 \end{bmatrix} \begin{bmatrix} p_{ref} \\ B_{w_{ref}} \end{bmatrix}
\tag{5.196}
$$

where,

$$
B_{\delta_a} = B_{bw} \begin{bmatrix} 1 & 0 \end{bmatrix}^T ; \quad B_{B_{w_{ref}}} = B_{bw} \begin{bmatrix} 0 & 1 \end{bmatrix}^T
\tag{5.197}
$$

The closed-loop model of Equation (5.196) will be augmented further as more control laws are added to the system. It is therefore convenient to write it in a more compact form as,

$$\dot{x}_p = A_p x_p + B_p u_p \tag{5.198}$$

with,

$$p = C_p x_p \tag{5.199}$$

so that the closed-loop transfer function from roll rate reference to measured roll rate is given by,

$$G_{p_{cl}}(s) = \frac{p(s)}{p_{ref}(s)} \tag{5.200}$$

$$= C_p (sI - A_p)^{-1} B_{p_{ref}}$$

where,

$$C_p = \begin{bmatrix} 0 & 1 & \mathbf{0}_{1 \times 4} \end{bmatrix} ; \quad B_{p_{ref}} = B_p \begin{bmatrix} 1 & 0 \end{bmatrix}^T \tag{5.201}$$

5.3.2.3 Placing the Closed-loop Poles

This section will discuss the selection of the closed-loop pole locations for the roll rate controller. Placement of the closed-loop poles involves selecting the location of the integrator pole and the roll mode pole. The design approach was to keep the roll mode pole at the open-loop location in order to minimise control effort, and to place the dominant integrator pole slightly slower than the roll mode pole. Figure 5.20 illustrates the pole-zero map and step response of the roll rate controller when,

$$p_1 = \left| \frac{L_P}{I_{xx}} \right| \tag{5.202}$$

$$= 8.1398 \text{ rad/s}$$

$$p_2 = \left(\frac{3}{4} \right) p_1 \tag{5.203}$$

$$= 6.1048 \text{ rad/s}$$

which yields the following closed-form solution feedback gains:

$$K_p = -0.0644 \tag{5.204}$$

$$K_i = -0.5245 \tag{5.205}$$

It is clear from Figure 5.20b that the roll rate response is characteristic of a fast, overdamped first-order system.

(a) Pole-zero map
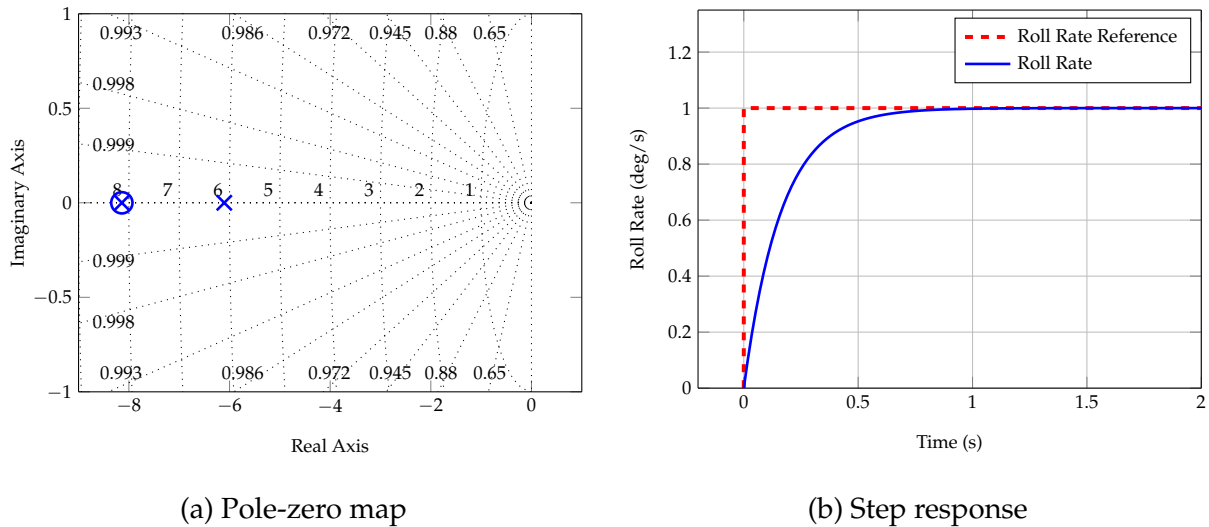
(b) Step response

Figure 5.20: Pole-zero map and step response of the roll rate controller on reduced lateral dynamics

5.3.3   Roll Angle Controller

This section presents the design and verification of a middle-loop roll angle controller. This controller is responsible for regulating the aircraft's roll/bank angle via the inner-loop roll rate controller. The controlled roll angle ϕ describes the rotation of the body reference frame with respect to the inertial frame. It is apparent from Figure 5.1 that the input to the roll angle controller stems from the guidance controller designed in Section 5.3.4. An EKF running the tilt/heading method is used to estimate the roll angle measurement on the practical test vehicle from on-board magnetometer and accelerometer readings.

5.3.3.1   Design

To maintain design fidelity in accordance with the preceding discussion on outer-loop controller design, the roll angle controller will be designed based on the full lateral model that encapsulates all corresponding inner-loop controller dynamics (LSA and roll rate) and inherent aircraft coupling effects. With reference to Figure 5.21, a proportional control law is defined as,

$$p_{ref} = -K_p e_\phi \tag{5.206}$$

with,

$$e_\phi = \phi - \phi_{ref} \tag{5.207}$$

where ϕ and ϕ_{ref} denote the roll angle measurement and corresponding reference command respectively. The transfer function from roll rate reference to roll angle is obtained from the state space model of Equation (5.196) through,

$$G_\phi(s) = \frac{\phi(s)}{p_{ref}(s)} \tag{5.208}$$

$$= C_\phi(s\boldsymbol{I} - \boldsymbol{A}_p)^{-1}\boldsymbol{B}_{p_{ref}}$$
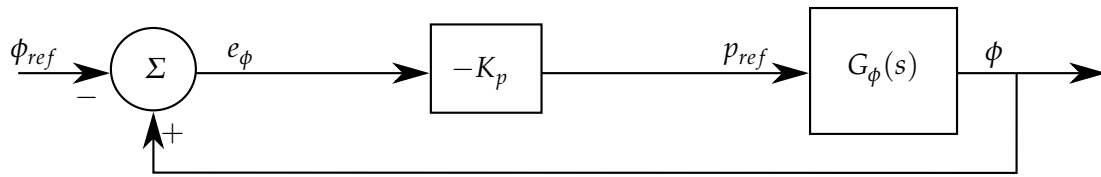
Figure 5.21: Roll angle controller block diagram

where,

$$C_\phi = \begin{bmatrix} \mathbf{0}_{1\times3} & 1 & \mathbf{0}_{1\times2} \end{bmatrix} \qquad (5.209)$$

The root locus of the roll angle controller with respect to the proportional gain K_p is shown in Figure 5.22a.

(a) Root locus (zoomed in)
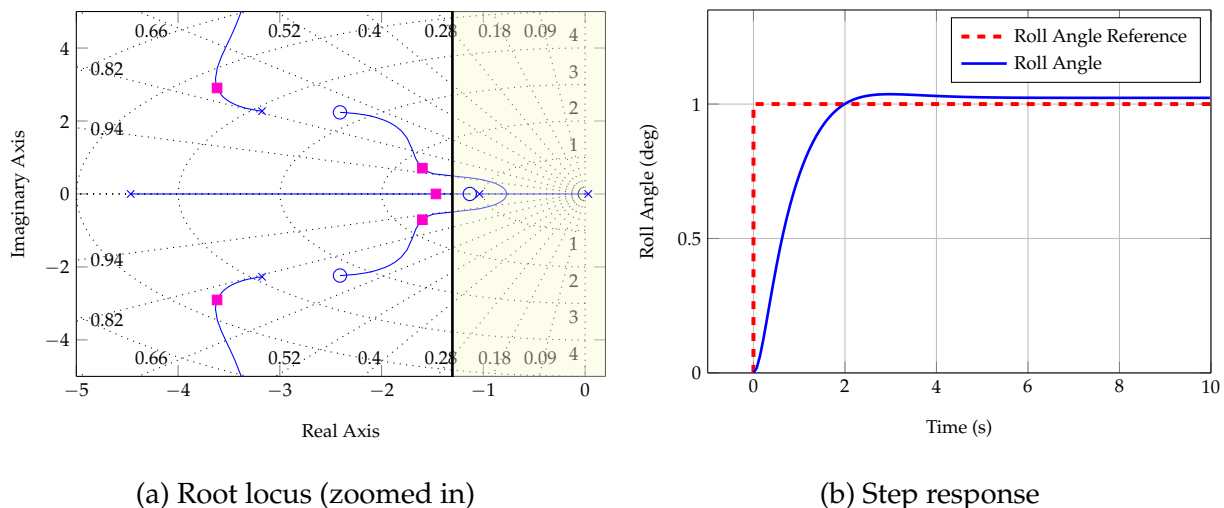
(b) Step response

Figure 5.22: Roll angle controller root locus and step response

The proportional gain was varied until the closed-loop poles were well damped and met the 2% settling time requirement of,

$$t_s < 3 \text{ s} \qquad (5.210)$$

so that a roll angle step would exhibit minimal overshoot with an acceptable speed of response. Figure 5.22b shows the roll angle step response when,

$$K_p = 1.3566 \qquad (5.211)$$

It is clear from the response that there is slightly more overshoot than expected. This can be attributed to the real zero that resides near the dominant real pole. The apparent steady-state error can be attributed to the proportional control law devoid of an integrator that would otherwise ensure perfect tracking of a step input. Although augmenting an integrator would ultimately improve steady-state tracking accuracy, it would also slow down the response and result in the

design of an inherently slower outer-loop controller. It was thus decided to keep a proportional control law for the middle loop, and fix any resulting cross-track errors by augmenting a limited integrator to the outer-loop guidance controller.

5.3.3.2 Closed-loop System

Substituting the roll angle control law into Equation (5.196) yields,

$$
\begin{bmatrix} \dot{x}_p \end{bmatrix} = \begin{bmatrix} A_p + \begin{bmatrix} B_{p_{ref}} \end{bmatrix} \begin{bmatrix} 0_{1\times3} & -K_p & 0_{1\times2} \end{bmatrix} \end{bmatrix} \begin{bmatrix} x_p \end{bmatrix} + \begin{bmatrix} K_p B_{p_{ref}} & B_{B_{w_{ref}}} \end{bmatrix} \begin{bmatrix} \phi_{ref} \\ B_{w_{ref}} \end{bmatrix} \tag{5.212}
$$

where,

$$
B_{p_{ref}} = B_p \begin{bmatrix} 1 & 0 \end{bmatrix}^T ; \quad B_{B_{w_{ref}}} = B_p \begin{bmatrix} 0 & 1 \end{bmatrix}^T \tag{5.213}
$$

The closed-loop model of Equation (5.212) will be augmented further as more control laws are added to the system. It is therefore convenient to write it in a more compact form as,

$$
\dot{x}_\phi = A_\phi x_\phi + B_\phi u_\phi \tag{5.214}
$$

with,

$$
\phi = C_\phi x_\phi \tag{5.215}
$$

so that the closed-loop transfer function from roll angle reference to measured roll angle is given by,

$$
G_{\phi_{cl}}(s) = \frac{\phi(s)}{\phi_{ref}(s)} \tag{5.216}
$$

$$
= C_\phi (sI - A_\phi)^{-1} B_{\phi_{ref}}
$$

where,

$$
C_\phi = \begin{bmatrix} 0_{1\times3} & 1 & 0_{1\times2} \end{bmatrix} ; \quad B_{\phi_{ref}} = B_\phi \begin{bmatrix} 1 & 0 \end{bmatrix}^T \tag{5.217}
$$

5.3.4 Guidance Controller

This section presents the design and verification of a guidance controller responsible for manoeuvring the aircraft between waypoints in the XY-plane of the inertial axis system. It can be seen from Figure 5.1 that the input to the guidance controller stems from the navigator, which calculates the cross-track error (y) between the current aircraft position and the intended waypoint track. The navigator is further discussed in Chapter 6. The guidance controller generates a roll angle command, proportional to the current cross-track error measurement, that the middle-loop roll angle controller should regulate via the inner-loop roll rate controller.

A saturation block ensures that commands do not exceed the physical roll angle limitations of the aircraft. It also ensures that the aircraft enters a constant bank for large cross-track commands. If the guidance controller is activated excessively far from the waypoint track, it will saturate and command a constant bank angle that results in aimless loitering as the aircraft tries to approach

the track. In order to address this issue, it is quite common to introduce two intermediate loops that govern inertially coordinated turn rate and heading so that a limit can be placed on the angle at which the aircraft approaches the waypoint track. Adding these controllers, however, will result in the design of an inherently slower guidance controller that might not be able to completely minimise cross-track errors by the time touchdown occurs. To this end, it was decided that these two intermediate controllers would be omitted under the assumption that the guidance controller is activated within a reasonable distance of the intended track. In order to improve steady-state tracking accuracy during constant circular turn manoeuvres, the expected bank angle was calculated using the angle of bank formula and fed-forward, as shown in Figure 5.23 - this concept is further discussed in Chapter 6. Inertially coordinated position and velocity measurements are obtained from a differential GPS mounted on board the practical test vehicle and propagated through an EKF to mitigate the adverse effects of GPS delay and to minimise sensor noise.

5.3.4.1   Design

To maintain design fidelity in accordance with the preceding discussion on outer-loop controller design, the guidance controller will be designed based on the augmented lateral model that encapsulates all corresponding inner-loop controller dynamics (LSA, roll rate, and roll angle) and inherent coupling effects. With reference to Figure 5.23, a Proportional Derivative (PD) control law is defined as,

$$\phi_{ref} = -K_p e_y - K_d \dot{y} \tag{5.218}$$

with,

$$e_y = y - y_{ref} \tag{5.219}$$

where y and y_{ref} denote the cross-track error and corresponding reference command respectively. It is important to note that the error signal is not explicitly differentiated for use in the control law; instead, the cross-track error rate ($\dot{y}$) is simply fed back to form a rate feedback loop, as seen in Figure 5.23.
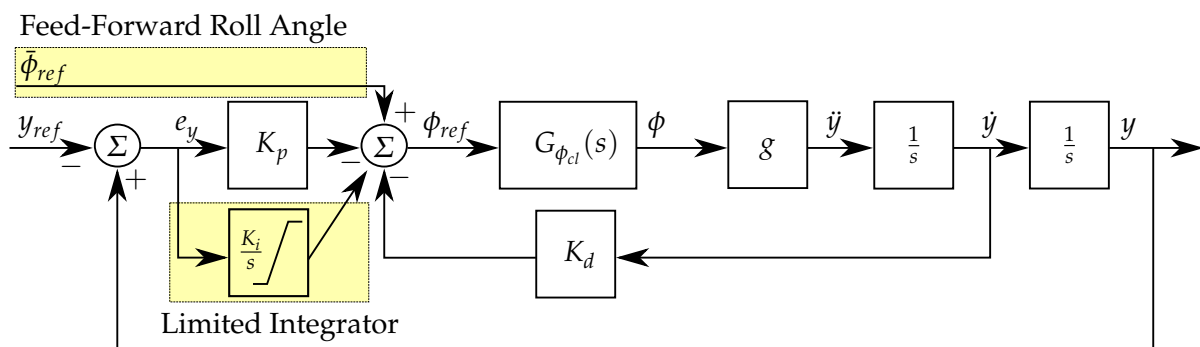
Figure 5.23: Guidance controller block diagram

It is first necessary to extract a lateral position and velocity state from the x_ϕ state vector before proceeding with the root locus design. Consider the diagram in Figure 5.24, where the aircraft is shown in a steady, constant altitude, banked turn.
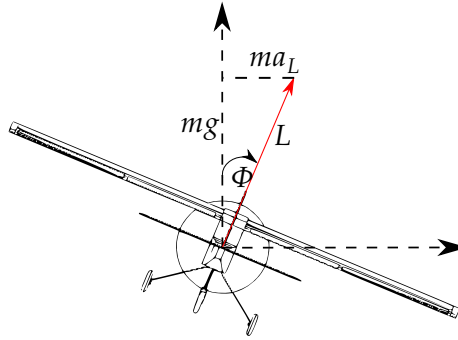
Figure 5.24: Aircraft in steady banked turn

The lift vector is responsible for countering the weight of the aircraft, and for providing the necessary centripetal acceleration during a turn manoeuvre. Lateral acceleration can therefore be written as,

$$a_L = g \tan \phi \tag{5.220}$$

For small bank angles, $\tan \phi \approx \phi$ and therefore Equation (5.220) can be simplified to,

$$\ddot{y} = g\phi \tag{5.221}$$

where $\ddot{y}$ denotes cross-track error acceleration. The transfer function from roll angle reference to cross track is obtained from the state space model of Equation (5.212) through,

$$G_y(s) = \frac{y(s)}{\phi_{ref}(s)} \tag{5.222}$$

$$= \left(\frac{g}{s^2}\right) C_\phi (sI - A_\phi)^{-1} B_{\phi_{ref}}$$

Figure 5.25a shows the root locus of the guidance controller with respect to the PD feedback gains K_p and K_d. For the sake of lateral landing accuracy, it is imperative that the guidance controller be fast enough to adequately minimise cross-track errors during the final approach before touchdown occurs. In light of the discussion on glideslope length and approach time in Section 5.2.4, the feedback gain values were adjusted until the closed-loop poles satisfied the following settling time requirement:

$$t_s < 15 \text{ s} \tag{5.223}$$

It is apparent from Figure 5.25a that the closed-loop damping ratio is given by,

$$\zeta_{cl} = 0.9 \tag{5.224}$$

which will ensure minimal overshoot in the outer-loop controller response. It should be noted that the nearby complex pole pair also satisfies the aforementioned settling time requirement and has a damping ratio of,

$$\zeta_{cl} = 0.76 \tag{5.225}$$

(a) Root locus (zoomed in)
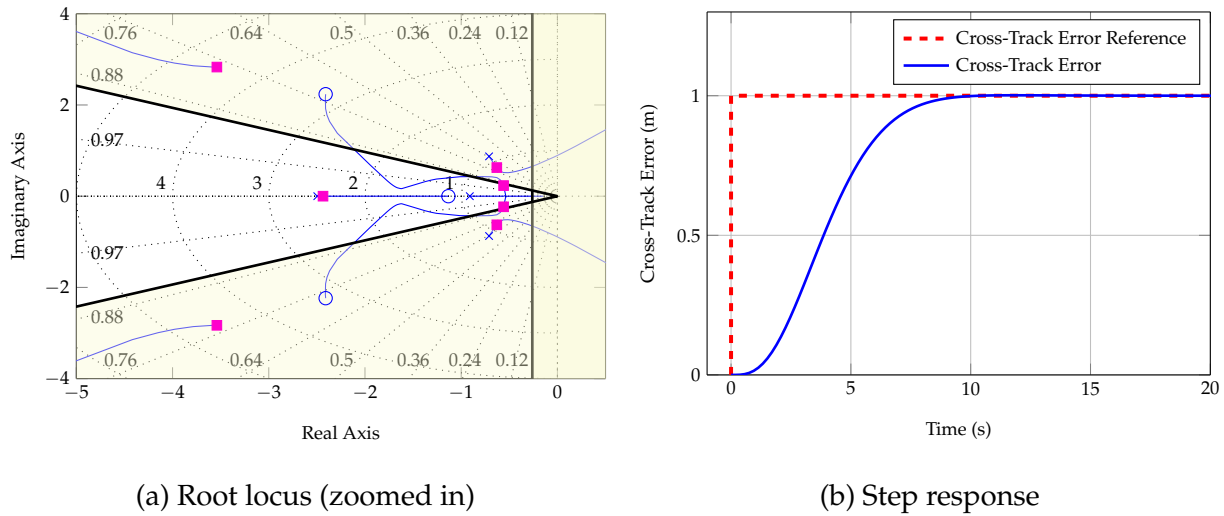
(b) Step response

Figure 5.25: Guidance controller root locus and step response

which is considered acceptable. Figure 5.25b shows the guidance controller step response when,

$$K_p = 0.015 \tag{5.226}$$

$$K_d = 0.061 \tag{5.227}$$

It is apparent that the response reaches its final value within 10 s (well within the time requirement), and exhibits minimal overshoot, in accordance with the required closed-loop damping ratio specified above.

It should be noted that a PD control law is not recommended for practical applications such as this. However, the root locus for a simple proportional controller resulted in unstable closed-loop poles for all gain values. This can be attributed to the double integrator associated with the dynamics from roll angle to cross-track error. A few adjustments were made to the guidance controller to improve performance on the practical test vehicle. Firstly, a limited integrator was added to the system to compensate for roll angle biases that would otherwise result in steady-state tracking errors. By limiting the integrator to an estimated value of the roll angle bias, the system was able to benefit from the steady-state advantages of integral control without the adverse transient effects. Secondly, the cross-track error rate was calculated using GPS ground speed measurements to avoid explicit differentiation of the cross-track error state, thereby reducing closed-loop sensitivity to noisy signals.

5.3.4.2   Closed-loop System

It is first necessary to augment the cross-track error and cross-track error rate to the x_ϕ state vector before the guidance control law can be augmented to the full lateral dynamics. Augmenting these additional states yields,

$$
\begin{bmatrix} \dot{x}_\phi \\ \ddot{y} \\ \dot{y} \end{bmatrix} =
\begin{bmatrix} & x_\phi & \\ \mathbf{0}_{1\times3} & g & \mathbf{0}_{1\times4} \\ \mathbf{0}_{1\times6} & 1 & 0 \end{bmatrix}
\begin{bmatrix} x_\phi \\ \dot{y} \\ y \end{bmatrix} +
\begin{bmatrix} B_\phi \\ \mathbf{0}_{1\times2} \\ \mathbf{0}_{1\times2} \end{bmatrix} u_\phi \tag{5.228}
$$

where Equation (5.221) has been used to indirectly extract lateral acceleration ($\ddot{y}$) from the x_ϕ state vector. Writing the augmented A matrix above in a more compact form as $A_{\dot{y}}$ and substituting the guidance control law of Equation (5.218) yields,

$$
\begin{bmatrix} \dot{x}_\phi \\ \ddot{y} \\ \dot{y} \end{bmatrix} = \left[A_{\dot{y}} + \begin{bmatrix} B_{\phi_{ref}} \\ 0 \\ 0 \end{bmatrix} \begin{bmatrix} 0_{1\times6} & -K_d & -K_p \end{bmatrix} \right] \begin{bmatrix} x_\phi \\ \dot{y} \\ y \end{bmatrix} + \begin{bmatrix} K_p B_{\phi_{ref}} & B_{B_{w_{ref}}} \\ 0 & 0 \\ 0 & 0 \end{bmatrix} \begin{bmatrix} y_{ref} \\ B_{w_{ref}} \end{bmatrix} \tag{5.229}
$$

where,

$$
B_{\phi_{ref}} = B_\phi \begin{bmatrix} 1 & 0 \end{bmatrix}^T ; \quad B_{B_{w_{ref}}} = B_\phi \begin{bmatrix} 0 & 1 \end{bmatrix} T \tag{5.230}
$$

It is convenient to write the dynamics of Equation (5.229) in a more compact form as,

$$
\dot{x}_y = A_y x_y + B_y u_y \tag{5.231}
$$

with,

$$
y = C_y x_y \tag{5.232}
$$

so that the closed-loop transfer function from cross-track error reference to cross-track error is given by,

$$
G_{y_{cl}}(s) = \frac{y(s)}{y_{ref}(s)} \tag{5.233}
$$

$$
= C_y(sI - A_y)^{-1} B_{y_{ref}}
$$

where,

$$
C_y = \begin{bmatrix} 0_{1\times7} & 1 \end{bmatrix} ; \quad B_{y_{ref}} = B_y \begin{bmatrix} 1 & 0 \end{bmatrix}^T \tag{5.234}
$$

5.3.5   Heading Controller

This section presents the design and verification of a heading controller responsible for executing both the de-crab and low-wing manoeuvres by aligning the aircraft's longitudinal axis with the runway during final approach. It can be seen from Figure 5.1 that the input to the heading controller stems from the state machine which governs the activation time of this controller based on the required crosswind landing technique. The heading controller generates a lateral specific acceleration command based on the current heading angle error, which the inner-loop LSA controller should regulate using the rudder. The proposed heading/LSA controller combination is not one typically used when controlling heading, yet the inclusion of the LSA controller proved invaluable as this allowed for a seamless integration of the inner-loop acceleration-based LSA, NSADLC, and roll rate controllers. An EKF running the tilt/heading method was used to estimate the heading angle measurement on the practical test vehicle from on-board magnetometer and accelerometer readings.

5.3.5.1 Design

The design strategy was to control heading indirectly through sideslip angle (β) by generating a lateral specific acceleration proportional to the heading angle error. Sideslip angle already forms part of the x_y state vector and it is therefore convenient to assume that,

$$\psi = \beta \tag{5.235}$$

which is valid for small perturbations about trim. An integrator was included in the control law to mitigate any errors resulting from this assumption, and the validity thereof is further investigated in Chapter 7.

To maintain design fidelity in accordance with the preceding discussion on outer-loop controller design, the heading controller is designed based on the full lateral model that encapsulates all corresponding inner-loop controller dynamics (LSA, roll rate, roll angle, and guidance) and inherent aircraft coupling effects. With reference to Figure 5.26, a PI control law is defined as,

$$B_{w_{ref}} = -K_p \dot{e}_\psi - K_i e_\psi \tag{5.236}$$

with,

$$\dot{e}_\psi = \psi - \psi_{ref} \tag{5.237}$$

where ψ and ψ_{ref} denote the heading measurement and corresponding reference command respectively.
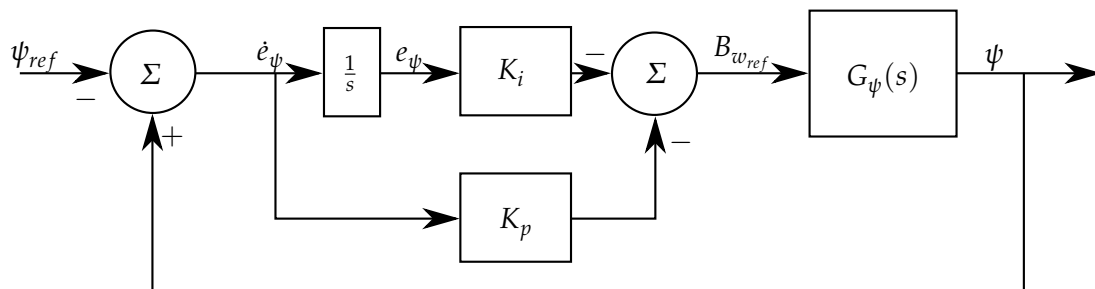
Figure 5.26: Heading controller block diagram

The transfer function from lateral specific acceleration reference to sideslip angle (and therefore heading angle) is obtained from the state space model of Equation (5.229) through,

$$G_\psi(s) = \frac{\psi(s)}{B_{w_{ref}}(s)} \tag{5.238}$$

$$= \frac{\beta(s)}{B_{w_{ref}}(s)}$$

$$= C_\beta(sI - A_y)^{-1} B_{B_{w_{ref}}}$$

where,

$$C_\beta = \begin{bmatrix} 1 & 0_{1\times 7} \end{bmatrix}; \quad B_{B_{w_{ref}}} = B_y \begin{bmatrix} 0 & 1 \end{bmatrix}^T \tag{5.239}$$

(a) Root locus (zoomed in)
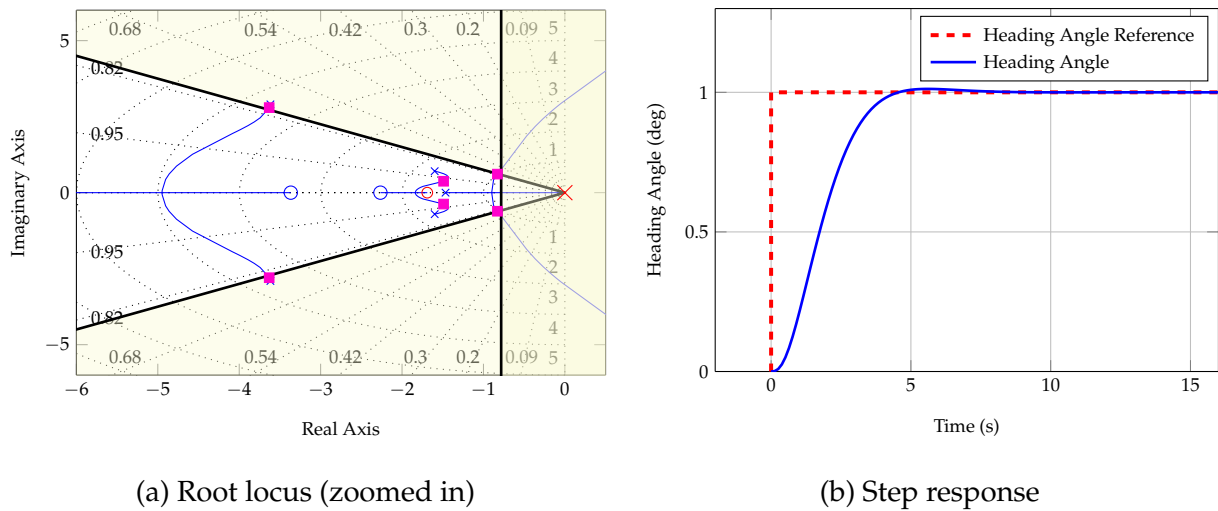
(b) Step response

Figure 5.27: Heading controller root locus and step response

Figure 5.27a shows the root locus of the heading controller with respect to the PI feedback gains K_p and K_i. The location of the heading controller zero was adjusted until the dominant branches of the root locus passed through closed-loop pole locations with the following specifications:

$$\zeta_{cl} = 0.8 \tag{5.240}$$

$$t_s < 5 \text{ s} \tag{5.241}$$

Figure 5.27 shows the heading controller step response when,

$$K_p = -0.8858 \tag{5.242}$$

$$K_i = -1.4971 \tag{5.243}$$

Placement of the closed-loop poles essentially involved a trade-off between minimal overshoot and a fast rise time to ensure that the FCS is able to safely and effectively de-crab the aircraft before touchdown, without exacerbating the very crab angle it tries to minimise. The response seen in Figure 5.27b was deemed acceptable, as it exhibits excellent transient response characteristics, and is able to track the reference input with zero steady-state error.

5.3.5.2   Closed-loop System

Augmenting the integrator state of Equation (5.237) under the assumption that $\psi = \beta$ yields,

$$\begin{bmatrix} \dot{x}_y \\ \dot{e}_\psi \end{bmatrix} = \begin{bmatrix} A_y & \mathbf{0}_{8\times1} \\ 1 & \mathbf{0}_{1\times8} \end{bmatrix} \begin{bmatrix} x_y \\ e_\psi \end{bmatrix} + \begin{bmatrix} B_y \\ \mathbf{0}_{1\times2} \end{bmatrix} u_y + \begin{bmatrix} \mathbf{0}_{8\times1} \\ -1 \end{bmatrix} \psi_{ref} \tag{5.244}$$

Writing the augmented A matrix above in a more compact form as $A_{\dot{e}_\psi}$ and substituting the heading control law of Equation (5.236) yields,

$$\begin{bmatrix} \dot{x}_y \\ \dot{e}_\psi \end{bmatrix} = \left(A_{\dot{e}_\psi} + \begin{bmatrix} B_{B_{w_{ref}}} \\ 0 \end{bmatrix} \begin{bmatrix} -K_p & \mathbf{0}_{1\times7} & K_i \end{bmatrix} \right) \begin{bmatrix} x_y \\ e_\psi \end{bmatrix} + \begin{bmatrix} B_{y_{ref}} & K_p B_{B_{w_{ref}}} \\ 0 & 1 \end{bmatrix} \begin{bmatrix} y_{ref} \\ \psi_{ref} \end{bmatrix} \tag{5.245}$$

where,

$$\boldsymbol{B}_{y_{ref}} = \boldsymbol{B}_y \begin{bmatrix} 1 & 0 \end{bmatrix}^T ; \ \ \boldsymbol{B}_{B_{w_{ref}}} = \boldsymbol{B}_y \begin{bmatrix} 0 & 1 \end{bmatrix}^T \tag{5.246}$$

It is convenient to write the dynamics of Equation (5.245) in a more compact form as,

$$\dot{\boldsymbol{x}}_\psi = \boldsymbol{A}_\psi \boldsymbol{x}_\psi + \boldsymbol{B}_\psi \boldsymbol{u}_\psi \tag{5.247}$$

with,

$$\psi = \boldsymbol{C}_\psi \boldsymbol{x}_\psi \tag{5.248}$$

so that the closed-loop transfer function from heading angle reference to measured heading angle is given by,

$$G_{\psi_{cl}}(s) = \frac{\psi(s)}{\psi_{ref}(s)} \tag{5.249}$$

$$= \boldsymbol{C}_\psi (s\boldsymbol{I} - \boldsymbol{A}_\psi)^{-1} \boldsymbol{B}_{\psi_{ref}}$$

where,

$$\boldsymbol{C}_\psi = \begin{bmatrix} 1 & \boldsymbol{0}_{1\times 8} \end{bmatrix} ; \ \ \boldsymbol{B}_{\psi_{ref}} = \boldsymbol{B}_\psi \begin{bmatrix} 0 & 1 \end{bmatrix}^T \tag{5.250}$$

5.4   Summary

The design of both the longitudinal and lateral flight controllers was presented in this chapter. A detailed design of the runway controllers has been included in Appendix D for further perusal. A successive loop closure technique was employed throughout the design process, beginning with stability augmentation provided by the inner loops, followed by attitude regulation from the middle loops and concluding with outer-loop trajectory control. The entire FCS was designed with landing accuracy in mind, which led to the development of a high-bandwidth, synergistic architecture capable of executing various crosswind landing techniques through effective controller sequencing. The control algorithms developed in this chapter require minimal processing power for implementation and are capable of regulating all motion variables desired for conventional flight. Gain scheduling is often used to enhance autopilot performance when operating over a wide range of velocities. The plots depicted in Appendix F show the effect of trim airspeed on controller performance when gain scheduling is not employed. It is apparent that the FCS performs adequately over the typical airspeed range, and it was therefore decided that the benefits of gain scheduling were not worth the added complexity in this case. However, if the autopilot system is extended to perform automatic take-offs, then gain scheduling is indeed recommended to maximise performance and ensure stability over the extended airspeed range. Now that the individual control loops have been developed and evaluated in a linear environment, the next chapter will focus on the development of navigation algorithms (for the navigator), and the design of a state machine responsible for high-level control of the autoland system.

CHAPTER 6

Navigation and Landing Strategies

This chapter is focused on the development of navigation and landing algorithms designed to maximise touchdown accuracy and ensure the safety of the aircraft. The first section deals with a definition of the guidance axis system and subsequent waypoint navigation techniques. Landing constraints are then investigated and consulted during the design considerations of the state machine discussed in the final section. Controller sequencing is discussed in Section 6.2.3, where the focus shifts towards the execution of the three landing techniques. The final section deals with the development of a state machine responsible for actively sequencing the controllers and monitoring important aircraft states.

6.1 Navigation

The guidance controller, discussed in Section 5.3.4, is responsible for guiding the aircraft along a particular flight path consisting of predefined waypoints. This controller is designed to minimise the cross-track distance between the aircraft's current position and the straight-line segments that connect the waypoints. The segment between two consecutive waypoints is known as the ground track, whilst the perpendicular distance from the ground track to the current aircraft position is known as the cross-track error. In summary, the purpose of the guidance controller is to guide the aircraft along the ground track by minimising the cross-track error to zero. Each waypoint is fully described by the following four parameters:

1. North position (m)

2. East position (m)

3. Altitude (m)

4. Airspeed (m/s)

Given the positional information of the source and destination waypoints, the heading and length of the ground track can be calculated from the diagram in Figure 6.1 using simple trigonometry. The track heading ψ_{track} (relative to north) is calculated with,

$$\tan \psi_{track} = \frac{E_{dst} - E_{src}}{N_{dst} - N_{src}} \tag{6.1}$$

and the track length L_{track} is calculated with,

$$L_{track} = \sqrt{(N_{dst} - N_{src})^2 + (E_{dst} - E_{src})^2} \tag{6.2}$$

The cross-track error y is shown in Figure 6.1 along with the in-track distance x, which is the distance of the aircraft's projection onto the track from the source waypoint. The navigation system continuously calculates the cross-track error and the in-track distance with every iteration of the control loop. An elegant way of calculating these is to define an auxiliary guidance axis system with the origin at the location of the source waypoint, as shown in Figure 6.1. The X_G-axis is parallel to the ground track, pointing in the direction of the destination waypoint; the Y_G-axis is perpendicular to the ground track; and the Z_G-axis coincides with the Z_E-axis of the inertial axis system. Essentially, the guidance axis system $F_G(O_G X_G Y_G Z_G)$ can be obtained by rotating the inertial axis system $F_E(O_E X_E Y_E Z_E)$ through the track heading angle ψ_{track} and shifting its origin to the location of the source waypoint.
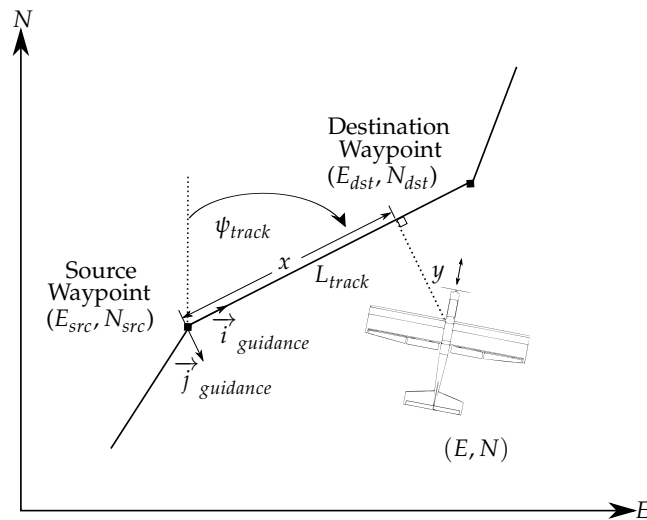
Figure 6.1: Guidance axis system

To obtain both the cross-track and in-track distances, the aircraft's position in the inertial frame is simply transformed to the guidance axis system with the following rotation through ψ_{track}:

$$\begin{bmatrix} x \\ y \end{bmatrix} = \begin{bmatrix} \cos \psi_{track} & \sin \psi_{track} \\ -\sin \psi_{track} & \cos \psi_{track} \end{bmatrix} \begin{bmatrix} N - N_{src} \\ E - E_{src} \end{bmatrix} \tag{6.3}$$

where N and E represent the north and east location of the aircraft in the inertial frame. It is then intuitive that the y-component is simply the cross-track error and the x-component is the in-track distance. To this end, an aircraft will fly directly over the ground track when its heading equals ψ_{track} and the observed cross-track error is zero.

A waypoint scheduler continually monitors the in-track distance and compares it with the L_{track} distance so that a new destination waypoint is loaded when the old one is reached. In the section on the design of the guidance controller, it was mentioned that the cross-track error rate is strategically obtained from inertial velocity measurements to avoid explicitly differentiating the cross-track error. With reference to Equation (6.3), cross-track error rate can be obtained from,

$$\dot{y} = -\dot{N}\sin\psi_{track} + \dot{E}\cos\psi_{track} \tag{6.4}$$

where $\dot{N}$ and $\dot{E}$ represent inertially coordinated north and east velocity measurements respectively.

The aforementioned navigation system works well for guiding the aircraft along straight-line segments, but is incapable of following circular trajectories in its current state. If the navigation algorithm could be extended to accurately navigate circular trajectories, like the one illustrated in Figure 6.2a, there would be a significant improvement in lateral landing accuracy, as the amount of overshoot that needs to be corrected during final approach would be minimised. A non-linear guidance method developed by Park et al. [11] proposes a way of flying perfectly smooth circular turns with minimal overshoot at the transition points.

The issue with this method, however, is that the designer is forced to accept any steady-state errors resulting from the non-linear tracking algorithm. The advantage of using a linear controller, like the one designed in this thesis, is that the designer is able to use linear control systems theory to mitigate steady-state errors by introducing an integrator into the system. An alternative would be to switch between the non-linear and linear navigation schemes when flying either circular or linear trajectories, in an attempt to exploit the advantages of each. For the sake of system predictability, it was later decided that it might not be a sensible idea to switch between linear and non-linear navigation schemes during autonomous flight. Ultimately, a more predictable and accurate navigator was developed, capable of executing smooth circular turns and performing straight-line navigation with zero error in the steady state. The focus now shifts towards the development of an accurate hybrid navigator.

(a) Circular turn   (b) Circular turn force balancing
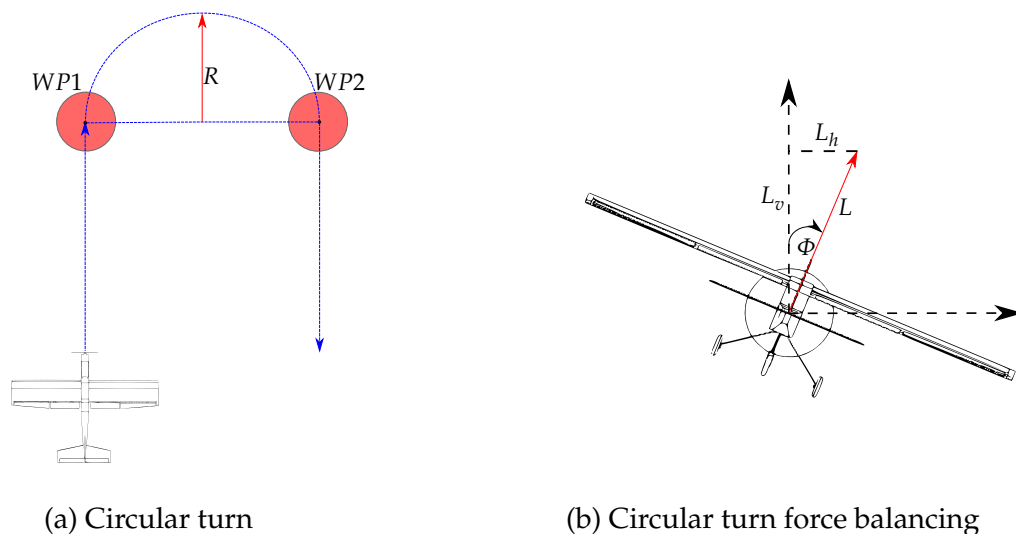
Figure 6.2: Circular turn development

Consider an aircraft flying straight and level approaching $WP1$, ultimately heading towards $WP2$, as shown in Figure 6.2a. In an ideal situation with no external disturbances, banking the aircraft at a predetermined angle Φ_t would cause it to enter into a constant turn rate and complete the circular turn with perfect accuracy. The bank angle required to complete a circular trajectory of radius R can be calculated by relating the individual lift components, depicted in Figure 6.2b, to centripetal and gravitational forces. With reference to Figure 6.2b, it is clear that,

$$\tan \Phi = \frac{L_h}{L_v} \tag{6.5}$$

Furthermore, centripetal force is given by,

$$C_f = m\frac{V^2}{R} \tag{6.6}$$

where m is the mass of the aircraft, V is its velocity, and R is the radius of the circular trajectory. Since the centripetal force acts in the lateral direction,

$$L_h = C_f \tag{6.7}$$

so that,

$$L_h = m\frac{V^2}{R} \tag{6.8}$$

The vertical component of lift should equal the gravitational force acting on the aircraft in order to maintain a constant altitude throughout the turn,

$$L_v = mg \tag{6.9}$$

where g is the gravitational acceleration constant. Substituting Equations (6.8) and (6.9) into (6.5) and solving for Φ yields,

$$\Phi = \arctan \frac{V^2}{gR} \tag{6.10}$$

which is known as the angle of bank formula. This formula is used to determine the amount of bank angle required to complete a circle of radius R with perfect accuracy in ideal situations. Realistically, however, disturbances would cause the aircraft to deviate from the circular trajectory if feedback control was not used to mitigate the effects. To this end, it can be concluded that this method of executing circular turns works perfectly in ideal situations, but is incapable of correcting cross-track errors resulting from inevitable external wind disturbances and sensor biases.

An alternative method would be to use the same guidance controller for both straight-line tracking and circular turn navigation by simply altering the cross-track error calculation algorithm. For the straight-line segments, Equation (6.3) would be used to calculate both the in-track distance and the cross-track error, as previously discussed. For a circular turn trajectory, Pythagoras's theorem would be used to calculate the cross-track error by obtaining the radial distance from the point of rotation to the current aircraft position, as shown in Figure 6.3. Each circular turn in the waypoint list is fully described by the following three parameters:

1. North position of circle centre (m)

    2. East position of circle centre (m)

    3. Turn radius (m)

With reference to Figure 6.3, it is simple enough to show that,

$$R_{pos} = \sqrt{(N - N_{cr})^2 + (E - E_{cr})^2} \tag{6.11}$$

$$C_{err} = R_{pos} - R \tag{6.12}$$

where N and E represent the aircraft's position in the inertial frame, N_{cr} and E_{cr} represent the circular turn centre coordinates, R represents the intended turn radius, and C_{err} represents the observed cross-track error.
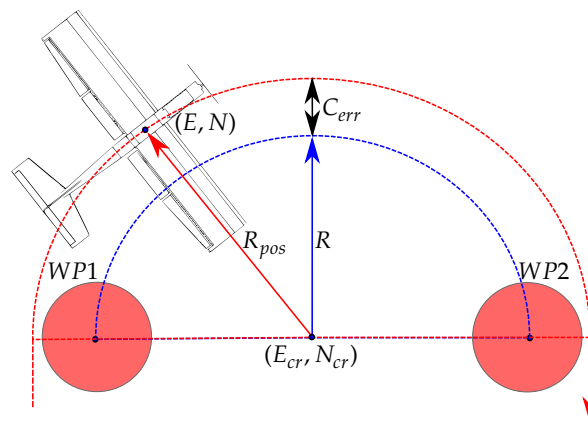
Figure 6.3: Circular turn cross-track calculation

    Calculating the cross-track error using Equations (6.11) and (6.12) enables the navigation system to follow an accelerating reference command, characteristic of a circular trajectory. It can be seen from the closed-loop transfer function of Equation (5.233) that the guidance controller is a type 2 system, and will therefore follow an accelerating reference with a constant, non-zero steady-state error. As mentioned in Section 5.3.4, the guidance controller is augmented with a limited integrator to compensate for inevitable roll angle biases resulting from IMU mounting offsets. However, this integrator is only able to compensate for roll angle biases that are less than $4°$, and is therefore incapable of completely minimising the additional steady-state error caused by an accelerating reference input. As a result, the aircraft will follow a circular trajectory with a constant steady-state offset.

    Up to this point, three methods of circular trajectory tracking have been discussed. The advantages and disadvantages associated with each technique are summarised in Table 6.1 for further perusal. Ultimately, the best performance was obtained when methods 2 and 3 were combined in such a way that the advantage of method 2 negates the disadvantage of method 3 and vice versa. This involved calculating the cross-track error using Equation (6.12), and minimising the steady-state error by feeding forward the expected bank angle obtained from Equation (6.10). The

Table 6.1: Advantages and disadvantages of various circular turn navigation methods

No.	Method	Advantage	Disadvantage
1	Non-linear guidance logic	Circular trajectory tracking with zero steady-state error	No integrator to compensate for sensor biases
2	Standard turn rate formula	Circular trajectory tracking with zero steady-state error	Incapable of minimising steady-state error if blown off course
3	Circular cross-track reference	Capable of correcting steady-state error if blown off course	Steady-state error when following a circular trajectory

feed-forward roll angle term minimises the steady-state error by reducing the amount of roll angle that the guidance controller integrator would ultimately have to provide. After the expected bank angle has been fed-forward, the guidance controller only needs to make small corrections from the new set point to compensate for external disturbances. This hybrid navigation technique exhibits strong disturbance rejection characteristics, and allows for circular trajectory tracking with zero error in the steady state. Figure 6.4 shows a comparison between method 3 and the hybrid technique.
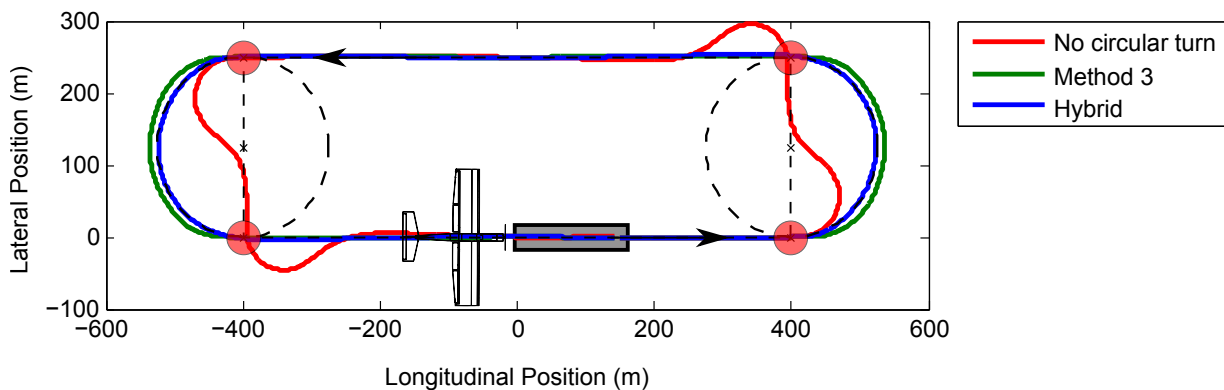
Figure 6.4: Circular turn method comparative trajectory plot. The trajectories depicted in this figure are obtained from the non-linear simulation environment discussed in Chapter 7.

It is clear from Figure 6.4 that executing circular turns is beneficial for cross-track error minimisation and significantly improves landing accuracy. The red trajectory shows a typical flight path when no circular turn method is executed - the large overshoot in cross-track error is the main reason that circular turn methods are investigated in such detail here. The green trajectory shows a typical flight path when using method 3 to navigate the circular turn. It is apparent that there is a finite, non-zero offset between the aircraft and the intended circular trajectory, denoted by the dashed lines. It is clear that the hybrid method, depicted by the blue trajectory, exhibits the best all-round performance, as it is able to compensate for external disturbances, and is capable of tracking both circular and linear trajectories with zero error in the steady state.

6.2   Crosswind Landing Techniques, Limitations and Constraints

Landing an aircraft in adverse weather conditions is not a trivial task, even for experienced pilots. The unpredictability of wind gusts and turbulence often complicates the landing procedure. Pilots make use of various landing techniques, each with their own advantages and disadvantages, that they employ during final approach to mitigate the associated risks. More specifically, for an aircraft to land in the presence of crosswind, two conditions must generally be met. Firstly, the flight path should be aligned with the runway to ensure lateral landing accuracy. Secondly, the longitudinal axis of the aircraft (heading) should be aligned with the direction of travel to minimise landing gear side-loads. Furthermore, the final approach needs to be altered somewhat to allow for a safe and successful landing in crosswind conditions. Two primary approach methods are typically employed by pilots when aligning the flight path with the runway, namely the crabbed approach and the sideslip or low-wing approach.

6.2.1   Approach Methods

An aircraft approaching the runway in a crabbed configuration relies on the use of thrust to counter the drag force induced by the incident flow, as seen in Figure 6.5. This is the most natural configuration for the aircraft, since there are no yawing moments or side forces due to sideslip that need to be countered with the rudder. Furthermore, the natural directional stability of the aircraft ensures that its longitudinal axis is aligned with the incident flow so that $\beta = 0$. To this end, it can be seen that the flight path points due north, in the direction of a fictitious runway, as it follows the terminal glideslope during a landing approach. From the rear view, it is clear that the aircraft is flying wings-level ($\Phi = 0$), and that the force of lift is coordinated vertically to cancel the force of gravity.
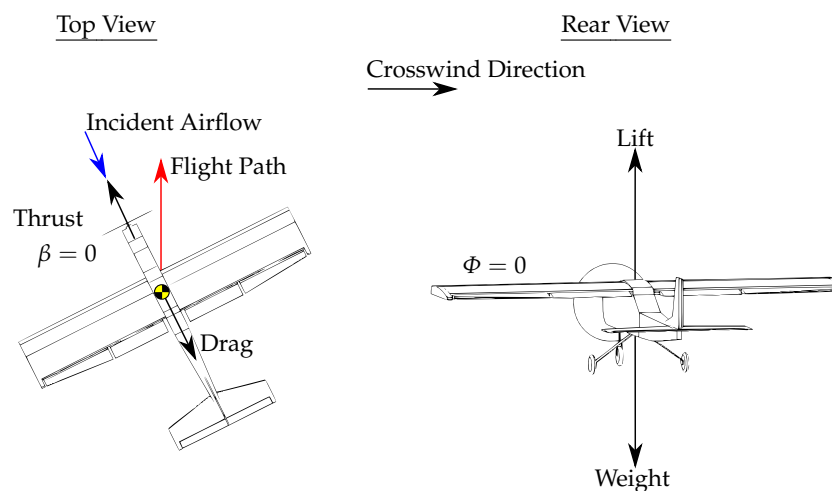
Figure 6.5: Force and moment diagram associated with the crabbed approach

An aircraft approaching the runway in a low-wing configuration aligns the flight path by banking in the direction of the crosswind, as seen in Figure 6.6. This results in the aircraft tracking the

glideslope with its heading aligned with the runway and a residual, non-zero bank angle to cancel the crosswind component, hence the name *low-wing* approach. It is clear from the figure that an aircraft flying in a slip (non-zero sideslip, $\beta \neq 0$) experiences additional forces and moments. The rudder produces a yawing moment to cancel the opposing yawing moment resulting from a non-zero sideslip angle β. However, the rudder side force is not sufficient to cancel the opposing side force due to sideslip, and it is therefore necessary to fly at a non-zero bank angle ($\Phi \neq 0$) to coordinate some of the gravitational force (weight) laterally in accordance with,

$$F_{B_{mg}} = mg \cos \Theta \sin \Phi \qquad (6.13)$$

where $F_{B_{mg}}$ is the lateral component of the gravitational force coordinated in the body axis, whilst m and g represent aircraft mass and gravitational acceleration respectively. The ailerons produce a rolling moment that counters the opposing dihedral rolling moment to keep the aircraft flying with the upwind wing low. Furthermore, it can be seen from Figure 6.6 that the component of drag along the longitudinal axis is mitigated with thrust. It can be concluded that the body axis forces and moments are in a state of equilibrium, resulting in the alignment of the flight path due north and in the direction of our fictitious runway.
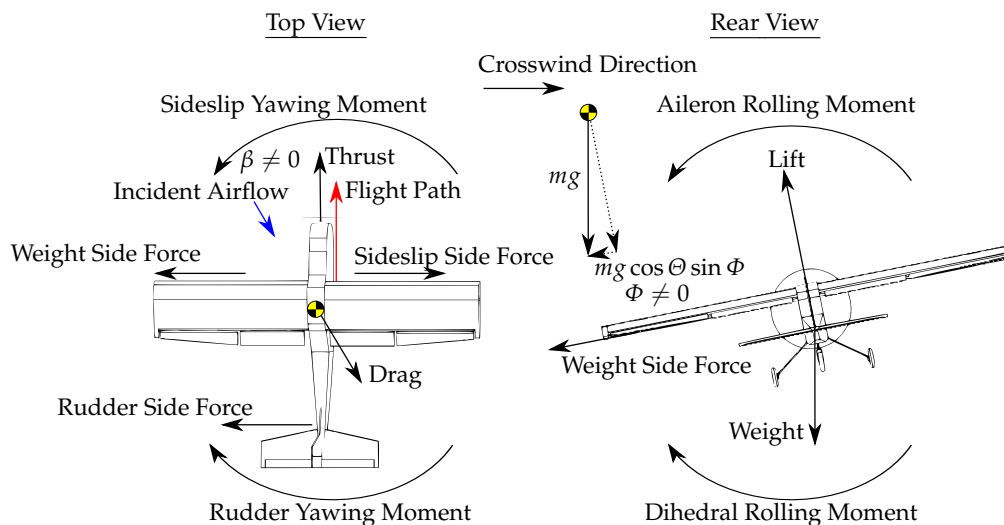
Figure 6.6: Force and moment diagram associated with the low-wing approach

6.2.2   Crosswind Limitations

Approaching the runway in a low-wing configuration demands significant actuator authority due to the inherent sideslip forces and moments that need to be countered. This places severe limitations on the maximum crosswind magnitude that a particular aircraft can handle. The main limiting factor is the amount of rudder authority available to generate an opposing yawing moment to keep the aircraft flying in a slip. The maximum allowable crosswind component for a low-wing approach can be approximated by comparing the aerodynamic coefficients that quantify yaw stiffness with the effectiveness of the rudder in creating an opposing yawing moment. The following

derivation is used to determine the crosswind limitations associated with a low-wing approach:

$$\epsilon = \left| \frac{C_{n_{\delta_R}}}{C_{n_\beta}} \right| \tag{6.14}$$

$$= 1.3079$$

Noting that the maximum allowable rudder deflection angle is limited to $12°$, and allowing a $4°$ buffer for gust alleviation so that $\delta_{R_{max}} = 8°$, the maximum AoSS (β_{max}) can be calculated as,

$$\beta_{max} = \epsilon \delta_{R_{max}} \tag{6.15}$$

$$= 10.4632°$$

Equation (3.16) can then be used to determine the maximum allowable $90°$ crosswind component as a function of airspeed for a low-wing approach,

$$V_{max} = \bar{V}_T \sin \beta_{max} \tag{6.16}$$

$$= 3.2689 \text{ m/s}$$

where $\bar{V}_T$ is the trim airspeed of 18 m/s. Ignoring the effects of turbulence and wind shear for comparative purposes, crosswind limitations for a crabbed approach are directly related to the amount of thrust available to keep the aircraft flying with a non-zero ground speed. With reference to Equation (6.17), it is apparent that $\bar{V}_T$ should be larger than V_{wind} so that $V_{ground} > 0$,

$$V_{ground} = \bar{V}_T + V_{wind} \tag{6.17}$$

where V_{ground} denotes ground speed and V_{wind} denotes wind speed coordinated in the inertial frame, with a headwind defined as negative. The amount of thrust required for a specific airspeed can be obtained using the Newton-Raphson method, described in Chapter 4. Noting that the maximum available thrust for this particular aircraft is limited to 40 N, and allowing 5 N for gust alleviation so that $T_{max} = 35$ N, the maximum attainable trim airspeed was calculated as $\bar{V}_{max} = 25.77$ m/s. This particular aircraft could theoretically fly at a trim airspeed of $\bar{V}_{max}$ to counter a wind of magnitude V_{wind} so that $V_{ground} > 0$. In reality, however, the effects of turbulence and wind shear would limit safe operation long before engine thrust became the limiting factor. Nevertheless, the limitations associated with a low-wing approach are still more restrictive than those associated with a crabbed approach.

6.2.3 Landing Techniques

It is clear from the preceding analysis that the crabbed approach is more effective in dealing with stronger crosswind magnitudes. The problem with this approach, however, is the amount of heading angle error between the aircraft and runway (crab angle), especially when landing in severe crosswind conditions. Landing with large crab angles imposes extreme side-loads on the landing gear, which significantly increases the chances of loss of directional control, and could result in structural damage to the airframe. Landing on dry runways with large crab angles will cause the aircraft to deviate violently from the touchdown point and usually results in a ground loop. It

is for this particular reason that large commercial aircraft (Boeing and Airbus) are not advised to touch down with crab angles larger than $5°$ [8]. Pilots will therefore make use of two specific techniques to align the aircraft's longitudinal axis with the runway before touchdown, and essentially minimise the crab angle to reduce side-loading and mitigate the risk of runway excursion events.

The de-crab landing technique, depicted in Figure 2.2a, involves flying most of the final approach in a crabbed configuration (Figure 6.5) before minimising the crab angle during the flare phase. If timed correctly, the aircraft will touch down with an acceptable crab angle and a slight roll angle due to the differential lift from the yaw rate perturbation. The low-wing landing technique, depicted in Figure 2.2b, involves flying the length of the glideslope in a sideslip configuration (Figure 6.6) with the aircraft's longitudinal axis aligned with the runway. Ideally, touchdown will occur with zero crab angle and with the upwind main wheel first. Establishing the sideslip early in the approach allows more time to determine the required control inputs and to minimise the crab angle. Using this method causes an increase in drag, and therefore requires pitch and power setting adjustment to maintain the appropriate airspeed and approach path.

It is indeed possible to make use of a combination of the three landing techniques to mitigate the disadvantage of one with the advantage of another. Consider an aircraft on final approach flying in the presence of a crosswind. Instead of completely minimising the crab angle at the start of the glideslope, Ψ_{crab} is reduced to a point where the rudder still has enough authority for effective gust alleviation.[1] The aircraft now approaches the runway in a quasi-crabbed, low-wing configuration, and is therefore able to handle stronger crosswind magnitudes whilst still operating within the bounds of linear control systems theory. If the heading angle error is still larger than $5°$ near the landing point, the remaining rudder authority can be used to de-crab the aircraft before touchdown occurs. The advantage of using this hybrid landing technique is twofold. Firstly, the heading controller will command smaller rudder deflections during the final approach, since there is less slip to maintain. This results in improved gust alleviation characteristics, as the FCS now has additional rudder authority at its disposal, and is able to use engine thrust to counter crosswind disturbances more effectively. Secondly, the de-crabbing manoeuvre only needs to minimise around $5°$ of the crab angle, which significantly decreases the risk of over-aggressive manoeuvres near the ground. This hybrid landing method can be used when crosswind limitations for a low-wing approach (shown in Equation (6.16)) are exceeded.

For each of the three landing techniques (crabbed, de-crab, and low-wing), it is imperative that the aircraft's roll angle be adequately maintained after touchdown. Consider an aircraft taxiing along the runway in crosswind conditions. The upwind wing will experience a greater lift force due to the increased angle of attack compared to the downwind wing. If this differential lift is left uncorrected, it is possible for the upwind wing to be raised high enough to cause the downwind wing to strike the ground.[2] It is also important that the final approach be flown at an acceptable landing airspeed V_{land} to avoid ballooning and Pilot-Induced-Oscillations (PIO) in the case of an RPV. In the case of an autoland system, large deviations from the trim airspeed will cause over-actuation (or under-actuation), and result in oscillatory behaviour if gain scheduling is not employed. To this end, it is apparent that the landing constraints imposed by various practical limitations should be investigated in order to minimise the risk of FCS failure and to ensure a safe

---

[1] A $4°$ buffer was chosen.

[2] Commonly referred to as wingstrike.

and successful crosswind landing.

6.2.4   Landing Constraints

An important state to monitor is the rate of descent (sink rate) that the aircraft experiences during a typical landing approach. The rate of descent, coordinated in the inertial frame, is calculated as follows:

$$\dot{D} = V_{ground} \sin \gamma \tag{6.18}$$

where $\dot{D}$, V_{ground}, and γ represent sink rate, ground speed, and glideslope angle coordinated in the inertial frame respectively. During a flare manoeuvre, the nose of the aircraft is raised, slowing the rate of descent, and allowing for a low-impact touchdown. Flaring during the final phase of landing, however, will cause the aircraft to float past the origin of the imaginary glideslope trajectory, resulting in degraded down-range landing accuracy. In order to maximise accuracy, it was decided that a flare would not be initiated even though this would result in increased strain on the airframe upon touchdown. A typical glideslope angle for a manned aircraft is $\gamma = 3°$, which equates to a sink rate of $\dot{D} = 0.837$ m/s in accordance with Equation (6.18) for a ground speed $V_{ground} = 16$ m/s. It was decided that a steeper glideslope angle of $\gamma = 4°$ would be adopted to minimise down-range landing inaccuracies resulting from glideslope tracking offsets. The steeper glideslope angle increases the sink rate from 0.84 m/s to 1.11 m/s and will therefore increase the force of impact upon touchdown. Considering these design decisions, it is important to determine if the airframe undercarriage is capable of handling the increased impact force. To this end, it is necessary to derive a simple formula that relates impact velocity to initial drop height. Consider an object released from an initial state of rest a distance h_0 above the ground. The object's vertical acceleration is given by,

$$\ddot{h} = g \tag{6.19}$$

Integrating once to obtain vertical velocity yields,

$$\dot{h} = \dot{h}_0 + gt \tag{6.20}$$

and integrating once more to obtain vertical distance travelled yields,

$$h = h_0 + \dot{h}_0 t + \frac{1}{2} g t^2 \tag{6.21}$$

The aim now is to derive a function that relates the height from which an object was dropped to its vertical impact velocity for the purpose of a more intuitive comparison. Since the object was released from a state of rest, the initial vertical velocity is zero ($\dot{h}_0 = 0$). Evaluating Equation (6.21) at the point of impact where $h = 0$, and rewriting so that h_0 is the subject of the formula yields,

$$h_0 = -\frac{1}{2} g t^2 \tag{6.22}$$

Rewriting Equation (6.20) so that t is the subject of the formula, noting that $\dot{h}_0 = 0$, and substituting into Equation (6.22) yields,

$$h_0 = \frac{\dot{h}^2}{2g} \tag{6.23}$$

which can be used to determine the approximate height from which an object was dropped, given its impact velocity. Based on this derivation, a sink rate of 1.11 m/s is comparable to dropping the aircraft from a height of 6.35 cm, which is considered acceptable for the aluminium landing gear on the test vehicle. In the same way that the glideslope angle (γ) is constrained by physical aircraft limitations, the glideslope length (d_g depicted in Figure 6.9) is constrained by certain practical limitations. Perhaps the most significant limitation regarding approach distance is the fact that the aircraft is required to remain within Visual Line Of Sight (VLOS). This ensures that the safety pilot is able to assume total control at any point and bring the aircraft back to a stable flight condition. Keeping the aircraft in VLOS will also ensure that all RF communication links remain solid and unhindered by occlusions. In light of this, it was decided that the maximum allowable distance would be limited to 500 m, which resulted in a glideslope distance $d_g = 250$ m so that the initial 250 m could be used to settle the inherent cross-track error before commencing the descent.

In Section 6.2.3, a phenomenon known as wingstrike was discussed, which is a result of landing with excessive bank angles. Similarly, excessive pitch angles (during overaggressive flares, for example) could result in *tailstrike*, and ultimately cause the nose wheel to violently impact the ground following a counter-rotation. With reference to Figure 6.7, the maximum pitch and roll angles upon touchdown can be calculated as follows:

$$\Theta_{max} = \arctan\left(\frac{h_t}{l_t}\right) \tag{6.24}$$

$$\Phi_{max} = \arctan\left(\frac{h_w}{l_w}\right) \tag{6.25}$$

where h_t, l_t, h_w, and l_w represent the effective lengths from the pivot point (main landing gear) to the tail and wingtip respectively.
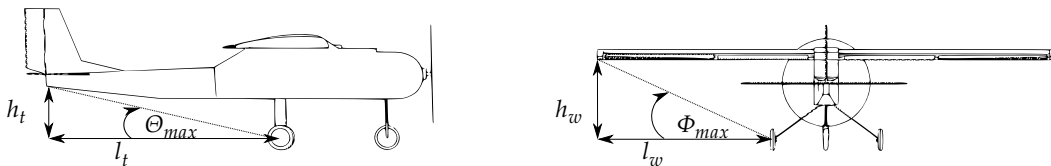
Figure 6.7: Maximum bank and pitch angle visualisation

In order to maximise landing accuracy, additional landing constraints were imposed on the amount of acceptable cross-track (lateral) and in-track (longitudinal) deviations observed during final approach. In order to land within a 1.5 m radius circle (primary objective), the maximum allowable cross-track error is simply constrained to $y < 1.5$ m, whilst the in-track error is highly dependent on glideslope tracking accuracy and the corresponding glideslope angle γ. Achieving the specified longitudinal landing accuracy requires that the maximum altitude deviation from the glideslope reference trajectory be constrained to,

$$h_{err} < 1.5\tan\gamma \tag{6.26}$$

$$< 10.5 \text{ cm}$$

Table 6.2 provides a summary of the landing constraints discussed in this section. It is intuitive that the corresponding variables should be closely monitored by the FCS during an autoland approach to ensure a safe and accurate landing. If at any point during the final approach one or more of the constraints are violated, the FCS should automatically abort the landing and execute a go-around. This sort of continuous hierarchical monitoring and decision-making is best implemented by a state machine.

Table 6.2: Landing constraints

Description	Symbolic Constraint	Units
Airspeed	$15 < V_{land} < 18$	m/s
Sink Rate	$\dot{D} < 1.5$	m/s
Crab Angle	$\Psi_{crab} < 5$	deg
Pitch Angle	$\Theta_{max} < 9$	deg
Roll Angle	$\Phi_{max} < 23$	deg
Cross-track Error	$y < 1.5$	m
Altitude Error	$h_{err} < 10.5$	cm

6.3   State Machine

This section details the design of a state machine responsible for risk mitigation through continuous hierarchical monitoring and effective controller sequencing. The state machine is comprised of six states that represent the various FCS modes of operation, shown in Figure 6.8. The FCS is initialised in the *RC Pilot* state, where the safety pilot has total control over the aircraft. A two-way switch on the safety pilot's remote initiates a transition to the *Waypoint Navigation* state, where the aircraft is fully controlled by the FCS as it autonomously navigates a predefined circuit. When a landing flag is activated from the ground station (discussed in Chapter 8), the FCS will enter the *Final Approach* state before commencing the final descent. The state machine ensures that the altitude error h_{err} is within bounds before transitioning to the *Glideslope Tracking* state, where the aircraft starts to track the terminal glideslope. The *Pre-landing* state can be thought of as the last line of defence for the autoland system, and it is therefore imperative that all safety criteria be well within specification before committing to the landing. As can be seen from Figure 6.8, the state machine will only transition to this state when the altitude error, cross-track error, sink rate, and airspeed denoted by h_{err}, y, $\dot{D}$, and $\bar{V}$ respectively are all within their individual bounds. Note that the constraints have been made more stringent than those shown in Table 6.2. If any of these variables are outside of the predefined bounds, the FCS will automatically abort the landing and return to the waypoint navigation state. Furthermore, the ground station operator is able to set a pseudo-landing flag, which forces the FCS to abort the landing procedure regardless of whether the necessary criteria has been satisfied or not. When the landing gear makes contact with the runway surface, an acceleration spike $\ddot{D}$ in the Z_B-axis larger than 20 m/s^2 will trigger a transition to the *Landed* state and activate the runway controllers as necessary. This transition will only occur

if the altitude measurement h is less than 0.5 m to prevent premature runway controller activation. In addition to activating the runway controllers after touchdown, the state machine is also responsible for:

1. Setting the throttle command to zero

2. Disabling the longitudinal flight controllers and setting the elevator to a predetermined offset

3. Disabling the roll rate controller integrator to prevent inevitable wind-up

4. Disabling the in-flight guidance controller and setting the roll angle command to zero. This is to prevent crosswind gusts from lifting the upwind wing and causing wingstrike

5. Disabling the LSA controller and changing the source of the rudder command to be driven by the runway controllers for improved ground control efficiency

Ideally the safety pilot will only need to toggle the RC_{switch} and transition to the *RC Pilot* state once the aircraft has come to a complete stop on the runway.
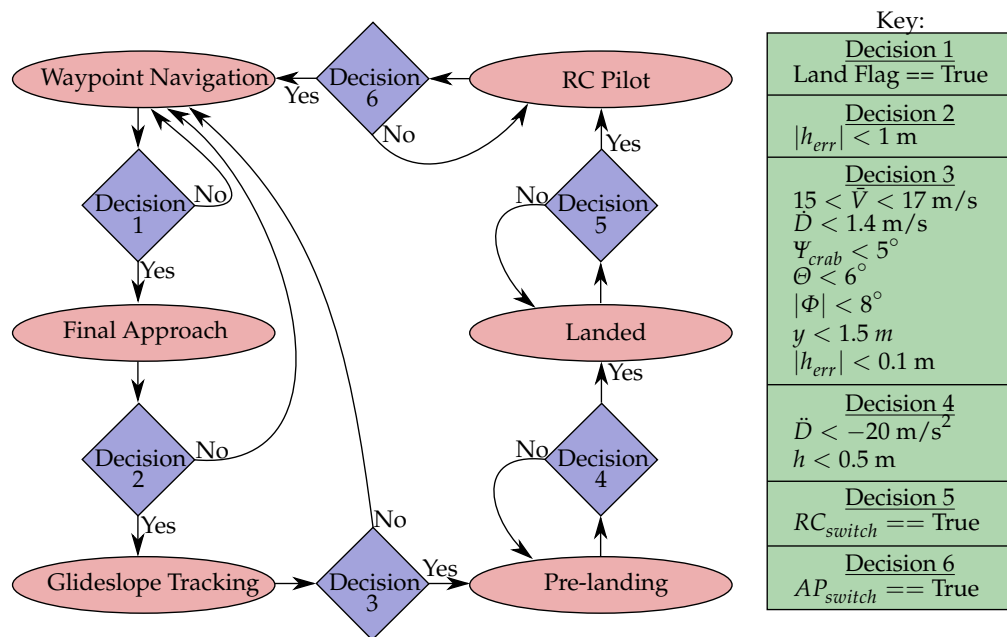
Figure 6.8: Landing state machine architecture.

It is important to note that the heading controller is responsible for executing both the de-crab and low-wing landing techniques. The difference between these two techniques lies primarily in the activation time of this particular controller. In addition to ensuring aircraft safety during landing, the state machine is also responsible for effectively sequencing the heading controller to execute each of the three crosswind landing techniques, as shown in Figure 6.9. The crabbed landing technique involves touching down in a crabbed configuration (non-zero crab angle), and therefore the heading controller is not activated at any stage of the descent. It can be seen from Figure 6.9 that the heading controller is activated towards the end of State 3 (*Pre-landing*) when executing the de-crab manoeuvre. The height h_d at which the de-crab manoeuvre should be executed is

calculated dynamically using the heading controller time constant and the average ground speed measured during State 2. Consider an aircraft tracking the glideslope with a ground speed of V_{ground} and a heading controller time constant τ_h. It is then intuitive that the heading controller should be activated at least a distance,

$$d_d = V_{ground}\tau_h \tag{6.27}$$

from the touchdown point to ensure enough time for effective crab angle minimisation. It can also be seen from Figure 6.9 that when executing a low-wing landing, the heading controller is activated at the beginning of State 2 (*Glideslope Tracking*), a distance d_g from the intended touchdown point. This ensures that the aircraft tracks the terminal glideslope with its heading aligned with the runway and a residual bank angle to counter the crosswind forces. Furthermore, it is clear from the figure that a transition to State 3 occurs at a distance d_t from the intended touchdown point. Since State 3 is the last abort state, it is imperative that the abort altitude h_t be large enough to allow for a safe change in trajectory if the landing is indeed aborted.
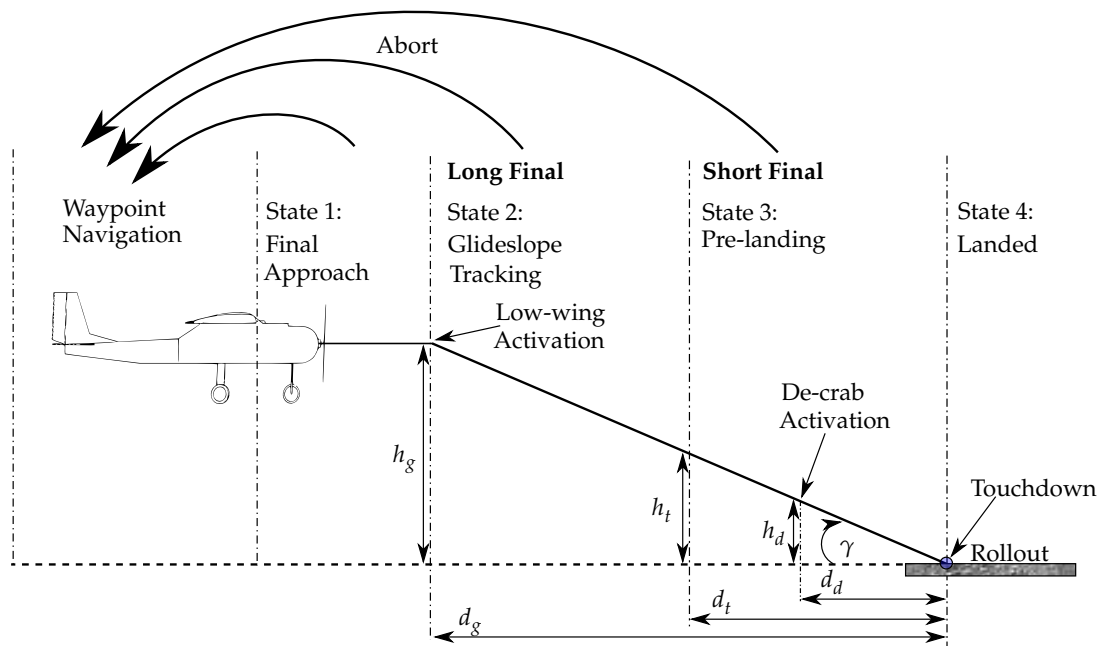
Figure 6.9: Illustration of the state transitions and controller activation intervals. Table 6.3 provides the typical numeric values associated with this figure.

6.4 Summary

In this chapter, the navigation system responsible for generating the cross-track error signal required by the guidance controller was developed. The conventional navigation algorithm was extended to include circular turn tracking capabilities, where the focus was to improve lateral landing accuracy by minimising the apparent cross-track error when traversing the base leg turn during a typical landing approach. This was then followed by an investigation into three crosswind landing techniques and an evaluation of their associated constraints. The requirement for

effective controller sequencing led to the development of a state machine responsible for driving the autoland system, and for ensuring the aircraft's safety through continuous hierarchical monitoring. This chapter marks the end of the theoretical development of the autopilot system, and the focus now shifts towards the evaluation thereof through non-linear simulation and practical flight testing.

Table 6.3: Typical landing parameters used for practical autopilot verification

Symbol	Numeric Value	Units
h_g	17.5	m
h_t	5	m
h_d	Dependent on V_{ground}	m
d_g	250	m
d_t	71.50	m
d_d	Dependent on V_{ground}	m
γ	4	deg

CHAPTER 7

Non-linear Simulations

In this chapter, the development of a simulation environment used for both software-in-the-loop (SIL) and hardware-in-the-loop (HIL) simulations is discussed. An overview of the environment architecture is first defined before a detailed analysis of the design is conducted for each of the constituent components. This chapter will cover the implementation of a non-linear aircraft model, the actuator and sensor models, wind models, a ground effect model as well as the non-linear ground model necessary for evaluating runway controller performance. Simulation results will be compared to the design requirements of Chapter 5 in order to evaluate controller performance and system fidelity on the non-linear aircraft model.

7.1   Simulation Environment

In order to evaluate system performance in its ability to land the aircraft accurately under adverse weather conditions, a high-fidelity MATLAB/Simulink simulation environment was developed. The control and navigation algorithms developed up to this point first needed to be verified through non-linear simulations if success is to be achieved in a minimum number of flight tests. The control algorithms in particular were designed based on linearised aircraft dynamics, and it was therefore imperative that these algorithms be thoroughly simulated in a non-linear environment that better describes the various non-linearities associated with flight mechanics. Figure 7.1 shows the simulation environment used for both SIL and HIL non-linear simulations.

7.1.1   Aircraft Model

The non-linear aircraft model is comprised of four components that contribute to the total forces and moments acting on the aircraft. The most complex of these components is the aerodynamic model, which essentially describes the aircraft's ability to overcome gravity and drag, allowing it to manoeuvre through the air as desired. A mathematical development of the full non-linear aerodynamic model was discussed in Section 3.4.2, where special mention of the aerodynamic stability
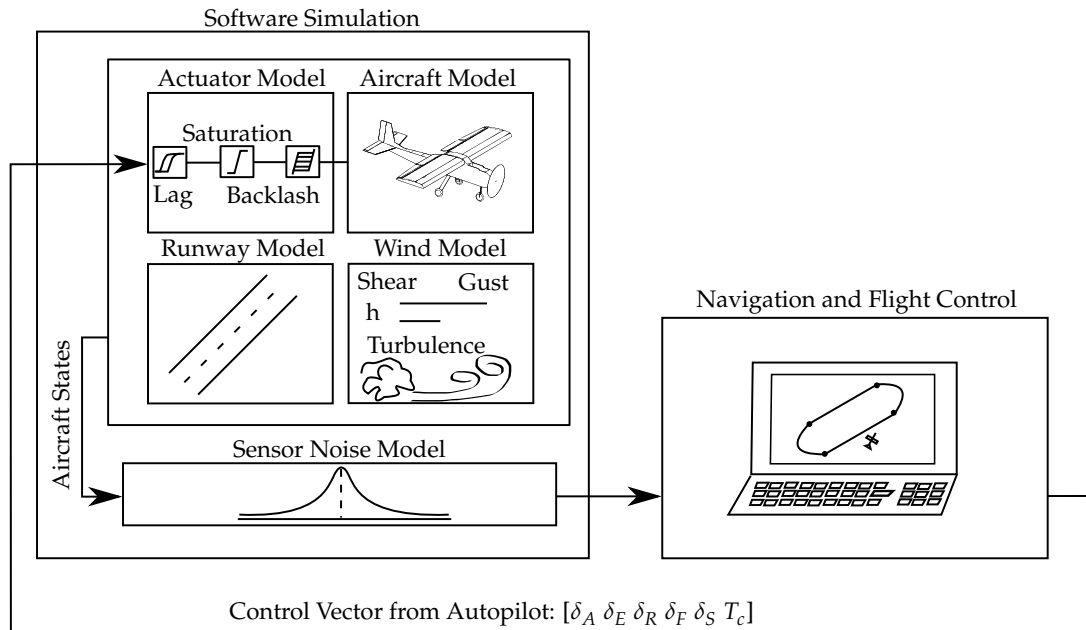
Figure 7.1: High-fidelity simulation environment

and control coefficients was made. These coefficients were obtained using AVL and incorporated into a Simulink block diagram describing the non-linear aerodynamic contributions as a function of the current aircraft state.

Some additions were made to the aerodynamic model to better represent real-world phenomena, and to develop a more complete environment for high-fidelity simulations. The most influential of these additions was a ground effect model that was added to the aerodynamic forces and moments block. In order to explain the ground effect phenomenon, it is first necessary to describe the formation of wingtip vortices that are apparent when a wing produces lift as it flies through the air. Lift is generated by creating a region of high pressure below the wing root and a region of low pressure above. A cambered wing exaggerates this effect by increasing the distance that air has to travel above the wing and decreasing the distance below. Since the air above the wing is at a lower pressure, the high-pressure air from below curls around at the wingtip in a vortex-like fashion, causing the lower-pressure air above to partially separate from the wing. Wingtip vortices are associated with lift-induced drag and the imparting of downwash, and are a fundamental consequence of three-dimensional lift generation [42].

When an aircraft in flight comes within several feet of the earth's surface, ground or water, a change occurs in the three-dimensional flow pattern around the wing [43]. The earth's surface has the effect of reducing the wing's upwash and downwash, and the formation of wingtip vortices by preventing them from curling around at the wingtips. Figure 7.2 illustrates the distortion of these aerodynamic phenomena when the aircraft is near the ground and is said to be *in ground effect*. The reduction of wingtip vortices due to ground effect alters the spanwise lift distribution and reduces the induced drag and induced AoA [43]. A wing that is influenced by ground effect will therefore require a lower AoA to produce the same amount of lift. It is then intuitive that if the AoA is maintained, the wing will produce more lift than it would have in the absence of ground effect. To incorporate this effect into the aerodynamic model, a simple multiplier was introduced

(a) Out of ground effect   (b) In ground effect
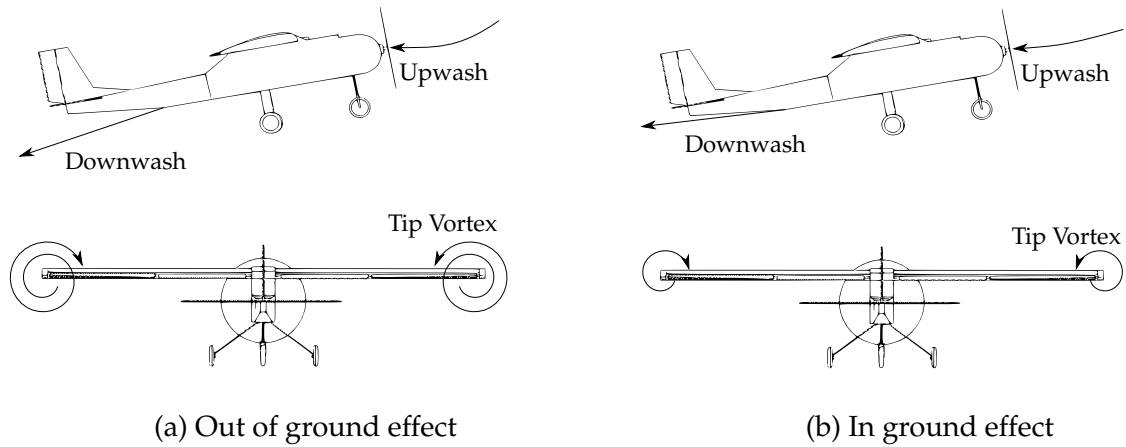
Figure 7.2: Effect of the earth's surface on aerodynamic phenomena

into the calculation of the C_L and C_D coefficients. When the aircraft is in ground effect, the lift and drag coefficients become,

$$C_L = G_L(h)C_L \tag{7.1}$$

$$C_D = C_{D_0} + G_D(h)\left(\frac{C_L^2}{\pi Ae}\right) \tag{7.2}$$

where $G_L(h)$ and $G_D(h)$ represent gains that vary with altitude and are given by Hull [44] as,

$$G_L(h) = 1.0 + (0.00211 - 0.0003(A - 3.0))e^{5.2(1-h/b)} \tag{7.3}$$

$$G_D(h) = 1.111 + 5.55\left(\frac{h}{b}\right) - \sqrt{29.8\left(\frac{h}{b} + 0.02\right)^2 + 0.817} \tag{7.4}$$

where h is the aircraft's altitude Above Ground Level (AGL), A is the aspect ratio of the wing, and b is the wing span. It should be noted that the equation for $G_D(h)$ is valid for $h < 0.9b$, otherwise, $G_D(h) = 1$. Figure 7.3 shows the variation in G_L and G_D as a function of the h/b ratio. It is apparent that there is a simultaneous increase in lift and reduction in drag when the aircraft is in ground effect ($h/b < 1$). It is also apparent that both $G_L(h)$ and $G_D(h)$ tend towards unity when out of ground effect ($h/b > 1$). This is an important real-world phenomenon to model, especially in this thesis, since it has a significant effect on landing accuracy. The aircraft will tend to "float" whilst in ground effect, and possibly overshoot the intended landing position if the controllers are not responsive enough to minimise the effects before touchdown.

The gravitational model, discussed in Section 3.4.3, was also implemented as a Simulink block diagram to model its contribution to flight dynamics. A uniform gravitational field, acting at the aircraft's centre of mass, was assumed - this assumption results in only a single force acting in the Z_E-axis with no moments produced by gravity. The thrust model, discussed in Section 3.4.4, was modelled as a simple first-order delay and produces only a single force along the X_B-axis passing directly through the centre of mass. All torques produced by aerodynamic phenomena and gyroscopic effects have been ignored, and thus no moments are generated by the thrust model.
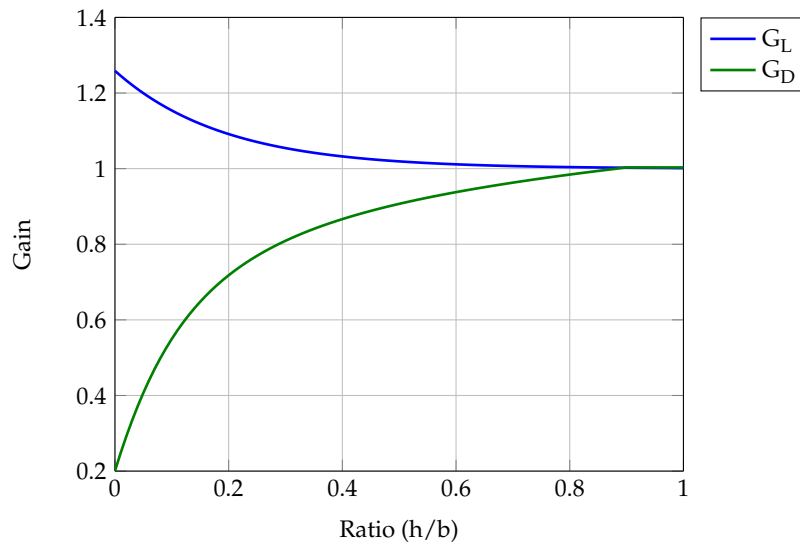
Figure 7.3: Multiplier for lift and drag coefficient in ground effect, where h denotes altitude and b denotes wing span

7.1.2   Actuator and Sensors Models

Actuator and sensor models were included into the environment to improve simulation fidelity and to incorporate practical limitations into the system. Band-limited white noise was added to each of the sensors to model sensor noise according to manufacturer guidelines and component datasheets. A random seed was generated to ensure that the sensor noise for every simulation is initialised with a new seed and therefore a new initialisation point. Sensor biases, quantisation, and bandwidth limitations were also incorporated into the models to more accurately simulate the characteristics of actual sensors. GPS delay of 100 ms was added to the model, as per manufacturer guidelines. This delay provides a more accurate representation of practical GPS update rates, and the inclusion thereof resulted in a more realistic evaluation of controller robustness. GPS drift and random walk were also included in the sensor model, although it was found that the amount of drift was negligibly small when using the GPS in differential mode. A simple first-order delay with saturation and backlash was used to model the high-speed servos that deflect the aerodynamic control surfaces through a system of linkages.

7.1.3   Runway Model

A non-linear runway model, developed by Roos [4], was included in the simulation environment to model the interaction between the aircraft and the runway surface. This model is essential for runway controller performance evaluation and for determining the landing position from the observed acceleration spike upon touchdown. Roos's runway model was developed for a three-wheeled aircraft with a tricycle undercarriage, characteristic of the test vehicle used in this thesis. There are three types of forces that act on the aircraft due to the runway, namely friction forces, cornering forces, and normal forces.

Longitudinal friction forces act on the aircraft due to the rolling resistance between the tyre and the runway surface. Friction between the wheel hub and the axle on which it rotates also contributes to the total longitudinal friction forces. Cornering forces are defined as the lateral

forces acting on the aircraft due to interaction with the runway surface. Roos [4] defines the slip angle (α) of a wheel as the angle between the direction of travel and the heading direction of the wheel. The slip angle and cornering forces of the nose wheel are responsible for generating a yawing moment about the CG to effectively manoeuvre the aircraft whilst taxiing. Normal forces acting on the aircraft are a result of the reaction forces between the runway surface and the wheels. These forces are of major importance, since both the frictional and cornering forces are modelled as being directly proportional to the normal force at each point of contact. As the aircraft gains airspeed along the runway, lift generated by the wings will reduce the reaction force on the wheels, subsequently minimising cornering forces and reducing the effectiveness of nose wheel steering.

7.1.4   Wind Model

With a focus on accurate crosswind landing, this thesis requires the development of a high-fidelity atmospheric model for realistic FCS performance evaluation through extensive SIL and HIL simulations. There are three types of disturbances that the atmospheric model is capable of generating, namely wind gusts, turbulence, and vertical wind shear. The atmospheric model was created as a Simulink block with airspeed, altitude, and DCM as dynamic inputs to the system. The model then generates wind velocities and angular rates coordinated in the body axis, which are added to the current aircraft states before being propagated through the aforementioned aerodynamic model. Wind azimuth (Ψ_w) and elevation (Θ_w) are specified in the inertial frame, with Ψ_w ranging from $0°$ north to $360°$ in a clockwise rotation, whilst Θ_w ranges from $0°$ parallel with the horizon to $90°$ perpendicular to it, as shown in Figure 7.4. Each of the aforementioned wind disturbances can be enabled and characterised independently, which allows for the creation of very specific atmospheric conditions.
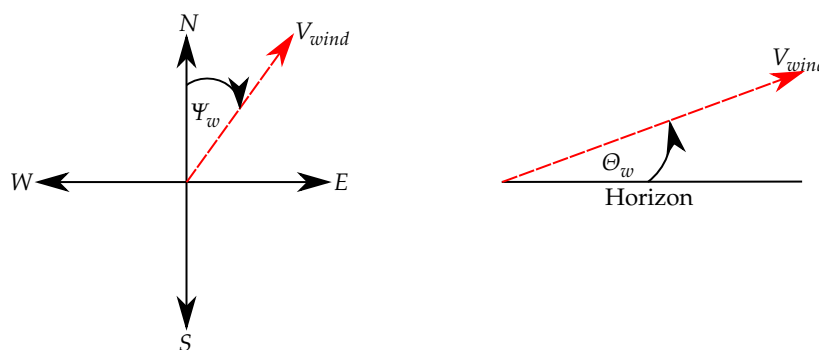
Figure 7.4: Wind model direction definitions

7.1.4.1   Gust Model

The gust model generates a disturbance following a "1-cosine" profile during the build-up phase, and an inverted "1-cosine" profile during the fade-out, as shown in Figure 7.5. A mathematical implementation of the gust model is derived from the military specification MIL-F-8785C [45], with slight modifications to cater for a fading gust response. The modified mathematical representation
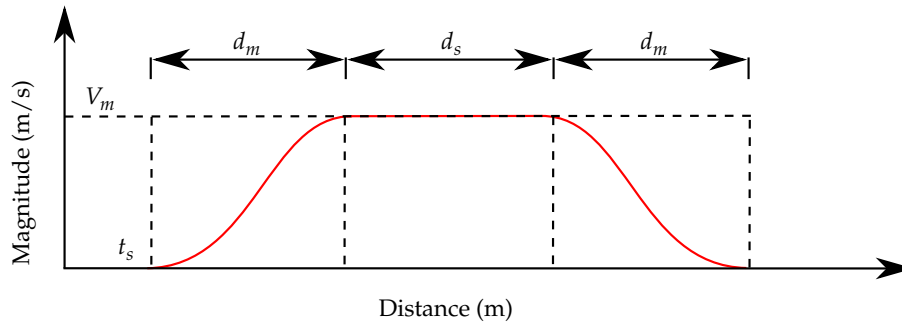
Figure 7.5: Gust profile

is given by the following piecewise function:

$$
V_{gust} = \begin{cases}
0 & t < t_s \\
\frac{V_m}{2}(1 - cos(\frac{\pi x}{d_m})) & 0 \leq x \leq d_m \\
V_m & x > d_m, \;\; x < (d_m + d_s) \\
\frac{V_m}{2}(1 + cos(\frac{\pi x}{d_m})) & (d_m + d_s) \leq x \leq (2d_m + d_s) \\
0 & x > (2d_m + d_s)
\end{cases}
\tag{7.5}
$$

where V_m is the maximum gust amplitude, x is the distance travelled by the aircraft, d_m is the gust build/fade distance, t is the elapsed simulation time, t_s is the gust start time, d_s is the distance at maximum magnitude before fade-out, and V_{gust} represents the resultant gust model output.

7.1.4.2   Turbulence Model

Atmospheric turbulence is perhaps the most difficult to model, as it introduces both linear and angular rates into the system. Atmospheric turbulence is realised by passing band-limited white noise with unit variance through shaping filters to achieve either the Dryden or Von Kármán spectral forms. The Dryden implementation gives an approximation of the actual turbulences, although an accurate filter can be defined to realise the results. The Von Kármán implementation, on the other hand, describes turbulence characteristics more accurately, but only an approximated filter can be defined. The mathematical implementation of the turbulence model is derived from the military specification MIL-HDBK-1797 [46] which describes turbulence as a stochastic process. The filter forms are derived from the spectral square roots of the spectrum equations summarised in Appendix E.

7.1.4.3   Wind Shear Model

Vertical wind shear describes the wind intensity as a function of altitude and the physical characteristics of the underlying terrain. The concept of wind shear was introduced in Chapter 4, where its effect on aircraft stability was discussed in detail. Figure 7.6 shows the mean wind shear profile as a function of altitude. A mathematical implementation of wind shear is derived from the military specification document MIL-HDBK-1797 [46] in the following form:

$$
u_{shear} = u_{20} \frac{ln(\frac{h}{z_0})}{ln(\frac{20}{z_0})} \qquad 3 \text{ ft} < h < 1000 \text{ ft}
\tag{7.6}
$$
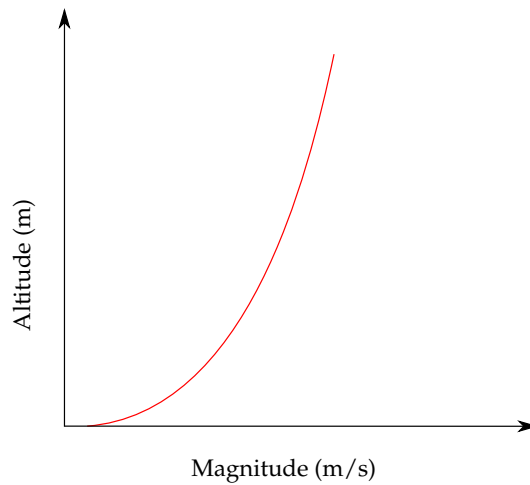
Figure 7.6: Wind shear profile

where u_{shear} is the mean wind speed, h is the current aircraft altitude, u_{20} is the measured wind speed at an altitude of 20 feet above the surface, and z_0 is a constant dependent on the flight phase. The flight phase constant z_0 is equal to 0.15 for category C flight (take-off, approach, and landing) and 2.0 for all other phases of flight.

7.1.5 Navigation and Flight Control

The flight control system, state machine logic, and supporting navigation algorithms discussed in Chapters 5 and 6 were written in C code and implemented as S-functions running on the simulation computer. Sensor information is parsed from the simulation environment to the navigation and flight control system, where difference equations are used to compute actuator outputs based on the current aircraft state and reference commands. The control vector generated by the autopilot is then parsed back to the simulation environment via the actuator model block before being propagated through the aircraft model in a process that determines the future of the states. This is the first step in debugging and verifying the control and navigation algorithms implemented in C code. Ultimately, these algorithms will be implemented on embedded hardware in an environment where testing and debugging are by nature more challenging. It is therefore imperative that thorough testing be conducted in this conducive environment before progressing to HIL simulations, discussed in the next chapter.

7.2 Simulation Results

Now that the non-linear simulation environment has been discussed, this section will focus on the analysis of non-linear simulation results. The results discussed in this section are obtained from high-fidelity, non-linear simulations with refined dynamic models that encapsulate the effects of sensor noise and external disturbances. The purpose of these simulations is to investigate the validity of numerous design assumptions, and to determine the effect of external disturbances on the autopilot system.

7.2.1   Linear vs Non-linear Controller Response

The control algorithms discussed in Chapter 5 were designed based on linearised aircraft dynamics following numerous assumptions. It is therefore important to compare FCS performance on the full non-linear aircraft model in order to establish confidence in the validity of these assumptions. The augmented linearised aircraft dynamics, developed during the controller design phase of Chapter 5, were further augmented to include actuator lag dynamics present in the non-linear simulation environment - this ensures a fair comparison between the linear and non-linear dynamics. Due to the successive augmentation strategy followed during the design phase, step responses obtained from the linear and non-linear environments are expected to correspond remarkably well.

7.2.1.1   Airspeed Controller

Figure 7.7a shows a comparative airspeed step response between the linearised, augmented longitudinal aircraft model and the non-linear simulation environment.

(a) Linear vs non-linear step response   (b) Associated thrust command
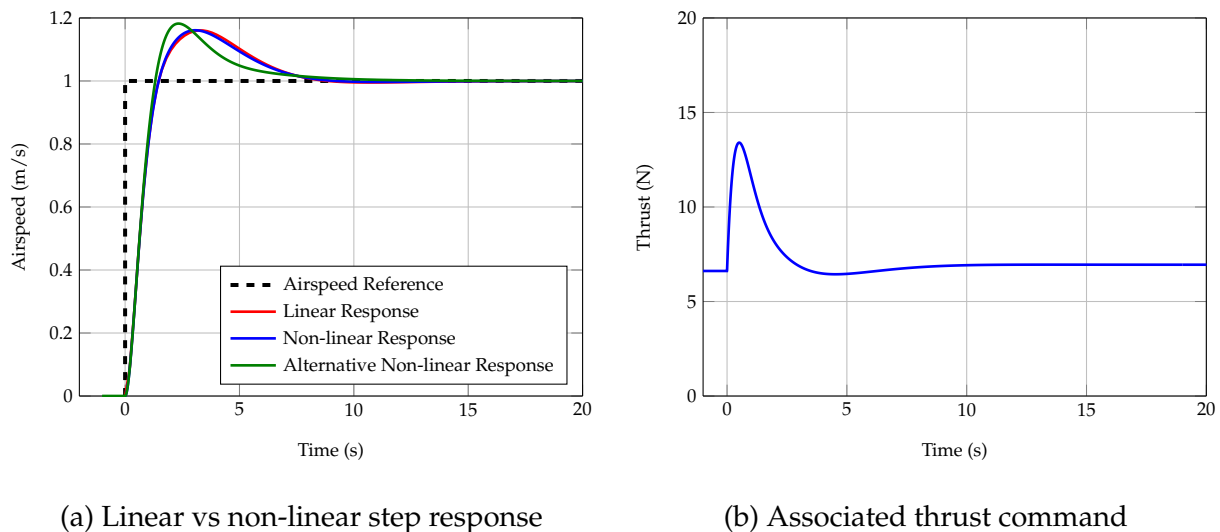
Figure 7.7: Airspeed controller comparison - the associated thrust command is extracted from the non-linear simulation environment

It is apparent that the two responses agree exceptionally well, and that the associated thrust command, depicted in Figure 7.7b, remains within practically attainable limits. In order to obtain the airspeed step in the non-linear environment, it is necessary to enable two of the remaining longitudinal controllers (NSA and climb rate) so as to keep the aircraft flying straight and level. Due to the inherent coupling that exists between airspeed and normal specific acceleration, any irregularities in the NSA controller step response will influence the observed airspeed response and vice versa. During the design phase of the hybrid NSA controller, normal specific acceleration was simply extracted from the state vector through Equations (5.30) and (5.44) under the assumption that airspeed remains constant. In reality, however, this is not the case, and it is intuitive that airspeed will vary as the exchange between kinetic and potential energy occurs. Furthermore, calculating normal specific acceleration in this way requires direct knowledge of the angle of attack

measurement, which is not available on the practical test vehicle. For practical implementations of the FCS, all accelerations are measured using a three-axis accelerometer included in the avionics stack and are therefore coordinated in the aircraft's body axis. To this end, the alternative non-linear response, depicted by the green line, illustrates the airspeed response when body axis accelerations are fed back in the NSA control loop. The variation in transient response characteristics can be attributed to the aforementioned coupling that exists between airspeed and normal specific acceleration. Aerodynamic forces and moments are strongly dependent on airspeed (due to the quadratic dynamic pressure relationship), therefore any observed airspeed variations would be apparent from the accelerometer measurement and in turn affect the dynamic response of the associated controllers.

7.2.1.2   Normal Specific Acceleration Controller

Figure 7.8a shows a comparative normal specific acceleration step response between the linearised, augmented longitudinal aircraft model and the non-linear simulation environment.
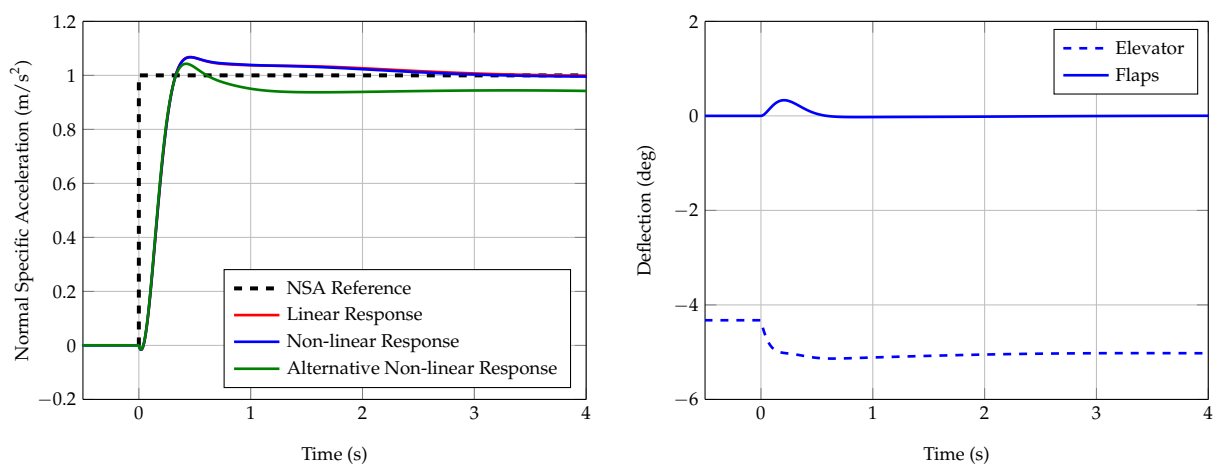
(a) Linear vs non-linear step response   (b) Associated elevator and flap command

Figure 7.8: NSA controller comparison - the associated elevator and flap commands are extracted from the non-linear simulation environment

Once again it is apparent that the two responses (red and blue lines) agree exceptionally well, and that both the associated elevator and flap commands, depicted in Figure 7.8b, remain within practically attainable limits. The fact that the responses agree to this extent bodes well for the fidelity of the augmentation strategy proposed during the design phase of the hybrid controller. The alternative non-linear response, depicted by the green line, illustrates the NSA response when body axis accelerations are fed back in the control loop. It is apparent that the NMP zero and rise time characteristics agree exceptionally well, but the resulting overshoot and steady-state dynamics tend to deviate somewhat. These deviations can be attributed to the static airspeed assumption and the fact that body axis accelerations (obtained from the accelerometer) are fed back in the control loop, as opposed to accelerations coordinated in the wind axis as per the design requirement - airspeed (and therefore dynamic pressure) decreases when an upward normal specific acceleration step is commanded due to the inherent gravitational coupling that exists. These

variations are expected to alter the response of both the middle-loop climb rate controller as well as the outer-loop altitude controller.

7.2.1.3   Climb Rate Controller

Figure 7.9a shows a comparative climb rate step response between the linearised, augmented longitudinal aircraft model and the non-linear simulation environment.

(a) Linear vs non-linear step response   (b) Associated elevator and flap command

Figure 7.9: Climb rate controller comparison - the associated elevator and flap commands are extracted from the non-linear simulation environment

It is apparent that the two responses (red and blue lines) agree exceptionally well, and that both the associated elevator and flap commands, depicted in Figure 7.9b, remain within practically attainable limits. During the design phase, climb rate was indirectly extracted from the state vector through Equation (5.100), and therefore also requires direct knowledge of the elusive angle of attack measurement. For practical applications, climb rate will be measured using the vertical component of the inertially coordinated GPS velocity. The alternative non-linear response, depicted by the green line, illustrates the climb rate response when body axis accelerations are fed back in the NSA control loop, and inertially coordinated GPS velocity measurements are fed back in the climb rate control loop. It is apparent that the rise time characteristics agree exceptionally well; however, the alternative response exhibits slightly more overshoot, with a decreased settling time when compared to the original non-linear response. These variations are expected to alter the response of the outer-loop altitude controller.

7.2.1.4   Altitude Controller

Figure 7.10a shows a comparative altitude step response between the linearised, augmented longitudinal aircraft model and the non-linear simulation environment. It is apparent that the two responses (red and blue lines) agree exceptionally well and that both the associated elevator and flap commands, depicted in Figure 7.10b, remain within practically attainable limits. The alternative non-linear response, depicted by the green line, illustrates the altitude response when body

(a) Linear vs non-linear step response

(b) Associated elevator and flap command
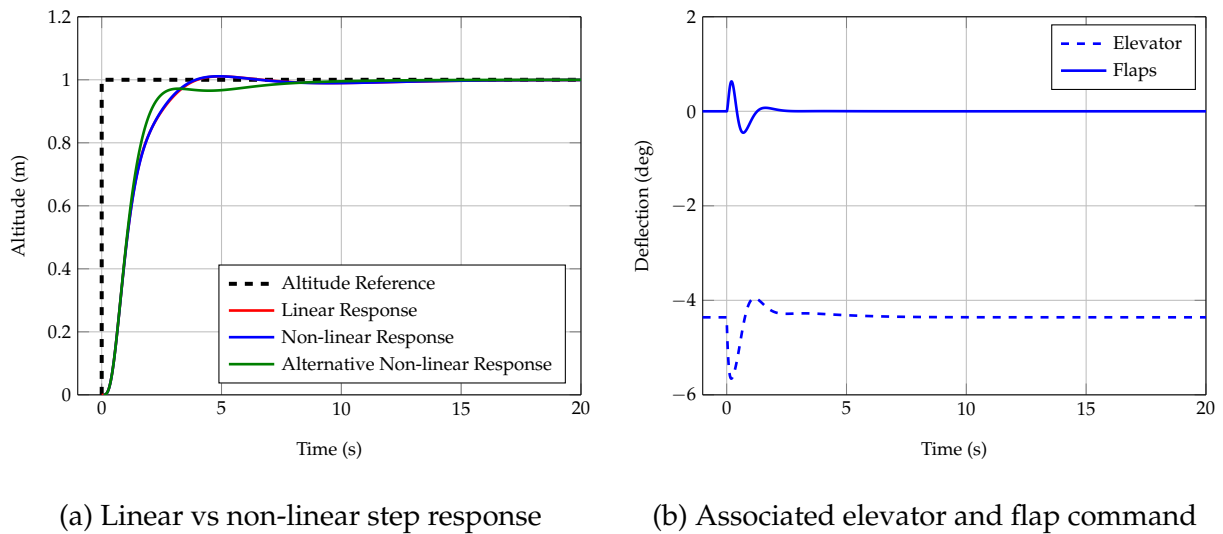
Figure 7.10: Altitude controller comparison - the associated elevator and flap commands are extracted from the non-linear simulation environment

axis accelerations are fed back in the NSA control loop, and inertially coordinated GPS velocity measurements are fed back in the climb rate control loop. It is also apparent that the initial rise time characteristics correspond well, even though the alternative response exhibits a slight undershoot before settling around the same time as the original non-linear response. Ultimately, all three of the aforementioned alternative step responses were deemed acceptable.

7.2.1.5   Roll Rate Controller

Figure 7.11a shows a comparative roll rate step response between the linearised, augmented lateral aircraft model and the non-linear simulation environment.

(a) Linear vs non-linear step response

(b) Associated aileron command
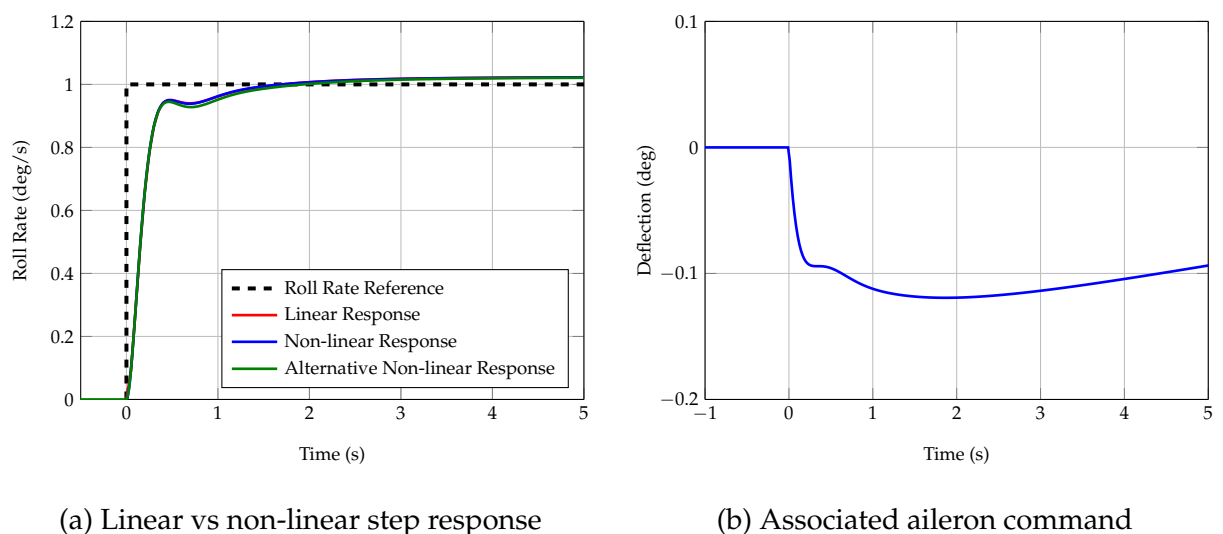
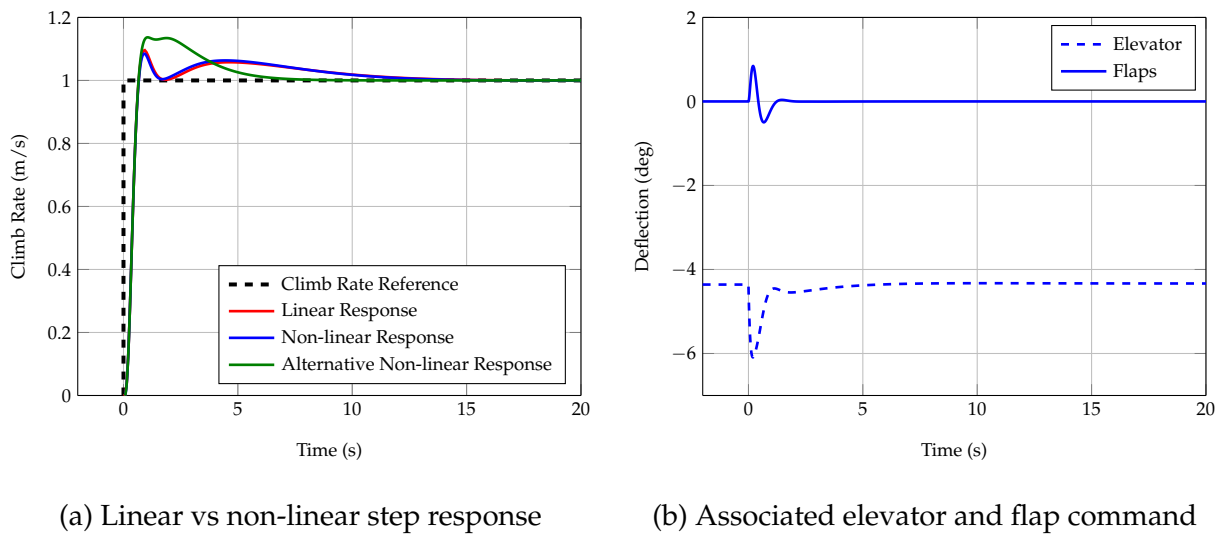**Figure 7.11:** Roll rate controller comparison - the associated aileron command is extracted from the non-linear simulation environment

It is apparent that the two responses agree exceptionally well, and that the associated aileron command, depicted in Figure 7.11b, remains within practically attainable limits. It is important to note that the lateral specific acceleration controller was active when the roll rate step was commanded. Due to the inherent coupling that exists between the lateral and directional aircraft dynamics, any irregularities in the LSA controller step response would influence the observed roll rate response and vice versa. During the design phase of the LSA controller, lateral specific acceleration was simply extracted from the state vector through Equation (5.139) under the assumption that airspeed remains constant. Following the same argument used earlier for the normal specific acceleration controller, it was concluded that is not entirely true. Furthermore, calculating lateral specific acceleration in this way requires direct knowledge of the sideslip angle measurement, which is not available on the practical test vehicle. To this end, the alternative non-linear response, depicted by the green line, illustrates the roll rate response when body axis accelerations are fed back in the LSA control loop. The slight variation in transient response characteristics can be attributed to the inherent coupling that exists between roll rate and lateral specific acceleration. Airspeed is significantly less affected by lateral perturbations than it is by longitudinal perturbations, and it therefore remains relatively constant throughout the course of a lateral manoeuvre. Albeit small, there is indeed a slight discrepancy in the LSA response, which manifests as a deviation in the roll rate response due to the inherent coupling that exists. However, this slight deviation is not expected to alter the response of the remaining lateral controllers. It is important to note that the aircraft's lateral dynamics are not stable until the roll angle control law is augmented to the system. It is for this particular reason that the step response fails to settle at the required steady-state value.

7.2.1.6 Roll Angle Controller

Figure 7.12a shows a comparative roll angle step response between the linearised, augmented lateral aircraft model and the non-linear simulation environment.

(a) Linear vs non-linear step response   (b) Associated aileron command

Figure 7.12: Roll angle controller comparison - the associated aileron command is extracted from the non-linear simulation environment

Once again it is apparent that the two responses agree exceptionally well, and that the associated aileron command, depicted in Figure 7.12b, remains within practically attainable limits. The alternative non-linear response, depicted by the green line, illustrates the roll angle response when body axis accelerations are fed back in the LSA control loop. On observation of the step response, it is clear that there exists a non-zero steady-state error (approximately 2%), which can be attributed to the lack of an integrator in the roll angle control law. As mentioned in the design section, a limited integrator will be augmented to the guidance controller to compensate for any resulting steady-state tracking errors.

7.2.1.7 Guidance Controller

Figure 7.13a shows a comparative cross-track step response between the linearised, augmented lateral aircraft model and the non-linear simulation environment.

(a) Linear vs non-linear step response   (b) Associated aileron command

Figure 7.13: Guidance controller comparison - the associated aileron command is extracted from the non-linear simulation environment

The alternative non-linear response, depicted by the green line, illustrates the cross-track response when body axis accelerations are fed back in the LSA control loop. It should be noted that all three of the responses agree exceptionally well, and that the associated aileron command, depicted in Figure 7.13b, remains within practically attainable limits.

7.2.1.8 Lateral Specific Acceleration Controller

Figure 7.14a shows a comparative lateral specific acceleration step response between the linearised, augmented lateral aircraft model and the non-linear simulation environment. It is apparent that the two responses (red and blue lines) agree exceptionally well, and that the associated rudder command, depicted in Figure 7.14b, remains within practically attainable limits. The alternative non-linear response, depicted by the green line, illustrates the LSA response when body axis accelerations are fed back in the control loop. There is a slight discrepancy in the NMP zero behaviour;
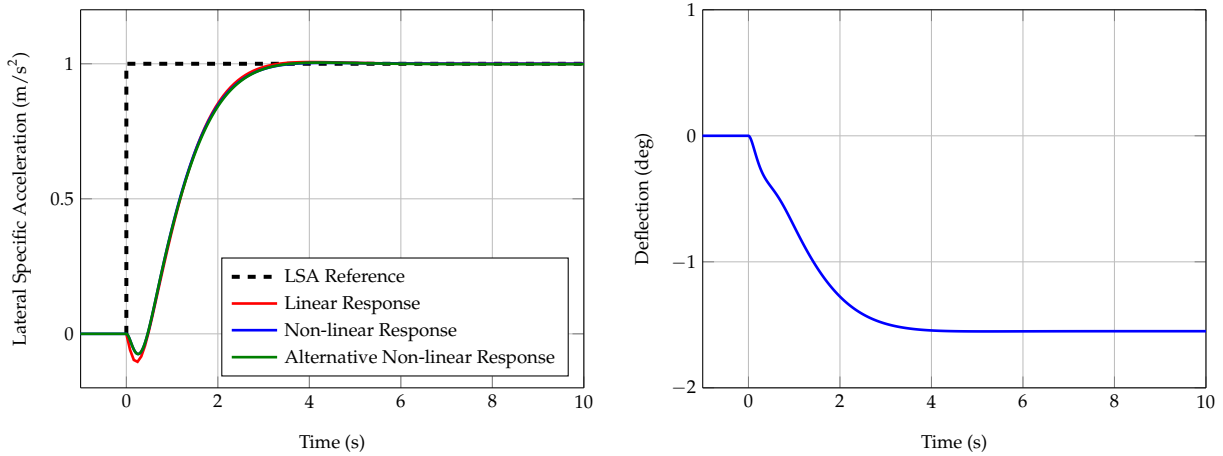
(a) Linear vs non-linear step response   (b) Associated rudder command

Figure 7.14: Lateral specific acceleration controller comparison - the associated rudder command corresponds to a 0.1 m/s^2 lateral specific acceleration step extracted from the non-linear simulation environment. The response has been scaled to match a unit step input.

nevertheless, the remaining transient response and lower-frequency dynamics agree exceptionally well. This slight variation is not expected to alter the response of the outer-loop heading controller.

7.2.1.9 Heading Controller

Figure 7.15a shows a comparative heading step response between the linearised, augmented lateral aircraft model and the non-linear simulation environment.
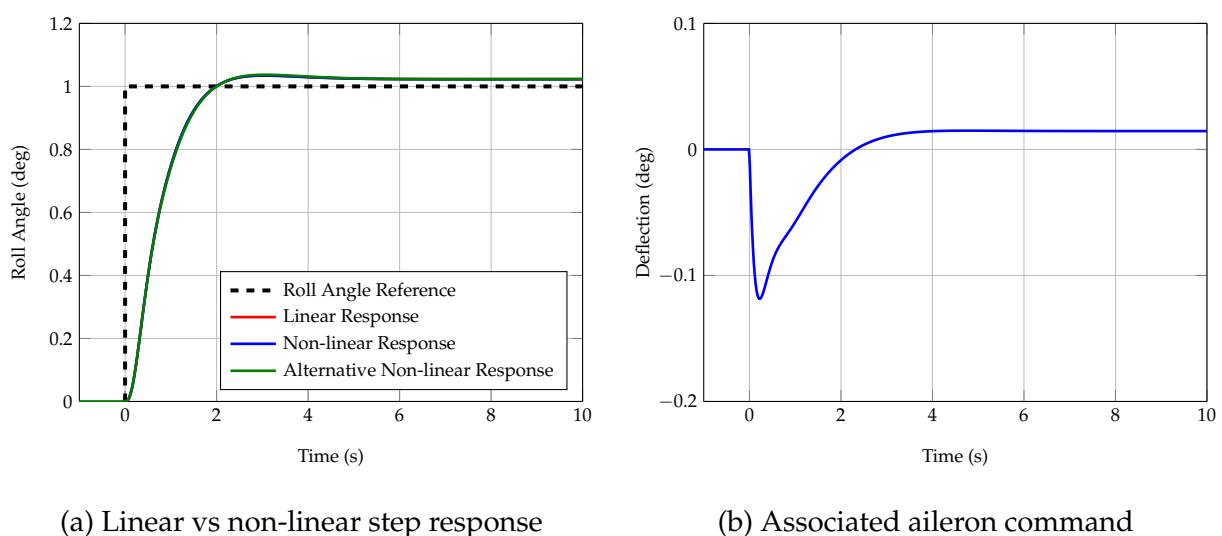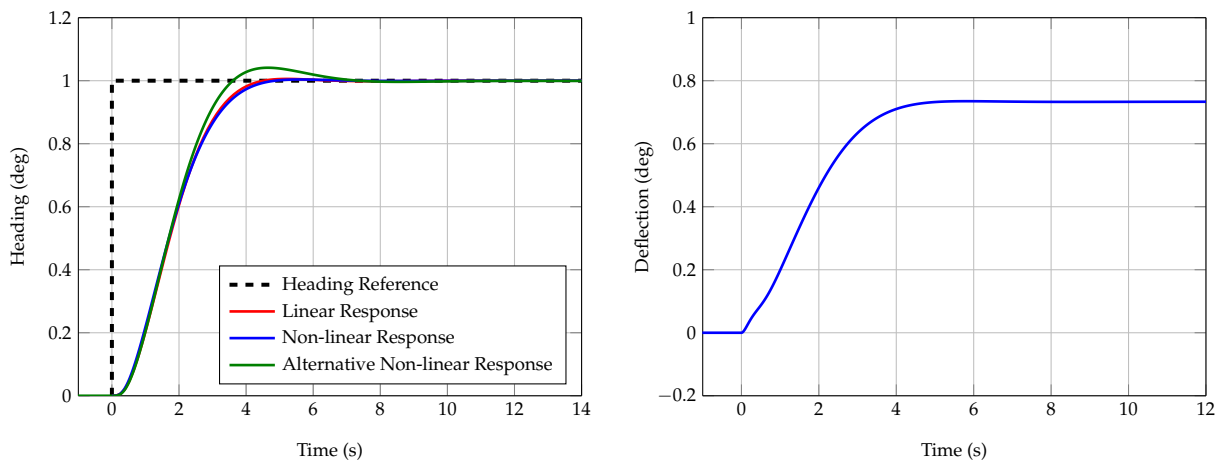

(a) Linear vs non-linear step response   (b) Associated rudder command
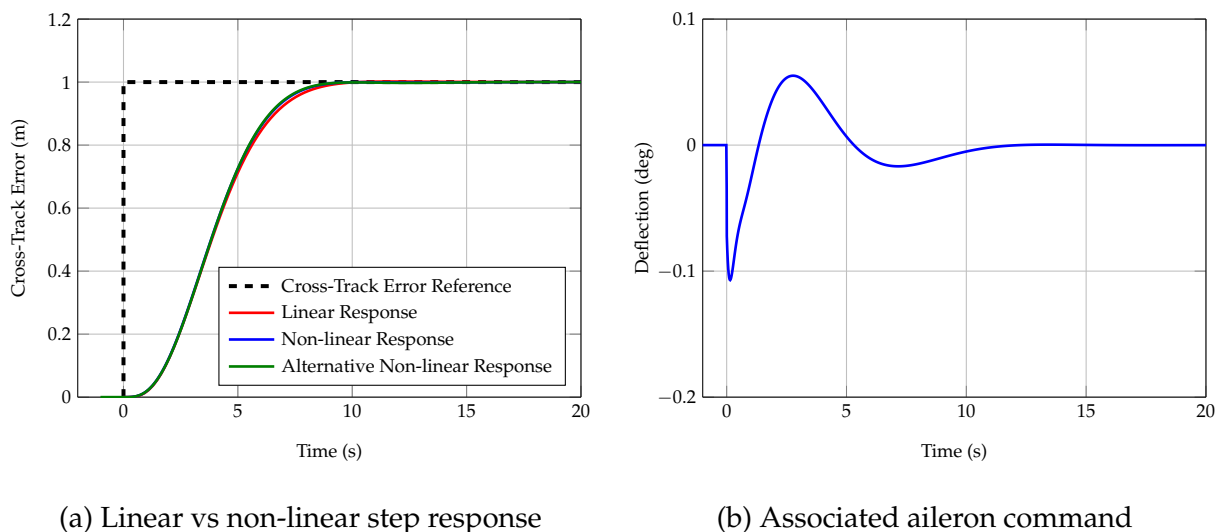
Figure 7.15: Heading controller comparison - the associated rudder command is extracted from the non-linear simulation environment

During the design phase of the heading controller, it was assumed that $\psi = \beta$ to simplify the process, as an AoSS state already formed part of the linearised aircraft model. The blue and red

lines are indicative of the controller response when sideslip angle β is fed back in the heading con-
trol loop. In essence, this structure is explicitly controlling sideslip angle rather than the desired
heading angle. The alternative non-linear response, depicted by the green line, illustrates the con-
troller response when heading angle ψ is explicitly fed back in the control loop (as opposed to β
being fed back). It is apparent that the rise time characteristics agree exceptionally well; however,
the alternative response exhibits slightly more overshoot, with an increased settling time when
compared to the original non-linear response. The overshoot in the controller response is less
than 5%, and the two-second increase in settling time simply means that the de-crab manoeuvre
should be executed slightly earlier during final approach. To this end, it can be concluded that
the approximations made during the design of the heading controller are valid for this particular
application. Furthermore, it is apparent that the associated rudder command, depicted in Fig-
ure 7.15b, remains within practically attainable limits for both of the non-linear simulation step
responses.

7.2.2 Navigation and Landing

Now that each component of the FCS has been investigated and the validity of the design assump-
tions assessed, the focus shifts towards evaluating the performance of the synergistic autopilot as
a whole. Figure 7.16a illustrates the accuracy of the navigation system in its ability to guide the air-
craft between various waypoints using the hybrid navigation algorithm developed in Chapter 6.

(a) Waypoint navigation   (b) Glideslope tracking
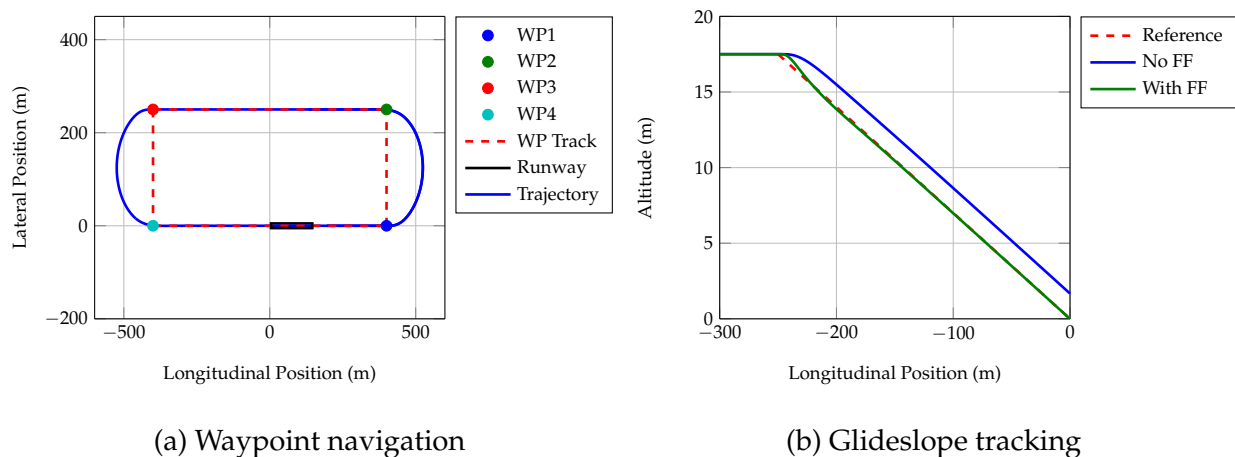
Figure 7.16: Waypoint navigation and glideslope tracking

It is apparent that the autopilot guides the aircraft with exceptional accuracy as it navigates
the oval track. It is also clear from Figure 7.16a that the aircraft is perfectly on track by the time it
reaches the runway - this bodes well for lateral landing accuracy. Longitudinal landing accuracy,
on the other hand, is highly dependent on the ability of the FCS to track the glideslope with
zero steady-state error. As mentioned in Chapter 6, glideslope tracking errors can result in large
down-range inaccuracies. Figure 7.16b illustrates the accuracy of the FCS in its ability to track the
glideslope during a landing approach. The blue line shows the aircraft's trajectory if the expected

climb rate is not fed-forward in the altitude control structure. It is clear that there exists a steady-state offset of approximately 2 m, which translates to a down-range offset of approximately 28 m for a $4°$ glideslope angle. In comparison, the green line shows the aircraft's trajectory when the expected climb rate is fed-forward in the altitude control structure, as shown in Figure 5.15. It is clear that the steady-state offset has been completely minimised, which allows the aircraft to touch down with centimetre accuracy.

7.2.3   Effect of Wind on Controllers

Up until this point, all of the non-linear simulation results have been portrayed in the absence of wind disturbances. The focus of this thesis, however, is to develop a synergistic control structure capable of landing a fixed-wing UAV accurately in adverse wind conditions. In light of this, the focus now shifts towards investigating FCS performance and landing accuracy under various wind conditions.

7.2.3.1   Gust Alleviation Characteristics

The idea of using direct lift control to improve gust alleviation characteristics was first proposed in Chapter 5. The conventional pitch-moment-based NSA controller was augmented with direct lift control capabilities to maximise closed-loop bandwidth, and to improve gust alleviation characteristics by using the flaps to generate lift instantaneously. Figure 7.17a shows a comparison of the climb rate response to a tailwind gust when direct lift control is employed.

(a) FCS gust alleviation characteristics

(b) Associated actuator commands
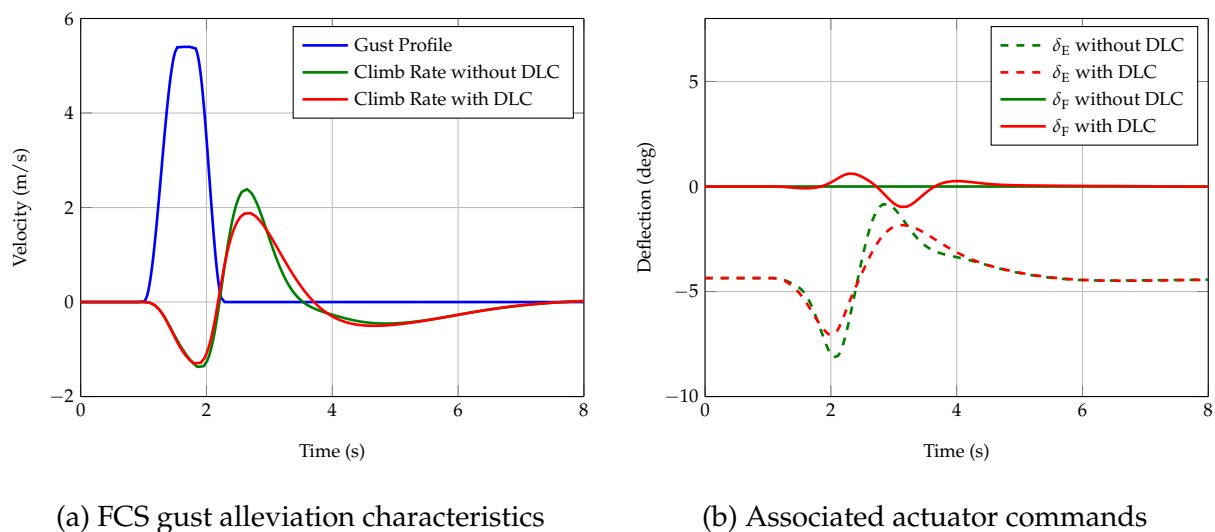
Figure 7.17: FCS gust alleviation characteristics rejecting a tailwind gust with a magnitude equal to 30% of the trim airspeed

It is apparent that the tailwind gust results in a loss of lift, and causes the aircraft to experience a negative climb rate (positive sink rate), as expected. However, the aircraft experiences less climb rate deviation (both positive and negative) when direct lift control is used to instantaneously compensate for the lift deficiency. Perhaps the greatest contribution can be observed from Figure 7.17b,

which shows a comparison of the control surface deflections. It is apparent that there is approx-
imately a 30% decrease in elevator deflection when direct lift control is employed. This enables
the FCS to handle gusts of larger magnitude before elevator saturation occurs. To this end, it can
be concluded that the FCS benefits from direct lift control, as it is able to reject gust disturbances
more effectively and with less elevator control authority.

7.2.3.2   Effect of Wind on Outer-loop Controllers

For the sake of a more thorough investigation, it was decided to analyse the effect of constant
winds on FCS performance. During the controller design phase, it was assumed that the aircraft
would be flying in still atmospheric conditions so that various linearising and decoupling assump-
tions could be made to simplify the process. In reality, however, the aircraft will not be flying in
calm atmospheric conditions, and it is therefore necessary to analyse the inaccuracies associated
with these assumptions. Only the most prevalent effects are highlighted in this section so as to
avoid a lengthy discussion that would otherwise not contribute much value to the investigation
as a whole. Throughout the design phase, it was assumed that climb rate was simply a function
of trim airspeed and flight path angle. In reality, however, vertical updrafts (and downdrafts) will
affect the rate of climb and could result in unsatisfactory FCS performance. Figure 7.18a shows a
comparative altitude step response when a constant wind (magnitude of 20% $\bar{V}_T$) is injected into
the simulation environment.

(a) Effect on altitude controller   (b) Effect on guidance controller
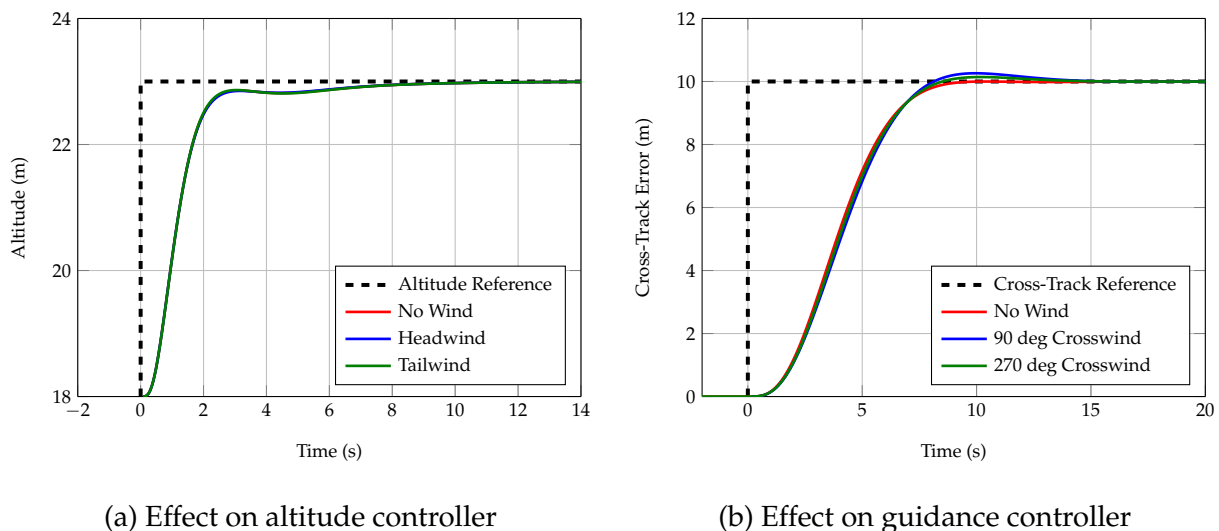
Figure 7.18: Effect of a constant wind on the altitude and guidance controllers. Wind magnitude
is equal to 20% of the trim airspeed.

The wind is predominately aligned in the longitudinal axis, with a $5°$ elevation angle to simu-
late a constant updraft. It is apparent that this wind scenario has a negligible effect on the altitude
response due to the relatively small vertical component. Obviously, stronger wind magnitudes
would have a more noticeable effect, but for this particular application, stronger updrafts are not
expected during typical flight. In a still atmosphere with no external disturbances, it was assumed
that cross-track error rate, and subsequently cross-track error, could be obtained by simply integ-
rating centripetal acceleration. The limitations of this assumption are apparent from Figure 7.18b,

which shows a comparative step response of the guidance controller when a constant $90°$ cross-wind (magnitude of 20% $\bar{V}_T$) is injected into the simulation environment. The additional overshoot results in a slight increase in settling time, which could potentially degrade lateral landing accuracy if the final approach distance is not sufficient. To this end, it is clear that constant winds of realistic magnitude are not expected to have a detrimental impact on FCS performance, or substantially degrade landing accuracy for that matter.

7.3 Analysis of Crosswind Landing Techniques

The discussions and analyses of the preceding section focused on general FCS performance in the presence of various wind conditions. The focus now shifts towards analysing and comparing the effectiveness and accuracy of the three crosswind landing techniques.

7.3.1 Attitude and Trajectory Tracking

Figure 7.19 establishes a baseline of some important variables associated with the final landing approach in calm atmospheric conditions. Figures 7.19a and 7.19b illustrate glideslope tracking performance and cross-track accuracy observed during final approach. The aircraft transitions onto the glideslope around 18 s, where it is apparent that the altitude error deviates slightly before returning to zero 5 s prior to touchdown at 35 s. It is clear that there is zero cross-track error throughout the entire landing phase, since there are no lateral perturbations that would otherwise cause the aircraft to drift off track. Figures 7.19c and 7.19d show the aircraft's attitude and control surface deflection angles throughout the landing phase. The pitch angle measurement experiences a deviation from straight and level trim flight at the glideslope transition point as expected. The aircraft will therefore land with a slightly nose-down configuration due to the omission of a flare manoeuvre usually conducted before touchdown, as per the discussion in Chapter 6. It is apparent that only the longitudinal control surfaces (elevator and flaps) experience perturbations at the glideslope transition point. This is due to the fact that there are no lateral disturbances, and fact that the aircraft is symmetrical. Now that a baseline of some important variables has been established, the analysis can continue with the evaluation of the individual crosswind landing techniques.

In order to successfully compare the performance of the autoland system for each of the three landing techniques, a $90°$ crosswind with a magnitude equal to 20% of the trim airspeed was generated. Atmospheric turbulence and sensor noise were also introduced into the simulation environment to determine their contribution to the observed performance. It should be noted that the effectiveness of each technique was evaluated at various crosswind angles and magnitudes, even though only the worst-case scenario is discussed in this section. Figure 7.20a shows a comparison of the altitude reference tracking error for each of the three techniques. As expected, there is not much difference in altitude tracking accuracy between the three techniques. Figure 7.20b, on the other hand, illustrates a significant difference in cross-track error between the low-wing landing and the other two techniques. The deviation starts at the glideslope transition point, where the heading controller is activated and the aircraft is forced into a low-wing configuration. Activating the heading controller results in a misalignment between the aircraft's longitudinal axis and the incident airflow. Unless sufficient bank angle is applied to mitigate the opposing crosswind force,

(a) Glideslope tracking

(b) Runway tracking

(c) Aircraft attitude

(d) Actuator deflections
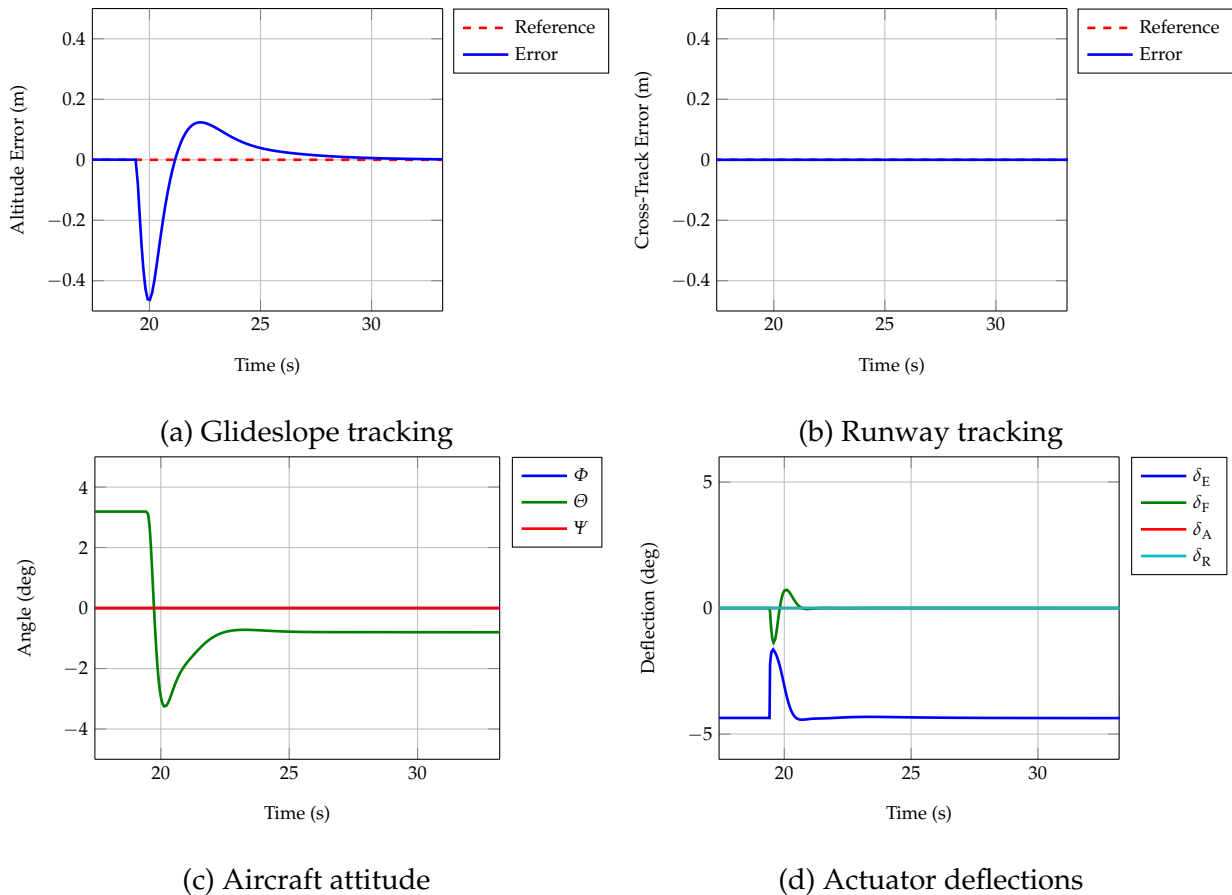
Figure 7.19: Autoland performance observed whilst landing in calm atmospheric conditions

deviations in cross-track will start to become apparent. Even though provision has been made by introducing a feed-forward term that prematurely banks the aircraft into the crosswind, it is clear that there is still a slight deviation in cross-track before the guidance controller commands the additional bank angle required to fully align the flight path. In comparison, the crabbed and de-crab landing techniques involve approaching the runway in a crabbed configuration, and will therefore exhibit similar flight path deviation characteristics. Simulation results show that the autoland system is capable of landing the aircraft within a 0.5 m radius of the intended touchdown point using each of the three techniques.

Up to this point, it seems as though there might not be any advantage of using one technique over another. However, upon observation of Figure 7.21 it is clear that this is not true. Consider a fictitious runway that is aligned perfectly in the north direction so that its heading in the inertial frame is zero. Figure 7.21a shows the aircraft's attitude when approaching and landing in a crabbed configuration on our fictitious runway. As can be seen, the aircraft approaches the runway with a $10°$ heading error and lands with this same error around 35 s. Landing with excessive heading error places severe side-loads on the landing gear and could potentially result in damage to the airframe, as discussed in Chapter 6. Furthermore, the aircraft will experience an excessive amount of lateral deviation after touchdown, since the landing gear is not aligned with the direction of travel. The runway controllers will therefore require higher actuation to negate the lateral deviation and bring the aircraft back to the runway centreline.

Figure 7.21c shows the aircraft's attitude when approaching the runway in a crabbed configu-

(a) Altitude deviation

(b) Cross-track deviation
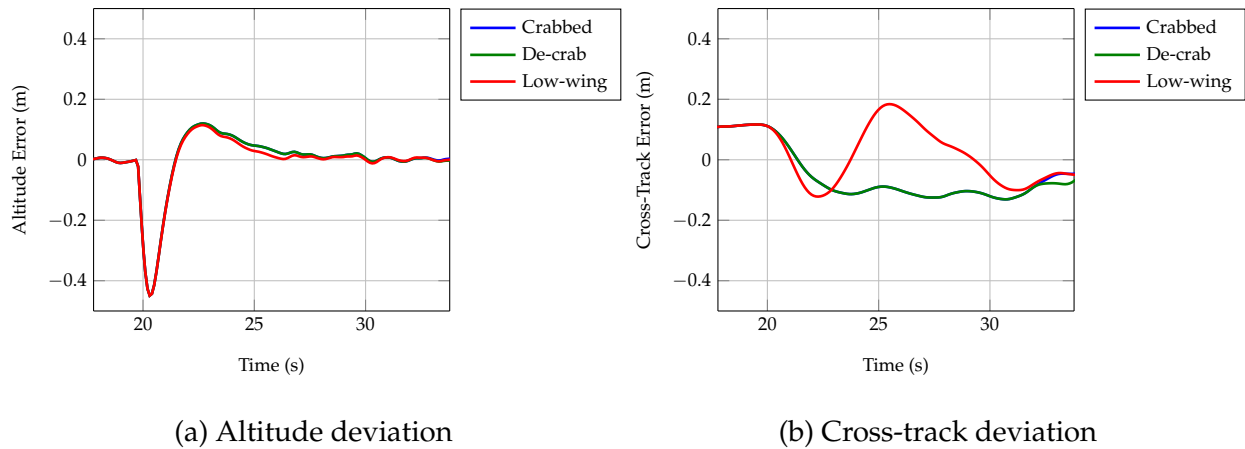
Figure 7.20: Lateral and longitudinal deviations observed during final approach in the presence of a crosswind. Crosswind magnitude is equal to 20% of the trim airspeed at 90° azimuth.

ration and executing the de-crab manoeuvre at approximately 33 s. It is apparent that the heading error is reduced from 10° to approximately 4° at the point of touchdown near 35 s. There is also a slight increase in the bank angle as the guidance controller tries to maintain a constant flight path during the de-crab manoeuvre. Touchdown occurs with a slight heading error and residual bank angle. Figure 7.21d shows the associated control surface deflections for the de-crab landing technique. When the heading controller is activated to execute the de-crab manoeuvre, it is clear that the rudder is deflected approximately 5°, whilst the ailerons experience only 2° perturbation from trim. The significant reduction in heading error will dramatically reduce landing gear side-loading and subsequently minimise the amount of lateral runway deviation experienced after touchdown.

Figure 7.21e shows the aircraft's attitude when approaching the runway and landing in a low-wing configuration on our fictitious runway. The heading controller is activated at the start of the glideslope around 20 s, at which point the heading error is reduced from 10° to less than 1°. The apparent undershoot in the heading measurement around 25 s is a result of the initial conflict that occurs between the heading and guidance controllers as the aircraft transitions into a low-wing configuration. Upon observation of the bank angle measurement Φ, it is clear that as the heading error is minimised, the upwind wing is simultaneously lowered as the aircraft banks approximately 4° in the direction of the crosswind to maintain a constant flight path. Touchdown occurs with the aircraft's heading fully aligned with the runway (zero crab angle) and a residual bank angle due to the low-wing nature of the approach. Figure 7.21f shows the associated control surface deflections for the low-wing landing technique. When the heading controller is activated, it is clear that the rudder is deflected approximately 8°, whilst the ailerons experience only 2° perturbation from trim. In order to remain within the bounds of linear control theory, the aerodynamic control surfaces are limited to a maximum of 12° perturbations from trim. In light of this, the rudder is the most likely of the actuators to reach saturation during a low-wing approach. Following extensive simulations, it was found that a 90° crosswind with a magnitude of more than 25% of the trim airspeed would result in rudder saturation for this particular airframe. To this end, it can be concluded that an aircraft approaching the runway in a crabbed configuration can handle stronger crosswind magnitudes than an aircraft in a low-wing approach. However, activating the heading controller earlier in the descent allows more time for effective heading alignment.

(a) Crabbed attitude

(b) Crabbed deflections

(c) De-crab attitude

(d) De-crab deflections

(e) Low-wing attitude

(f) Low-wing deflections
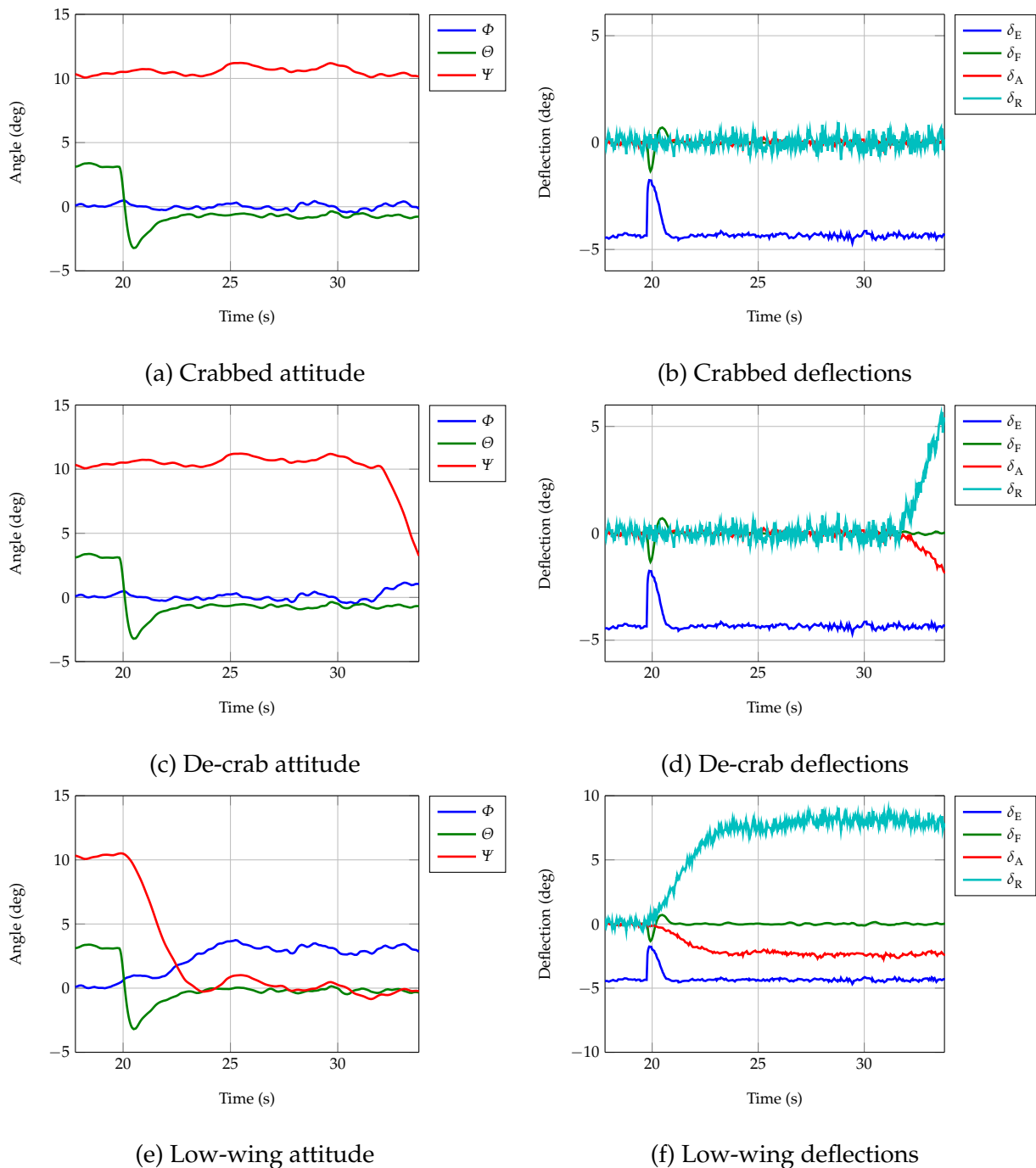
Figure 7.21: Autoland performance observed during final approach in the presence of a crosswind. Crosswind magnitude is equal to 20% of the trim airspeed at 90° azimuth.

Figure 7.22 shows the amount of lateral runway deviation associated with each of the three crosswind landing techniques. The excessive crab angle associated with the crabbed landing technique clearly causes the aircraft to deviate about 2.5 m from the runway centreline. This is one of the main reasons why it is necessary to strategically activate the heading controller and minimise the amount of crab angle before touchdown. In comparison, the de-crab and low-wing techniques exhibit less deviation, as the heading controller is able to align the aircraft's landing gear with the direction of travel before touchdown.
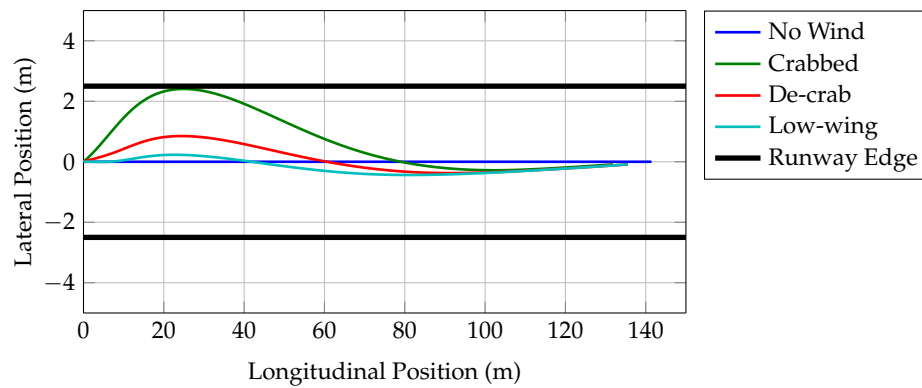
Figure 7.22: Comparative runway deviation

7.3.2   Monte Carlo Simulations

The preceding discussion focussed on the performance of the autoland system observed during the final approach for each of the three landing techniques. In an attempt to compare specific landing accuracies more thoroughly, a Monte Carlo simulation was conducted for various wind scenarios. Gusts of varying intensity, duration, and starting position on the terminal glideslope were injected into the non-linear simulation environment to analyse gust alleviation performance and to compare the landing accuracies associated with each of the three techniques. Wind shear and turbulence were kept constant at 10% of the trim airspeed so that the only variation between consecutive simulations would be specific to the gust model.[1] Algorithm 1 illustrates the basic concept of the Monte Carlo simulation.

Algorithm 1: Monte Carlo simulation for landing accuracy evaluation

Data: varying gust parameters

Result: landing accuracy prediction

initialization;

for *GustPos from GP_{min} to GP_{max}* **do**

    for *GustDist from GD_{min} to GD_{max}* **do**

        for *GustMag from GM_{min} to GM_{max}* **do**

            for *n from 1 to N* **do**

                execute the landing simulation

                determine the north and east landing position

                determine the aircraft's attitude at the point of touchdown

---

GustPos denotes the gust starting position, *GustDist* denotes the distance the aircraft travels in the presence of the gust (gust duration), and *GustMag* denotes the particular gust magnitude. *GustPos* is measured in metres from the intended touchdown point, and ranges from 0 m to 250 m in increments of 50. *GustDist* ranges from 1 m to 100 m in increments of 20, and *GustMag* ranges from 0 m/s to 1.5 m/s in increments of 0.3.

---

[1]Wind shear magnitude = 1.8 m/s.

It is clear that the algorithm consists of four nested for-loops that vary specific parameters of the gust model. The algorithm can therefore be thought of as a type of grid search that scans through predetermined parameters, with the inclusion of an inner loop that runs the simulation with the same set of parameters N times. The purpose of this inner loop is to capture the contribution of randomly seeded white noise models (such as turbulence and sensor noise) to the observed touchdown positions. Due to the inherent inefficiency of nested for-loops and the limited speed at which the non-linear environment can be simulated, it was necessary to investigate an optimal number of inner-loop iterations N that would yield adequate results in the least amount of time. A statistical concept known as confidence intervals proved useful in this regard. Conceptually, a confidence interval describes an estimated range of values which is likely to include the true value of an unknown population parameter with some probability (known as the confidence level). For a known standard deviation, the confidence interval is calculated as follows:

$$\gamma = \left(\bar{x} - z^* \frac{\sigma}{\sqrt{N}}, \bar{x} + z^* \frac{\sigma}{\sqrt{N}} \right) \tag{7.7}$$

where $\bar{x}$ is the population mean, σ is the standard deviation, N is the number of observations, and z^* is used as the critical value, which is dependent on only the confidence level for a particular test. The critical value is given as $z^* = 1.96$ for 95% confidence that the true value lies within the calculated interval. Determining the optimal number of inner-loop iterations N involved a trade-off between the highest certainty (smallest confidence interval) and the lowest simulation runtime. Figure 7.23a shows the confidence interval for the observed two-dimensional (longitudinal and lateral) landing positions, whilst Figure 7.23b shows the associated simulation runtime. It is clear that the confidence interval decreases exponentially, whereas the simulation runtime increases linearly with N. Based on this information, it was decided that the optimal number of observations for this particular experiment should be $N = 80$.

(a) Confidence interval   (b) Simulation runtime
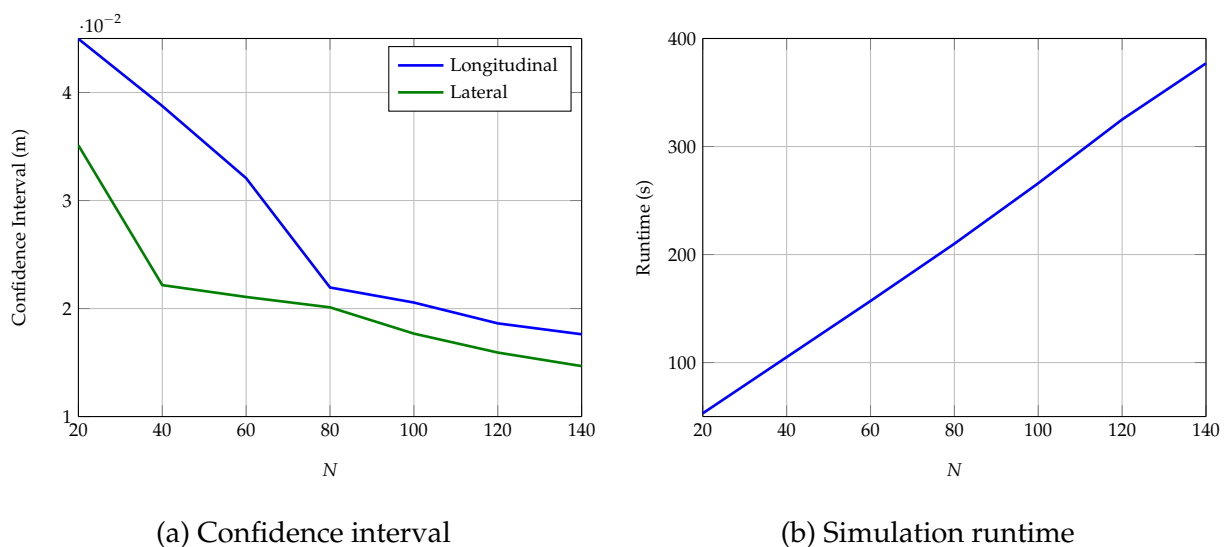
Figure 7.23: Determining the optimal number of observations

Figure 7.24a shows a point cloud of the touchdown positions and associated 2σ deviations (from the mean) for each of the three crosswind landing techniques. It is immediately apparent

from the figure that improved gust alleviation characteristics are observed when approaching the runway in a crabbed configuration. The de-crab landing technique shows a slight deviation in the mean longitudinal landing position, and the Gaussian ellipse is slightly skewed laterally. These observations can be attributed to differential lift and the cross-coupling effects associated with a typical de-crab manoeuvre. As expected, the low-wing approach exhibits poorer gust alleviation performance when compared to the crabbed approach. This is due to the additional heading controller dynamics and the excessive cross-coupling effects that are apparent when the aircraft is slipping.[1] As a result, the mean landing accuracy has degraded substantially in the lateral direction, whilst the Gaussian ellipse has been skewed both longitudinally and laterally, showing a larger deviation in both directions. For all three of the landing techniques, however, it is clear that the mean landing positions and 2σ boundaries fall within a 0.5 m radius circle. This finding bodes well for the successful achievement of the accuracy objective stated in Section 1.4.

Figure 7.24b shows the mean and 2σ deviation of the heading error (crab angle) upon touchdown for each of the three techniques. The relatively large values associated with the crabbed landing technique are directly related to the ratio between trim airspeed and the apparent crosswind magnitude. It is clear that both the mean and standard deviation of the heading error are significantly reduced when either the de-crab or the low-wing technique is employed during the landing procedure.

(a) Landing position point cloud   (b) Heading angle error
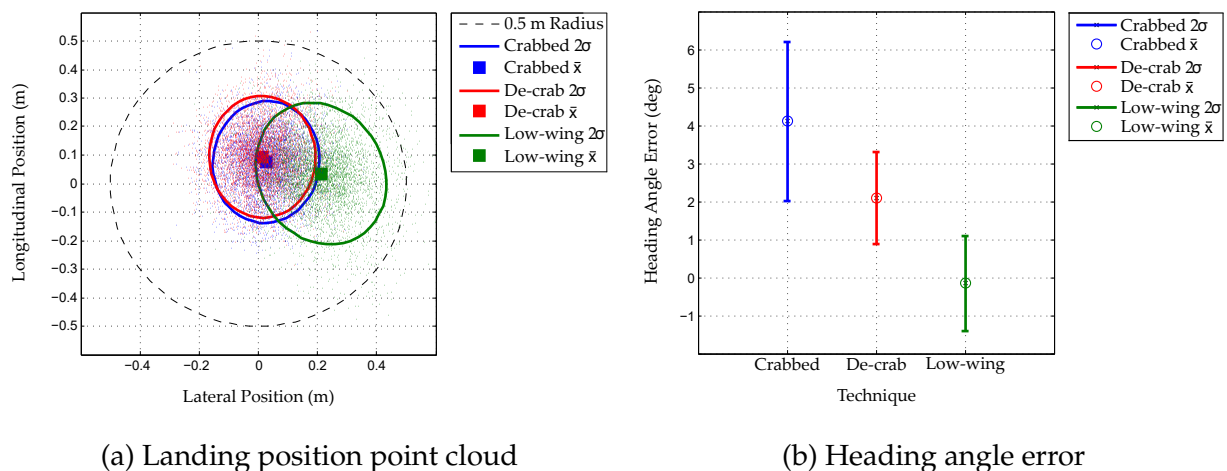
Figure 7.24: Landing accuracy investigation for a 90° crosswind

From the preceding discussions, it can be concluded that there are clear advantages and disadvantages associated with each of the three crosswind landing techniques. It has been shown that the crabbed technique exhibits strong disturbance rejection characteristics, but landing with excessive heading errors in severe crosswind conditions limits its applicability. The de-crab technique shows a slightly degraded longitudinal landing accuracy in the presence of wind gusts, but the heading controller is able to minimise the error to within 5° before touchdown.[2] The low-wing technique exhibits the poorest landing accuracy due to inherently degraded gust alleviation

---

[1]Slipping refers to an aircraft that is flying with a non-zero sideslip angle so that $\beta \neq 0$.

[2]The reader should recall that 5° was stated as the maximum allowable error.

characteristics associated with slipping, but the heading controller is given ample time to completely minimise the error before touchdown. Table 7.1 provides a comparative summary of the advantages and disadvantages associated with each of the landing techniques.

It is important to note that the validity of the results discussed in this section is highly dependent on the accuracy of the non-linear aircraft model. For this particular reason, it is imperative that the results obtained from the Monte Carlo simulations be validated through practical flight testing so as to inspire confidence in the landing accuracy prediction system.

7.4   Summary

A high-fidelity, non-linear simulation environment with refined dynamic models was developed in this chapter. The simulation environment was then used to evaluate the functionality and performance of the controllers and navigation algorithms developed in Chapters 5 and 6. It was found that the FCS, together with the autonomous navigation strategy and landing state machine, performed exceptionally well and was able to land the aircraft accurately in various crosswind conditions. This environment was also used to develop a landing accuracy prediction system that provides statistical information regarding the expected touchdown accuracy given predefined wind conditions. The positive results presented in this chapter inspire confidence in the system, and help to verify the validity of the assumptions made during the design phase. Now that a simulation environment has been developed and the functionality of the FCS evaluated through extensive software simulations, the focus shifts towards further evaluation through hardware-in-the-loop simulations and practical flight testing. These topics are the subject of the next chapter.

Table 7.1: Comparative summary of landing techniques

Method	Advantages	Disadvantages
Crabbed	Highest landing accuracy	Excessive side-loading and lateral runway deviation
De-crab	Partial heading error minimisation	Slightly degraded landing accuracy
Low-wing	Complete heading error minimisation	Degraded landing accuracy and prone to rudder saturation

CHAPTER 8

HIL Simulations and Flight Test Results

This chapter focuses on the practical verification of the autopilot system through high-fidelity hardware-in-the-loop (HIL) simulations and a strategically planned flight test campaign. The non-linear simulation environment, discussed in the preceding chapter, will be used for extensive HIL simulations, in which the Technology Readiness Level (TRL) will be assessed before the commencement of practical flight testing. A typical HIL simulation involves testing of all hardware, avionics, and algorithms on a real-time computer-simulated model. This is imperative to ensure proper functioning of all hardware and subsystems before flights, and significantly reduces the risks associated with potential system failure. The first part of this chapter contains a structural overview of the autopilot system, which is then followed by a brief discussion of the avionics and associated hardware necessary for fully autonomous flight. The ground station developed specifically for this project is then discussed before model verification is conducted to evaluate the fidelity of the aircraft model. The chapter concludes with a comparative analysis of the flight test results and associated HIL simulation results.

8.1 Structural Overview

The overall operation of the aircraft is governed by both the ground station operator and the safety pilot. The safety pilot is primarily responsible for ensuring the aircraft's safety in the event of a system failure, whilst the ground station operator has the authority to activate high-level functionality of the FCS. It is important to note that the safety pilot has absolute authority over the procedure, and can assume total control instantly via a safety switch on the Remote Control (RC). Figure 8.1 shows a structural overview of the autopilot.

The servos used to actuate the aerodynamic surfaces are controlled via a separate servo control board shown in Figure 8.1. The servo control board is responsible for appropriately allocating control authority between the RC pilot and the FCS. In the event that commands from the On-Board Computer (OBC) fail, absolute control authority is enforced via the servo control board.
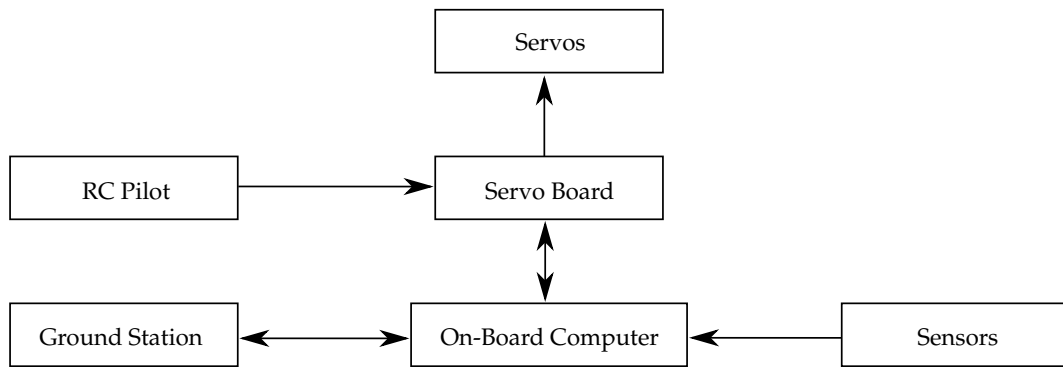
Figure 8.1: Overview of the autopilot system

Control allocation is specifically designed in such a way that the safety pilot maintains complete authority over the aircraft until such time as both the ground station operator and the safety pilot authorise the autopilot system - should the OBC fail, control is automatically returned to the safety pilot.

The OBC is the central processing unit of the entire FCS and is responsible for executing numerous tasks associated with autonomous flight. It is used to estimate system states based on various sensor readings, and executes the control and estimation algorithms when enabled. It also provides high-level functionality, including waypoint navigation and autonomous crosswind landing capabilities. Commands are sent from the ground station to the OBC via an RF link connected to the ground station hardware.

Hardware-in-the-loop simulation functionality is implemented via a separate HIL interface board that transcodes emulated sensor information from the simulation environment to a format recognisable by the OBC. During a typical HIL simulation, actuator commands generated by the FCS are parsed back to the emulation computer and propagated though the non-linear simulation environment in a process that determines theoretical state values. These values are then converted to theoretical sensor measurements and parsed back to the OBC so that the process can be repeated. MATLAB's real-time toolbox is used to maintain real-time accuracy during simulations. In the case of a SIL simulation, all control and estimation algorithms are computed within the MATLAB environment by the emulation computer. A HIL simulation, on the other hand, involves parsing emulated sensor measurements to external target hardware (OBC) running the control and estimation algorithms.

It is important to note that the non-linear simulation environment is identical for both SIL and HIL simulations, and thus there should be little to no difference in FCS performance between the two. This assumption was indeed validated through extensive SIL/HIL simulation matching, although the results are omitted here due to limited space.

8.2 Avionics and Associated Hardware

The avionics and associated flight control hardware on board the practical test vehicle are based on a general hardware structure used at the Electronic Systems Laboratory. A photograph of the avionics stack can be found in Figure 8.2 and a structural overview thereof in Figure 8.3. It is important to note that the avionics and associated flight control hardware have been refined over

the years and are used mostly unchanged in this project. For more detailed information regarding the development of this hardware, see [5], [6], [9], and [33].

Figure 8.2: Photograph of the avionics stack

The OBC is a custom-designed printed circuit board, which features two dsPIC32f microcontrollers and a host of auxiliary components that allow for external communication and circuit protection. On-board CAN bus controllers are used as the primary communication channel between the integrated modules. The dual microprocessor layout is required for optimised load sharing, so that one processor is used exclusively for GPS message parsing whilst the other is featured as a general purpose chip, which is utilised to run the estimation, control, and data transmission algorithms. The IMU board, magnetometer, and servo control board are directly connected to the OBC via the CAN bus. An RF link is established via a paired 2.4 GHz MaxStream module theoretically capable of maintaining a ten-mile link.[1]

The sensor boards used for the IMU, airdata, and magnetometer also feature dsPIC microcontrollers capable of facilitating CAN bus communication and analog-to-digital conversion. Inertial measurement information is obtained using the ADIS16355 IMU, which is an embedded unit containing a three-axis accelerometer and gyroscope. The airdata board features a differential pressure sensor to measure impact pressure from the pitot-static tube mounted on the left wing of the aircraft. This differential pressure measurement is then converted to Indicated Airspeed (IAS) through the dynamic pressure equation. Magnetic information is obtained using the HMC2003 magnetometer produced by Honeywell. The differential GPS that forms part of the avionics stack is the Novatel OEMV-1G operated with ProPak V3 to provide exceptionally accurate differential position information necessary for precise crosswind landings.

An external HIL board is used to introduce HIL functionality through direct communication via CAN and UART protocols. The HIL board comprises yet another dsPIC microcontroller responsible for packet routing and transcoding between the necessary protocols. It is thus required to maintain a high-speed serial link for communicating actuator values to, and sensor information from, the simulation environment running on the host computer. Simultaneously, it is also responsible for emulating GPS packet information by transcribing simulated inertial position and velocity measurements into the relevant GPS packets transmitted via the UART link. This setup allows for high-fidelity hardware simulations using a software-based model, comprised of refined

---

[1]According to the MaxStream 24XStream module datasheet.

dynamic models, designed to accurately encapsulate the effects of sensor noise and external disturbances. A few minor additions were made to the existing hardware, the most significant of which was the addition of a battery voltage sensor that was developed and integrated with the existing hardware to monitor the voltage of the main flight battery.
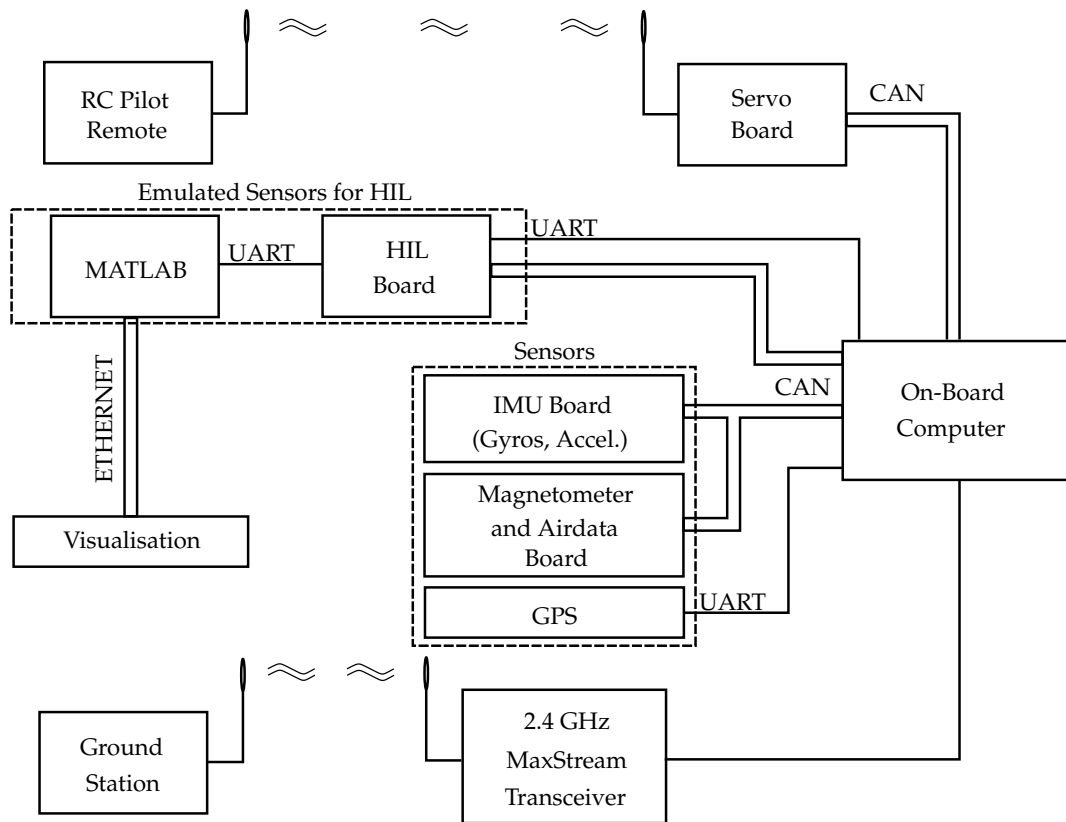
Figure 8.3: Structural overview of the hardware and avionics

8.3 Embedded Software

An Extended Kalman Filter (EKF) implemented on one of the dsPIC microcontrollers is responsible for state estimation based on GPS, IMU, and magnetometer measurements. This particular implementation allows for accelerometer-based propagation of position estimates, as well as two different methods of calculating attitude - the TRIAD and tilt/heading update methods. The EKF provides the following state estimates:

$$\hat{x} = \begin{bmatrix} \hat{N} & \hat{E} & \hat{D} & \dot{\hat{N}} & \dot{\hat{E}} & \dot{\hat{D}} & \hat{\phi} & \hat{\theta} & \hat{\psi} \end{bmatrix}^T \tag{8.1}$$

where $\hat{N}$, $\hat{E}$, $\hat{D}$, and $\dot{\hat{N}}$, $\dot{\hat{E}}$, $\dot{\hat{D}}$ represent the inertial position and velocity estimates respectively, and $\hat{\phi}$, $\hat{\theta}$, $\hat{\psi}$ represent the attitude estimates. Airdata, IMU, and magnetometer measurements are received at 50 Hz through the CAN bus, whilst GPS measurement updates are received at a slower rate of 10 Hz. Both the control and estimation algorithms are propagated at 50 Hz. Autonomous navigation and landing capabilities are implemented via a state machine, with high-level state transitions commanded by the ground station operator.

It is important to note that controller-related variables are reset until such time as the autopilot is activated, either by the safety pilot or the ground station operator. When a hard reset flag is raised, controller commands are set to zero, integrators are cleared, and the outer set points are set to the relevant measurement values. This ensures a smooth transition from remote pilot mode to the various autonomous flight modes. The received safety pilot commands are reflected on the control surfaces until such time as both the ground station operator and the safety pilot enable the autopilot system. Important flight data is logged to an external SD card at a variable rate selectable by the ground station operator (the default logging rate is 50 Hz).

8.4 Ground Station

The ground station is defined as the platform through which the ground station operator is able to interact with the FCS via a wireless RF link. Telemetry data transmission rates are limited to 2 Hz, 1 Hz, and 0.5 Hz due to the scope of information and bandwidth limitations associated with the RF link. Telemetry data includes updates on controller and estimator states and variables, information on FCS modes and states, specific status information relating to servo outputs and battery voltage, as well as operation times and general system information. Commands are sent from the ground station to the FCS asynchronously as required. A summary of the ground station capabilities is provided in Table C.2, whilst Figures C.1, C.2, C.3, and C.4 in Appendix C show screenshots of the ground station software application developed for this particular project.

8.5 Overview of the Flight Test Campaign

With the control and navigation algorithms fully designed and the avionics and ground station in place, the autopilot was complete and ready for flight testing. Over a period of five months, sixteen days of successful flight tests were conducted. During this time, the aircraft model was verified, longitudinal and lateral controller performance was evaluated, and the success of the autopilot was demonstrated in various atmospheric conditions. The lack of serious complications can be largely attributed to the extensive simulations that were conducted prior to flight testing. Formal flight test documentation was generated and consulted during each test to maximise chances of success. The document also ensured that the integrity of the airframe was continually checked and that nothing was overlooked during preparation. Formal flight test documentation is included in Appendix G for further perusal.

Wednesday the 2nd of December 2015 was the first time that the newly built aircraft ever flew. Three remotely piloted flight tests were conducted on that day, the first of which involved trimming the actuators for straight and level flight, whilst simultaneously allowing the safety pilot to familiarise himself with the aircraft. The second flight involved manually flying the aircraft at various altitudes and speeds so that sensor readings and estimated states could be verified to avoid using nonsensical data for the purposes of feedback control. The third and final flight involved conducting a series of Programmed Test Inputs (PTIs) designed to excite specific modes of motion through rudder, aileron, and elevator doublets. The open-loop aircraft response to these PTIs were then used for model verification to ensure that the aircraft model, used extensively throughout the design phase, adequately matched the dynamics of the practical test vehicle.

Flight testing resumed on the 20th of January 2016 and over the course of five months, fifteen flight tests with varying degrees of autonomy were conducted. The first few flight tests were focused on evaluating the performance of individual control loops by observing their response to step commands. This was done to gain confidence in the individual controllers before activating the navigation system and attempting risky autonomous crosswind landings. The first fully autonomous landing was conducted on Wednesday the 4th of May 2016 during calm wind conditions. All three landings conducted on this day were successful, as the FCS was able to land the aircraft within 30 cm (both laterally and longitudinally) of the intended touchdown point. This level of landing accuracy boded well for the focus of this thesis, which was the design of a fully autonomous landing system capable of executing accurate crosswind landings. The flight test campaign was concluded on the 16th of May 2016, when six successful crosswind landings were conducted. The tests involved two fully autonomous landings using each of the three crosswind landing techniques (six crosswind landings in total). In each case, the FCS was able to autonomously land the aircraft within the accuracy requirement of 1.5 m, making the concluding day of flight tests a resounding success.

It should be noted that landing accuracies varied considerably with crosswind magnitude, especially when approaching the runway in a low-wing configuration, as expected. In conclusion, it can be said that the flight test campaign was very successful, and yielded results that closely matched those observed during the extensive HIL simulations. Figure 8.4 shows two photographs captured during an autonomous landing test.

(a) Pre-flight checks

(b) Autonomous landing approach

Figure 8.4: Flight test images

8.6 Model Verification

Model verification is a technique that involves comparing simulated data to recorded flight data with the aim of evaluating open-loop model fidelity. A reliable estimation of the stability and control derivatives from recorded flight data requires the aircraft modes to be excited properly [47]. Figure 8.5 shows the typical inputs used to excite specific modes of motion. The 3211 input is found to have power over a wide frequency range, whilst doublet control inputs tend to excite a more specific and narrower band of frequencies. Pulse inputs have power at low frequencies
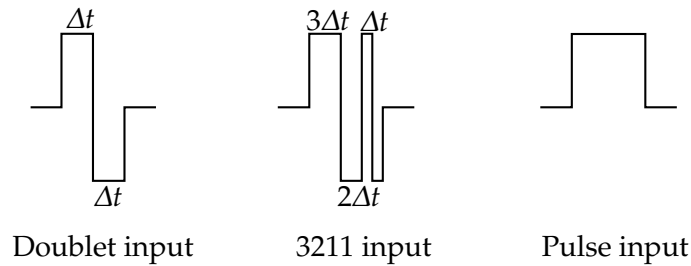
Figure 8.5: Specific input types: doublet, 3211, and pulse (Δt is the step width in seconds)

and are therefore suitable for exciting the low-frequency modes of the system [47]. The doublet control input excites the higher-frequency aircraft dynamics, and is typically used to excite the short period mode and the Dutch roll mode for the purposes of parameter estimation. Verification of the aircraft model by comparing estimated and calculated parameters can be quite a lengthy process, requiring multiple flight tests and precise excitation of the modes of motion.

Due to strict time constraints, a series of PTIs was superimposed on the safety pilot's control inputs during an earlier flight test in order to excite specific modes of motion. Recorded actuator data was then simply replayed through the non-linear simulation environment, and compared with the recorded flight data in order to verify the model. PTIs consisted of elevator doublets to excite the short period mode, rudder doublets to excite the Dutch roll mode, and aileron doublets to excite the roll mode. The following equation, developed by Raol et al. [47], can be used to calculate the approximate duration of the time unit Δt for a doublet control input, given that the natural frequency ω_n of the particular mode is known:

$$\Delta t = \frac{1.5}{\omega_n} \qquad (8.2)$$

Actuator deflections should be small enough in magnitude so that the aircraft states conform to linearity assumptions. It is important, however, that actuator deflections be large enough so that the modes are at least recognisable from the noisy flight data. Therefore the signal-to-noise ratio consideration is important for small aircraft state manoeuvres.

The vortex lattice program (AVL) used to obtain the aerodynamic stability and control derivatives is known to produce poor estimates of the parasitic drag C_{D_0} and the side force coefficient C_{Y_β} - the latter is mainly due to an incorrect calculation of the body side force contribution. The safety pilot was therefore instructed to trim the aircraft for straight and level flight so that a more accurate representation of the parasitic drag term could be obtained by comparing IAS with the recorded thrust command. The side force coefficient was slightly more challenging to obtain, as this required an AoSS sensor, which was not available on the practical test vehicle. Nevertheless, it was possible to compare the lateral specific acceleration measurement (indicative of side force) to a change in heading angle (indicative of change in sideslip angle) during a yaw rate perturbation. Albeit rudimentary, this method should give a more realistic estimation of the side force coefficient C_{Y_β}. After adjusting the aforementioned parameters in the non-linear aircraft model, PTIs were injected into the simulation environment so that the results could be compared with recorded sensor data. It is intuitive that the damping ratio and frequency of the natural aircraft modes would vary as a function of dynamic pressure. In order to ensure a fair and accurate model verification procedure, it was necessary to activate the airspeed controller so that IAS remains

regulated near the intended linearisation point of $V_T = 18$ m/s when the PTIs are executed.

Figure 8.6a shows a comparison of the pitch rate (Y-axis of gyroscope) after an elevator doublet, depicted in Figure 8.6b, was used to excite the aircraft's short period mode.

(a) Pitch rate comparison

(b) Associated elevator command
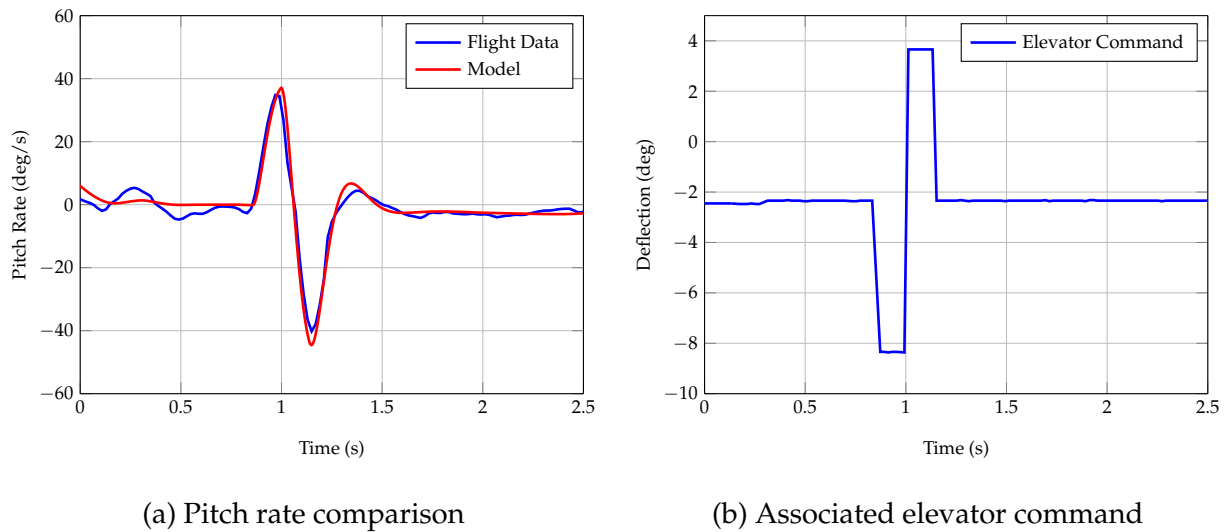
Figure 8.6: Practical vs simulated pitch rate response to an elevator doublet

It is apparent that the frequency and damping of the short period mode was captured exceptionally well by the non-linear aircraft model. Figure 8.7a shows a comparison of the yaw rate (Z-axis of gyroscope) after a rudder doublet, depicted in Figure 8.7b, was used to excite the aircraft's Dutch roll mode.

(a) Yaw rate comparison

(b) Associated rudder command
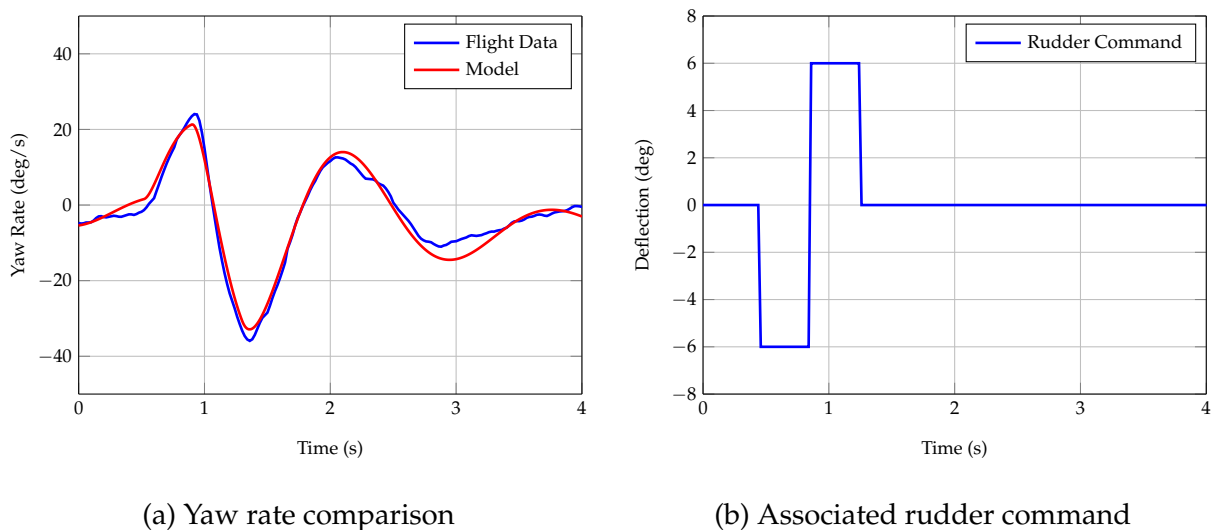
Figure 8.7: Practical vs simulated yaw rate response to a rudder doublet

Once again it is apparent that the frequency and damping of the Dutch roll mode was captured well by the non-linear aircraft model. Figure 8.8a shows a comparison of the roll rate (X-axis of gyroscope) after an aileron doublet, depicted in Figure 8.8b, was used to excite the aircraft's roll mode.

(a) Roll rate comparison

(b) Associated aileron command
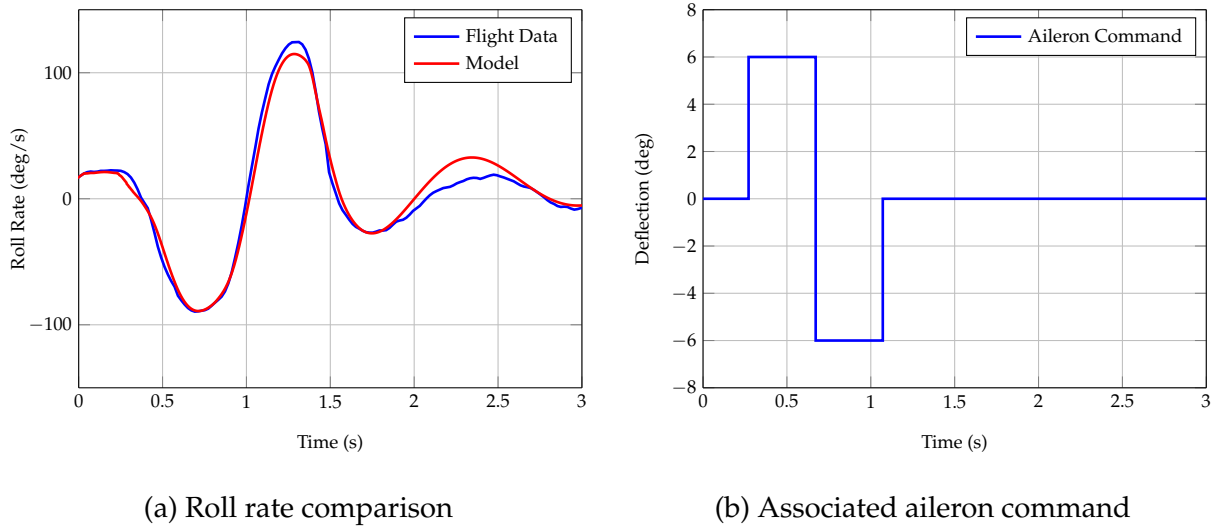
Figure 8.8: Practical vs simulated roll rate response to an aileron doublet

The PTI input originally intended to excite the roll mode was calculated incorrectly and resulted in the excitation of the lower-frequency Dutch roll mode. According to Equation (8.2), the approximate duration of the time unit Δt for an aileron doublet should be on the order of 0.18 s, but it is clear from Figure 8.8b that the actual time unit was twice as large. Nevertheless, the result was purposely included in this discussion, as it shows how the Dutch roll mode can also be excited through correctly timed aileron doublets. Once again the simulation data agrees with the recorded flight data.

The damping and natural frequency of the Dutch roll mode can be obtained by observing the first two peaks in Figure 8.7a after the rudder PTI has been executed. Firstly, the damped natural frequency can be obtained using,

$$\omega_d = \frac{2\pi}{T_{p-p}} \tag{8.3}$$

where T_{p-p} represents the peak-to-peak time of the response. Secondly, the inverse of the time constant σ can be obtained from the envelope of the response,

$$r(t) = Ae^{-\sigma t} \tag{8.4}$$

where A is a constant that can be calculated by setting $t = 0$, and $r(t)$ is the magnitude of the response at time t. With the complex pole pair describing the Dutch roll mode of motion defined as,

$$s = -\sigma \pm w_d i \tag{8.5}$$

Equations (8.3) and (8.4) yield,

$$s = -0.595 \pm 3.64i \tag{8.6}$$

for the simulated response and,

$$s = -0.577 \pm 3.79i \tag{8.7}$$

for the practical response. The damping ratio and natural frequency of the simulated response can thus be calculated as,

$$\zeta = 0.161 \tag{8.8}$$

$$\omega_n = 3.69 \text{ rad/s} \tag{8.9}$$

and the practical response as,

$$\zeta = 0.171 \tag{8.10}$$

$$\omega_n = 3.83 \text{ rad/s} \tag{8.11}$$

It is apparent that both the damping ratio and natural frequency of the model correspond well with those of the practical aircraft. In light of the preceding discussion, it can be concluded that the non-linear aircraft model is of high fidelity and captures the important flight dynamics associated with the practical test vehicle. Now that the model has been verified, it is safe to activate the autopilot system and continue with practical FCS verification.

8.7   Autopilot Results

In this section the results obtained following numerous flight tests are discussed. The results are separated into four different subsections, evaluating system performance in the phases of its development. The first two subsections describe longitudinal and lateral controller performance by evaluating the response to various step commands in calm atmospheric conditions. The third subsection deals with the navigation system, whilst the final subsection describes the autopilot's ability to accurately and autonomously land the aircraft in crosswind conditions.

8.7.1   HIL vs Practical Flight Data

A comparative analysis between HIL simulation data and recorded flight data is provided in this section. It should be noted that the inner-loop controllers (NSA, LSA, and roll rate) are not explicitly tested due to the unstable nature of the aircraft without the climb rate and roll angle controllers engaged. These controllers are therefore indirectly tested through their corresponding outer-loop controllers.

Before proceeding with a comparison of the results obtained from the HIL simulations and those obtained from practical flight tests, it is first necessary to discuss a particular attribute of the control linkages on board the practical test vehicle. Backlash is an undesirable non-linearity that is often unavoidable and quite common in most mechanical linkage systems. Due to the simplistic design and cost-effective nature of the test vehicle, the linkage system is rather rudimentary as it consists of flexible steel rods guided by plastic tubing that connect the servos to the aerodynamic control surfaces. Although simple, this linkage system results in backlash that becomes more apparent as the linkage length increases. The servos are located near the front of the aircraft and it is therefore intuitive that the elevator and rudder linkages are the most susceptible to backlash. It was expected that this non-linearity would result in decreased controller performance and most likely manifest as a limit cycle oscillation. In order to investigate this hypothesis, two comparative

HIL simulations were conducted. The control linkages in the first simulation were configured with zero backlash and the flight control system was commanded to maintain a constant climb rate. The second simulation was configured with half a degree of elevator backlash and, once again, the flight control system was commanded to maintain a constant climb rate. This specific amount of backlash was chosen as it represents a value that is difficult to measure physically, and therefore difficult to mitigate, but large enough that it has a noticeable influence on the flight control system. Figure 8.9 shows a comparison of the climb rate and pitch angle regulation when backlash is introduced into the simulation environment.

(a) Climb rate regulation   (b) Pitch angle regulation
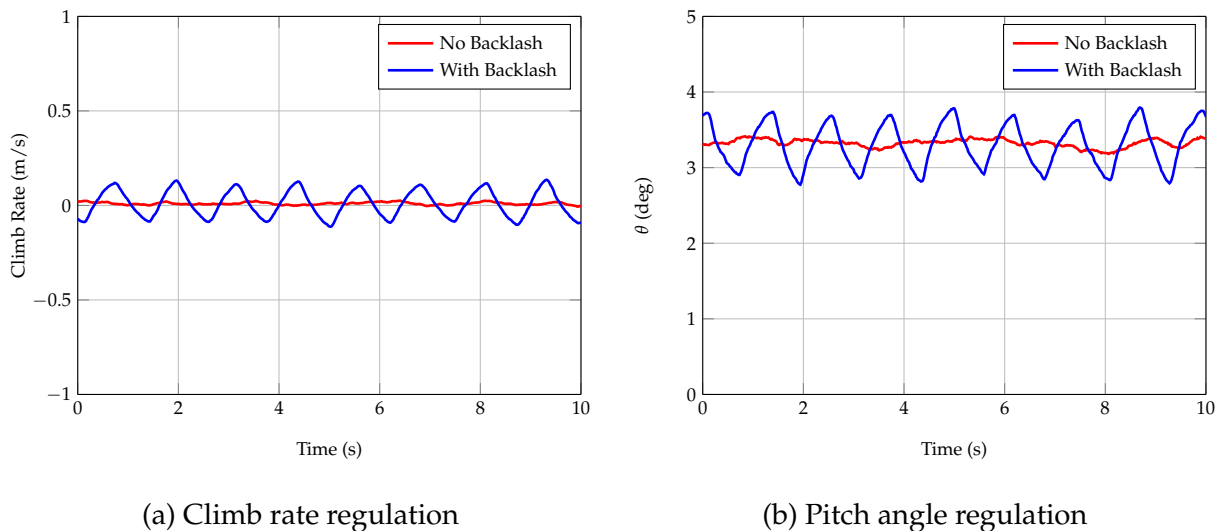
Figure 8.9: The effect of elevator backlash on climb rate and pitch angle regulation during a typical HIL simulation

Benign limit cycle behaviour is clearly visible on both figures when just half a degree of backlash is modelled in the elevator linkage. The limit cycle has a period of approximately one second, and more importantly, the amplitude remains constant throughout the duration of the test. It is important to note that this type of behaviour should not be mitigated by redesigning the control system; instead, the amount of backlash in the linkages should be minimised mechanically in order to restore linear functionality. Although every effort was made to minimise backlash in the linkage system, the most effective way would be to replace the steel rods with a hydraulic actuator system, which was far outside the scope of this project. However, it is clear from the plots depicted in Figure 8.9 that the amplitude of the benign limit cycle is relatively small and does not cause the aircraft to become unstable. Furthermore, the amplitude and period of the limit cycle are small enough that it should not have a significant effect on altitude regulation. The fact that altitude control remains mostly unaffected is an important aspect to consider, since down-range landing accuracy is highly dependent on glideslope tracking performance. To this end, it can be concluded that backlash is an undesirable non-linearity, characteristic of mechanical linkage systems, that is difficult to mitigate and usually results in oscillatory behaviour. Reference will be made to this discussion upon investigation of the practical flight test results later in this section.

8.7.1.1   Airspeed Controller

In following a strategic and systematic approach to practical FCS verification, the controllers were tested sequentially to inspire confidence between successive activations. This means that when the longitudinal controllers were tested, the lateral controllers had not yet been evaluated, and the safety pilot was therefore instructed to maintain lateral control of the aircraft. Figure 8.10a shows a comparative airspeed step response between HIL simulation and practical flight data. It is apparent that the two responses agree exceptionally well, and that the associated thrust command, depicted in Figure 8.10b, remains within practically attainable limits. The accuracy of the thrust response matching can be attributed to the drag coefficient, which was amended during the model verification phase detailed in Section 8.6. The original AVL drag coefficient resulted in a trim thrust of approximately 7 N for straight and level flight at 18 m/s. However, it is apparent from Figure 8.10b that the trim thrust is on the order of 20 N for the practical aircraft. It is apparent that the airspeed response is adequately damped with a peak time of approximately 3 s, which is considered acceptable for this application.

(a) HIL vs practical flight data

(b) Associated thrust command
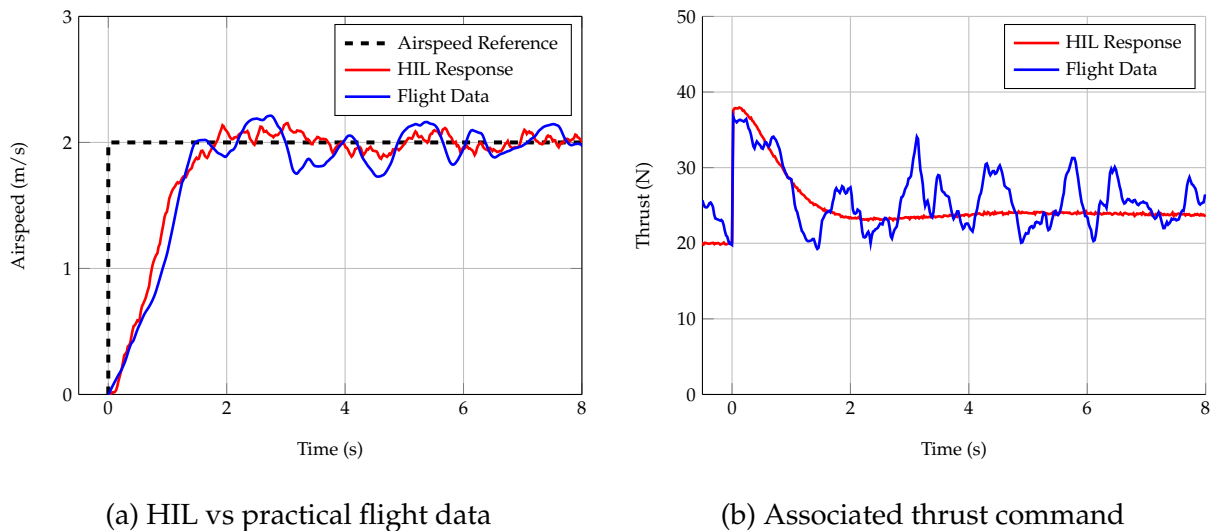
Figure 8.10: Airspeed controller comparison

8.7.1.2   Climb Rate Controller

Figure 8.11a shows a comparative climb rate step response between HIL simulation and practical flight data. Once again, it is apparent that the two responses agree exceptionally well despite the noisy data obtained from the practical flight. The first plot in Figure 8.11b shows the associated inner-loop NSA command generated by the climb rate controller. The second and third plots in Figure 8.11b show the associated elevator and flaps command generated by the inner-loop NSA controller. It is apparent that the practical NSA response and associated actuator deflections correspond well with the HIL simulation data. Note the benign limit cycle in the practical flight test data. This can be attributed to the non-linear effects of backlash in the elevator linkage, as discussed in Section 8.7.1.

(a) HIL vs practical flight data   (b) Inner-loop and actuator commands
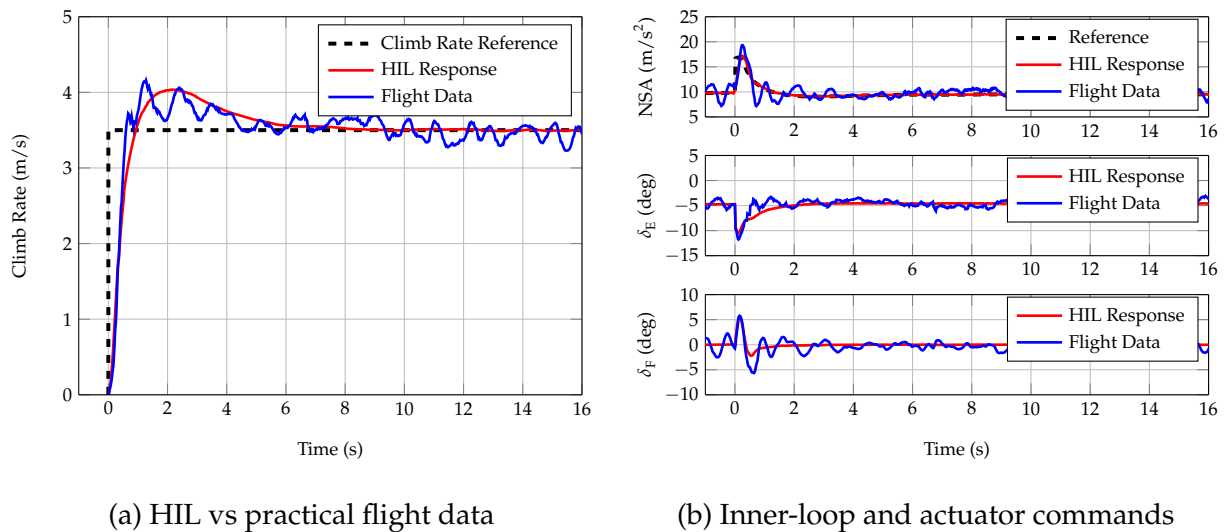
Figure 8.11: Climb rate controller comparison

8.7.1.3   Altitude Controller

Figure 8.12a shows a comparative altitude step response between HIL simulation and practical flight data. The two responses agree exceptionally well despite the safety-pilot-induced disturbances that occur around 12 s.[1] The first plot in Figure 8.12b shows the associated climb rate command generated by the altitude controller. The second and third plots in Figure 8.12b show the associated elevator and flaps command generated by the inner-loop NSA controller. The practical climb rate response and associated actuator deflections clearly correspond well with the HIL simulation data. Note that the observed limit cycle, apparent in the climb rate response of Figure 8.11a, does not have a significant effect on the altitude response and will therefore not degrade down-range landing accuracy.

(a) HIL vs practical flight data   (b) Inner-loop and actuator commands
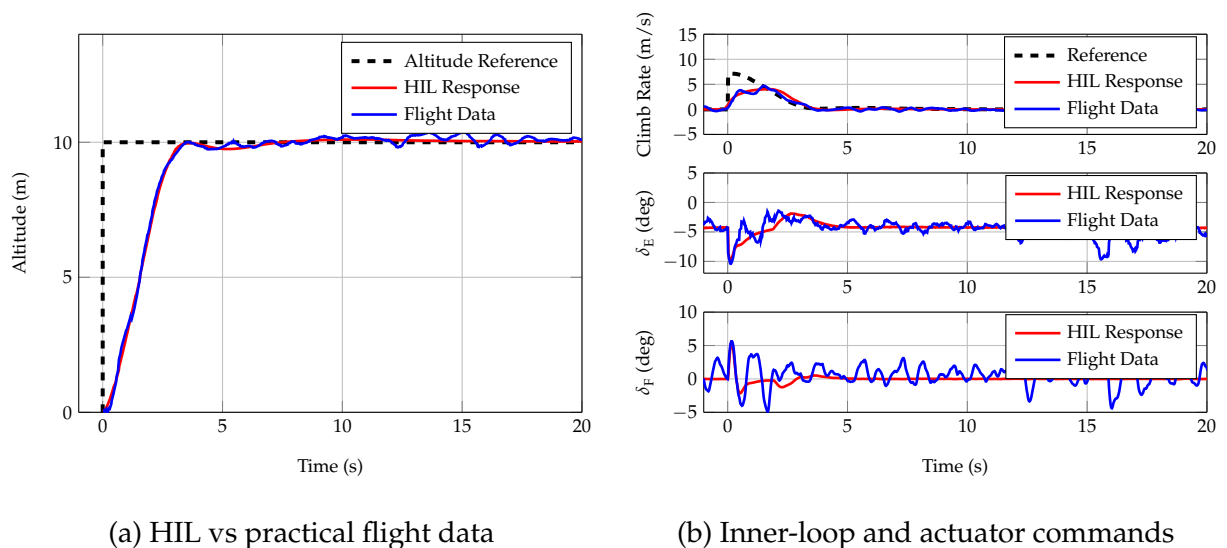
Figure 8.12: Altitude controller comparison

---

[1]Safety-pilot-induced disturbances are a result of the safety pilot contaminating the lateral control inputs.

8.7.1.4 Roll Angle Controller

With the verification of the longitudinal controllers detailed in the preceding sections, verification of the lateral controllers can proceed with the longitudinal controllers engaged - this will mitigate the risk of safety-pilot-induced disturbances. Figure 8.13a shows a comparative roll angle step response between HIL simulation and practical flight data. The two responses correspond adequately despite the noisy data obtained from the practical flight. It became apparent during flight testing that roll angle data was very susceptible to atmospheric disturbances, which were more pronounced during this particular test. Nevertheless, it is apparent that the transient response and steady-state characteristics correspond well. The first plot in Figure 8.13b shows the associated roll rate command generated by the roll angle controller. The second plot in Figure 8.13b shows the associated aileron command generated by the inner-loop roll rate controller. As can be seen, the practical roll rate response and associated actuator deflections correspond well with the HIL simulation data.

(a) HIL vs practical flight data

(b) Inner-loop and actuator commands
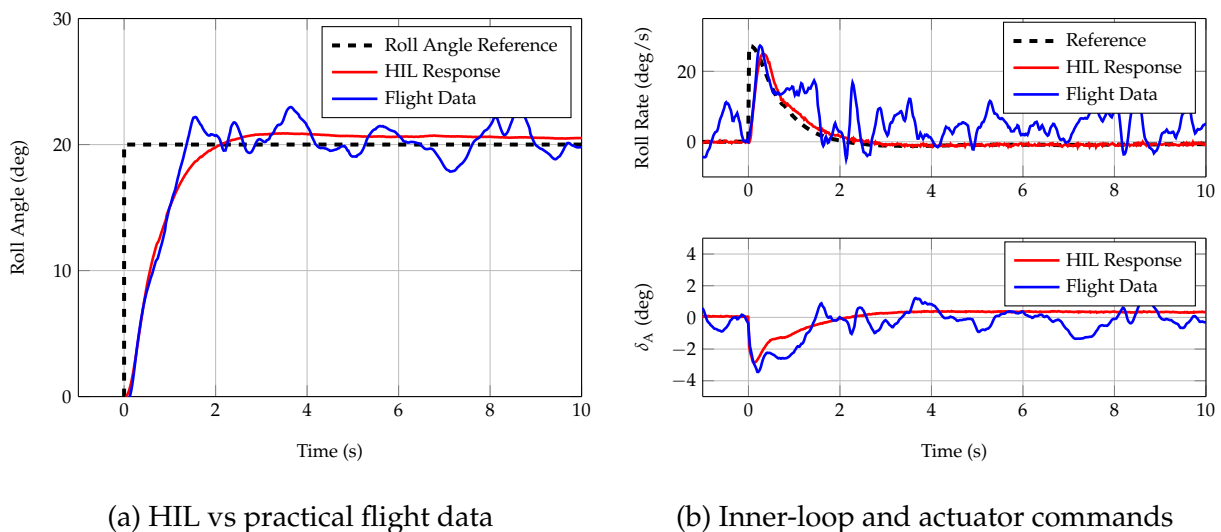
Figure 8.13: Roll angle controller comparison

8.7.1.5 Guidance Controller

Undoubtedly the most challenging controller to evaluate from a step response perspective was the guidance controller. The requirement for the aircraft to remain within VLOS complicated the testing process, as this severely shortened the length of track with which the step could be executed. The second limiting factor was the telemetry system, which showed signs of premature degradation (later attributed to high RF noise floor on the day). This meant that step commands would only be received when the aircraft was merely 200 m away. This resulted in the safety pilot assuming lateral control before the guidance controller had completely settled. In an attempt to reduce pilot workload and simplify the test procedure, the autopilot was put into waypoint navigation mode so that it would navigate the rectangular circuit whilst cross-track steps were initiated from the ground station. However, the degradation of the telemetry system meant that steps would often start before the guidance controller had completely settled after navigating a

corner. Nevertheless, after numerous attempts the response shown in Figure 8.14a was obtained. It should be noted that the response has been shifted to coincide with simulation data for comparative purposes. It is apparent that the responses agree exceptionally well despite the complicated procedure. The first plot in Figure 8.14b shows the associated roll angle command generated by the guidance controller. The second plot in Figure 8.14b shows the associated aileron command generated by the inner-loop roll rate controller. As seen here, the practical roll angle response and associated actuator deflections correspond well with the HIL simulation data.

(a) HIL vs practical flight data   (b) Inner-loop and actuator commands
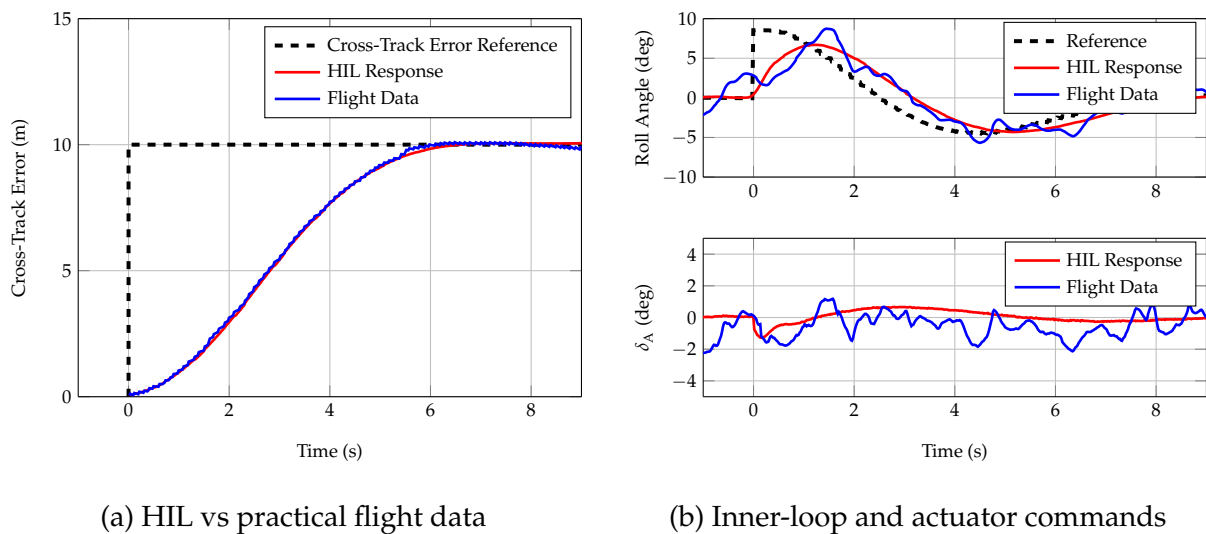
Figure 8.14: Guidance controller comparison

8.7.1.6 Heading Controller

Figure 8.15a shows a comparative heading step response between HIL simulation and practical flight data. It is apparent that the two responses correspond adequately despite the noisy data obtained from the practical flight. Due to the aircraft's natural directional stability, atmospheric disturbances have a significant effect on the heading controller response, especially when forcing the aircraft into a sideslip configuration. Incorrectly modelled side force coefficients also contribute to the observed discrepancies. Nevertheless, the practical response is deemed acceptable for the purpose of de-crabbing the aircraft and initiating a low-wing approach. The first plot in Figure 8.15b shows the associated LSA command generated by the heading controller. The second plot in Figure 8.15b shows the associated rudder command generated by the inner-loop LSA controller. Clearly, the practical LSA response and associated actuator deflections correspond well with the HIL simulation data. Note the benign limit cycle in the practical flight test data. This can be attributed to the non-linear effects of backlash in the rudder linkage, as discussed in Section 8.7.1.

For each controller response discussed in this section, the effects of atmospheric disturbances are most evident on the inner loops, becoming less evident with each successive loop closure. This can be attributed to the strong disturbance rejection characteristics of the fast inner-loop controllers and the carefully designed flight control architecture depicted in Figure 5.1.

(a) HIL vs practical flight data

(b) Inner-loop and actuator commands
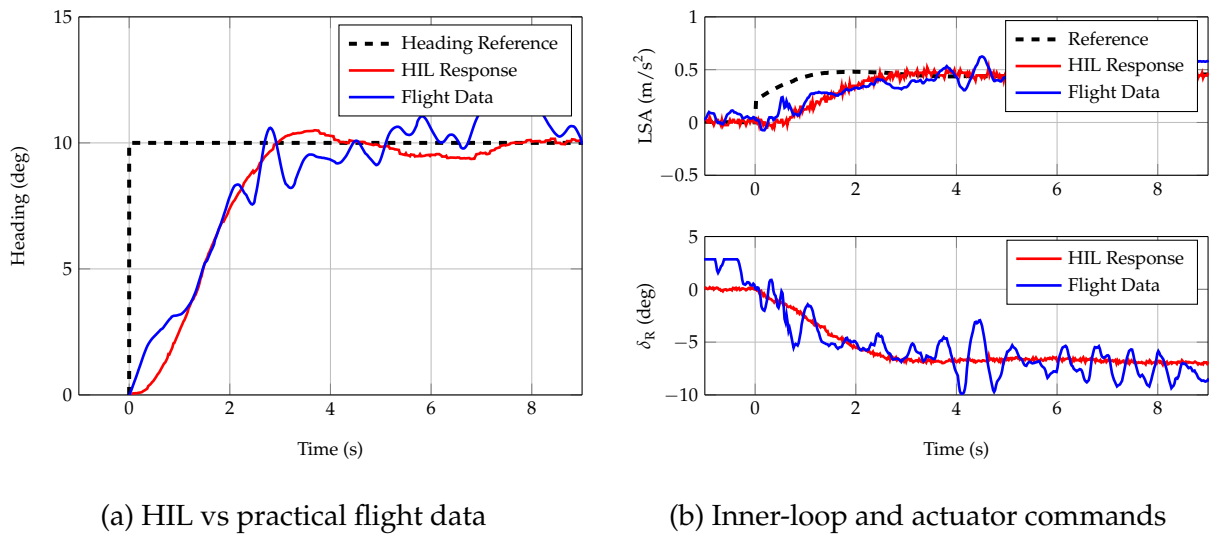
Figure 8.15: Heading controller comparison.

8.7.2   Navigation and Landing

Once the individual longitudinal and lateral controllers had been evaluated, the focus of the flight tests shifted towards fully autonomous flight, unassisted by safety pilot control except in the event of an emergency. Figure 8.16a shows the aircraft's trajectory when autonomously navigating a particular waypoint track in the simulation environment compared to that observed during practical flight testing.

(a) Waypoint navigation

(b) Glideslope tracking
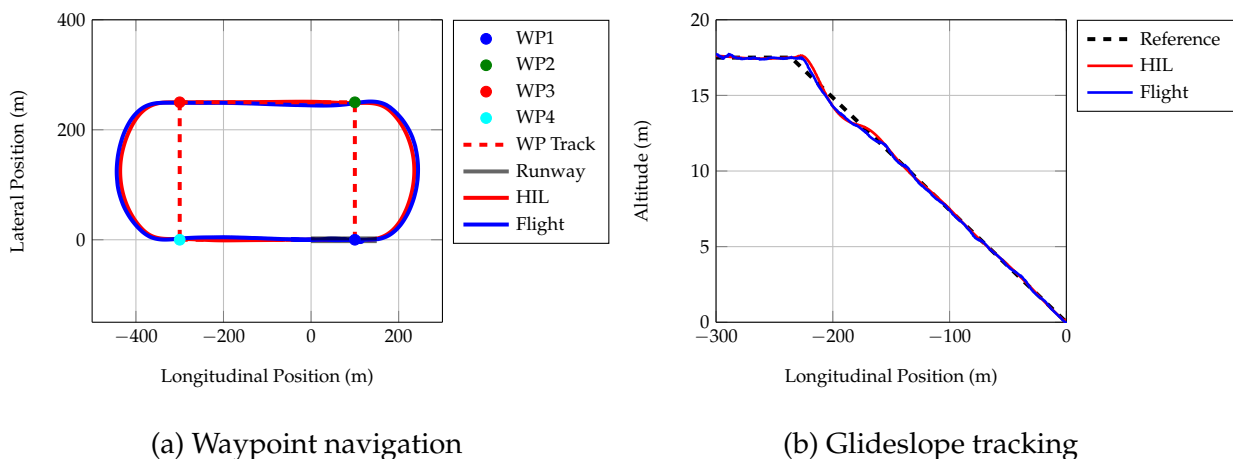
Figure 8.16: Waypoint navigation and glideslope tracking

It is apparent that the trajectories agree exceptionally well, despite the slight overshoot at the completion of a turn that the practical data exhibits - this can be attributed to atmospheric disturbances not present during the associated HIL simulation. Nevertheless, the slight deviation is minimised well before the runway and it can be concluded that the navigation system is capable of executing clean, accurate circular turns that should maximise lateral landing accuracy. Figure 8.16b shows the aircraft's altitude when autonomously tracking a glideslope trajectory in the simulation environment compared to that observed during practical flight testing. It is apparent

that the trajectories agree exceptionally well, to the extent that even the initial transient response at the transition point corresponds with simulation data. It is imperative that glideslope tracking in a practical environment be as accurate as the simulations suggest, since relatively small altitude tracking errors result in large down-range offsets due to the inherently shallow glideslope angle. The data depicted in Figure 8.16 is complemented by an exceptionally accurate landing, the position of which is illustrated as the blue cross overlaid on the point cloud of Figure 8.18b. It should be noted that two additional landings in calm atmospheric conditions were also conducted on the same day, with similar results.

8.7.3 Practical Verification of Landing Techniques

Up to this point, all of the data presented was obtained during flight in calm atmospheric conditions. It is first necessary to test autoland performance in calm conditions, so as to obtain a baseline for comparative purposes, in order to successfully evaluate the extent of the performance degradation associated with crosswind landings. The focus of the remaining flight tests was centred around evaluating the landing accuracies associated with each crosswind technique, and then comparing those positions with the landing accuracy prediction system developed in Chapter 7. The flight data presented in this section was all obtained on the final day of testing in the presence of a 13 km/h, $40°$ crosswind (approximate). The exact wind profile, obtained from a weather station located at the flight test facility, is shown in Figure E.1 for further perusal - crosswind landing data discussed in this section was captured during the *Test Set 1* time interval.

It is important to note that for the following plots, touchdown occurs at approximately 15 s, where the graph axis ends. Figure 8.17a shows a comparative altitude error plot during final approach as the aircraft transitions onto the glideslope and proceeds to the intended touchdown position. Perhaps the most noticeable difference is that the negative altitude error is actually more pronounced for flight in calm atmospheric conditions. This could be attributed to the additional lift caused by varying gust disturbances, which reduced the amount of altitude loss experienced at the glideslope transition point for this particular test. Nevertheless, the error plots follow a similar pattern for each technique, as expected, with the only major variations arising from wind gusts and other atmospheric disturbances. It is possible to minimise the amount of altitude deviation observed at the transition point by rate-limiting the feed-forward climb rate command instead of providing an instantaneous step. However, it is apparent that the altitude error is sufficiently minimised during the last five seconds prior to touchdown, resulting in exceptional down-range landing accuracy.

Figure 8.17b shows a comparative lateral deviation plot as the aircraft approaches the runway. Due to the low bandwidth of the outer-loop guidance controller, the initial cross-track error in each case is a result of the circular turn that happens just before the glideslope transition point. Both the crabbed and de-crab techniques follow a similar profile to flight in calm atmospheric conditions, with the slight variation attributed to varying gust disturbances that in fact pushed the aircraft closer to the intended waypoint track in this instance. It is clear that the low-wing approach exhibits a significantly different lateral deviation profile in comparison to the other two techniques. This is expected, since the heading controller is activated at the glideslope transition point, resulting in an initial conflict with the guidance controller as the aircraft enters into

a low-wing configuration. Nevertheless, it is apparent that the guidance controller is capable of minimising the cross-track error in each case before touchdown.

(a) Glideslope tracking   (b) Cross-track deviation
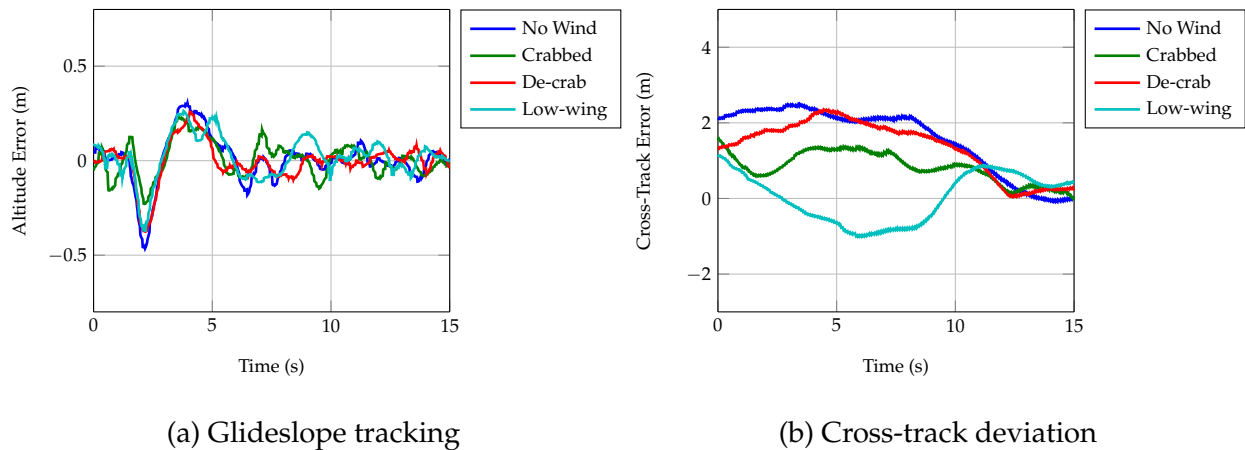
Figure 8.17: Glideslope tracking and observed cross-track deviation. Crosswind magnitude and direction are shown in Figure E.1.

Figure 8.18a shows a comparative attitude plot for each landing technique observed during final approach. As can be seen, the aircraft touches down with a heading angle error of approximately $15°$ when a crabbed landing is executed. This excessive heading angle error actually caused the aluminium landing gear on the test vehicle to bend slightly and resulted in the aircraft veering off the runway. The de-crab technique was able to minimise this error to approximately $5°$, significantly reducing landing gear side-loads and violent runway deviations. The error is reduced even further by the low-wing technique, as the heading controller is engaged much earlier in the approach. It is apparent from Figure 8.18a that as the heading angle error is minimised, the resultant bank angle increases from zero to approximately $5°$ when the low-wing technique is executed.

(a) Aircraft attitude   (b) Landing position point cloud
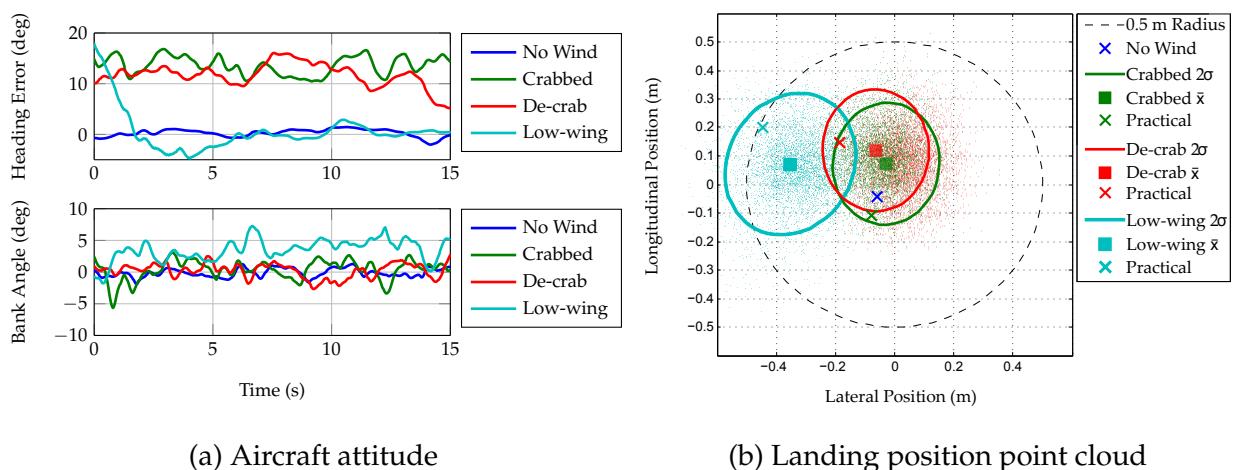
Figure 8.18: Autoland performance in the presence of a crosswind. Crosswind magnitude and direction are shown in Figure E.1.

The landing accuracy prediction system developed in Chapter 7 was post-simulated with wind conditions that appropriately described the recorded wind data. Touchdown positions associated with each technique are overlaid on the landing accuracy prediction point cloud of Figure 8.18b. The recorded touchdown positions seem to fall within their respective 2σ deviation ellipse, which bodes well for the fidelity of both the prediction system and the associated non-linear simulation environment. It should be noted that data points obtained from three practical landings in windy conditions are not sufficient to fully validate the prediction system and simulation environment in their entirety. This would typically require multiple flight tests under various crosswind conditions for which certain constraints did not allow here. These include time, availability of staff, weather, and cost. However, the aforementioned procedure outlines the typical validation process.

The practical results discussed above were obtained from flight in moderate crosswind conditions. During the same day of flight testing, the wind picked up significantly and gust magnitudes in the region of 20 km/h were recorded by the weather station - *Test Set 2* in Figure E.1. Landing in these conditions proved challenging and the results were predictable. Autonomous landing using both the crabbed and de-crab technique proved successful, although landing accuracies were significantly degraded. The low-wing landing technique proved unsuccessful in these severe conditions, as the rudder saturation problem significantly degraded controllability. As a result, the guidance controller was incapable of adequately minimising the cross-track error before the state machine entered its *Pre-land* state. This resulted in automatic landing abortion, and a go-around was initiated by the autoland system after every unsuccessful attempt. Ultimately, the de-crab landing technique was used to land the aircraft safely. These findings correspond with the observations made during various HIL simulations. In moderate conditions, the low-wing landing technique has the advantage of completely minimising the heading error before touchdown. However, in severe conditions the rudder is prone to saturation and the guidance controller is unable to adequately minimise the cross-track error. Based on the findings presented throughout this thesis, it can be concluded that the de-crab technique is the most efficient and safest way of landing this particular aircraft under severe crosswind conditions.

8.8   Summary

This chapter introduced the hardware layout, avionics structure, and ground station equipment required for further verification through HIL simulations and practical flight testing. An overview of the flight test campaign showed that careful and strategic planning was conducted before each test to minimise the risk of failure. The aircraft model was first verified by comparing flight data to simulated HIL data in an attempt to increase model fidelity and inspire confidence in the system before engaging the autopilot. Flight test results were then critically analysed and compared with simulation data in order to evaluate system performance and to identify the cause of possible discrepancies. Explanations for any discrepancies between simulation and practical results were provided, and the limitations associated with each crosswind landing technique were also discussed. It was concluded that the de-crab landing technique is the most efficient and safest way of landing this particular aircraft under severe crosswind conditions. In general, recorded practical flight data matched simulation data exceptionally well, and the results proved that the autoland system is capable of accurately landing the aircraft in both calm and crosswind conditions.

<div align="right">

CHAPTER 9

</div>

Conclusion and Recommendations

9.1 Conclusion

This thesis has reported the design and practical implementation of an autopilot capable of accurately landing a fixed-wing aircraft in adverse weather conditions. A standardised model was developed as a function of physical aircraft parameters, which allows it to be readily applied to other conventional aircraft. The aircraft model was then verified and critically analysed to ensure the design of a high-fidelity, high-bandwidth control system architecture capable of meeting strict design requirements. Physical landing constraints were assessed and closely monitored by a state machine that governs controller activation times through strategically planned state transitions. Flight control system performance was then verified through high-fidelity, non-linear simulations with refined dynamic models that encapsulate the effects of sensor noise and external disturbances. Finally, the autopilot was subjected to numerous practical flight tests, which yielded excellent results. The results clearly demonstrate that the autoland system is capable of executing fully autonomous landings, accurate to well within a 1.5 m radius of the intended touchdown point, in both calm and adverse atmospheric conditions. The primary objective of this research has therefore been achieved. Additionally, the system proved that it was capable of minimising landing gear side-loads and runway excursion events through effective sequencing of the heading controller. The secondary objective of this research has therefore also been achieved. The practical success of the autopilot can be largely attributed to the high-bandwidth controller architecture and the extensive system verification through high-fidelity, non-linear simulations. Based on the findings presented in this thesis, it can be concluded that the de-crab technique is the most efficient and safest way of landing this particular aircraft under severe crosswind conditions.

The detailed list of objectives, described in Section 1.4, provided the study with both direction and purpose. The achievement of the stated objectives also provided a way of quantifying the overall success of the project. Table 9.1 shows the objectives and achievements cross-reference table that links the stated objectives to the chapters in the thesis where they have been achieved.

Table 9.1: Objectives and achievements cross-reference table

No.	Category	Status	Chapters in Thesis
1	Modelling	Achieved	Chapters 3 and 4
2	Control system design	Achieved	Chapter 5
3	Navigation and landing strategies	Achieved	Chapter 6
4	Verification	Achieved	Chapters 7 and 8

With the successful achievement of the aforementioned objectives, it can be concluded that the work presented in this thesis features a practically verified autoland system capable of accurately landing a fixed-wing unmanned aircraft under crosswind conditions.

9.2 Contributions

The work completed for this thesis offers the following contributions to the Autonomous Systems research group at the Electronic Systems Laboratory:

Primary contributions:

- A fine-tuned, high-performance control system architecture with strong disturbance rejection characteristics was developed.

- A high-fidelity simulation environment with refined dynamic models was designed, implemented and verified.

- A high-fidelity landing accuracy prediction system was developed and validated through practical flight testing.

Secondary contributions:

- The practical test vehicle used for autopilot verification was purpose-built from scratch using high-quality components, and will serve as a reliable test bed for future research. The work contained in this thesis demonstrates that the aircraft model is accurate and that the FCS functions as the simulations suggest.

- The newly installed sensory system has been calibrated to the highest possible standard, which should contribute to the accuracy and success of future flight tests.

- The groundwork has been established for further research into accurate autonomous landings, which could include aspects such as landing a fixed-wing UAV on a moving platform in crosswind conditions.

- The system was designed in a modular fashion, with each submodule responsible for a particular system function, to maximise re-usability across various UAV platforms.

- The concept of variable logging rates was introduced to prioritise more important information so that data-logging cycles do not inadvertently impact control loop times.

- An embedded data extraction module was written in C code to replace the inefficient MAT-LAB extraction script previously used in the ESL.

- Instead of simply relying on conservative predetermined flight times, a battery voltage monitoring board was designed and developed to monitor the propulsion system's battery capacity in an attempt to maximise flight test efficiency.

- The wind models were evaluated and ultimately redeveloped, as numerous bugs and flaws plagued the existing models.

9.3   Recommendations for Further Research

Recommendations regarding the improvement and possible extension of the current autopilot system are discussed in point form below. It should, however, be noted that adding complexity to a system increases its chances of failure, and thus additions should always be considered in light of the ultimate goal.

Airframe and Avionics:

- The nose wheel linkage should be substantially shortened to reduce backlash and improve runway controller performance.

- The aluminium landing gear is prone to flexing during hard landings and should be replaced with a more rigid setup.

- The reliability of the 2.4 GHz MaxStream data link was a significant limiting factor during the practical flight tests. The original monopole antenna was even replaced with a directional Yagi antenna on the ground station in an attempt to improve link quality. It is recommended that a higher-power data link solution be investigated.

- A DGPS with faster update rates would minimise the latency associated with position and velocity measurements, resulting in improved autoland accuracy.

- The data-logging system on board the aircraft should be redesigned, as this often leads to delays in the control loop time. Introducing the concept of variable logging rates significantly reduced these delays, although the associated hardware is now the limiting factor.

Control System:

- A ground track heading controller and turn rate regulator should be introduced as intermediate components between the roll angle controller and guidance controller. This should effectively deal with the problem of activating the autopilot far from the intended ground track. As mentioned in this thesis, activating the guidance controller when the aircraft is far from the intended track will result in aimless loitering as the bank angle command is saturated.

- Instead of using a conventional PI control law for the airspeed controller, it is recommended to use integral control in the forward path and proportional control in the feedback path. This will remove the controller zero and minimise undesirable overshoot at the cost of a slower controller.

- The climb rate command that is fed-forward during the glideslope tracking phase should be rate limited to minimise the adverse transient effects at the transition point.

- Gain scheduling is often used to enhance autopilot performance when operating over a wide range of velocities. For the autoland procedure, it was decided that the benefits were not worth the added complexity for such a small velocity range. However, if the autopilot system is extended to perform automatic take-off, then gain scheduling is indeed recommended.

- In order to further improve landing accuracy in windy conditions, the concept of Direct Drag Control (DDC) should be investigated.

Further expansion of operational capabilities:

- With the successful implementation and verification of an accurate landing system presented in this thesis, an arrester cable mechanism could be used to capture the aircraft after touchdown on a short runway.

- The capabilities of the autopilot system could be extended to include autonomous landing on a moving platform in crosswind conditions, e.g. on an aircraft carrier out at sea. The addition of such capabilities would require prediction and estimation of the ship's motion. Research conducted by Fourie [48] could serve as a basis for further expansion.

APPENDICES

APPENDIX A

Appendix A: Mathematical Expressions

A.1   Vector Operations
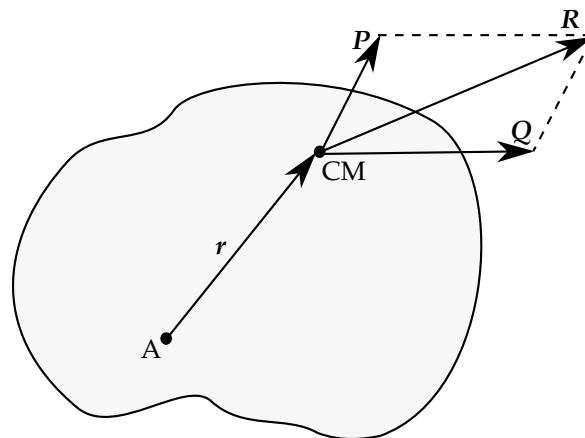
Figure A.1: Free body diagram with vector notation

A.1.1   Vector Notation

Vector quantities are written in capital or lower case boldface type, e.g. $\boldsymbol{P}$ or $\boldsymbol{r}$.

A.1.2   Unit Vectors

Unit vectors are expressed as,

$$\boldsymbol{i}, \quad \boldsymbol{j}, \quad \boldsymbol{k} \tag{A.1}$$

so that,

$$\boldsymbol{P} = \boldsymbol{i}P_x + \boldsymbol{j}P_y + \boldsymbol{k}P_z \tag{A.2}$$

where the magnitude of the vector is given by,

$$|\boldsymbol{P}| = \sqrt{P_x^2 + P_y^2 + P_z^2} \tag{A.3}$$

A.1.3   Differentiating a Vector

$$\frac{d\boldsymbol{P}}{dt} = \dot{\boldsymbol{P}} \tag{A.4}$$

$$= \boldsymbol{i}\dot{P}_x + \boldsymbol{j}\dot{P}_y + \boldsymbol{k}\dot{P}_z$$

$$\frac{d\left(\boldsymbol{P} \times \boldsymbol{Q}\right)}{dt} = \boldsymbol{P} \times \dot{\boldsymbol{Q}} + \dot{\boldsymbol{P}} \times \boldsymbol{Q} \tag{A.5}$$

A.1.4   Time Derivative of a Vector Measured from a Translating-rotating System

The time derivative of any vector $\boldsymbol{P}$ as observed from the fixed X, Y, Z reference frame is equal to the time rate of change of $\boldsymbol{P}$ as observed from the x, y, z translating-rotating reference frame [49],

$$\dot{\boldsymbol{P}}_{XYZ} = \dot{\boldsymbol{P}}_{xyz} + \boldsymbol{\omega} \times \boldsymbol{P} \tag{A.6}$$

where $\boldsymbol{\omega}$ is the angular velocity of the x, y, z reference frame relative to the fixed X, Y, Z reference frame.

A.2   Small Angle Approximation

The standard small angle approximations are given by,

$$\cos A \approx 1 \tag{A.7}$$

$$\sin A \approx A \tag{A.8}$$

where A is a small angle.

APPENDIX B

Appendix B: Aircraft Model

B.1   Standard Flight Conditions

The standard flight conditions are defined in this section. These values are used in the analysis of the linear aircraft model, as well as in the design of the flight control system.

Air Density: Air density is inversely proportional to altitude and is largely dependent on air temperature and humidity. Air density was approximated as a constant because of the relatively small ranges involved during practical flight testing. The aircraft will not fly higher than 150 m from the ground and not more than 500 m from the take-off location. The airfield at which practical flight tests were conducted is nearly at sea level, and tests are often performed in the early morning. To this end, air density can be approximated as,

$$\rho = 1.225 \text{ kg/m}^3 \tag{B.1}$$

which corresponds to the density of air at sea level at $15^\circ C$.

Gravitational Acceleration: It was assumed for the case of a rigid body in a uniform gravitational field that,

$$g = 9.81 \text{ m/s}^2 \tag{B.2}$$

Trim Airspeed: Trim airspeed was selected as,

$$\bar{V}_T = 18 \text{ m/s} \tag{B.3}$$

which is the velocity around which the linearisation of the aircraft dynamics was conducted.

B.2   Airframe Specifications

Physical aircraft parameters are discussed in this section.

Mass: The total aircraft Take-Off-Weight (TOW) was measured using a high-accuracy digital scale and was found to be,

$$m = 6.35 \, \text{kg} \tag{B.4}$$

Moment of Inertia: The moments of inertia for this aircraft were determined experimentally using the double pendulum method as described by Peddle [3]. This method involves suspending the aircraft by two equally long strings parallel to the moment of inertia axis of concern. The aircraft is then perturbed from its state of rest and the period of oscillation recorded. The equation that relates oscillation period to the moment of inertia is [11],

$$I = \frac{mgd^2}{4\pi^2 l} T^2 \tag{B.5}$$

where d is the distance between each string and the axis of concern, l is the length of each string, and T is the period of oscillation measured in seconds. Using this equation, the moments of inertia were calculated as,

$$\mathbf{I} = \begin{bmatrix} 0.722 & 0 & 0 \\ 0 & 0.514 & 0 \\ 0 & 0 & 0.925 \end{bmatrix} \tag{B.6}$$

Engine Model Parameters: The maximum thrust of the electric motor was measured by means of a thrust test jig and was found to be,

$$T_{max} = 40 \, \text{N} \tag{B.7}$$

and the time delay between the commanded and generated thrust was measured as,

$$\tau_e = 0.25 \, \text{s} \tag{B.8}$$

Geometric Properties: Table B.1 summarises the geometric properties of the test vehicle. The Oswald efficiency factor e was estimated from basic aircraft geometric parameters in accordance with work done by Nita and Scholz [31]. In this work, an empirical diagram is obtained from flight data, which allows the Oswald efficiency factor to be calculated as,

$$e = \frac{1}{Q + P\pi A} \tag{B.9}$$

where A is the aspect ratio of the wing, and Q and P are constant experimental values equal to 1.05 and 0.007 respectively.

Table B.1: Wing geometric parameters

Parameter	Symbol	Value	Unit
Root chord	c_r	0.373	m
Tip chord	c_t	0.333	m
Mean chord	$\bar{\bar{c}}$	0.363	m
Wing span	b	1.918	m
Wing area	S	0.6975	m^2
Aspect ratio	A	5.28	ND
Oswald efficiency factor	e	0.858	ND

B.3   Aerodynamic Model Parameters

The aerodynamic model parameters consist of non-dimensional stability and control derivatives. As mentioned in Section 3.4.2 these derivatives were obtained using a Vortex Lattice program known as Athena Vortex Lattice (AVL). The airframe was modelled in AVL, as shown in Figure B.1, with the main wing modelled as a Clark-Y airfoil, and the horizontal and vertical stabilisers modelled as NACA 0004 airfoils. Note that a flat rectangular fuselage is added to the model in order to obtain a more accurate estimation of the side force derivatives.
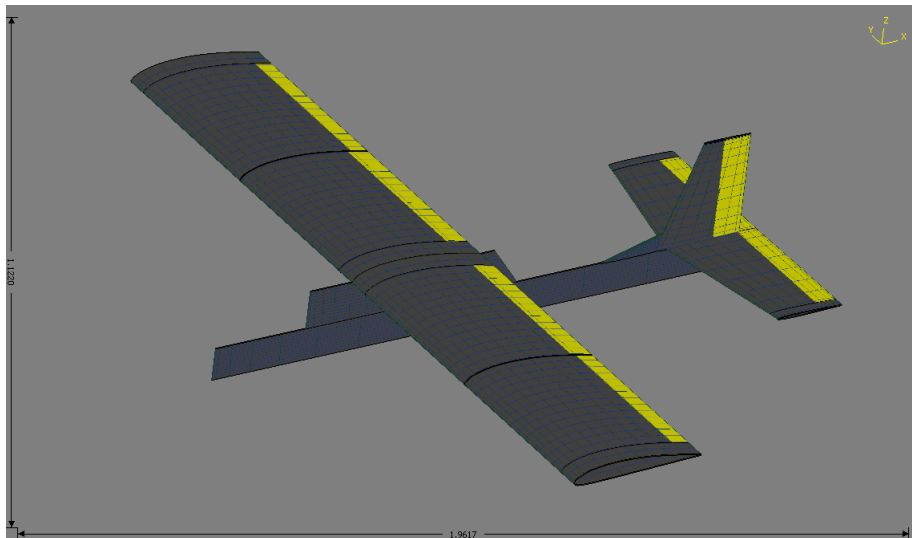
Figure B.1: Aircraft geometry in AVL using dimensions for the Phoenix Trainer .60 model

B.3.1   Aerodynamic Coefficients

The stability and control derivatives obtained from AVL are summarised in Tables B.2 and B.3 below.

Table B.2: Force derivatives obtained from AVL. Note that the value for parasitic drag was changed to $C_{D_0} = 0.12$ following practical flight test data analysis.

Lift force	Value	Side force	Value	Drag force	Value
C_{L_0}	0.243200	C_{y_0}	0.000000	C_{D_0}	0.033600
C_{L_α}	4.240906	C_{y_α}	0.000000		
C_{L_β}	0.000000	C_{y_β}	-0.211019		
C_{L_P}	0.000000	C_{y_P}	0.108287		
C_{L_Q}	7.046092	C_{y_Q}	0.000000		
C_{L_R}	0.000000	C_{y_R}	0.150403		
$C_{L_{\delta_E}}$	0.419064	$C_{y_{\delta_E}}$	0.000000		
$C_{L_{\delta_F}}$	0.936323	$C_{y_{\delta_F}}$	0.000000		
$C_{L_{\delta_A}}$	0.000000	$C_{y_{\delta_A}}$	0.000780		
$C_{L_{\delta_R}}$	0.000000	$C_{y_{\delta_R}}$	0.115794		

Table B.3: Moment derivatives obtained from AVL

Roll moment	Value	Pitch moment	Value	Yaw moment	Value
C_{l_0}	0.000000	C_{m_0}	-0.026700	C_{n_0}	0.000000
C_{l_α}	0.000000	C_{m_α}	-0.780993	C_{n_α}	0.000000
C_{l_β}	-0.056602	C_{m_β}	0.000000	C_{n_β}	0.038208
C_{l_P}	-0.415489	C_{m_P}	0.000000	C_{n_P}	-0.031465
C_{l_Q}	0.000000	C_{m_Q}	-7.220962	C_{n_Q}	0.000000
C_{l_R}	0.127831	C_{m_R}	0.000000	C_{n_R}	-0.067882
$C_{l_{\delta_E}}$	0.000000	$C_{m_{\delta_E}}$	-0.922107	$C_{n_{\delta_E}}$	0.000000
$C_{l_{\delta_F}}$	0.000000	$C_{m_{\delta_F}}$	0.111822	$C_{n_{\delta_F}}$	0.000000
$C_{l_{\delta_A}}$	-0.257631	$C_{m_{\delta_A}}$	0.000000	$C_{n_{\delta_A}}$	0.007213
$C_{l_{\delta_R}}$	0.000920	$C_{m_{\delta_R}}$	0.000000	$C_{n_{\delta_R}}$	-0.049972

B.3.2   Trim

Table B.4 summarises the values contained in the trim state vector $\boldsymbol{R}_T$ for this particular airframe, with the standard flight conditions and aircraft-specific parameters as defined in the preceding sections.

Table B.4: Trim state variables

Symbol	Label	Value	Unit
Trim angle of attack	α_T	3.1898	deg
Trim sideslip angle	β_T	0	deg
Trim roll angle	Φ_T	0	deg
Trim elevator deflection angle	δ_{E_T}	-4.3596	deg
Trim flap deflection angle	δ_{F_T}	0	deg
Trim aileron deflection angle	δ_{A_T}	0	deg
Trim rudder deflection angle	δ_{R_T}	0	deg
Trim engine thrust	T_T	6.6152	N

B.3.3   Lateral-directional Dynamic Decoupling

Lateral-directional dynamic decoupling conditions and constraints:

$$\left| \frac{C_{n_P}}{C_{l_P}} \right| = 0.0757 \ll 0.5310 = \left| \frac{C_{n_R}}{C_{l_R}} \right| \tag{B.10}$$

$$\left| \frac{C_{n_P}}{C_{l_P}} \right| = 0.0757 \ll 0.6750 = \left| \frac{C_{n_\beta}}{C_{l_\beta}} \right| \tag{B.11}$$

$$\left| \frac{C_{n_{\delta_A}}}{C_{l_{\delta_A}}} \right| = 0.0280 \ll 0.5310 = \left| \frac{C_{n_R}}{C_{l_R}} \right| \tag{B.12}$$

$$\left| \frac{C_{n_{\delta_A}}}{C_{l_{\delta_A}}} \right| = 0.0280 \ll 0.6750 = \left| \frac{C_{n_\beta}}{C_{l_\beta}} \right| \tag{B.13}$$

$$\left| \frac{C_{n_P}}{C_{l_P}} \right| = 0.0757 \ll 54.3174 = \left| \frac{C_{n_{\delta_R}}}{C_{l_{\delta_R}}} \right| \tag{B.14}$$

$$\left| \frac{Y_R}{m\bar{V}_T} \right| = 0.0097 \ll 1 \tag{B.15}$$

B.4   Linearised Aircraft Model

The standard linearised aircraft model detailed in this section is provided by Etkin and Reid [21]. This simplified model is used to verify the model obtained from the unsimplified linearisation

process detailed in Chapter 4. The simplified longitudinal aircraft model is given as,

$$
\begin{bmatrix} \dot{\bar{v}} \\ \dot{\alpha} \\ \dot{q} \\ \dot{\theta} \end{bmatrix} = \begin{bmatrix} \frac{\rho \bar{V}_T S C_{X_T}}{m} & \frac{\bar{q}_T S}{m}\left(C_{L_\alpha}\alpha_T + C_{L_T} - \frac{2C_{L_T}C_{L_\alpha}}{\pi A e}\right) & 0 & -g\cos\Theta_T \\ -\frac{\rho S C_{L_T}}{m} & -\frac{\bar{q}_T S}{m\bar{V}_T}C_{L_\alpha} & 1 - \frac{\bar{q}_T S}{m\bar{V}_T}\frac{\bar{c}}{2\bar{V}_T}C_{L_Q} & -\frac{g}{\bar{V}_T}\sin\Theta_T \\ 0 & \frac{\bar{q}_T S \bar{c}}{I_{yy}}C_{m_\alpha} & \frac{\bar{q}_T S \bar{c}}{I_{yy}}\frac{\bar{c}}{2\bar{V}_T}C_{m_Q} & 0 \\ 0 & 0 & 1 & 0 \end{bmatrix} \begin{bmatrix} \bar{v} \\ \alpha \\ q \\ \theta \end{bmatrix}
$$

$$
+ \begin{bmatrix} 0 & 0 & \frac{1}{m} \\ -\frac{\bar{q}_T S}{m\bar{V}_T}C_{L_{\delta_E}} & -\frac{\bar{q}_T S}{m\bar{V}_T}C_{L_{\delta_F}} & 0 \\ \frac{\bar{q}_T S \bar{c}}{I_{yy}}C_{m_{\delta_E}} & \frac{\bar{q}_T S \bar{c}}{I_{yy}}C_{m_{\delta_F}} & 0 \\ 0 & 0 & 0 \end{bmatrix} \begin{bmatrix} \delta_e \\ \delta_f \\ \Delta T \end{bmatrix}
\tag{B.16}
$$

and the lateral model as,

$$
\begin{bmatrix} \dot{\beta} \\ \dot{p} \\ \dot{r} \\ \dot{\phi} \end{bmatrix} = \begin{bmatrix} \frac{\bar{q}_T S}{m\bar{V}_T}C_{y_\beta} & \frac{\bar{q}_T S}{m\bar{V}_T}\frac{b}{2\bar{V}_T}C_{y_P} & \frac{\bar{q}_T S}{m\bar{V}_T}C_{y_R} - 1 & -\frac{g}{\bar{V}_T}\cos\Theta_T \\ \frac{\bar{q}_T S b}{I_{xx}}C_{l_\beta} & \frac{\bar{q}_T S b}{I_{xx}}\frac{b}{2\bar{V}_T}C_{l_P} & \frac{\bar{q}_T S b}{I_{xx}}\frac{b}{2\bar{V}_T}C_{l_R} & 0 \\ \frac{\bar{q}_T S b}{I_{zz}}C_{n_\beta} & \frac{\bar{q}_T S b}{I_{zz}}\frac{b}{2\bar{V}_T}C_{n_P} & \frac{\bar{q}_T S b}{I_{zz}}\frac{b}{2\bar{V}_T}C_{n_R} & 0 \\ 0 & 1 & \tan\Theta_T & 0 \end{bmatrix} \begin{bmatrix} \beta \\ p \\ r \\ \phi \end{bmatrix}
$$

$$
+ \begin{bmatrix} \frac{\bar{q}_T S}{m\bar{V}_T}C_{y_{\delta_A}} & \frac{\bar{q}_T S}{m\bar{V}_T}C_{y_{\delta_R}} \\ \frac{\bar{q}_T S b}{I_{xx}}C_{l_{\delta_A}} & \frac{\bar{q}_T S b}{I_{xx}}C_{l_{\delta_R}} \\ \frac{\bar{q}_T S b}{I_{zz}}C_{n_{\delta_A}} & \frac{\bar{q}_T S b}{I_{zz}}C_{n_{\delta_R}} \\ 0 & 0 \end{bmatrix} \begin{bmatrix} \delta_a \\ \delta_r \end{bmatrix}
\tag{B.17}
$$

where $\bar{q}_T$ represents the dynamic pressure at the trim airspeed,

$$
\bar{q}_T = \frac{1}{2}m\bar{V}_T^2
\tag{B.18}
$$

and Θ_T represents the trim pitch angle where,

$$
\Theta_T = \alpha_T
\tag{B.19}
$$

for a straight and level flight condition. Evaluating Equations (B.16) and (B.17) with the standard flight conditions and aircraft-specific parameters detailed in the preceding sections yields,

$$
\begin{bmatrix} \dot{\bar{v}} \\ \dot{\alpha} \\ \dot{q} \\ \dot{\theta} \end{bmatrix} = \begin{bmatrix} -0.0544 & 9.1674 & 0 & -9.7944 \\ -0.0606 & -5.1358 & 0.9138 & -0.0307 \\ 0 & -76.4721 & -7.1412 & 0 \\ 0 & 0 & 1.0000 & 0 \end{bmatrix} \begin{bmatrix} \bar{v} \\ \alpha \\ q \\ \theta \end{bmatrix}
$$

$$
+ \begin{bmatrix} 0 & 0 & 0.1575 \\ -0.5075 & -1.1339 & 0 \\ -90.2895 & 10.9492 & 0 \\ 0 & 0 & 0 \end{bmatrix} \begin{bmatrix} \delta_e \\ \delta_f \\ \Delta T \end{bmatrix}
\tag{B.20}
$$

for the longitudinal dynamics and,

$$
\begin{bmatrix} \dot{\beta} \\ \dot{p} \\ \dot{r} \\ \dot{\phi} \end{bmatrix} =
\begin{bmatrix}
-0.2555 & 0.0070 & -0.8179 & 0.5441 \\
-20.8132 & -8.1398 & 2.5043 & 0 \\
10.9662 & -0.4811 & -1.0380 & 0 \\
0 & 1.0000 & 0.0564 & 0
\end{bmatrix}
\begin{bmatrix} \beta \\ p \\ r \\ \phi \end{bmatrix}
$$

$$
+ \begin{bmatrix}
0.0009 & 0.1402 \\
-94.7338 & 0.3383 \\
2.0702 & -14.3426 \\
0 & 0
\end{bmatrix}
\begin{bmatrix} \delta_a \\ \delta_r \end{bmatrix}
\tag{B.21}
$$

for the lateral dynamics.

APPENDIX C

Appendix C: Hardware and Software

C.1 Aircraft

C.1.1 Aircraft-specific Hardware

Table C.1 summarises the basic hardware required for remote pilot operation of the practical test vehicle. This table does not include the autopilot hardware and the avionics required for autonomous flight.

Table C.1: Hardware on board the practical test vehicle excluding sensors, avionics, and flight control hardware

Component	Description
Airframe	Phoenix Model 60 Trainer Aircraft
Power Plant	E-flight Power 60 Electric Motor running APC 15x8 propeller
Main Battery	X-Power 6S 5000 mAh Lithium Polymer high discharge
Avionics Battery	Gens Ace 3S 2500 mAh Lithium Polymer
Backup Battery	Turnigy 2300 mAh NiMH Low Self Discharge
Actuators	Hi_{TEC} HS-7975HB, Karbonite Gear, Coreless Digital Servo
RC Receiver	Spektrum AR9100 DSM2 9-Channel PowerSafe Receiver

C.2 Ground Station

This section details the features of the custom-designed GCS software used by the ground station operator to issue high-level commands and monitor important vehicle states. A summary of the

ground station capabilities is discussed in Table C.2, whilst Figures C.1, C.2, C.3, and C.4 show screenshots of the ground station software application developed for this particular project.

Table C.2: Summary of ground station capabilities

No.	Class	Description
1	General Status Information	Information relating to general system states (OBC uptime, system temperatures, battery voltages, modes and states etc.)
2	Controller Related Functions	Commands can be given to activate and test individual control loops. Controller references and saturations are monitored for stability. Gains and saturation limits can be modified as required.
3	Autonomous Functionality	Commands can be given that enable specific modes, including waypoint navigation and various autonomous crosswind landing techniques. FCS modes and states are monitored closely.
4	Estimator Initialisation and Status Information	The estimator can be initialised for various configurations whilst variables are monitored.
5	Sensor Monitoring	Display sensor measurements from rate gyroscope, accelerometer, pressure sensor, magnetometer, and GPS.
6	Actuator Monitoring and Configuration	Display actuator readings and settings that can be used to test remote control calibration and actuator trims.
7	GPS Setup	Differential GPS can be initialised for various configurations. Allows for GPS setup to be monitored.
8	SD Card Logging	Individual logging rates can be varied to prioritise more important information.

Figure C.1: GCS screenshot depicting the controller tab

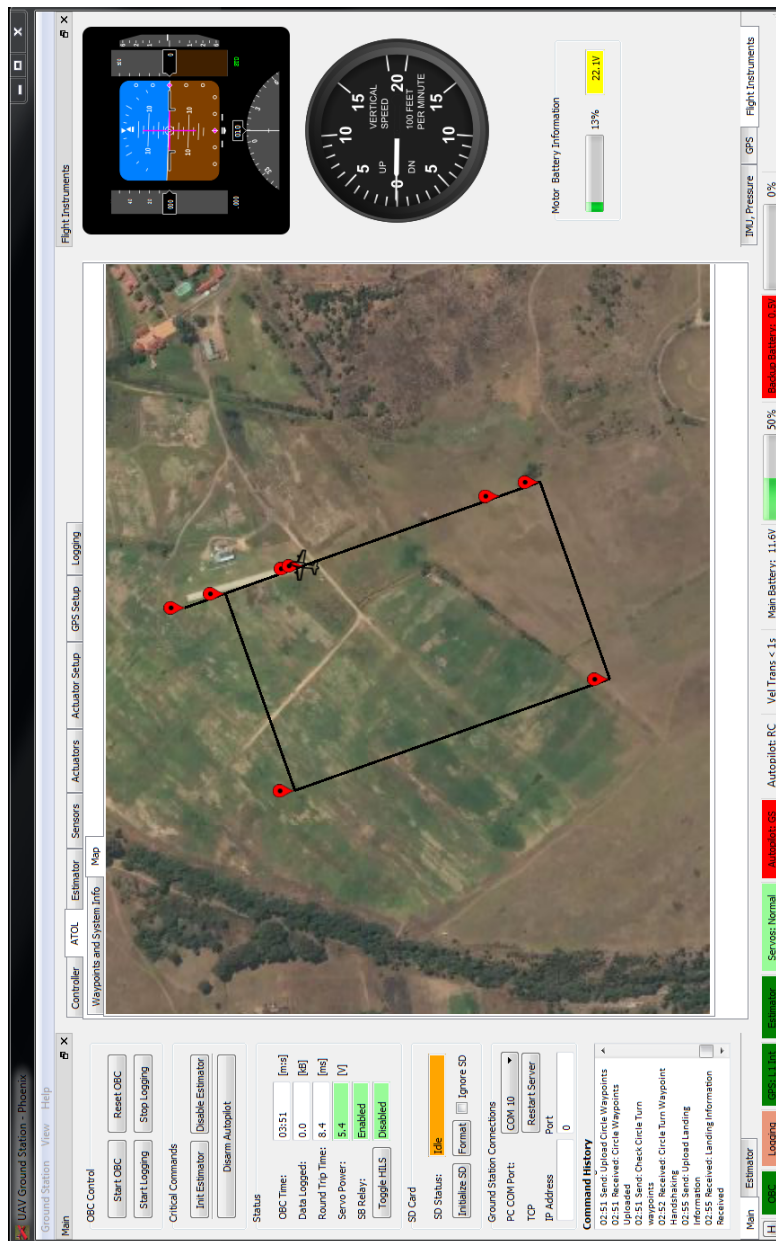**Figure C.2:** GCS screenshot depicting the ATOL tab

Figure C.3: GCS screenshot depicting the flight map

Figure C.4: GCS screenshot depicting the logging tab

APPENDIX D

Appendix D: Runway Controller Design

D.1   Runway Controller Design

The design and verification of the aircraft's runway controllers are discussed in this appendix. Each subsection begins with a discussion of the design approach before the details of the controller are considered and the results verified by linear simulation. The cascaded design approach starts with the augmentation of a yaw rate controller by closing the first control loop around simplified runway dynamics. This is then followed by the design and augmentation of a middle-loop heading controller and finally concluding with the addition of an outer-loop guidance controller. It is important to note that active anti-wind up protection was added to the yaw rate controller integrator.

D.1.1   Runway Model

The runway model used in the non-linear simulation environment was developed by Roos [4]. Roos also provides a simplified dynamic model that describes the aircraft's yaw rate dynamics as a combination of the aerodynamic effects and physical runway contact. After the aircraft has landed it does not cease to be an aircraft, and it is obvious that aerodynamic effects will have a significant contribution - especially at higher airspeeds. It is therefore necessary to take these aerodynamic forces into account and in fact use them to improve lateral control efficiency. Roos defines the following relationship,

$$\dot{r} I_{zz} = N_a + N_r \tag{D.1}$$

The aerodynamic contribution is given by,

$$N_a = \left(\frac{qSb^2 C_{n_R}}{2\bar{V}} \right) r + \left(\bar{q} Sb C_{n_{\delta_R}} \right) \delta_r \tag{D.2}$$

where the aerodynamic coefficients and geometric properties are standard as defined in Appendix B. The runway contribution is given by,

$$N_r = \left(\frac{l_m l_s N C_{\alpha\alpha}}{\bar{V}_g}\right) r + \left(\frac{l_m l_s N C_{\alpha\alpha}}{(l_m + l_s)}\right) \delta_s \tag{D.3}$$

with,

$$N = mg - 0.5\rho\bar{V}^2 S C_{L_T} \tag{D.4}$$

where $C_{\alpha\alpha}$ is the cornering coefficient, δ_s is the nose wheel deflection angle, V_g is the ground speed measurement, l_m is the main wheel moment arm (distance from CG to main wheels), and l_s is the nose wheel moment arm (distance from CG to nose wheel). Table D.1 provides values specific to the airframe used during practical verification of the autopilot.

Table D.1: Physical parameters of the runway model

Symbol	Value
$C_{\alpha\alpha}$	0.25
l_m	0.2
l_s	0.4

It is apparent from Equation (D.4) that N becomes smaller as $\bar{V}$ increases, since the natural wing camber generates more lift as the airspeed increases. From Equation (D.3), this means that there will be a degradation in nose wheel control authority at higher airspeeds. The rudder, however, is more effective at higher airspeeds and thus using a combination of the rudder and nose wheel often yields the best results. It is important to note that the rudder will no longer be driven by the lateral specific acceleration controller after the aircraft makes contact with the runway surface, instead it will driven by the inner-loop yaw rate controller acting as slave to the nose wheel command. The rudder essentially mimics the nose wheel command according to a predetermined ratio, in order to improve lateral control efficiency by exploiting the aircraft's aerodynamic control characteristics. According to Roos [4], the most effective ratio for this size aircraft with a tricycle wheel configuration is,

$$\delta_r = 2\delta_s \tag{D.5}$$

Define the virtual actuator,

$$\delta_{rs} = \delta_s \tag{D.6}$$

$$= \frac{\delta_r}{2}$$

Substituting Equations (D.2) and (D.3) into (D.1) yields,

$$\left[\dot{r}\right] = \left[\frac{qSb^2 C_{n_R}}{2\bar{V}I_{zz}} + \frac{l_m l_s N C_{\alpha\alpha}}{\bar{V}_g I_{zz}}\right] r + \left[\frac{2\bar{q}SbC_{n_{\delta_R}}}{I_{zz}} + \frac{l_m l_s N C_{\alpha\alpha}}{(l_m + l_s)I_{zz}}\right] \delta_{rs} \tag{D.7}$$

where the virtual actuator of Equation (D.5) has been used to replace δ_r and δ_s. The lateral runway model of Equation (D.7) can now be used to design a set of cascaded lateral runway controllers. The runway controllers will be activated at the point of touchdown, and remain active throughout the entire ground roll phase until the aircraft comes to a complete stop on the runway. It is intuitive that some form of gain scheduling is required to prevent over/under actuation due to the inherently large velocity range - from touchdown airspeed to a complete stop. The design will therefore be centred around a nominal ground speed of 10 m/s, and the control gains scaled according to the current ground speed measurement. It is apparent from Equation (D.7) that both airspeed ($\bar{V}$) and ground speed ($\bar{V}_g$) form part of the dynamic model; however, for the sake of design simplicity, the following assumption was made,

$$\bar{V} = \bar{V}_g \tag{D.8}$$

which is a common design assumption that assumes zero wind speed. To this end, the aforementioned parameters are now substituted into the simplified runway model of Equation (D.7) to yield,

$$\dot{r} = \begin{bmatrix} -0.4488 \end{bmatrix} r + \begin{bmatrix} -6.7226 \end{bmatrix} \delta_{rs} \tag{D.9}$$

It is convenient to write the open-loop runway model in a more compact form as,

$$\dot{x}_g = A_g x_g + B_g u_g \tag{D.10}$$

D.1.2   Yaw Rate Controller

This section presents the design and verification of an inner-loop yaw rate controller. The yaw rate controller is responsible for regulating the aircraft's yaw rate throughout the ground roll phase via the rudder and nose wheel. A three-axis gyroscope included in the avionics stack on board the practical test vehicle provided yaw rate measurements for the purpose of feedback control. It is apparent from Figure 5.1 that the yaw rate controller is driven by the middle-loop heading controller.

D.1.2.1   Design

With reference to Figure D.1, a Proportional Integral (PI) control law is defined as,

$$\delta_{rs} = -K_p \dot{e}_r - K_i e_r \tag{D.11}$$

with,

$$\dot{e}_r = r - r_{ref} \tag{D.12}$$

where r and r_{ref} denote the yaw rate measurement and corresponding reference command respectively. The transfer function from virtual actuator input to yaw rate is obtained from the state space model of Equation (D.10) through,

$$G_r(s) = \frac{r(s)}{\delta_{rs}(s)} \tag{D.13}$$

$$= C_g \left(sI - A_g \right)^{-1} B_g$$
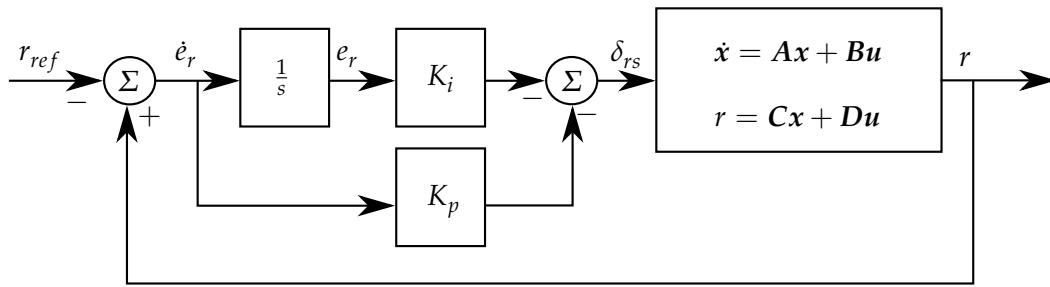
Figure D.1: Runway yaw rate controller block diagram

where C_g is a unity gain. Figure D.2a shows the root locus of the yaw rate controller with respect to the PI feedback gains K_p and K_i. The location of the yaw rate controller zero was adjusted until the dominant branches of the root locus passed through closed-loop pole locations that satisfied the following 2% settling time requirement,

$$t_s < 2.5 \text{ s} \tag{D.14}$$

The controller zero that resides near the closed-loop poles results in unwanted overshoot that would ultimately degrade the response of the remaining outer-loop controllers. It was decided to place the closed-loop poles at the same location on the real axis (critical damping) with the knowledge that the nearby zero causes additional overshoot. Figure D.2b shows the yaw rate step response when,

$$K_p = -0.482 \tag{D.15}$$

$$K_i = -0.506 \tag{D.16}$$

It is apparent from the step response that there is more overshoot than expected from a critically damped system; however, the amount of overshoot is approximately 7% and is therefore considered adequate for this application. The 2% settling time is exactly 2.4 s and therefore satisfies the aforementioned settling time requirement.

(a) Root locus (zoomed in)
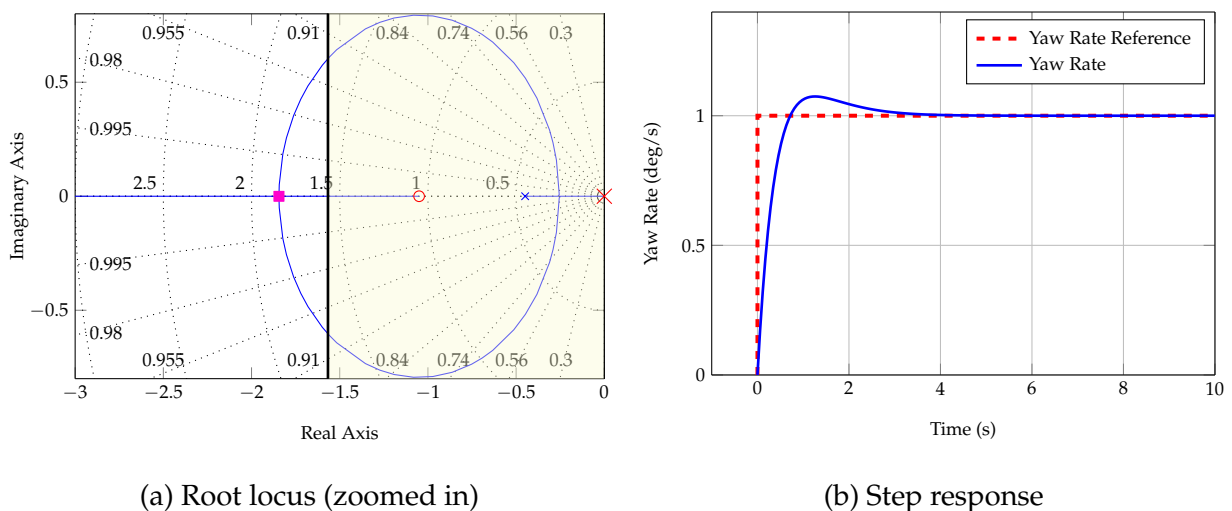
(b) Step response

Figure D.2: Runway yaw rate controller root locus and step response

D.1.2.2 Closed-loop System

In order to maintain design fidelity of the remaining runway controllers, it is necessary to augment the dynamics of Equation (D.10) with the yaw rate control law. Augmenting the integrator state of Equation (D.12) yields,

$$
\begin{bmatrix} \dot{\boldsymbol{x}}_g \\ \dot{e}_r \end{bmatrix} = \begin{bmatrix} \boldsymbol{A}_g & 0 \\ 1 & 0 \end{bmatrix} \begin{bmatrix} \boldsymbol{x}_g \\ e_r \end{bmatrix} + \begin{bmatrix} \boldsymbol{B}_g \\ 0 \end{bmatrix} \boldsymbol{u}_g + \begin{bmatrix} 0 \\ -1 \end{bmatrix} r_{ref}
\tag{D.17}
$$

Substituting the yaw rate control law of Equation (D.11) yields,

$$
\begin{bmatrix} \dot{\boldsymbol{x}}_g \\ \dot{e}_r \end{bmatrix} = \left[\begin{bmatrix} \boldsymbol{A}_g & 0 \\ 1 & 0 \end{bmatrix} + \begin{bmatrix} \boldsymbol{B}_g \\ 0 \end{bmatrix} \begin{bmatrix} -K_p & -K_i \end{bmatrix} \right] \begin{bmatrix} \boldsymbol{x}_g \\ e_r \end{bmatrix} + \begin{bmatrix} K_p \boldsymbol{B}_g \\ -1 \end{bmatrix} r_{ref}
\tag{D.18}
$$

The closed-loop model of Equation (D.18) will be augmented further as more control laws are added to the system. It is therefore convenient to write it in a more compact form as,

$$
\dot{\boldsymbol{x}}_r = \boldsymbol{A}_r \boldsymbol{x}_r + \boldsymbol{B}_r \boldsymbol{u}_r
\tag{D.19}
$$

with,

$$
r = \boldsymbol{C}_r \boldsymbol{x}_r
\tag{D.20}
$$

so that the closed-loop transfer function from yaw rate reference to measured yaw rate is given by,

$$
G_{r_{cl}}(s) = \frac{r(s)}{r_{ref}(s)}
\tag{D.21}
$$

$$
= \boldsymbol{C}_r \left(s\boldsymbol{I} - \boldsymbol{A}_r \right)^{-1} \boldsymbol{B}_r
$$

where,

$$
\boldsymbol{C}_r = \begin{bmatrix} 1 & 0 \end{bmatrix}
\tag{D.22}
$$

D.1.3 Heading Controller

This section presents the design and verification of a middle-loop heading controller. The heading controller is responsible for regulating the aircraft's heading throughout the ground roll phase by generating a yaw rate reference that the aforementioned yaw rate controller should regulate via the rudder and nose wheel. An EKF running the tilt/heading method was used to estimate the heading angle on the practical test vehicle from on-board magnetometer and accelerometer readings. It is apparent from Figure 5.1 that the heading controller is driven by the outer-loop guidance controller.
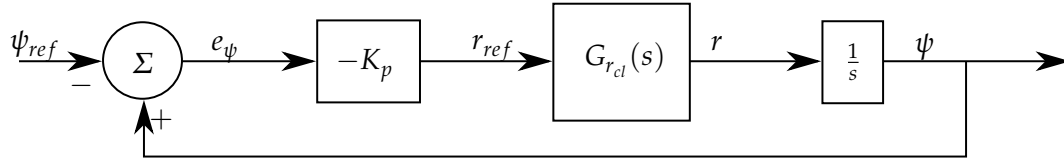
D.1.3.1 Design

With reference to Figure D.3, a proportional control law is defined as,

$$
r_{ref} = -K_p e_\psi
\tag{D.23}
$$

with,

$$e_\psi = \psi - \psi_{ref} \tag{D.24}$$

where ψ and ψ_{ref} denote the heading measurement and corresponding reference command respectively.

Figure D.3: Runway heading controller block diagram

The transfer function from yaw rate reference to heading is obtained from the state space model of Equation (D.19) through,

$$G_\psi(s) = \frac{\psi(s)}{r_{ref}(s)} \tag{D.25}$$

$$= \frac{1}{s} C_r \left(sI - A_r \right)^{-1} B_r$$

The root locus of the heading controller with respect to the proportional gain K_p is shown in Figure D.4a. The proportional gain was varied until the dominant closed-loop pole lay on the real axis with a 2% settling time requirement of,

$$t_s < 5\,\text{s} \tag{D.26}$$

so that a heading step would exhibit minimal overshoot, with an acceptable speed of response. Figure D.4b illustrates the heading step response when,

$$K_p = 1.28 \tag{D.27}$$

It is clear from the response that the initial rise time characteristics are dominated by the faster complex pole pair. The apparent undershoot that occurs after 2 s can be attributed to the dominate real pole that resides near the closed-loop zero. Nevertheless, the response is still adequately damped and exhibits a 2% settling time of exactly 3.4 s, which satisfies the aforementioned settling time requirement.

D.1.3.2 Closed-loop System

In order to further maintain design fidelity, it is necessary to augment the dynamics of Equation (D.19) with the heading control law. However, it is first necessary to augment a heading state to the x_r state vector before the heading control law can be augmented to the system. Augmenting the heading state under the assumption that $\dot{\psi} = r$ yields,

$$\begin{bmatrix} \dot{x}_r \\ \dot{\psi} \end{bmatrix} = \begin{bmatrix} A_r & 0_{2\times1} \\ 1 & 0_{1\times2} \end{bmatrix} \begin{bmatrix} x_r \\ \psi \end{bmatrix} + \begin{bmatrix} B_r \\ 0 \end{bmatrix} r_{ref} \tag{D.28}$$

(a) Root locus (zoomed in)   (b) Step response
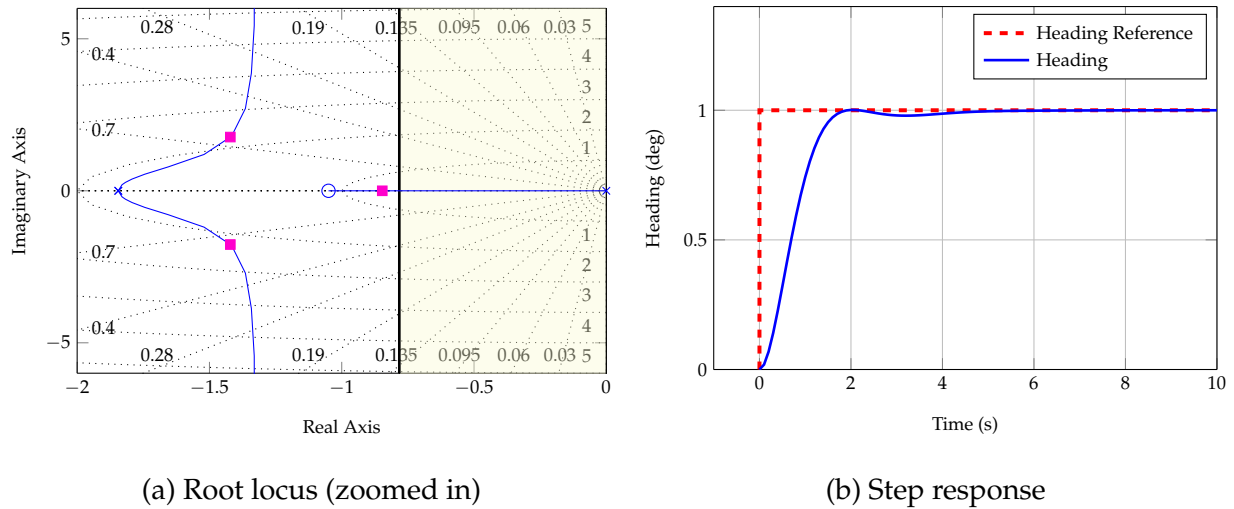
Figure D.4: Runway heading controller root locus and step response

Writing the augmented A matrix in a more compact form as $A_{\dot{\psi}}$, and substituting the heading control law of Equation (D.23) yields,

$$\begin{bmatrix} \dot{x}_r \\ \dot{\psi} \end{bmatrix} = \left[A_{\dot{\psi}} + \begin{bmatrix} B_r \\ 0 \end{bmatrix} \begin{bmatrix} \mathbf{0}_{1\times 2} & -K_p \end{bmatrix} \right] \begin{bmatrix} x_r \\ \psi \end{bmatrix} + \begin{bmatrix} K_p B_r \\ 0 \end{bmatrix} \psi_{ref} \tag{D.29}$$

It is convenient to write the dynamics of Equation (D.29) in a more compact form as,

$$\dot{x}_\psi = A_\psi x_\psi + B_\psi u_\psi \tag{D.30}$$

with,

$$\psi = C_\psi x_\psi \tag{D.31}$$

so that the closed-loop transfer function from heading reference to measured heading is given by,

$$G_{\psi_{cl}}(s) = \frac{\psi(s)}{\psi_{ref}(s)} \tag{D.32}$$

$$= C_\psi \left(sI - A_\psi \right)^{-1} B_\psi$$

where,

$$C_\psi = \begin{bmatrix} \mathbf{0}_{1\times 2} & 1 \end{bmatrix} \tag{D.33}$$

D.1.4 Guidance Controller

This section presents the design and verification of a guidance controller responsible for guiding the aircraft along the runway centreline after touchdown. It can be seen from Figure 5.1 that the input to the guidance controller stems from the navigator, which calculates the cross-track error (y) between the current aircraft position and the intended waypoint track - the navigator is further discussed in Chapter 6. The same navigator is used for both the *In Air* and *On Ground* states, which dramatically reduces system complexity and simultaneously improves FCS predictability.

A single runway waypoint is appended to the waypoint list, which defines a ground track reference between the touchdown waypoint and the end of the runway. The guidance controller generates a heading command, proportional the current cross-track error measurement, that the middle-loop heading controller should maintain via the inner-loop yaw rate controller. Inertially coordinated position and velocity measurements were obtained from a differential GPS, mounted on board the practical test vehicle, and propagated through an EKF to mitigate the adverse effects of GPS delay and to minimise sensor noise.

D.1.4.1 Design

With reference to Figure D.5, a proportional control law is defined as,

$$\psi_{ref} = -K_p e_y \tag{D.34}$$

with,

$$e_y = y - y_{ref} \tag{D.35}$$

where y and y_{ref} denote the cross-track error and corresponding reference command respectively.
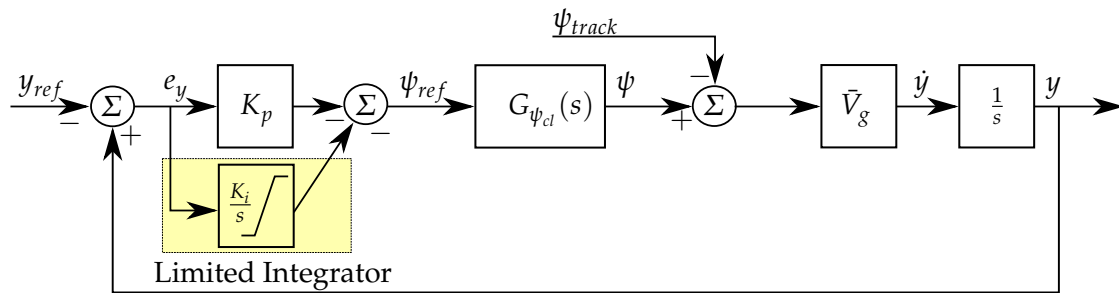
Figure D.5: Runway guidance controller block diagram

It is first necessary to extract cross-track error from the x_ψ state vector before proceeding with the root locus design. Consider the diagram in Figure D.6, which shows the aircraft flying at a constant heading relative to the ground track. The cross-track error rate is the projection of the aircraft's ground speed onto the cross-track axis, and is represented by the following equation [34],

$$\dot{y} = \bar{V}_g \sin(\psi - \psi_{track}) \tag{D.36}$$

For small angles relative to the ground track heading, Equation (D.36) can be written as,

$$\dot{y} = \bar{V}_g(\psi - \psi_{track}) \tag{D.37}$$

 To this end, the transfer function from heading reference to cross-track error is obtained from the state space model of Equation (D.30) through,

$$G_y(s) = \frac{y(s)}{\psi_{ref}(s)} \tag{D.38}$$

$$= \left(\frac{\bar{V}_g}{s}\right) C_\psi \left(sI - A_\psi\right)^{-1} B_\psi$$
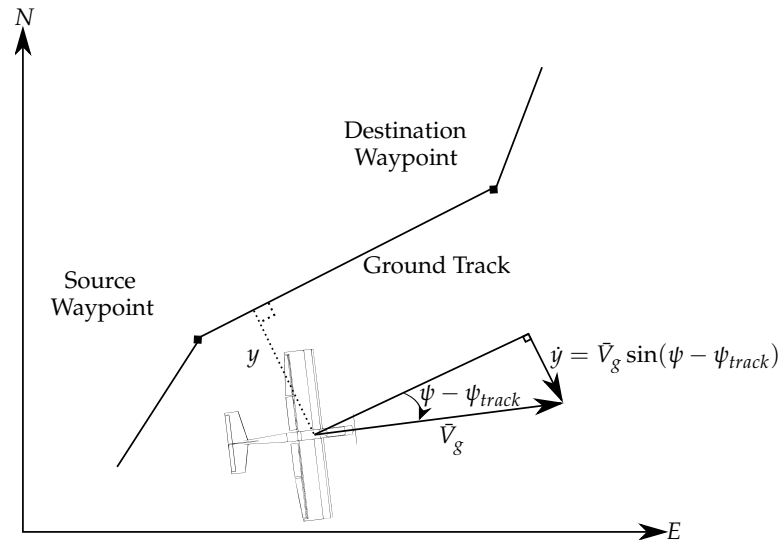
Figure D.6: Cross-track error rate

where Equation (D.37) has been used to indirectly extract cross-track error rate from the x_ψ state vector. The root locus of the guidance controller with respect to the proportional gain K_p is shown in Figure D.7a. The proportional gain was varied until the dominant closed-loop poles satisfied the following requirements,

$$\zeta = 0.9 \tag{D.39}$$

$$t_s < 7 \text{ s} \tag{D.40}$$

so that a cross-track step would exhibit minimal overshoot with an acceptable speed of response. Figure D.7b shows the guidance controller step response when,

$$K_p = 0.0403 \tag{D.41}$$

It is apparent that the response is well damped and exhibits a 2% settling time of exactly 6.6 s, which satisfies the aforementioned settling time requirement. It is important that the guidance controller is not overly aggressive, as this may result in excessive lateral manoeuvres that could cause the aircraft to tip over and strike a wing. After numerous simulations and practical tests on the runway, the response shown in Figure D.7b proved fast enough to bring the aircraft back to the runway centreline without causing it to tip over from excessive lateral perturbations. The natural integration from cross-track error rate to cross-track error makes this a type 1 system, which means it should be able to follow a cross-track reference with zero error in the steady state. However, a limited integrator was included in the practical implementation of this controller to compensate for heading angle biases and constant crosswind disturbances.

D.1.4.2 Closed-loop System

It is first necessary to augment the cross-track error state to the x_ψ state vector before the guidance control law can be augmented to the system. Augmenting the cross-track error state yields,

$$\begin{bmatrix} \dot{x}_\psi \\ \dot{y} \end{bmatrix} = \begin{bmatrix} A_\psi & 0_{3\times1} \\ 0_{1\times2} & \bar{V}_g & 0 \end{bmatrix} \begin{bmatrix} x_\psi \\ y \end{bmatrix} + \begin{bmatrix} B_\psi \\ 0 \end{bmatrix} \psi_{ref} \tag{D.42}$$

(a) Root locus (zoomed in)   (b) Step response
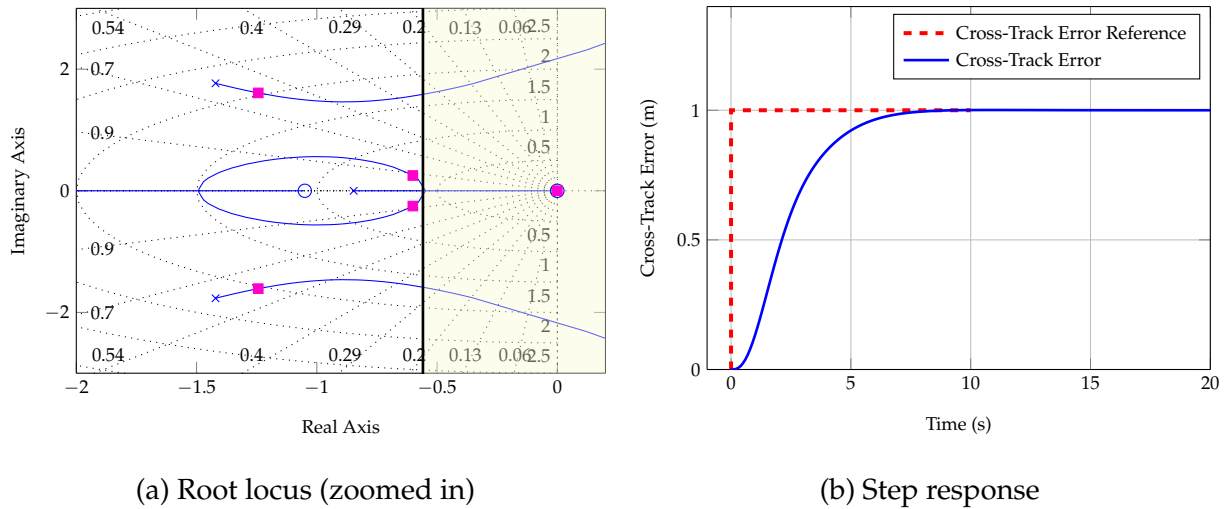
Figure D.7: Runway guidance controller root locus and step response

where Equation (D.37) has been used to indirectly extract cross-track error rate ($\dot{y}$) from the x_ψ state vector. Writing the augmented A matrix in a more compact form as $A_{\dot{y}}$, and substituting the guidance control law of Equation (D.34) yields,

$$\begin{bmatrix} \dot{x}_\psi \\ \dot{y} \end{bmatrix} = \left[A_{\dot{y}} + \begin{bmatrix} B_\psi \\ 0 \end{bmatrix} \begin{bmatrix} \mathbf{0}_{1\times 3} & -K_p \end{bmatrix} \right] \begin{bmatrix} x_\psi \\ y \end{bmatrix} + \begin{bmatrix} K_p B_\psi \\ 0 \end{bmatrix} y_{ref} \tag{D.43}$$

It is convenient to write the dynamics of Equation (D.43) in a more compact form as,

$$\dot{x}_y = A_y x_y + B_y u_y \tag{D.44}$$

with,

$$y = C_y x_y \tag{D.45}$$

so that the closed-loop transfer function from cross-track error reference to cross-track error is given by,

$$G_{y_{cl}}(s) = \frac{y(s)}{y_{ref}(s)} \tag{D.46}$$

$$= C_y \left(sI - A_y \right)^{-1} B_y$$

where,

$$C_y = \begin{bmatrix} \mathbf{0}_{1\times 3} & 1 \end{bmatrix} \tag{D.47}$$

APPENDIX E

Appendix E: Wind Data

E.1   Wind Models

Table E.1 summarises the spectrum equations defined in the military specification document MIL-HDBK-1797 [46]. These equations are used to implement the atmospheric turbulence model discussed in Chapter 7. With reference to Table E.1, b is the aircraft's wing span, V is the current airspeed, σ represents the turbulence intensities, and L represents the turbulence scale lengths. For altitudes below 1000 ft, scale lengths are defined in the military specification document as,

$$2L_w = h \tag{E.1}$$

$$L_u = 2L_v \tag{E.2}$$

$$= \frac{h}{(0.177 + 0.000823h)^{1.2}}$$

and the turbulence intensities as,

$$\sigma_w = 0.1u_{20} \tag{E.3}$$

$$\frac{\sigma_u}{\sigma_w} = \frac{\sigma_v}{\sigma w} \tag{E.4}$$

$$= \frac{1}{(0.177 + 0.000823h)^{0.4}}$$

where u_{20} is the mean wind speed at 20 ft above the surface and h is the current aircraft altitude, which is lower-limit saturated to avoid over-aggressive non-linear scaling. A look-up table is used to determine turbulence intensities for altitudes above 2000 ft; however, such altitudes are not of concern in this thesis and the derivation has subsequently been omitted.

Table E.1: MIL-HDBK-1797 filter forms

Direction	Dryden	Von Kármán
	Longitudinal	
$H_u(s)$	$\sigma_u\sqrt{\dfrac{2L_u}{\pi V}}\cdot\dfrac{1}{1+\frac{L_u}{V}s}$	$\dfrac{\sigma_u\sqrt{\frac{2}{\pi}\frac{L_u}{V}}\left(1+0.25\frac{L_u}{V}s\right)}{1+1.357\frac{L_u}{V}s+0.1987\left(\frac{L_u}{V}\right)^2s^2}$
$H_p(s)$	$\sigma_w\sqrt{\dfrac{0.8}{V}}\cdot\dfrac{\left(\frac{\pi}{4b}\right)^{\frac{1}{6}}}{(2L_w)^{\frac{1}{3}}\left(1+\left(\frac{4b}{\pi V}\right)s\right)}$	$\sigma_w\sqrt{\dfrac{0.8}{V}}\cdot\dfrac{\left(\frac{\pi}{4b}\right)^{\frac{1}{6}}}{(2L_w)^{\frac{1}{3}}\left(1+\left(\frac{4b}{\pi V}\right)s\right)}$
	Lateral	
$H_v(s)$	$\sigma_v\sqrt{\dfrac{2L_v}{\pi V}}\cdot\dfrac{1+\frac{2\sqrt{3}L_v}{V}s}{\left(1+\frac{2L_v}{V}s\right)^2}$	$\dfrac{\sigma_v\sqrt{\frac{1}{\pi}\frac{2L_v}{V}}\left(1+2.7478\frac{2L_v}{V}s+0.3398\left(\frac{2L_v}{V}\right)^2s^2\right)}{1+2.9958\frac{2L_v}{V}s+1.9754\left(\frac{2L_v}{V}\right)^2+0.1539\left(\frac{2L_v}{V}\right)^3s^3}$
$H_r(s)$	$\dfrac{\mp\frac{s}{V}}{\left(1+\left(\frac{3b}{\pi V}\right)s\right)}\cdot H_v(s)$	$\dfrac{\mp\frac{s}{V}}{\left(1+\left(\frac{3b}{\pi V}\right)s\right)}\cdot H_v(s)$
	Vertical	
$H_w(s)$	$\sigma_w\sqrt{\dfrac{2L_w}{\pi V}}\cdot\dfrac{1+\frac{2\sqrt{3}L_w}{V}s}{\left(1+\frac{2L_w}{V}s\right)^2}$	$\dfrac{\sigma_w\sqrt{\frac{1}{\pi}\frac{2L_w}{V}}\left(1+2.7478\frac{2L_w}{V}s+0.3398\left(\frac{2L_w}{V}\right)^2s^2\right)}{1+2.9958\frac{2L_w}{V}s+1.9754\left(\frac{2L_w}{V}\right)^2+0.1539\left(\frac{2L_w}{V}\right)^3s^3}$
$H_q(s)$	$\dfrac{\pm\frac{s}{V}}{\left(1+\left(\frac{4b}{\pi V}\right)s\right)}\cdot H_w(s)$	$\dfrac{\pm\frac{s}{V}}{\left(1+\left(\frac{4b}{\pi V}\right)s\right)}\cdot H_w(s)$

E.2   Measured Wind Data

Figure E.1 shows the wind profile measured by an iWeathar station located at the testing facility during the final practical flight test.
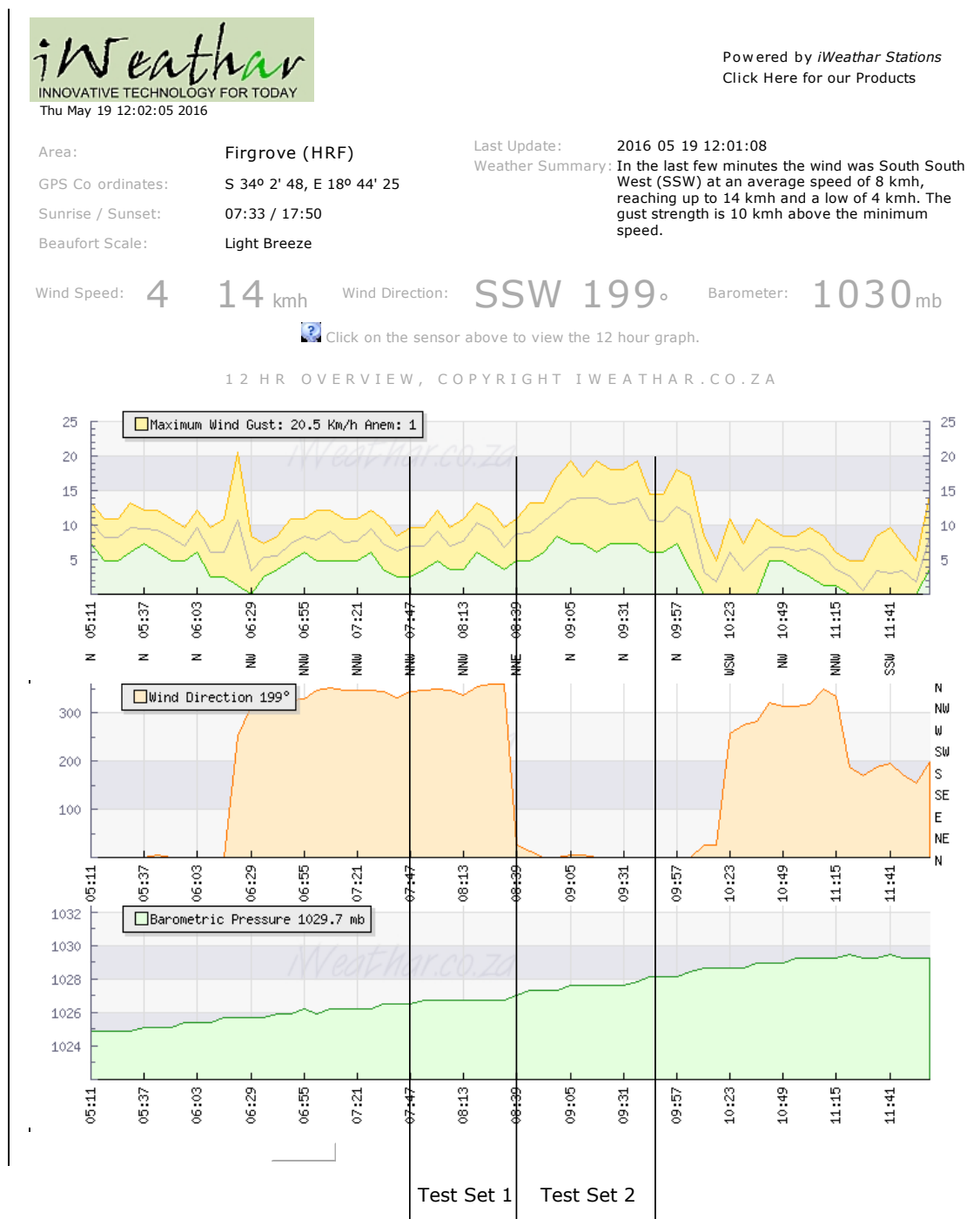
Figure E.1: Wind profile from iWeathar station

APPENDIX F

Appendix F: Controller Robustness Investigation

This appendix includes pole-zero plots and step responses that were used to evaluate the robustness of the autopilot to changes in trim airspeed. For each of the plots shown below, controller gains remain constant whilst trim airspeed ranges from 16 m/s to 20 m/s. The results essentially demonstrate the effect of trim airspeed on controller performance when gain scheduling is not employed. It is apparent that the FCS performs adequately over the typical airspeed range, and it was therefore decided that the benefits of gain scheduling were not worth the added complexity. However, if the autopilot system is extended to perform automatic take-off, then gain scheduling is indeed recommended to maximise performance and to ensure stability over the extended airspeed range. This appendix is divided into two sections:

- Longitudinal controller robustness to change in trim airspeed

- Lateral controller robustness to change in trim airspeed

F.1   Longitudinal Controllers
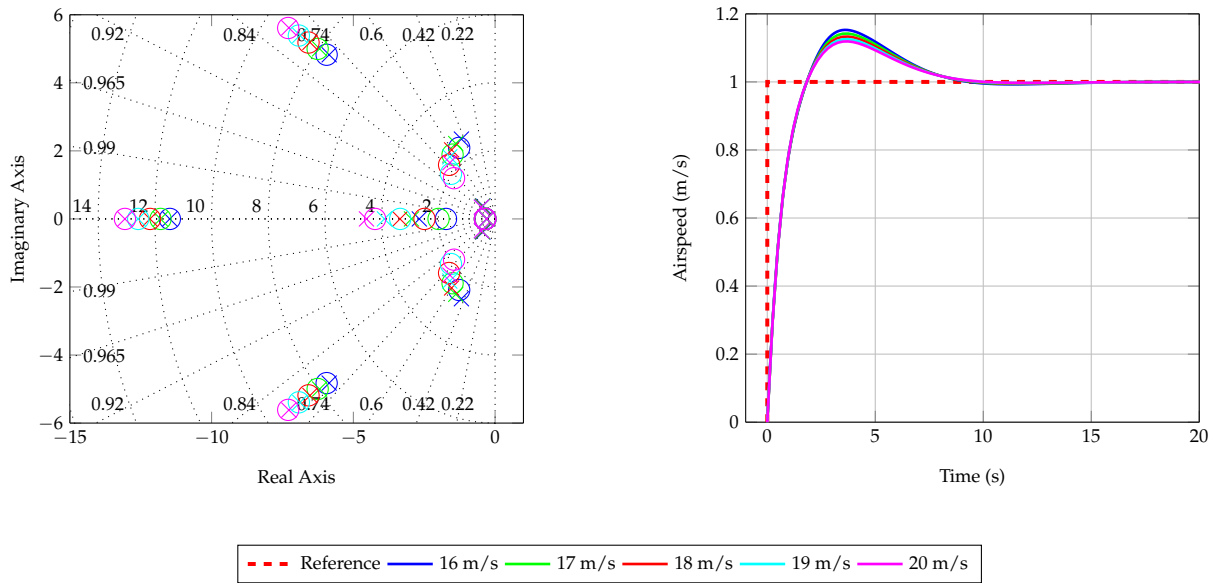
Figure F.1: Airspeed controller robustness investigation with trim airspeed ranging from 16 m/s to 20 m/s
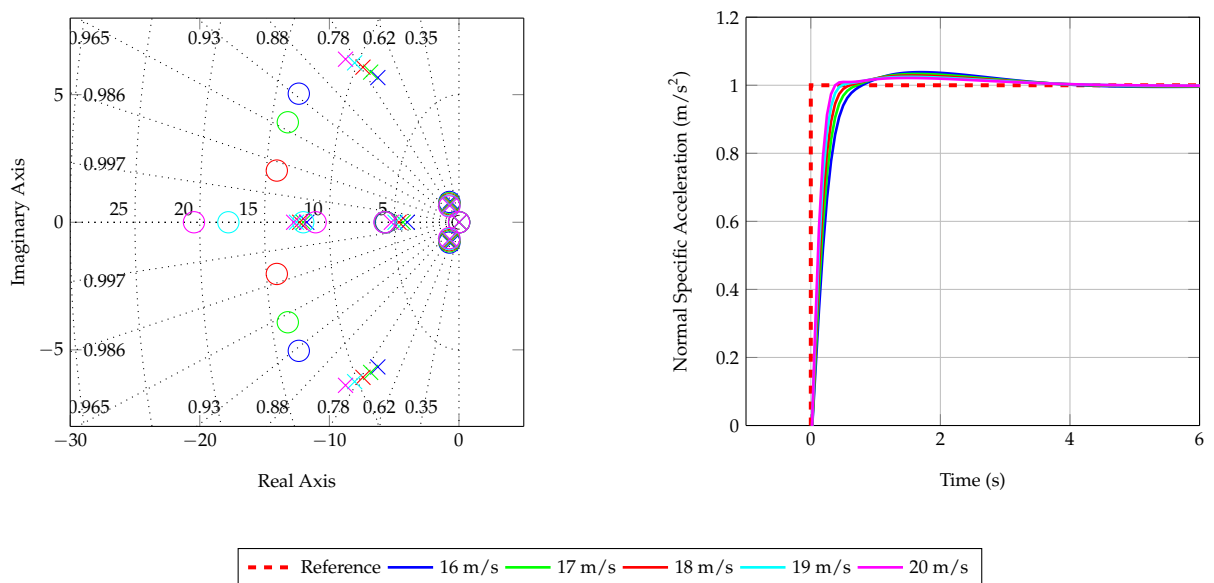
Figure F.2: Normal specific acceleration controller robustness investigation with trim airspeed ranging from 16 m/s to 20 m/s
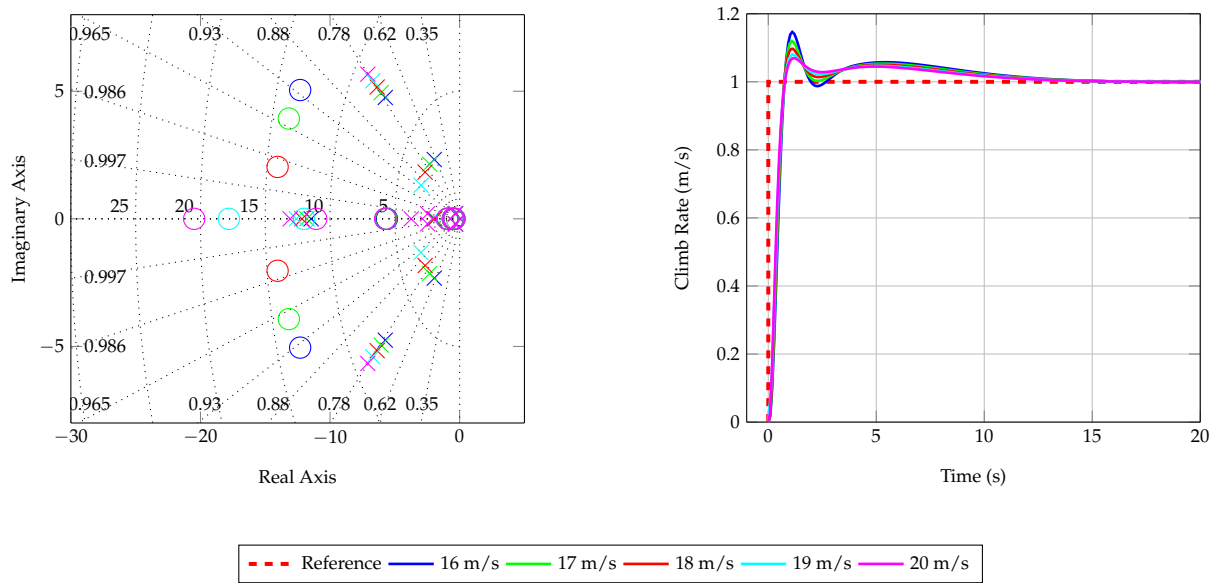
Figure F.3: Climb rate controller robustness investigation with trim airspeed ranging from 16 m/s to 20 m/s
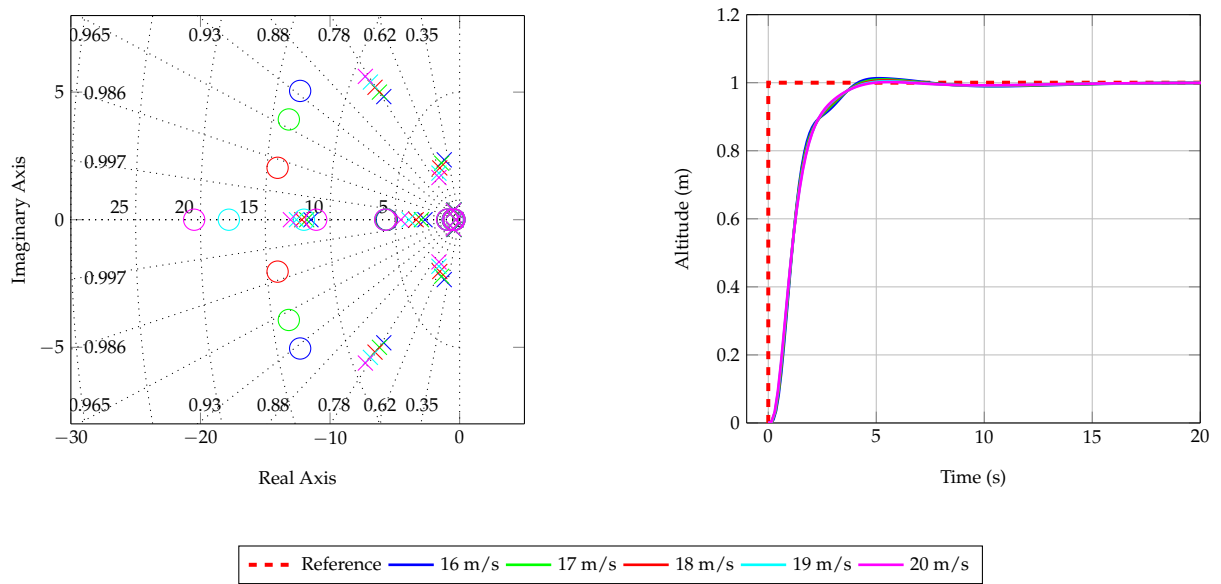
Figure F.4: Altitude controller robustness investigation with trim airspeed ranging from 16 m/s to 20 m/s

F.2 Lateral Controllers
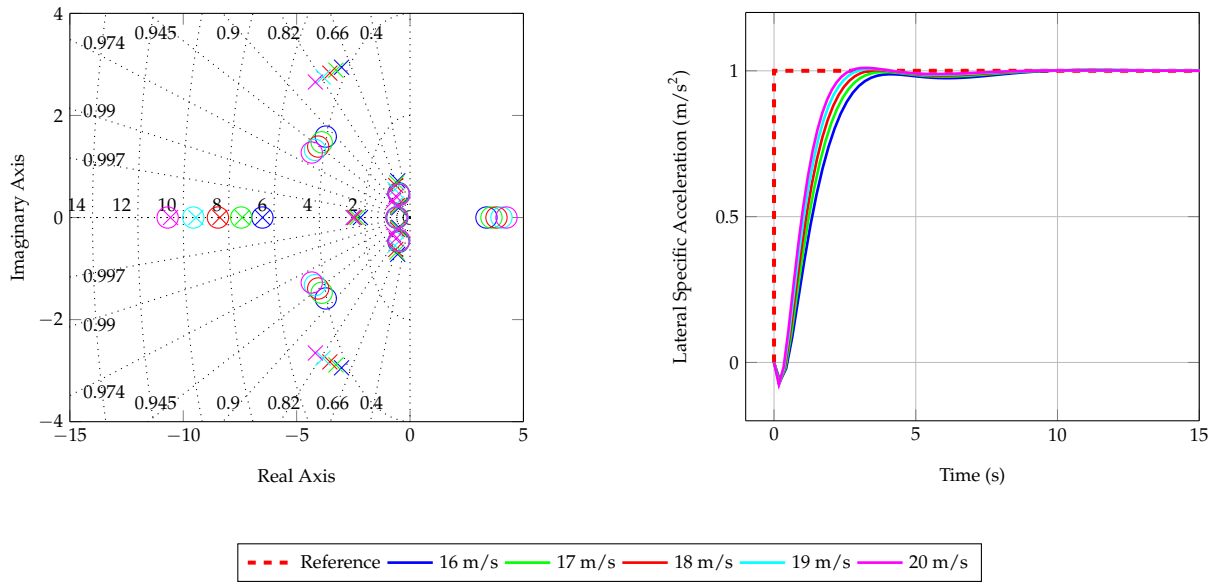
Figure F.5: Lateral specific acceleration controller robustness investigation with trim airspeed ranging from 16 m/s to 20 m/s
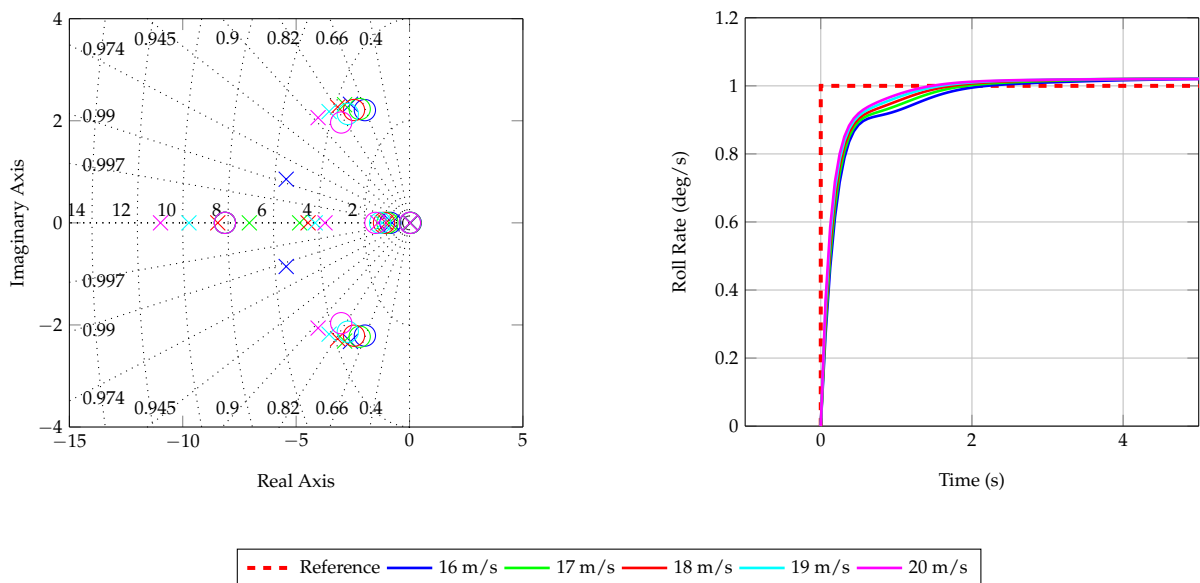
Figure F.6: Roll rate controller robustness investigation with trim airspeed ranging from 16 m/s to 20 m/s
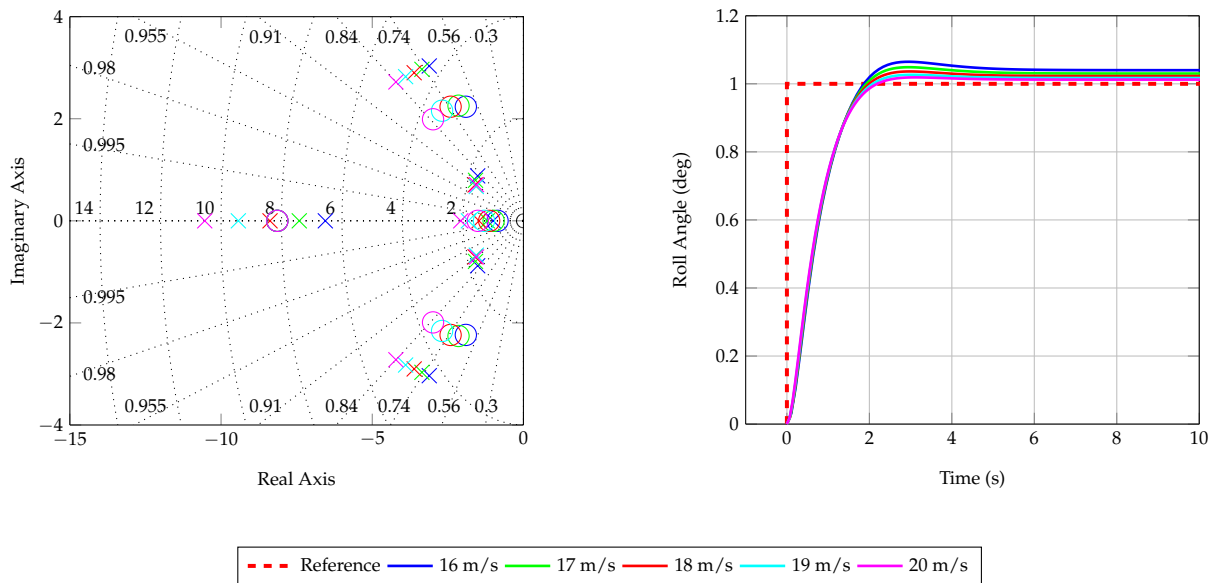
Figure F.7: Roll angle controller robustness investigation with trim airspeed ranging from 16 m/s to 20 m/s
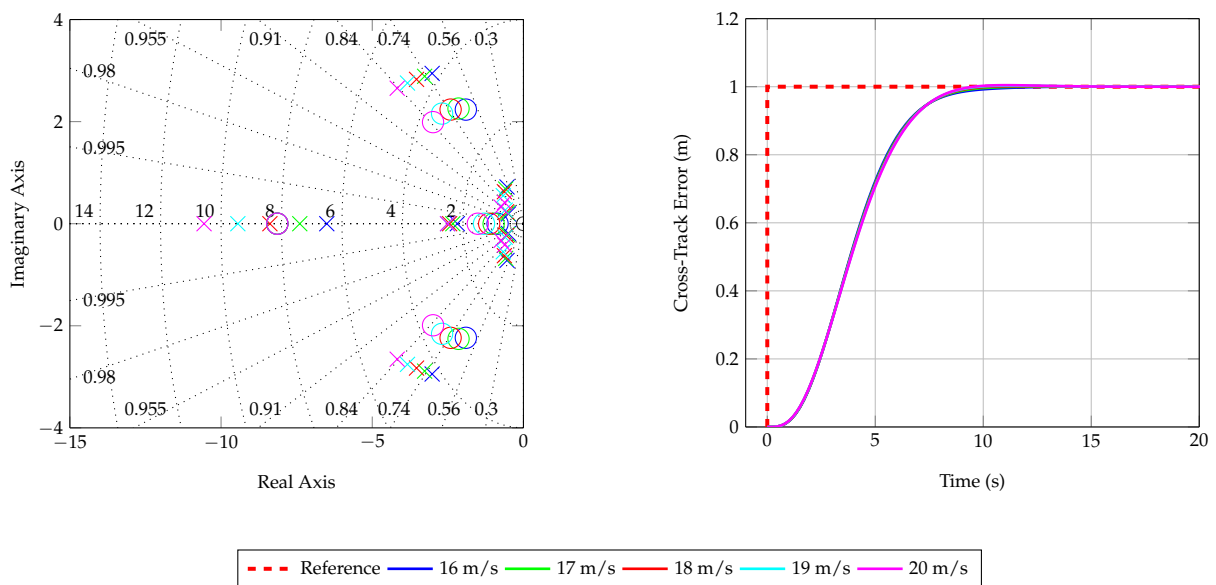
Figure F.8: Guidance controller robustness investigation with trim airspeed ranging from 16 m/s to 20 m/s

APPENDIX G

Appendix G: Formal Flight Test Documentation

VTRE–160516 16 May 2016

Electronic Systems Laboratory

Department of Electrical and Electronic Engineering

University of Stellenbosch

ACCURATE AUTONOMOUS LANDING OF A FIXED-WING UNMANNED AIRCRAFT UNDER CROSSWIND CONDITIONS

Flight Test 16
Flight Test 16: Landing test in adverse wind conditions

The ESL vulture.

Andrew de Bruin

Contents

1   Flight Test Plan

Flight Test Details	
Name of test:	Landing test in adverse wind conditions
Date of test:	17 May 2016
Location of test:	Helderberg Radio Flyers Club

I, the undersigned, fully understand my role in the execution and safety of the above flight test:

Team Member	Print Name	Signature	Date
Coordinator	Andrew de Bruin		
Safety Pilot	Michael Basson		
Assistant	Ryan Maggott		
Assistant	Piero Ioppo		
Assistant	Gideon Hugo		

2 Introduction

2.1 Background

As part of ongoing research in the Electronic Systems Laboratory, several projects in the past have been executed with Phoenix as the test vehicle, including autonomous navigation, autonomous landing and fault tolerance. Most recently, Albert's project titled *Accurate Autonomous Landing of a Fixed-Wing Unmanned Aerial Vehicle* showed that an accurate landing is possible using DGPS. A new airframe has since been constructed (ESL Vulture) which will be used for future autonomous landing projects. Andrew de Bruin will be implementing a synergistic controller architecture with strong disturbance rejection characteristics that should allow the aircraft to land accurately in adverse wind conditions. Vulture was constructed by Andrew de Bruin and was completed on the 9th of November 2015.

2.2 Test Objectives

This test is aimed at evaluating crosswind landing performance through practical flight testing. Each test will consist of a sudo landing approach followed by an actual landing depending on the success of the sudo approach. The test will be structured in such a way that all three of the crosswind landing techniques are evaluated. The test will be structured as follows:

- Sudo crabbed landing

- Crabbed landing (depending on the success of sudo)

- Sudo de-crab landing

- De-crab landing (depending on the success of sudo)

- Sudo low-wing landing

- Low-wing landing (depending on the success of sudo)

The data captured will also be compared with the HIL simulation results to determine the efficacy of each controller. Any anomalies will be identified and isolated so that they can be fixed on the next iteration of controller code. If all of the aforementioned objectives are successfully achieved and the recorded flight data is deemed acceptable, no further flight testing is required unless time permits.

2.3 Description of the Test Item

The ESL vulture is a Phoenix Boomerang model 60 trainer RC aircraft, similar to the previous airframe used in the ESL (Phoenix). The latest version of Chris Fourie's ground station software will be used, modified to accompany the new controllers and commands. The OBC has also been updated with the new controller architecture, updated logging code and more efficient sensor filtering.

3 Test Preparation

3.1 Project Team

- Michael Basson

- Thomas Jones

- Gideon Hugo

3.2 Logistical Support

No logistical support is required for this flight test.

3.3 Briefings and Debriefings

Flight briefing and debriefing will take place at the airfield.

3.4   Safety

- Briefing to the relevant team members about hazards will take place at the airfield. This includes general safety around the UAV.

- A first aid kit must be available in case of injury.

- A fire extinguisher must be available in case of electrical fire.

- Adherence to the checklists would reduce the risk of hazards.

See the risk assessment for further details.

4   Details of the Test

4.1   Objective 1 – Landing in adverse wind conditions

Objective

The aim of this test is to evaluate autoland accuracy in crosswind conditions.

Test Methods

1. The aircraft will start on the runway and zeroed.

2. Takeoff will proceed under safety pilot control.

3. A path will be flown in line with the predetermined waypoints under safety pilot control.

4. The airspeed and altitude controller will be activated from the ground station to maintain the current altitude at an airspeed of 18 m/s.

5. The pilot will be instructed to fly the aircraft down the runway leg and arm the controller. At this point both the ground station AP switch and the RC pilot AP switch are engaged.

6. The altitude controller will be given a reference altitude of 17.5 m above the ground in preparation for the waypoint navigation state.

7. The guidance and LSA controllers will be activated and the state machine transitioned from RC pilot state to waypoint navigation state.

8. A series of sudo landing attempts will be made to ensure that the safety pilot is happy with the approach.

9. A real landing will be conducted once the safety pilot has given the go ahead.

Test Conditions

Weather conditions are the most significant factor that may hinder the test. During this phase of the project, it is not recommended to continue with a test if strong winds or rain are present. The severity of conditions will be determined by the safety pilot and safety officer.

Data Required and Analysis

All conventional sensor data from the GPS, accelerometers and gyroscopes will be logged in order to compare it with the HIL simulation results. All relevant controller data will be logged and compared to the designed controller response and the HIL response in terms of time constants, overshoot, settling times and tracking performance. Any anomalies during the flight will be noted for further analysis at a later stage before the next flight test.

Acceptance Criteria

The test will be regarded as successful if the logged sensor and estimator data corresponds well with the HIL simulation results. Anomalies are expected as the simulation conditions do not perfectly represent the real flight conditions on the particular flight test day. These will be evaluated based on the severity of the anomaly.

5 Test Schedule

The test schedule should stand as detailed below. Hindrances caused by weather, attendance emergencies, etc. will likely delay the test by no more than one week.

NO	OBJ. NO	TEST DATE	FLIGHT TIME [H]	TEST DESCRIPTION
A	B	C	D	E
1	1	17 May 2016	10 minutes	Landing tests - Crabbed landing test
1	2	17 May 2016	10 minutes	Landing tests - De-crab landing test
1	3	17 May 2016	10 minutes	Landing tests - Low-wing landing test

6   Test Cards

TEST CARD: Landing in adverse wind conditions			
VEHICLE: Vulture			

Electronic Systems Laboratory

Test No: 1	**Airframe Fit No:** N.A.	**Test Name:** Landing in adverse wind conditions	
Test Coordinator: Ryan Maggot	**Safety Pilot:** Michael Basson	**Location:** Helderberg Radio Flyers Club	**Date:** 17 May 2016
		Ground Station: Andrew de Bruin	**Test Leader:** Andrew de Bruin

Configuration and Status:
Changes since last flight:

1. Added functionality to switch between estimated climb rate and GPS climb rate to see if that helps with climb rate oscillations.

Restrictions:
Maximum flight time of 30 minutes in total.
No excessive manoeuvres, keep to trim flight.

Notes:

Take-Off #   1

Test #	Test Goals	Pilot Information	Expected Behaviour
1	Landing attempts	The safety pilot is responsible for: 1. the takeoff procedure; 2. activating the autopilot switch; 3. emergency aircraft control in the event of dangerous or unforeseen aircraft behaviour.	A series of sudo and actual landings will be conducted in order to test autoland performance in adverse wind conditions.

7   Risk Assessment

RISK ASSESSMENT / RISIKO ANALISE   REV. NR. 1

US Number:	16458826
Assessment Undertaken: (Date)	17 May 2016
People Involved: (**Print Names**)	Andrew de Bruin
	Michael Basson
	Japie Engelbrecht
	Ryan Maggott
	Gideon Hugo
	Piero Ioppo
Safety Supervisor Authorisation: (**Print Name**)	Safety Officer
Assessment Review Date:	

Building / Area / Project:
Helderberg Radio Flyers Club

Job or Task:
Flight Test 16: Landing tests in adverse wind conditions

UNIVERSITEIT
STELLENBOSCH
UNIVERSITY

Department of
Electrical & Electronic
Engineering

STEP 1 HAZARD AND HAZARD EFFECT	STEP 2 WHO / WHAT MIGHT BE HARMED?	STEP 3 IS THE RISK ADEQUATELY CONTROLLED?	STEP 4 WHAT FURTHER ACTION IS NECESSARY TO CONTROL THE RISK?	STEP 5 WHO IS RESPONSIBLE FOR THE ACTIONS?
Look only for hazards, which you could reasonably expect to result in significant harm under the conditions in your workplace. Use the following examples as a guide: • Slipping / tripping hazards (e.g. poorly maintained floors or stairs) • Fire (e.g. from flammable materials) / welding / burning. • Electricity (e.g. poor wiring). • Chemicals (e.g. battery acid). • Gas, fumes and dust. • Moving parts of machinery (e.g. blades). • Fume (e.g. welding). • Work at height (e.g. from mezzanine floors). • Manual handling. • Ejection of material (e.g. from plastic moulding). • Noise. • Pressure systems (e.g. steam / hydraulics / compressed air). • Poor lighting • Vehicles (e.g. fork-lift trucks). • High / Low Temperatures. • Hazards to the environment. • Confined spaces. • Suspended loads. • Lone working. • Spills • Explosion. • Installation / Commissioning Hazards. • Any other hazards. You can only get a clear picture by looking at the work area.	There is no need to list individuals by name – just think about groups of people doing similar work or who may be affected, for example: • Office staff. • Maintenance personnel. • Contractors. • People sharing your workplace. • Operators. • Cleaners. • Members of the public. **Pay particular attention to:** • Staff with disabilities. • Inexperienced staff. • Visitors. • Lone workers. • Pregnant women. • Young workers (work experience). They may be more vulnerable. How will it harm the environment?	Have you already taken precautions against the risks from the hazards you listed? For example, have you provided: • Adequate control measures. • Adequate information. • Included information in operating and maintenance instructions? • Adequate systems or procedures? • Adequate protective equipment. **Do the precautions:** • Meet the standards set by a legal requirement? • Represent good practice? • Comply with a recognised industry standard? • Reduce risk as far as reasonably practicable? If so, the risks are adequately controlled, but you need to indicate the precautions you have in place. You may refer to procedures, manuals, company rules etc. giving this information. List other risk assessments, if applicable, for example SafeNet (Africa), noise, manual handling, provision and use of work equipment, display screen equipment, confined spaces risk assessment etc.	What more could you reasonably do fro those risks which you found were not adequately controlled? You will need to give priority to those risks, which affect large numbers of people and/or could result in serious harm. Apply the principles below when taking further action, if possible in the following order: • Remove the risk completely. • Try a less risky option. • Prevent access to the hazard (e.g. by guarding). • Organise work to reduce exposure to the hazard. • Issue personal protective equipment. • Provide welfare facilities. • Include immediate short-term actions (e.g. erect warning notice and/or barriers).	• List the person who will do the work for immediate actions (e.g. erect barriers or notices). • List the person responsible for long-term actions (e.g. arrange engineering work to remove hazard). • Record the target date for completing the job. Ensure that the team is briefed on the precautions. Ensure actions are closed out before undertaking the work.

1 HAZARD AND HAZARD EFFECT List Here:	2 WHO / WHAT MIGHT BE HARMED? List groups of people who are especially at risk from significant hazards which you have identified.	3 IS THE RISK ADEQUATELY CONTROLLED? List existing controls here or note where information may be found:	4 WHAT FURTHER ACTION IS NECESSARY TO CONTROL THE RISK? List the risks that are not adequately controlled and the action you will take where it is reasonably practicable to do more. You are entitled to take cost into account, unless the risk is high:	5 WHO IS RESPONSIBLE FOR THE ACTIONS? Person responsible and by when:		
				Person	Date for Completion	Date Completed
Uncontrolled aircraft / aircraft crash	Anyone in the vicinity of the airfield	All the people present are fully aware of the dangers involving the test. Warnings will be issued to anyone nearby that may be endangered by the test. Manoeuvres will only be performed in the specified flying zone where only pilots and helpers are allowed. If the aircraft moves outside of the zone or shows any dangerous behaviour, the pilot will take immediate control of the aircraft and fly it towards the allowable fly zone, after which the current test will likely be cancelled. The safety pilot can always override the autopilot to prevent disaster.	None	Safety Officer	17 May 2016	17 May 2016
Spinning propeller	Anyone in front of the aircraft while active	All the people present are fully aware of the dangers involving the test. Warnings will be issued to anyone nearing the front of the vehicle. A first aid kit is available in case cuts.	None	Safety Officer Flight Test Assistants	17 May 2016	17 May 2016
Electrical fire	Anyone near the aircraft or batteries catching fire	All the people present are fully aware of the dangers involving the test. Warnings will be issued to anyone nearby that may be endangered by the test. A fire extinguisher will be available to bring the fire under control.	None	Safety Officer Flight Test Assistants	17 May 2016	17 May 2016
Electrical shock	Anyone touching the aircraft's wiring or batteries	All the people present are fully aware of the dangers involving the test. Warnings will be issued to anyone nearby that may be endangered by the test. A first aid kit is available in case of electrical burns.	None	Safety Officer Flight Test Assistants	17 May 2016	17 May 2016

10

8 Checklists

Day Before Flight

Charge
OBC batteries.
Motor batteries.
Backup battery
Laptop battery.
RC battery.
RC battery (backup).
Camera.
Radio comms.
NovAtel lead-acid.
ALIGN lead-acid.

Mechanical Check
Fuselage.
Undercarriage and nose wheel.
Flaps, ailerons, rudder, elevator.
Servo motors (note deflection direction).
Main motor.

Systems Check
Bind RC to vehicle.
RC comms.
Gyroscope measurements, verify on estimator.
Accelerometer measurements, verify on estimator.
Magnetometers measurements, verify on estimator.
GPS measurements, verify on estimator.

Other
Most recent code loaded on OBC and GCS.
Predicted weather conditions at airfield.
Contact safety pilot.

Morning of Flight

Pack
Laptop.
Laptop battery.
Laptop charger.
Laptop mouse.
RF module and USB cable.
Vehicle.
Wing Struts.
Wing bolts.
Battery enclosure nylon screws.
SD card.
OBC batteries.
Motor batteries.
Backup battery.
RC remote.
RC battery.
RC battery (backup).

	Radio comms.
	Camera.
	Tripod.
	Bind plug.
	Table.
	Chairs.
	Pens and paper.
	Clipboards.
	Chargers.
	Power supply.
	Power cord.
	Extension cord.
	Multiplug.
	Fire extinguisher.
	First-Aid kit.
	Flight toolbox.
	Orange toolbox.
	Blue toolbox.
	NovAtel Flight Case.
	NovAtel base.
	Novatel USB cable.
	NovAtel spares toolbox.
	NovAtel lead-acid.
	NovAtel lead-acid (backup).
	NovAtel tripod.
	Base antenna.
	Antenna mount.
	Antenna cable.
	Serial cable (backup).
	USB-Serial (backup).
	Antenna cable (backup).
	ALIGN Lead-acid.
	Lead-acid (backup).

Other	
	Predicted weather conditions at airfield.
	Contact safety pilot.

Pre-Flight

Mechanical Check	
	Fuselage.
	Undercarriage and nose wheel.
	Flaps, ailerons, rudder, elevator.
	Main motor.
	Servo motors (note deflection direction).

Vehicle	
	Connect batteries.
	Insert SD card.
	Turn on OBC.
	Format SD card.
	Ensure TX and RX bind.
	Range check.
	Weight distribution.

Estimator Check
Gyroscope and Euler angles.
Accelerometer and velocities.
Magnetometers.
GPS measurements and position.

Post-Test

Other
Weather conditions at airfield.
Download SD card (OBC) data.
Download SD card (camera) data.

Flight Tests (GCS Version)

			Test 1: Crabbed Landing attempts
			Switch on the GCS.
			Connect OBC batteries.
			Insert SD card.
			RADIO: Turn on OBC...
			Connect to COM port.
			Check SD card detection.
			Start logging.
			Check battery voltages of main and backup.
			Check GPS satellites, acquisition of L1Int.
			Zero gyroscopes.
			Zero airspeed.
			Reset flight timer.
			Upload and check waypoints.
			RADIO: Connect motor battery, move to runway...
			Initialise estimator.
			Enable estimator.
			RADIO: Ready for takeoff...
			RADIO: Arming all Longitudinal Controllers.
			RADIO: Arm Autopilot
			Observe.
			RADIO: Set altitude to 17.5 m
			RADIO: Arming long range guidance with landing speed set at 16 m/s.
			RADIO: Let the aircraft fly one full circuit and then activate the sudo landing flag.
			RADIO: Are you happy with the aircraft approach and airspeed?
			If safety pilot is happy then activate real landing flag with crabbed landing.
			RADIO: Observe runway control - takeover if necessary.
			Stop logging.
			Disable estimator.
			Stop sending RTK.
			RADIO: Turn off motor and OBC...

Test 2: De-crab Landing attempts			
			Switch on the GCS.
			Connect OBC batteries.
			Insert SD card.
			RADIO: Turn on OBC...
			Connect to COM port.
			Check SD card detection.
			Start logging.
			Check battery voltages of main and backup.
			Check GPS satellites, acquisition of L1Int.
			Zero gyroscopes.
			Zero airspeed.
			Reset flight timer.
			Upload and check waypoints.
			RADIO: Connect motor battery, move to runway...
			Initialise estimator.
			Enable estimator.
			RADIO: Ready for takeoff...
			RADIO: Arming all Longitudinal Controllers.
			RADIO: Arm Autopilot
			Observe.
			RADIO: Set altitude to 17.5 m
			RADIO: Arming long range guidance with landing speed set at 16 m/s.
			RADIO: Let the aircraft fly one full circuit and then activate the sudo landing flag.
			RADIO: Are you happy with the aircraft approach and airspeed?
			If safety pilot is happy then activate real landing flag with de-crab landing.
			RADIO: Observe runway control - takeover if necessary.
			Stop logging.
			Disable estimator.
			Stop sending RTK.
			RADIO: Turn off motor and OBC...

Test 3: Low wing Landing attempts			
			Switch on the GCS.
			Connect OBC batteries.
			Insert SD card.
			RADIO: Turn on OBC...
			Connect to COM port.
			Check SD card detection.
			Start logging.
			Check battery voltages of main and backup.
			Check GPS satellites, acquisition of L1Int.
			Zero gyroscopes.
			Zero airspeed.
			Reset flight timer.
			Upload and check waypoints.
			RADIO: Connect motor battery, move to runway...
			Initialise estimator.
			Enable estimator.
			RADIO: Ready for takeoff...
			RADIO: Arming all Longitudinal Controllers.
			RADIO: Arm Autopilot
			Observe.
			RADIO: Set altitude to 17.5 m
			RADIO: Arming long range guidance with landing speed set at 16 m/s.
			RADIO: Let the aircraft fly one full circuit and then activate the sudo landing flag.
			RADIO: Are you happy with the aircraft approach and airspeed?
			If safety pilot is happy then activate real landing flag with low-wing landing.
			RADIO: Observe runway control - takeover if necessary.
			Stop logging.
			Disable estimator.
			Stop sending RTK.
			RADIO: Turn off motor and OBC...

Flight Tests (Pilot Version)

Test 1: Crabbed Landing attempts			
			RADIO: Turn on OBC...
			RADIO: Connect motor battery, move to runway...
			RADIO: Ready for takeoff...
			RADIO: Arming all Longitudinal Controllers.
			RADIO: Arm Autopilot
			RADIO: Set altitude to 17.5 m
			RADIO: Arming long range guidance with landing speed set at 16 m/s.
			RADIO: Let the aircraft fly one full circuit and then activate the sudo landing flag.
			RADIO: Are you happy with the aircraft approach and airspeed?
			RADIO: Activating landing flag for crabbed landing.
			RADIO: Observe runway control - takeover if necessary.
			RADIO: Turn off motor and OBC...

			Test 2: De-crab Landing attempts
			RADIO: Turn on OBC...
			RADIO: Connect motor battery, move to runway...
			RADIO: Ready for takeoff...
			RADIO: Arming all Longitudinal Controllers.
			RADIO: Arm Autopilot
			RADIO: Set altitude to 17.5 m
			RADIO: Arming long range guidance with landing speed set at 16 m/s.
			RADIO: Let the aircraft fly one full circuit and then activate the sudo landing flag.
			RADIO: Are you happy with the aircraft approach and airspeed?
			RADIO: Activating landing flag for de-crab landing.
			RADIO: Observe runway control - takeover if necessary.
			RADIO: Turn off motor and OBC...

References

[1]   I. K. Peddle, "Acceleration Based Manoeuvre Flight Control System for Unmanned Aerial Vehicles," Ph.D. dissertation, Stellenbosch University, 2009. 1.1, 1.2, 2.1, 4.5.2.3, 5.1, 5.1, 5.2.1.1, 5.2.1.1, 5.2.2.1, 5.2.2.2, 5.2.2.4, 5.3.1, 5.3.1, 5.3.1.1, 5.3.1.2, 5.3.1.2, 5.3.1.4

[2]   J. D. Blom, *Unmanned Aerial Systems: A Historical Perspective*.   Combat Studies Institute Press, 2009. 1.1

[3]   I. K. Peddle, "Autonomous Flight of a Model Aircraft," Master's thesis, Stellenbosch University, 2005. 1.1, 1.2, 2.1, 3.1.1, 4.2, 4.5.1.1, 4.5.2.3, B.2

[4]   J. C. Roos, "Autonomous Take-Off and Landing of a Fixed Wing Unmanned Aerial Vehicle," Master's thesis, Stellenbosch University, 2007. 1.2, 2.1, 5.1, 7.1.3, D.1.1, D.1.1

[5]   F. N. Alberts, "Accurate Autonomous Landing of a Fixed-Wing Unmanned Aerial Vehicle," Master's thesis, Stellenbosch University, 2012. 1.2, 2.1, 2.2.1, 3.4.2, 4.5.2.3, 5.2.2, 5.2.2, 5.2.2.1, 5.2.2.1, 8.2

[6]   S. J. A. Smit, "Autonomous Landing of a Fixed-Wing Unmanned Aerial Vehicle using Differential GPS," Master's thesis, Stellenbosch University, 2013. 1.2, 2.1, 3.4.2, 4.5.2.3, 8.2

[7]   C. T. le Roux, "Autonomous Landing of a Fixed-Wing Unmanned Aerial Vehicle onto a Moving Platform," Master's thesis, Stellenbosch University, 2016. 1.2, 2.1

[8]   Airbus, *Flight Operations Briefing Notes - Crosswind Landings*, 1 Rond Point Maurice Bellonte - 31707 BLAGNAC CEDEX France, March 2008. 1.3, 6.2.3

[9]   B. J. Visser, "Die presisie landing van 'n onbemande vliegtuig," Master's thesis, Stellenbosch University, 2008. 2.1, 3.4.2, 4.5.2.3, 8.2

[10] M. Gerrits, "Direct Lift Control for the Cessna Citation II," Master's thesis, Eindhoven University of Technology, 1994. 2.1, 5.2.2, 5.2.2

[11] S. Park, J. Deyst, and J. How, "A New Nonlinear Guidance Logic for Trajectory Tracking," *Proceedings of the AIAA Guidance Navigation and Control Conference*, 2004. 2.1, 6.1, B.2

[12] A. Cho, J. Kim, S. Lee, S. Choi, B. Lee, B. Kim, N. Park, D. Kim, and C. Kee, "Fully automatic taxiing, takeoff and landing of a UAV using a single-antenna GPS receiver only," in *Control, Automation and Systems, 2007. ICCAS '07. International Conference on*, Oct 2007, pp. 821–825. 2.2.1

[13] Z. Liu, Y. Wang, and X. Hao, "Coordinated landing control of an Unmanned Aerial Vehicle," in *Electronics, Communications and Control (ICECC), 2011 International Conference on*, Sept 2011, pp. 1965–1970. 2.2.1

[14] J. López, R. Dormido, S. Dormido, and J. P. Gómez, "A fully autonomous unmanned aerial vehicle landing controller synthesis," *Journal of Aerospace Engineering*, 2011. 2.2.1, 2.2.2, 2.2.2, 2.2.2

[15] I. Salfi, U. Ahsun, and H. A. Bhatti, "Lateral and longitudinal guidance and control design of a UAV in auto landing phase," in *Applied Sciences and Technology (IBCAST), 2009 6th International Bhurban Conference on*, Jan 2009, pp. 162–168. 2.2.1

[16] S. Singh and R. Padhi, "Automatic path planning and control design for autonomous landing of UAVs using dynamic inversion," in *American Control Conference, 2009. ACC '09.*, June 2009, pp. 2409–2414. 2.2.1

[17] S. Pouya and F. Saghafi, "Autonomous Runway Alignment of Fixed-Wing Unmanned Aerial Vehicles in Landing Phase," in *Autonomic and Autonomous Systems, 2009. ICAS '09. Fifth International Conference on*, April 2009, pp. 208–213. 2.2.1

[18] R. M. Hueschen, "The Design, Development, and Flight Testing of a Modern-Control-Designed Autoland System," in *American Control Conference, 1985*, June 1985, pp. 1481–1489. 2.2.1

[19] W. Rui, Z. Zhou, and S. Yanhang, "Robust Landing Control and Simulation for Flying Wing UAV," in *Control Conference, 2007. CCC 2007. Chinese*, July 2007, pp. 600–604. 2.2.1

[20] *Aeronautical Information Manual*, Federal Aviation Administration, 2014. 2.2.2

[21] B. Etkin and L. D. Reid, *Dynamics of Flight, Stability and Control*, 3rd ed. John Wiley and Sons, 1996. 2.2.3, 4.2, 4.3, 4.5, 4.5.4, 4.5.4, 5.2.2.1, B.4

[22] G. Schänzer, "Influence of Wind Shear on Flight Safety," Technical University Braunschweig, Tech. Rep., 1992. 2.2.3

[23] R. König, P. Krauspe, and G. Schänzer, "Preceures to improve Flight Safety in Wind Shear Conditions," *Proceedings of the 12th Congress of the International Council of the Aeronautical Sciences*, 1980. 2.2.3

[24] G. Schänzer, "The Effect of Gust and Wind Shear for Automatic STOL Approach and Landing," *AGARD Conference Proceedings CP 140, Flight in Turbulence*, 1973. 2.2.3

[25] R. Brockhaus and P. Wüst, "Open Loop Compensation of Wind Shear Effects in Low Level Flight," *AGARD Conference Proceedings CP 240 .Guidance and Control Design Considerations for Low Altitude and Terminal Area Flight*, 1977. 2.2.3

[26] J. Borowski and W. Sobieraj, "The Effect of Automatic Flight Control System Structure on Attenuation of the Short-Period Aircraft Vibrations due to Atmospheric Turbulence," *Journal of Theoretical and Applied Mechanics*, pp. 67–80, 1998. 2.2.3

[27] M. V. Cook, *Flight Dynamics Principles*, 2nd ed. Elsevier Ltd, 2007. 3.1.1, 3.4.1, 3.4.1, 4.5.1.2, 4.5.2.1, 4.5.2.2, 4.5.2.3, 4.5.2.3

[28] J. H. Blakelock, *Automatic Control of Aircraft and Missiles*, 2nd ed. John Wiley and Sons, 1991. 3.2, 3.2, 3.2, 3.2

[29] L. V. Schmidt, *Introduction to Aircraft Flight Dynamics*, 2nd ed. AIAA education series, 1998. 3.3.2

[30] M. C. Koen, "Modelling and Simulation of an RPV for Flight Control System Design Purposes," Department of Electronic and Computer Engineering, University of Pretoria, 2006. 3.4.2, 3.4.2

[31] M. Nita and D. Scholz, "Estimating the Oswald Factor from Basic Aircraft Geometrical Parameters," *Deutscher Luft-und Raumfahrtkongress*, 2012. 3.4.2, B.2

[32] R. S. Shevell, *Fundamentals of Flight*, 1st ed. Prentice-Hall, 1983. 3.4.2

[33] W. Beeton, "Fault Tolerant Flight Control of a UAV with Asymmetric Damage to its Primary Lifting Surface," Master's thesis, Stellenbosch University, 2013. 3.4.2, 8.2

[34] I. K. Peddle and J. A. A. Engelbrecht, "Introductory Course to Aircraft Dynamics," Advanced Automation 833 course notes, 2015. 3.4.4, 4.1, 4.3, 4.3, 5.1, D.1.4.1

[35] G. E. Urroz, *Solution of Non-linear Equations*, Utah State University, September 2004. 4.1

[36] M. Cavcar, "Stall speed," PLT 225 Aerodynamics course notes, 2014. 4.5

[37] D. A. Caughey, "Introduction to Aircraft Stability and Control," Course Notes for MAE 5070, 2011. 4.5.1.1, 4.5.1.2

[38] T. A. Talay, *Introduction to the Aerodynamics of Flight*, 1st ed. National Aeronautics and Space Administration, 1975. 4.5.2.2

[39] J. R. Raol, G. Girjia, and J. Singh, *Modelling and Parameter Estimation of Dynamic Systems*, 1st ed. Institution of Engineering and Technology, 2004. 4.5.3, 4.5.3

[40] J. Gera, "The Influence of Vertical Wind Gradients on the Longitudinal Motion of Airplanes," National Aeronautics and Space Administration, Tech. Rep., 1971. 4.5.4, 4.5.4

[41] W. J. G. Pinsker, "The Control Characteristics of Aircraft Employing Direct-Lift Control," Aeronautical Research Council Reports and Memoranda, Tech. Rep., 1970. 5.2.2, 5.2.2, 5.2.2, 5.2.2

[42] L. J. Clancy, *Aerodynamics*, 1st ed. Pitman Publishing Limited, 1975. 7.1.1

[43] Federal Aviation Administration, *Pilot's Handbook of Aeronautical Knowledge*, U.S. Department of Transportation, 2016. 7.1.1, 7.1.1

[44] D. G. Hull, *Fundamentals of Airplane Flight Mechanics*, 1st ed.   Springer, 2007. 7.1.1

[45] U.S. Department of Defence, *Flying Qualities of Piloted Aircraft MIL-F-8785C*, Washington, November 1980. 7.1.4.1

[46] ——, *Flying Qualities of Piloted Aircraft MIL-HDBK-1797*, Washington, June 1995. 7.1.4.2, 7.1.4.3, E.1

[47] J. R. Raol, G. Girija, and J. Singh, *Modelling and Parameter Estimation of Dynamic Systems*, 1st ed. The Institution of Engineering and Technology, 2004. 8.6, 8.6

[48] C. K. Fourie, "The Autonomous Landing of an Unmanned Helicopter on a Moving Platform," Master's thesis, Stellenbosch University, 2015. 9.3

[49] R. Hibbeler, *Engineering Mechanics: Dynamics*, 12th ed.   Prentice Hall, 2010. A.1.4